SIGNAL INTERACTIONS BETWEEN LIDAR SCANNERS

A Dissertation
Presented to
The Academic Faculty

by

Gerald B. Popko

In Partial Fulfillment
of the Requirements for the Degree
Master of Science in the
School of Electrical and Computer Engineering

Georgia Institute of Technology
MAY 2019

SIGNAL INTERACTIONS BETWEEN LIDAR SCANNERS

Committee Members:

Dr. Christopher Valenta, Advisor
Georgia Tech Research Institute
Georgia Institute of Technology

Dr. Thomas Gaylord, Co-Advisor
School of Electrical and Computer Engineering
Georgia Institute of Technology

Dr. Gee-Kung Chang
School of Electrical and Computer Engineering
Georgia Institute of Technology

Dr. Andrew Stark
Georgia Tech Research Institute
Georgia Institute of Technology

Date Approved: March 29, 2019

To my amazing wife, Amy

ACKNOWLEDGEMENTS

Thank you to my advisor, Dr. Christopher R. Valenta, and co-advisor, Prof. Thomas K. Gaylord, for their tireless support in this academic venture. Your guidance, wisdom, and patience have been well balanced in allowing me to learn through self-discovery and failure. Your enthusiasm for the work and ever questioning inquiry was infections, which I hope to carry with me throughout my life.

Thank you to Yijun Bao for your large contributions to Chapter 4 of this work. Your extraordinary analytical and theoretical attention to detail were instrumental in the quality of the material. Your approach to problem solving, particularly with visual representation, left an impression on me from which I hope to draw from throughout my career.

To the team at GTRI's Electro-Optical Systems Laboratory, thank you for your tireless patience and unquestioning support to help me with equipment and resources. Your technical knowledge and creativity were inspiring. Aside from directly assisting me in my research, thank you for your work towards supporting the country with innovative and technical solutions.

Thank you to my family for their continual support and unwavering insistence on education. I am eternally grateful to you for imbuing onto me my love of learning. You have all embodied the importance of an inquisitive and open mind.

And finally, but not least, thank you to my amazing and beautiful wife, Amy. Thank you for your unbelievable support throughout not only graduate school, but my career. You

have wholeheartedly supported my interests and never doubted my motivations to pursue them. Your academic drive has been equally as inspiring. I love you.

TABLE OF CONTENTS

LIST OF TABLES

LIST OF FIGURES

and d) total occurrences of interference events as a function scan angle. The normalized inverse pathlength squared between scanners and the wall by scan angle is overlaid on (d) to facilitate comparison for radiometric considerations

LIST OF SYMBOLS AND ABBREVIATIONS

2-D, 3-D	two and three dimensions, respectively
A	amplitude of continuous wave signal
AMCW	amplitude modulated continuous wave
APD	avalanche photodiode
c	the speed of light
CW	continuous wave
EXNOR	Boolean logical EXCLUSIVE NOR operation
F	fraction of time (or angular orientations) two lidars' beams intersect over a full period of angular orientations between two scanners
$\tilde{F}$	Fraction of time (or angular orientations two lidars' beams intersect over a single rotation of one lidar
f_2/f_1	the ratio of rotational frequencies of lidar scanners 1 and 2
f_2'/f_1'	the ratio of rotational frequencies of lidar scanners 1 and 2 equivalent to the reciprocal of f_2/f_1
f_m	rotational frequency of lidar scanner m
f_{mod}	modulation frequency of continuous wave signal
FOV	field-of-view
GmAPD	Geiger-mode avalanche photodiodes
h	distance from the center of the cord connecting two lidar scanners to the center of the circle formed by the locus of the two scanners' intersection points
L	distance between lidar scanner in the two-lidar reference frame
lidar	light detection and ranging
LOS	line of sight
m	lidar scanner number

MOSARIM	More Safety for All by Radar Interference Mitigation
N_m	number of turns of lidar scanner m to evaluate a full temporal period of intersection
n	index of refraction
n_m	integer number of rotations lidar scanner m has completed starting with 0
NIR	near infrared
p_m	sequentially numbered pulse from lidar scanner m
PRF	pulse repetition frequency
R	range to target
r	the center of the circle formed by the locus of two scanners' intersection points
$s\{\theta(t)\}$	square wave function of a scanner's angular orientation
$s_F(t)$	square wave function for intersection between two rotational beams
SWaP	size, weight, and power
T	combined period of angular orientations between two lidar scanners
T_m	period of a single rotation of lidar scanner m
t	time
TDC	time-to-digital converter
TOF	time of flight, referring to the ranging methodology
Δt	round trip time or time of flight of a lidar signal, referring to the quantity of time
$\Delta_{\Theta,\theta}$	translation angle between two-scanner reference frame and single-scanner reference frame
$\Delta\theta$	difference between instantaneous angular orientations of two lidars' beams
$\Delta\theta''$	interior vertex angle of $\Delta\theta$
$\Delta\theta_0$	difference between initial angular orientations of two lidars' beams

$\Delta\phi$ phase difference of modulated continuous wave signal

Θ_m instantaneous scan angle of scanner m's beam relative to the lidar's scan angle field-of-view

$\Theta_{m,0}$ scan angle reference phase of scanner m defined as the scan angle orientation at time equal to zero

$\Theta_{m,total}$ total scan angle or scan field-of-view of scanner m

θ_r optical angle of incidence

θ_m instantaneous angular orientation of lidar m's beam relative to a another lidar's location

$\theta_{m,0}$ initial angular orientation of lidar beam

$\theta'_{m,0}$ initial angular orientation of lidar m with rotational frequency f'_m

$\theta''_{m,0}$ interior vertex angle to $\theta_{m,0}$

θ_r optical angle of reflection

ν speed

ϕ phase of modulated continuous wave signal

$\cdot$ Boolean logical AND operation

$\odot$ Boolean logical EXCLUSIVE NOR (EXNOR) operation

$+$ Boolean logical OR operation

$\overline{}$ Boolean logical NOT operation

SUMMARY

Light detection and ranging (lidar) is used for obtaining precision spatial data to aid autonomous vehicle navigation. However, little published work exists regarding signal interference between lidar devices. Lidar signal interference is the undesired reception of signal energy that may compromise the accuracy of spatial data. A theory of lidar interference is presented which characterizes two types of interference – direct and scattered interference. Direct interference results from the direct coupling of light from a second lidar into the lidar's receiver. Scattered interference results from the detection of another lidar's light scattered from a target. Both can result in erroneous ranging data.

A mathematical model is presented that describes the limits and occurrences of scattered interference. The upper limit of scattered interference is the fraction of beam intersection time between two lidar scanners and shown to have a minimum and maximum value of 0 and $1/2$, respectively, with most scanner arrangements converging to $1/4$. The concept of intersection point density is introduced from the locus of the beams' intersection points and shown to be a predictor of scattered interference.

Five test case experiments were conducted that demonstrated the occurrence of lidar interference. Angularly, direct interference is shown to be categorized by a higher occurrence of out-of-tolerance points while scattered interference results in larger average of ranging errors. A Monte Carlo simulation is presented that models the interference between two lidars using the proposed theory. A comparison of the simulated and experimental results demonstrates the theory's general explanation of lidar interference occurrences, while further refinement may be found from radiometric considerations.

CHAPTER 1. INTRODUCTION

Key Conclusions:

- **Light detection and ranging (lidar) devices are used to obtain precision spatial measurements using light.**
- **Lidar scanners are a popular sensing technology to enable autonomous vehicle navigation.**
- **Signal interference between lidar devices can occur if multiple devices are located within range of each other potentially compromising the integrity of ranging data.**
- **Little published work exists that explains the mechanisms and effects of lidar interference.**
- **This thesis proposes lidar interference theory, presents analytical tools for analyzing lidar interference, experimentally analyzes lidar interference, and evaluates the theory against experimental observation by way of a Monte Carlo simulation.**

Light detection and ranging (lidar) uses light from a laser source and the speed of light to measure the range to a target. Its development has spanned over 50 years, with some of it first uses in 1962 to measure the distance of the moon – a feat eventually demonstrated to accuracy of within 3 cm [1, 2]. As far back as 1965, it has been vehicle mounted for spatial mapping with its first primitive uses on aircraft [3, 4]. Though its roots were as a niche technology, today lidar continues to penetrate many applications of remote

sensing and automated control. Lidar has found uses in forestry [5], cartography [6], military [7], coastal mapping [8], aircraft power line detection [9], wildlife surveys [10], infrastructure monitoring [11], and spacecraft navigation [12] applications to name a few. But perhaps most popularized is lidar's keystone potential in developing commercial autonomous vehicles that will likely require lidar as an integral part of the vehicles' suite of sensors [13].

Lidar represents a popular paradigm for autonomous vehicle sensing technology. Complimenting millimeter radar, ultrasonic sensing, and chromatic imaging, it can enable autonomous vehicle navigation by offering real-time detection of targets [14]. Of all these sensing methods, lidar can offer some of the highest range resolutions. However, navigation decisions will rely on the accuracy of these sensing technologies and preserving their sensing integrity will be key in these future applications.

Likely due to the historic cost of laser sources and optics, alongside the large amounts of data lidar's produce, lidar employments were exclusive, making it generally been prohibitive to deploy large numbers of sensors at a time. Accordingly, signal interference risks between lidar scanners – the undesired reception of energy that compromises a desired signal – were inherently low. However, technology trends suggest that lidar costs will continue to drop, sensors will be increasingly more power efficient, and processing capability will be increasingly easier to obtain [15, 16]. With these trends, the technology will logically proliferate. Therefore, manufacturers must prepare to contend with unprecedentedly dense sensor environments out of which the risks and effects of lidar signal interference are widely unknown.

Despite the technology's wide spread use over the last several decades, little published information exists in the public domain regarding the extent and effects of signal interference between lidar sensors.

1.1 Demonstrations of Interference

Given the scarcity of publications, preliminary studies are solely referenced to justify the occurrence of lidar interference. Perhaps the most widely cited of these works is [17, 18]. These works demonstrated that two lidars with common scanning angles will induce signal interference. Qualitatively, the group showed that ranging errors manifested from these occurrences by plotting recorded erroneous ranging points against actual target locations. Beyond this, the team assessed the occurrence of successive interference events and gave cursory interference theory in the work's introduction. The team introduced the terms "direct" and "indirect" in reference to interference. However, the work did not investigate the magnitude of the resulting ranging error, nor did it attempt to categorize these occurrences despite some readily evident differences in the events. Moreover, the method the team used to identify interference events applied arbitrary tolerances that may have over identified some instances of interference, while not counting others. In the end, these investigations left much in the way of further inquiry into developing a satisfactory understanding of lidar's interference mechanisms and effects.

Diehm et al [19] found similar results to [17, 18] and partially expanded their analysis into the temporal occurrence of the phenomenon. From their investigation, the team proposed data processing methods to reduce the effects of mutual interference in the resultant data product. Their method utilized a spatio-temporal filtering algorithm to

identify outliers between three consecutive point clouds (groups of ranging points). These outliers were then removed from the interpreted spatial data. However, the team's analysis still left much unanswered about the specific mechanisms and effects of lidar interference. As a result, without a thorough understanding of lidar interference's behavior, it may be premature to propose algorithms that attempt to characterize and remove spatial data.

1.2 Lidar Hacking

Outside of the unintended occurrences of interference, there are bodies of work from security researchers that explore the possibilities of intentional attacks on lidar sensors with a focus on autonomous vehicle applications. Petit et al [20] demonstrated that erroneous ranging data could be remotely introduced into a lidar sensor by using an in-band optical source. Shin et al [21] expanded this work by demonstrating the ability to directly incapacitate and trick a common, commercially available lidar, the Velodyne VLP-16. The team demonstrated attacks by way of sensor saturation – overloading the input signal – and signal spoofing – the deception of a receiving sensor – with a laser source [21]. These works highlight the vulnerabilities of lidar devices to interference events; however, they focus on the intentional, malicious disablement or deception of the sensor. What is not explained is the inherent interference risk that exists in the normal, coincidental operation of two or more sensors. Moreover, [20] and [21] both proposed solutions to overcome sensor attacks, which both included sensor redundancy. However, this would likely compound the risk to inter-device interference since it would set to increase the number of in-band sources on the roadway.

1.3 Lidar Designs Against Interference

Despite the lack of published work to explain lidar interference, there are a number of research groups who claim to have designed “interference immune” or “resistant” lidars [22-27]. These designs attempt to use modulating methods to encode their device’s ranging signal such that it remains uniquely identifiable in the presence of other in-band signals. These proposed designs may ensure the fidelity of a received ranging pulse such that the device can discriminate against the erroneous interpterion of another device’s signal.

Of these works, [22] presented preliminary theory of interference in the introduction of their work. However, this work only identified cursory, hypothetical situations. Furthermore, the theory only described interference in terms of the lidar range equation (discussed in Section 2.1), the number of photons exchanged, and probability of detection. The impetus of this theory was to support a statistical strategy for interference mitigation in a niche type of lidar – Geiger-mode avalanche photodiode (GmAPD) lidar, which are discussed briefly in Section 2.1.3. However, GmAPD lidar is not representative of the most widely used types of lidars in autonomous vehicle testing today, which is overwhelmingly found to be pulsed lidar [28]. As a result, the limited theory only addresses probabilistic detection problems which are unique to GmAPDs and not directly extendable to the mainstream methods of lidar detection.

Though these groups have demonstrated innovative solutions for multiplexing lidar signals, they avoid adequately addressing instances where these sensors are blinded by the direct illumination from another source as demonstrated by [20] and [21]. Furthermore, many of these techniques utilize niche technologies that are not representative of the bulk, commercially viable solutions implemented in autonomous vehicle testing today [28]. Therefore, without understanding the scope of the problem, the direction of the lidar

community remains uniformed as to the optimal way of preventing this undesirable phenomenon.

1.4 Radar Interference

Despite the underdeveloped understanding of lidar interference, extensive analysis has been conducted for interference in lidar's close relative, radar [29-41]. One such large scale study was conducted for mutual interference between passenger vehicle radar sensors by the European Union. It included a 36 month comprehensive study called More Safety for All by Radar Interference Mitigation (MOSARIM) [31]. The investigation's conclusion found that automotive radar interference is detectable at close ranges, and it is most likely to manifest itself as an increase in signal noise [30]. This event could result in the failure to detect a target if the target's return signal strength fell below the noise floor. For vehicles relying on these sensors for navigation and braking, this situation could result in a collision.

However, given the high directivity of lasers, modulation methods, and beam steering techniques; lidar interference analysis is expected to differ from that of radar. Despite this, the few lidar interference related works today use radar references without fully extending the theory. Moreover, the vehicle radar interference analysis conducted by MOSARIM lagged commercial deployment of vehicle radar technology. One can imagine that such studies could discover unrealized but avoidable safety consequences that may risk lives and threaten a newly forming industry still in its infancy. Therefore, it is critical that lidar technology is designed to mitigate interference with future proliferation in mind rather than as an afterthought. As such, theory needs to be developed to assess the potential

and effects of lidar signal interference so that sensors may be designed to minimize this risk.

Table 1 provides a summary of the primary literature for lidar interference and its related works. Given the lack of lidar interference theory and [17, 18]'s centrality to current lidar interference related work, this thesis set to validate and extended the analysis of [17, 18]. Though much original theory is introduced by this thesis, the experimental work by [17, 18] formed the trajectory off of which to investigate.

This work proposes a theory of lidar interference. This theory develops the classification for two distinct lidar interference phenomena – direct and scattered interference. Direct interference will be shown to occur over the angular limits that which two lidar scanners are directly observing/illuminating each other. On the other hand, scattered interference will be shown to be a function of both target geometry and beam path intersection between an interference source and the victim receiver. Mathematical models and geometric interpretations will be introduced for analyzing this geometry. The analysis of experimentally measured interference will be presented the which supports the classifications of and distinction between direct and scattered interference. Finally, a simulation that utilizes the geometric assumptions of lidar interference occurrences is compared to the experimentally measure results to assess the validity of the theory. The end state of this work is to establish a theoretical foundation that may guide future interference inquiry and the lidar community to make informed engineering decisions to mitigate lidar interference risks.

Table 1 – Summary of lidar interference and related literature.

Author	Type of Work	Contribution	Theory for Interference	Interference Work Cited
Brooker, 2007 [35]	Peer-Reviewed Journal	Probability of millimeter-wave radar interference	Radar only	Various radar publications
MOSARIM, 2012 [30-34, 38, 39, 41]	Joint Government and Industry Investigation	Vehicle Radar Interference	Radar only	Original Testing
Kim, 2015 [17, 18]	Conference Paper	Demonstrated lidar interference	Cursory	Brooker [35], MOSARIM [31], Various radar publications
Petit, 2015 [20]	Conference Paper	Demonstrated lidar attack	No	None
Al-Hourani, 2018 [29]	Peer-Reviewed Journal	Stochastic Modeling for Radar Interference	Radar only	Brooker [35], Various radar publications
Shin, 2017 [21]	Conference Paper	Demonstrated commercial lidar blinding and spoofing	No	Petit [20], Various radar publications
Zhang, 2017 [22]	Peer-Reviewed Journal	Statistical method for GmAPD interference avoidance	Cursory/ limited utility/ not experimentally validated	Brooker [35], Al-Hourani [29], Kim [18], Various radar publications
Fersch, 2017 [26]	Peer-Reviewed Journal	Design of CDMA lidar for interference robustness	No	None
Diehm, 2018 [19]	Conference Paper	Demonstrated lidar interference and interference filtering algorithm	Cursory	Kim [18], Various radar publications
Cheng, 2018 [25]	Peer-Reviewed Journal	3D Pulsed Chaos lidar reported to be interference resistant	No	Kim [18], Petit [20]

CHAPTER 2. BACKGROUND

Key Conclusions:

- **Lidar technology has several variants based on application, method of measuring range, and how the devices is directionally scanned.**
- **Autonomous vehicle concepts commonly use pulsed lidars which measure the range to a target by recording the round-trip time a pulse of laser light takes to travel to and return from the target.**
- **Beam steering techniques are used to achieve spatial awareness along more than one direction with pulsed lidars commonly using a rotating mirror to direct the transmitted laser and received pulse.**

Lidars are used in several remote sensing applications. Bathymetric lidars seek to range targets below the surface of water, while atmospheric lidars provide a profile of atmospheric conditions [15]. In autonomous vehicle navigation, hard target lidars are used to identify obstacles and paths for vehicle navigation. Hard target lidars use a ranging signal and the speed of light to measure the range to a target. To achieve spatial awareness beyond a single direction, they employ beam steering techniques. One popular such method of beam steering it to circularly scan the lasers beam by way of rotating a mirror or other optical method. Therefore, this construction will be the primary focus of this work. Beyond beam steering techniques, hard target lidars employ several methods of ranging targets. An understanding of each facilitates a better understanding of how lidar interference may occur.

2.1 Ranging Methods

Hard target lidar ranging methodologies can be generally put into three categories: time of flight (TOF), phase comparison, range encoded intensity [42]. This thesis will focus on the first two methods as they are commonly discussed in modern lidar literature. Range encoded intensity, is a less common, older form of lidar ranging not widely pursued for autonomous vehicle applications at this time. TOF lidar are generally classified as pulsed systems, however, there are alternative ranging methods that can be broadly considered TOF systems such as 3-D flash lidar and Geiger-mode avalanche photodiode (GmAPD) lidar. Phase comparison lidars are generally understood to employ modulated continuous wave laser sources.

2.1.1 Pulsed Lidars

A pulsed lidar, shown in Figure 1, uses precision timing circuitry to record the time it takes for a pulse of laser light to travel from the lidar's laser transmitter to a target and back to the receiver. If enough of the scatter pulse is returned to the receiver – determined by a detected light intensity threshold – the lidar records the time the return pulse is received. This elapsed time Δt represents the round-trip time it took the pulse of light to travel to and return from the target. Since the speed of light c is well known, solving for the target's range is straight forward. The range to the target R is calculated by multiplying the elapsed time by the speed of light and dividing by two (accounting for the roundtrip distance). The resulting equation for the target's range R is commonly referred to as the lidar ranging equation and is given by [43]

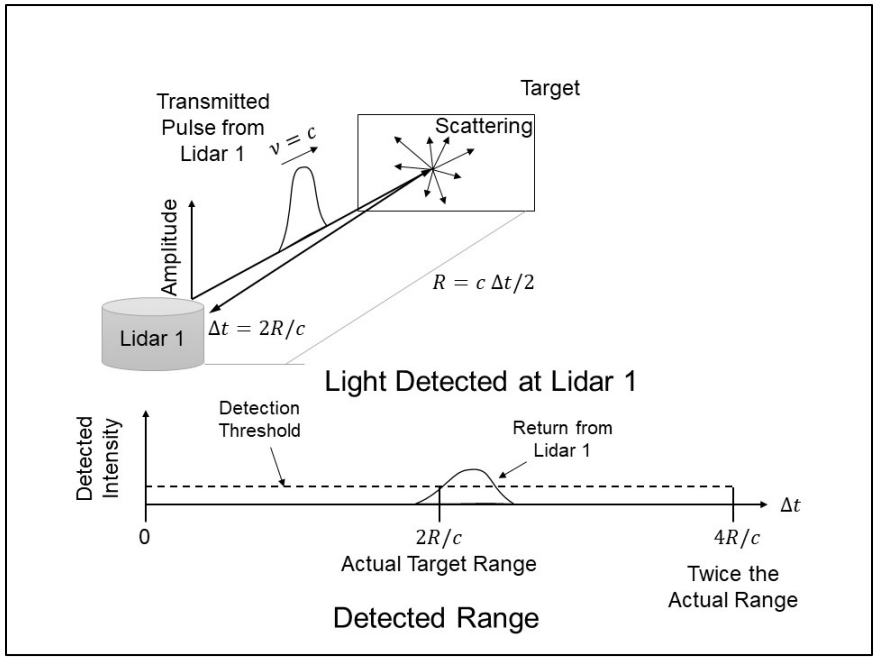

Figure 1 – Basic operating principles of a pulsed or time-of-flight (TOF) lidar.

$$R = c\frac{\Delta t}{n2}. \tag{1}$$

Here n is the index of refraction of the transmission medium which is typically taken to be unity for air. Given the method of measuring, these systems are also referred to as time-of-flight (TOF) lidars. The range along with its azimuth (scan angle) define a point in space representative of a target. The collection of these points is commonly referred to as a point cloud. These can be either a 2-D profile in a single plane or 3-D representation for multiple scan planes.

The lidar's transmitted ranging signal is commonly referred to as its transmitted pulse, while the scattered signal that is returned to the detector is referred to as the return or echo. The rate at which ranging pulses are transmitted is called the pulse repetition frequency (PRF) expressed in Hz (pulses per second). A lidar's PRF along with its

rotational frequency determine the density of points and the angular resolution between sequential pulses.

Another performance measure of a pulsed lidar is its ability to record the range of a single return or multiple returns per transmitted pulse. Single return lidars just record the range for one target per transmission of a ranging pulse. This is generally taken to be the first return outside of the lidar's minimum range that satisfies the detection threshold. Multiple return lidars can record the ranges to more than one return per pulse transmitted. Multiple returns can arise when partially transmissive targets exist along the transmission axis. These may include glass, water, foliage, smoke, or fog. These lidar's are further quantified by the number of returns they are capable of recording per ranging pulse.

2.1.2 Continuous Wave Lidar

A continuous wave (CW) lidar works by temporally modulating a CW laser and detecting the modulation's delay in the returned signal. Though several methods of CW lidars exist, Figure 2 shows an example of a CW lidar using amplitude modulation in what is referred to as an amplitude modulated continuous wave (AMCW) lidar [44]. In this example, the laser's amplitude is modulated with a frequency f_{mod}. The modulated signal is optically split, with a portion of the signal transmitted and the other portion diverted to be used as a reference. If a target is present, the transmitted waveform is scattered. If the signal returns to the receiver with enough energy, the received waveform is compared to the reference waveform to determine the phase difference $\Delta\phi$ between the two periodic functions. This phase difference $\Delta\phi$ is given by

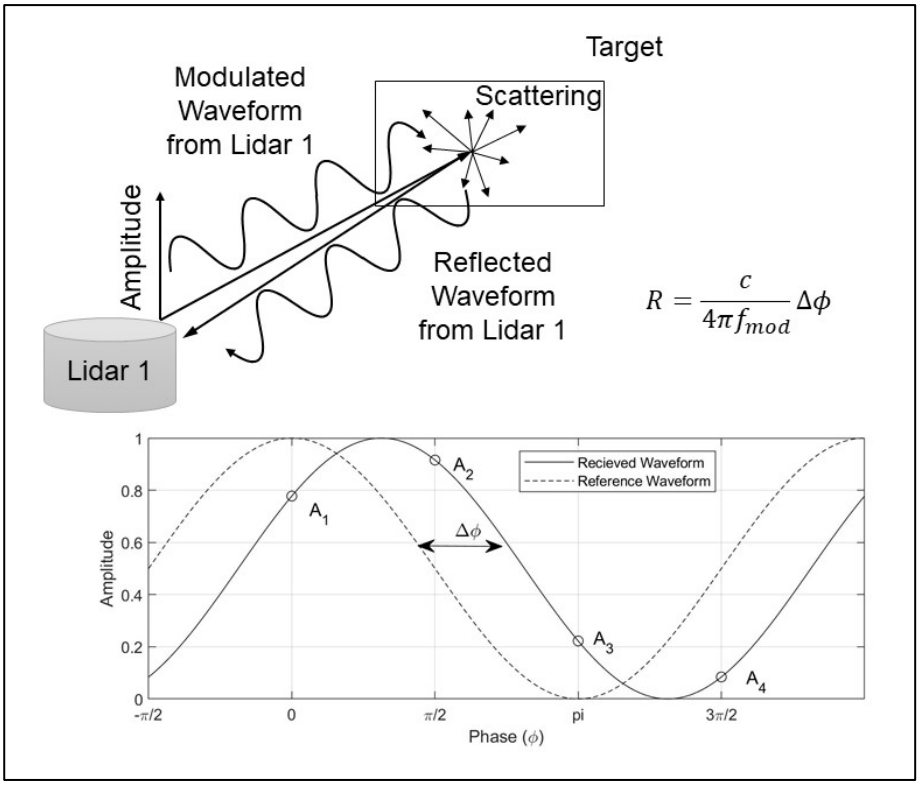

Figure 2 – Basic operating principles of a continuous wave (CW) lidar.

$$\Delta\phi = 2\pi f_{mod}\Delta t \tag{2}$$

where Δt is the time delay between the two periodic functions, thus representing the time of flight of the transmitted beam. Solving for the time of flight yields

$$\Delta t = \frac{\Delta\phi}{2\pi f_{mod}}. \tag{3}$$

Substituting (3) into the lidar range equation (1) yields the phase comparison range equation given by

$$R = \frac{c}{4n\pi f_{mod}}\Delta\phi. \tag{4}$$

If amplitude modulation is used, four measurements of the amplitude (A_1 through A_4) sampled at a fourth of the modulation frequency ($f_{mod}/4$) can yield the phase difference $\Delta\phi$ by the relation [45]

$$\Delta\phi = \arctan\left(\frac{A_4 - A_2}{A_1 - A_3}\right). \quad (5)$$

Another popular variant of CW employs frequency modulation in what is called frequency modulated continuous wave (FMCW). This is done using the same principle, except that the laser's frequency is modulated rather than its intensity.

Of note, for illustrative purposes Figure 2 shows the waveform repeating itself several times over the transmission between the lidar and target. However, a waveform of this high modulation frequency would result in a negative effect known as range ambiguity and therefore, the modulation frequency should be less that the inverse of the round-trip time to avoid this effect.

Just as with pulsed lidar, the range and scan angle define a target's location with a point. The frequency at which phase shift is sampled along with the scanning rate defines the density of the resulting point cloud.

2.1.3 Alternative Ranging Methods

Several other ranging methods exist that are considered for use in autonomous vehicles. For completeness two popular methods will be briefly presented, though to constrain the foci of the study, will not be consider in depth. Namely, these two methods are 3-D flashing imaging and Geiger-mode avalanche photodiodes lidars.

2.1.3.1 3-D Flash Imaging

3-D flash imaging is a lidar technique that seeks to image a target area within a single field-of-view (FOV) [46]. This technique is accomplished by flooding an area with light and focusing the returned image onto a 2-D detector array. Each pixel then returns ranging information for a subtense of the detector's FOV, in turn, producing a three-dimensional image. The width and height of the array captures two dimensions while the range information obtained by each pixel captures the third dimension. The advantages are that flash lidars can scan at much slower rates as compared to single pixel detectors and obtain higher point cloud densities, thus reducing the system's size, weight and power (SWaP) [43].

2.1.3.2 Geiger-mode Avalanche Photodiodes

Geiger-mode avalanche photodiodes (GmAPDs) are a type of avalanche photodiode (APD) that are biased above their breakdown voltage [47]. The result is an extreme receiver sensitivity that can detect individual photons [48]. Nonetheless, these devices use the same TOF principles as pulsed systems. However, due to the exponential amplification of the receiver, the detection of photons is a binary event and temporal resolution is lost in the return waveform due to the detector's deadtime between detection events. To balance the extreme sensitivity of the receiver, GmAPD lidars transmit with only enough power to return a relatively low number of photons. By using the cumulative density function of the returned photon's binomial distribution, return detection is determined statistically depending on the desired tradeoff between the probability of a false alarm (detecting a return when one is not present) and the probability of detection [49, 50].

Once a return is detected, the TOF is recorded and the target's range is determined in the same way as described for pulsed systems.

In any of these ranging methods, the introduction of foreign in-band energy can compromise the detection of the ranging signal. Due to their popularity in many commercial hard target lidars, this thesis focuses on the application of circularly scanning, pulsed lidar systems. However, further investigation is warranted into the effects of inference in all cases.

CHAPTER 3. PROPOSED THEORY

Key Conclusions:

- **Signal interference can compromise the integrity of a desired received signal.**
- **Lidar interference sources include other in-band optical source, solar radiation, and other lidar scanners.**
- **By considering ray tracing, two cases of lidar interference can be identified – direct and scattered interference.**
- **Direct interference occurs when two lidar scanners are oriented/emitting directly at one another and the energy from one device is coupled into the other.**
- **Scattered interference occurs when the ranging signal from a harassing lidar is scattered from a target and received by a victim scanner.**
- **By assuming a coaxial receiving/transmitting lidar design, scattered interference may be further extrapolated to occur when the two lidars' beams intersect, and a target is present at the intersection point.**
- **Lidar interference can result in an increase of detector noise or the formation of false (ghost) targets.**
- **False targets may be near or far sided with respect to a real target depending on the timing of the received interference signal.**

3.1 Signal Interference

In signal detection, interference is the undesired reception of signals that distort, interrupt, or prevent the reception of a desired signal [51]. With regards to lidar, sources of

interference would include other radiation within the receiver's bandpass wavelengths (natural or artificial) and FOV that compete with the sensor's returned pulse. One likely source of interference would be other lidar devices – a situation expectedly common to encounter as the density of lidar enabled autonomous vehicles on roads increase. For interference between two lidars to occur, the signal from one system must be received and erroneously processed as a return by another. In discussions of interference taken from radar analysis, the device interpreting the interference is referred to as the *victim* and the device that is introducing the interference is referred to as the *harasser*.

3.2 Types of Signal Interference

By considering ray tracing, there are several district circumstances that could result in signal interference between two lidar scanners as shown in Figure 3 [52]. These can be

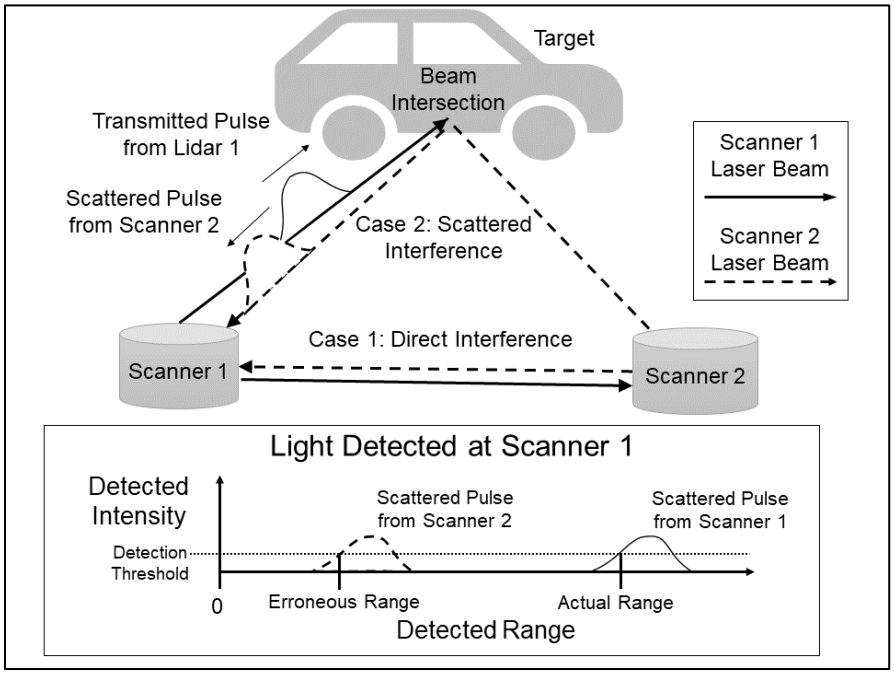

Figure 3 – Ray tracing examples of signal interference between two lidar devices showing two district cases of interference – direct and scattered interference.

referred to as direct and scattered interference. Direct interference occurs when two lidar's are oriented at each other and a signal from one is coupled into the other's receiver. Alternatively, scattered interference results when the target scattering of one lidar's signal is received by another. Scattered interference is similar to the concept of "indirect" interference proposed by [17], however, nuanced to represent the occurrence of the interference signal's scattering. In either interference case, the FOV of the victim and the beam divergence of the harasser determines the susceptibility of the victim to interference. The greater either of these values, the greater the susceptibility to inter-device interference. So, to minimize these implications and reduce the effects of optical noise, manufactures commonly engineer their device's FOV and beam divergence to be as narrow as possible.

3.2.1 Conditions of Interference

3.2.1.1 Direct Interference

For direct interference to occur, both lidars must be oriented such that light is coupled from one scanner to the other. Assuming a narrow FOV, this scenario would occur when both scanners are oriented/transmitting within the angular limits of the other scanner. Coupling has been hypothesized outside of these limits, however, this again becomes a function of FOV determining the victim's susceptibility to interference [21]. Quantifying these occurrences is rather rudimentary and becomes a function of the lidars' rotationally scanning frequency and the two scanners' angular widths.

3.2.1.2 Scattered Interference

For scattered interference to occur, two conditions must be met [52]. First, the victim lidar's FOV must intersect with the harassing lidar's beam divergence at the same point in the same epoch. Second, the signal from the harassing lidar must be scattered by a target and received by the victim scanner. By assuming a co-axial lidar receiver's FOV is engineered to match its laser beam divergence (to reduce optical background noise) this condition can be further simplified to occur when the two beams intersect, and a target is present as shown in case 2 of Figure 3 [52]. In other words, given the design of lidars, the beam path and FOV can be thought of as synonymous.

Since the nature of the surrounding targets is trying to be gleaned by the use of lidar, a probabilistic approach must generally be taken for which stochastic modeling methods exist to assess [29]. However, the occurrence of beam intersection is geometric and with the knowledge of the two scanners' operating parameters, is deterministic. Moreover, barring multiple reflecting surfaces, the amount that the two beams intersect becomes the upper limit that which scattered interference can occur.

3.2.2 Effects of Signal Interference

From studies of radar, interference effects can include increased receiver noise and the generation of ghost targets (targets that are not actually present) [30, 36]. Noise is all undesired signals that compete with a desired signal. These sources can be internal to the optical receiver, such as shot and thermal noise, or external, such as solar radiation from the sun. The summation of the noise standard deviations forms what is referred to as the noise floor. If the signal from a harasser falls below the criteria of the victim's receiver to register it as a return signal, then this interference would contribute to the noise floor. If

the noise floor becomes too high and the victim's ranging signal return falls below the noise floor, then the return may go without detection, resulting in the victim sensor failing to identify an actual target.

Alternatively, if a harasser's signal meets the victim lidar's detection threshold, the victim lidar could erroneously interpret this as a return and record a point, thus creating a false or ghost target. Either occurrence can be dangerous for an autonomous vehicle since decision algorithms could either fail to identify an actual collision risk or take evasive maneuvers to avoid a false target which may jeopardize the safety of those on the road. Such extreme cases can be mitigated by use of redundant sensors to validate targets, such as the use of radar and lidar together in autonomous vehicles. But without quantifying the extent of interference, the sufficiency of this redundancy cannot be ensured.

3.2.2.1 Ranging Errors

Figure 4 and Figure 5 show two examples of ranging errors resulting from scattered interference. These ranging errors are the deviation an erroneous return's range from an actual target along its transmission path.

In Figure 4, a waveform of a harassing lidar is scattered and returned to a victim lidar before the reception of the victim's ranging return. As a result, the lidar could erroneously register this as a false target that is closer than the actual target at that azimuth. Alternatively, Figure 5 shows an example of a far side ranging error. This event could result

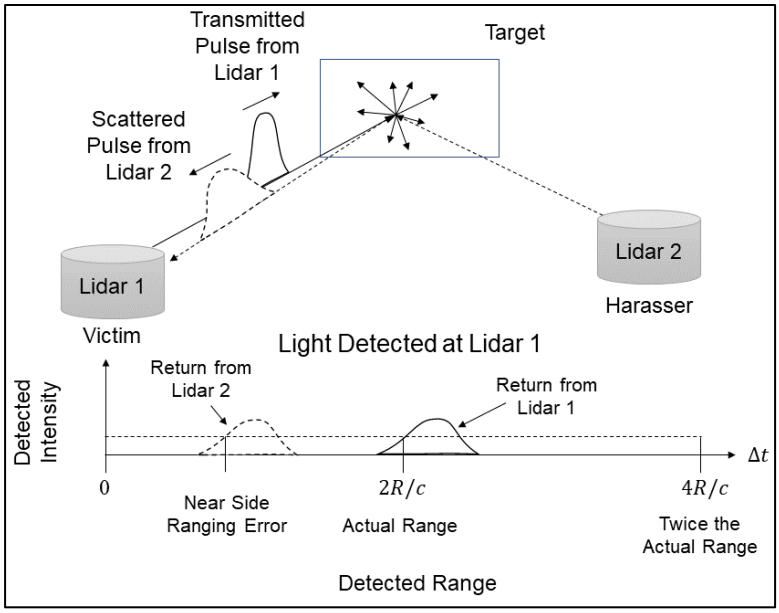

Figure 4 – The manifestation of near side ranging errors from scattered interference between two lidar sensors.

if the scattered waveform from a harassing lidar is received after the returned signal of the victim lidar along the same scan angle. The victim lidar may then incorrectly interpret this as another target at a farther range than the actual target.

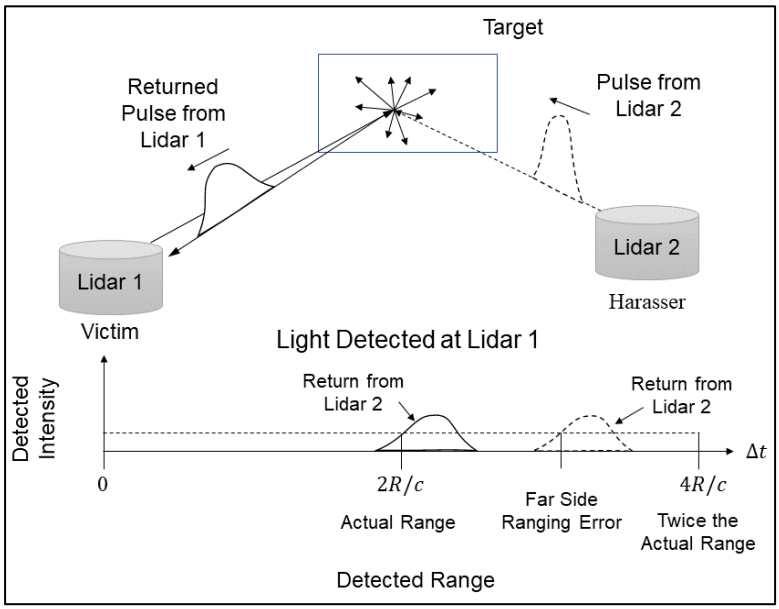

Figure 5 – The manifestation of far side ranging errors from mutual interference between two lidar sensors.

Assuming the transmission of ranging pulses between two lidars is not coordinated, the reception timing of these hypothesized signals should be stochastic. As a result, the repeated reception of these interference signals should form a generally uniform distribution of ranging errors spanning from the minimum to the maximum detection range of the victim lidar.

CHAPTER 4. QUANTIFYING SCATTERED INTERFERENCE WITH BEAM INTERSECTION

Key Conclusions:

- **The upper limit of scattered interference can be established by modeling beam intersection between two lidars.**
- **Beam intersection can be quantified by the fraction of time (or scanning angles), referred to as F, over which the two beams intersect through a unique period of the two beams rotations referred to at T.**
- **F is a function of the two scanners' rotational frequencies and reference phases.**
- **The lower and upper limits of F are 0 and $1/2$, respectively; however, these extrema represent a few special cases outside of which most combinations approach $1/4$.**
- **Arrangements of two, three, and four scanners can be achieved with zero intersection, given control over the scanners' locations, rotational frequencies, and reference phases.**
- **These limits can change if the two scanners are moving relative to one another.**

From Section 3.2.1.2, occurrences of scattered interference require beam intersection between two lidar scanners. Given knowledge or control over two scanners, their beam intersection is deterministic and potentially reducible, in turn, reducing the risk of scattered interference, independent of target locations. Moreover, the fraction of time

that these beams intersect forms a deterministic upper limit of interference between two scanners. Therefore, a quantitative description of intersection between two lidar scanner beams is desirable to understand the limits of scattered interference and mitigate its occurrence.

A mathematical description that quantifies beam intersection is presented. From this analysis, the scan frequencies and phases of the two scanners may be adjusted to minimize their intersection, in turn, minimizing scattered interference. Four configurations that produce zero intersection between two scanners are presented. By extension, configurations for three and four scanners with zero intersection are also presented for cases when control of the scanning frequency, phase, and location is available for each scanner. Each of these configurations then has the potential to greatly reduce the risk of interference between detectors. This chapter is the work presented in [52].

4.1 Two-Scanner Configuration

The geometric representation of a two-lidar reference frame is shown Figure 6. Each lidar scanner is represented by a point separated by a distance L. The two lidars scan $360°$ in the same plane and are assumed to have collimated (non-diverging), co-oriented FOVs and laser beams represented by rays. The rotational frequencies of scanners 1 and 2 are f_1 and f_2 with instantaneous angular orientation represented by θ_1 and θ_2, respectively. The instantaneous angle θ_m, where $m = 1$ or 2, is a function of time such that

$$\theta_m(t) = 360° \, f_m \, t + \theta_{m,0}, \tag{6}$$

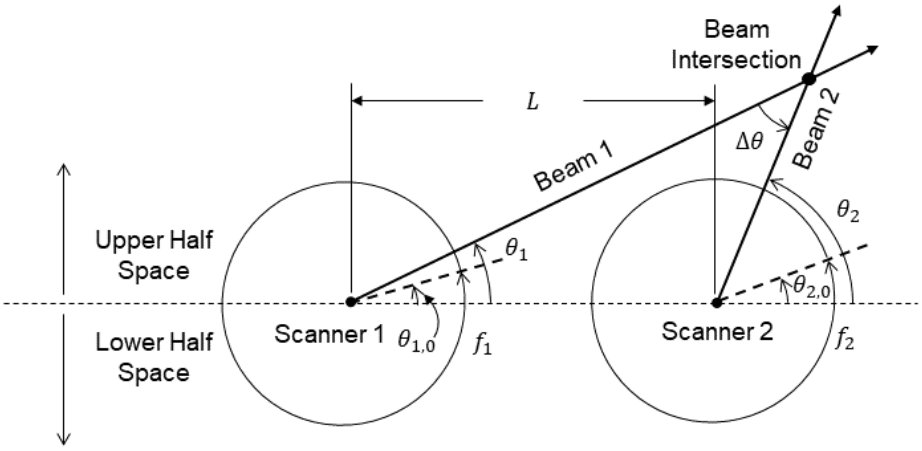

Figure 6 – Representation of two 360° lidar scanners, points 1 and 2, with geometric objects that depict their beam paths, rays 1 and 2, and angular orientations during scanning.

where t is the elapsed time and $\theta_{m,0}$ is the reference phase of the scanner. The reference phase is the initial angular orientation of the scanner at $t = 0$. The difference between the instantaneous angles is represented by $\Delta\theta$ where

$$\Delta\theta = \theta_2 - \theta_1. \tag{7}$$

The difference between reference phases $\Delta\theta_0$ is given by

$$\Delta\theta_0 = \theta_{2,0} - \theta_{1,0}. \tag{8}$$

For simplification in this work, unless otherwise stated, $\theta_{1,0}$ will be taken to be zero such that at $t = 0$ scanner 1 is pointing at scanner 2.

To extend the geometric model to pulsed lidar, time can be discretely represented by the lidar's PRF and the current sequentially numbered pulse from the lidar, p_m. Time can be then be expressed in terms of these values as

$$t = p_m / PRF_m. \tag{9}$$

Substituting Equation (9) into Equation (6) yields the instantaneous angular orientation as a function of discrete pulse number given as

$$\theta_m[p_m] = \frac{360°}{PRF_m} f_m p_m + \theta_{m,0}. \tag{10}$$

As shown, p_m starts at 0 and increments 1 for each subsequent pulse.

4.2 Beam Intersection

The amount of time, or angular orientations, over which two rotating beams intersect – and are susceptible to scattered interference – is a function of the two scanners' rotational frequencies and reference phases. To illustrate, the scanners may be simply visualized in the real-space representation which depicts the beam orientations in temporal snapshots through their rotational progression. Figure 7 shows an example in which the two scanners' rotational frequencies are equal, and scanner 2's reference phase $\theta_{2,0}$ equals

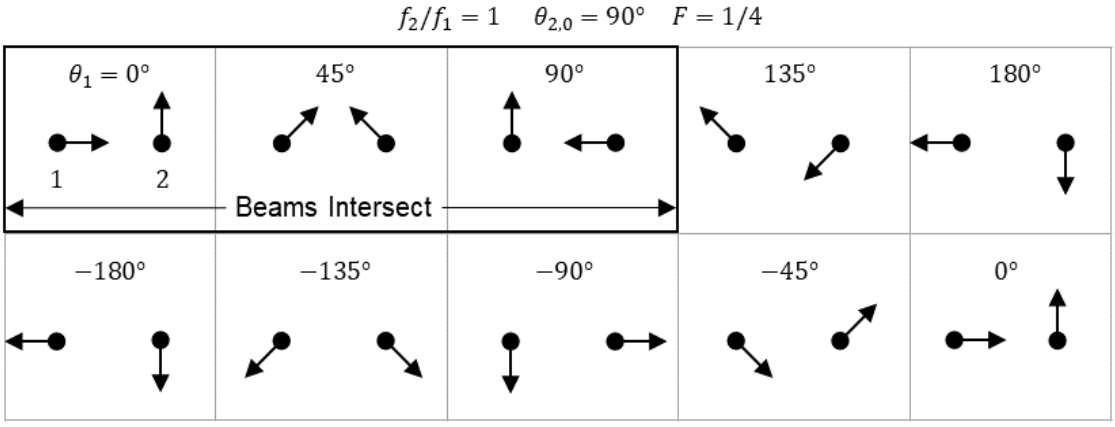

Figure 7 – Directions of the two scanners' beams rotating with a scan frequency ratio of $f_2/f_1 = 1$ and $\theta_{2,0} = 90°$, resulting in $F = 1/4$.

90°. If the ratio of the scan frequencies f_2/f_1 is rational and constant, then the angular relationship between the two scanners' beam orientations in time is a repeating pattern with a combined period T. In Figure 7, T is equal to the time to complete a single rotation of the scanners, since both scanners return to their starting orientations after a single rotation and the pattern between the two will repeat. The fraction of the time that two beams intersect during one combined period T is designated as F. In Figure 7, the beams intersect from $\theta_1 = 0°$ to 90°; however, through the remainder of T, the two beams do not intersect. From this depiction, $F = 1/4$ since $90°/360°$ or 25% of the rotational time the two beams are intersecting.

4.2.1 Fraction of Time Beams Intersect, F

F can equivalently be defined as the ratio of the angular orientations over which intersection occurs to the total angular range for one combined period T. That is,

$$F \equiv \frac{\text{time (or angular range) over which beams 1 and 2 intersect}}{\text{total time (or total angular range) for all possible rotation angle combinations}} \quad (11)$$

It is important to consider F in these terms for lidar, since the fraction of time is directly proportional to the fraction of points in a point cloud, and angular range is directly proportion to angular range of scan angles for target acquisition.

There exist two conditions for which scanners 1 and 2 have intersecting beams. The first occurs when the scanners' angular orientations, θ_1 and θ_2, are between 0° and 180° and θ_2 is greater than θ_1 (intersection in the upper half space). The second condition is when θ_1 and θ_2 are between $-180°$ and 0°, and θ_1 is greater than θ_2 (intersection in the

lower half space). No other combination of the scanners' angular orientations will result in the two beams' intersection.

For an irreducible, rational ratio of scanner frequencies f_2/f_1 expressed as

$$\frac{f_2}{f_1} = \frac{N_2}{N_1} = \frac{T_1}{T_2}, \tag{12}$$

N_1 and N_2 represent the number of rotations each scanner completes in a combined period T, and T_1 and T_2 represent the period of each scanner's single rotation. The combined period T can be obtained as

$$T = N_1 T_1 = N_2 T_2. \tag{13}$$

If the ratio of the scan frequencies f_2/f_1 is irrational, no repeating pattern occurs. As a result, T goes to infinity. In Figure 7, given that f_2/f_1 is unity, the two beams repeat their intersecting pattern every rotation and $N_1 = N_2 = 1$.

Using a square wave function $s\{\theta(t)\}$ to represent the time dependent, half space orientations of θ_1 and θ_2 and the inequality $\Delta\theta = \theta_2 - \theta_1$, each the parameters can be characterized as

$$s\{\theta_1(t)\} = +1 \text{ for } 0° < \theta_1 < 180° \text{ and } s\{\theta_1(t)\} = 0 \text{ for } -180° < \theta_1 < 0°, \tag{14}$$

$$s\{\theta_2(t)\} = +1 \text{ for } 0° < \theta_2 < 180° \text{ and } s\{\theta_2(t)\} = 0 \text{ for } -180° < \theta_2 < 0°, \tag{15}$$

and

$$s\{\Delta\theta(t)\} = +1 \text{ for } \theta_1 < \theta_2 \text{ and } s\{\Delta\theta(t)\} = 0 \text{ for } \theta_1 > \theta_2. \quad (16)$$

Using this notation, intersection between the two beams occurs when $s\{\theta_1(t)\} = s\{\theta_2(t)\} = s\{\Delta\theta(t)\} = 1$ (intersection in upper half space) or $s\{\theta_1(t)\} = s\{\theta_2(t)\} = s\{\Delta\theta(t)\} = 0$ (intersection in lower half space). A square wave function, $s_F(t)$ then describes when the beams intersect. The quantity $s_F(t)$, expressed in terms of Boolean logical operations, can be given as

$$s_F(t) = s\{\theta_1(t)\} \cdot s\{\theta_2(t)\} \cdot s\{\Delta\theta(t)\} + \overline{s\{\theta_1(t)\}} \cdot \overline{s\{\theta_2(t)\}} \cdot \overline{s\{\Delta\theta(t)\}} \quad (17)$$

where "$\cdot$" represents the Boolean logical AND operation, "$+$" represents the OR operation, and "$\overline{\ }$" represents the NOT operation. The function is equal to unity when the beams intersect and zero when the beams do not intersect. Other equivalent expressions for $s_F(t)$ are given in Appendix A.

To obtain F, the function $s_F(t)$ is integrated over a combined period T, then normalized. The resulting expression is

$$F = \frac{1}{T} \int_0^T s_F(\mathrm{t})\, dt, \quad (18)$$

where F is the time weighted average of $s_F(t)$ and depends on the parameters f_1, f_2, $\theta_{1,0}$, and $\theta_{2,0}$ and thus, $F = F(f_1, f_2, \theta_{1,0}, \theta_{2,0})$. When expressed as a function a scanner's reference phase, $F(\theta_{m,0})$ is a triangle wave.

4.3 Representation in θ_1, θ_2 Space

A less intuitive but more powerful representation of the two beams is in so called θ_1, θ_2 space, as shown in Figure 8. This graphical representation plots the scanners' instantaneous angles θ_1 and θ_2 on the horizontal and vertical axes of a Cartesian plane. The two shaded regions (intersection areas) in Figure 8 are θ_1, θ_2 coordinates when the two beams are intersecting. Each intersection area is bounded by three lines: the θ_2 axis (scanner 1 points at scanner 2), θ_2 is equal to $\pm 180°$ (scanner 2 points as scanner 1), and θ_1 equals θ_2 (beams are parallel). Any θ_1, θ_2 combination that falls on or outside any of these boundaries are not intersecting. Though signal interactions between the lidars may occur when the two are looking directly at each other, this case is not considered.

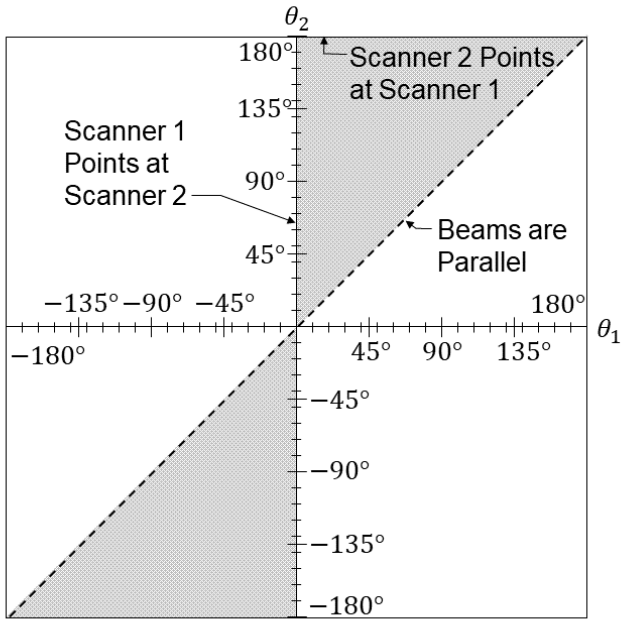

Figure 8 – The θ_1, θ_2 coordinate space where the shaded region represents θ_1 and θ_2 coordinates that which rays 1 and 2 are intersecting.

A plotted line in θ_1, θ_2 space, which shows how θ_1 and θ_2 vary with time, is referred to as a 'trajectory.' A trajectory's slope is equal to the ratio of the scan frequencies

f_2/f_1 whilst if $\theta_{1,0} = 0°$, the θ_2 intercept is equal to scanner 2's reference phase $\theta_{2,0}$. The fraction of the length of the line that lies within the shaded intersection area is equal to F.

4.4 Fraction F in Specific Cases

4.4.1 Case of $f_2/f_1 = 1$

When the rotational frequencies of the two scanners are matched (f_2/f_1 equals unity), one gets the trajectory shown in Figure 9(a) with a slope equal to unity. For positive rotation, the trajectory moves upward and right wrapping from top to bottom and from the right edge back to the left edge of the of the diagram until it intercepts the θ_2 axis again, thus completing a full rotation ray 1. When the plot terminates into its starting location, scanner 1 has completed N_1 rotations – in this case unity. The arrows inscribed on the

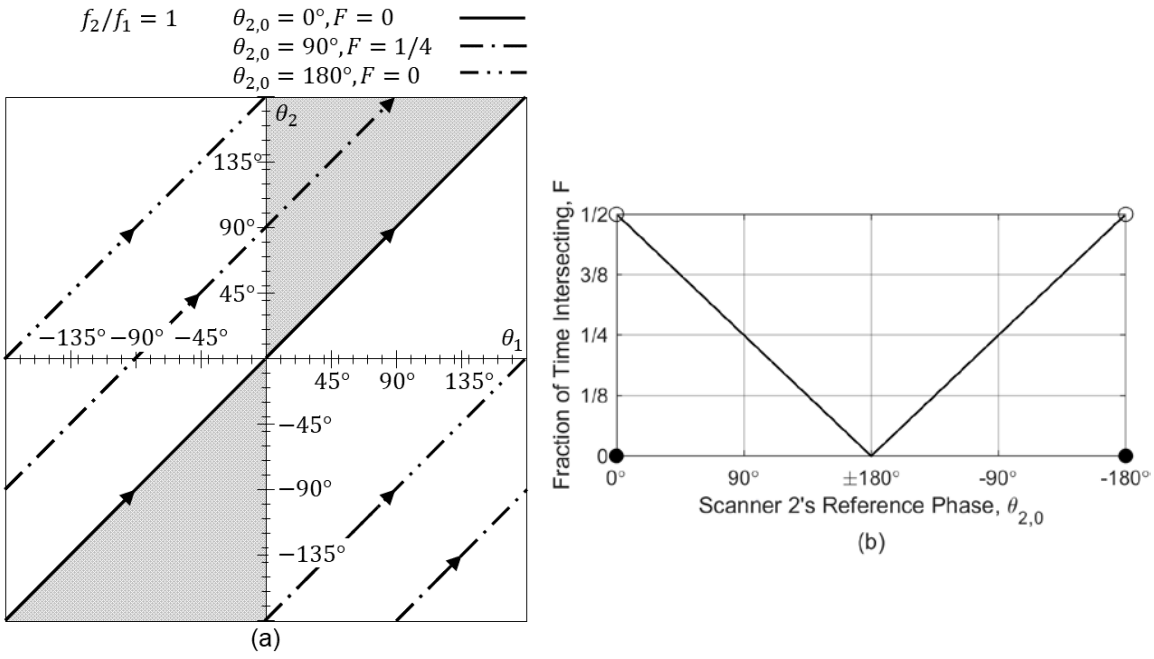

Figure 9 – Representation of rays 1 and 2 for $f_2/f_1 = 1$ in (a) θ_1, θ_2 space for $\theta_{2,0} = 0°$ (solid line), 90° (single dotted dashed line), and 180° (double dot dashed line) and (b) F as a function of $\theta_{2,0}$.

plotted lines shown in Figure 9(a) represent positive time progression. Depending on the reference phase, F ranges from from 0 to a limit approaching $1/2$. Two reference phases of $\theta_{2,0}$, 0° (beams parallel) and 180° (beams point away from each other), result in $F = 0$ and would avoid scattered interference. However, $\theta_{2,0}$ equals 0° represents an unstable case of zero intersection between the beams. Since the two scanners' beams are parallel, their trajectory borders the two intersection spaces – resulting in F being equal to 0. However, given any perturbation in $\theta_{2,0}$, F approaches $1/2$, since nearly half of the line would be within the shaded region. This means that with a reasonable tolerance in the scanner's rotational frequency, two devices may risk interference. This discontinuity of F as a function of $\theta_{2,0}$ is shown in Figure 9(b).

A change in the reference phase of scanner 2 results in a linear change in F. In Figure 9, transitioning from $\theta_{2,0}$ equals 180° to 90° to approach 0°, F linearly approaches $1/2$ from 0. If continued from 0° to $-90°$ to $-180°$, F linearly decreases back down to zero which agrees with the triangle wave nature of $F(\theta_{2,0})$. For better familiarization with θ_1, θ_2 space, one can compare Figure 7 and the single dotted, dashed line in Figure 9(a), which represent the same cases in both the real and θ_1, θ_2 spaces.

4.4.2 Case of $f_2/f_1 > 1$

When the rotational frequencies between the scanners are not matched, intersection occurrences change as a function of the ratio between the two scanners' rotational frequencies. Figure 10 provides an example when the scanning frequency ratio is greater than unity, specifically when $f_2/f_1 = 2/1$. The two beams now intersect when $\theta_{2,0}$ equals 0° and F is at a maximum of $1/2$. However, when $\theta_{2,0}$ equals 180°, the two beams never

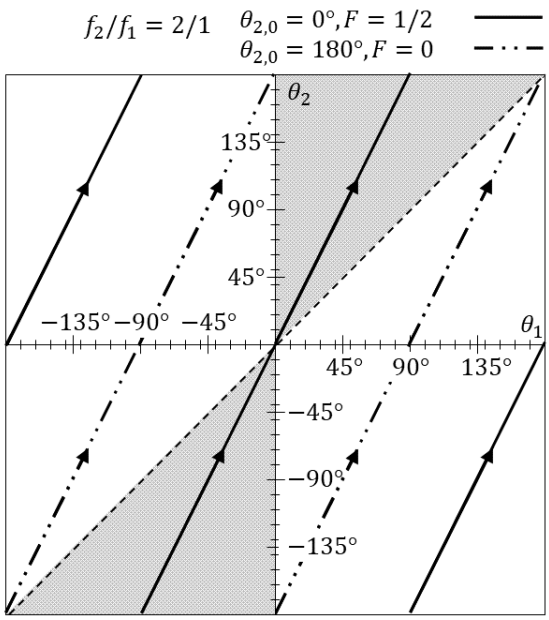

Figure 10 – Representation of rays 1 and 2 in $\boldsymbol{\theta_1, \theta_2}$ space for $\boldsymbol{f_2/f_1 = 2/1}$ and $\boldsymbol{\theta_{2,0} = 0°}$ and $\boldsymbol{90°}$.

intersect and F equals 0. Between these reference phases, F linearly increases and decreases between these minima and maxima. As the ratio of the rotational frequencies changes (the slope of the trajectory), so too does the period of which F's extrema occurs with respect to scanner 2's reference phase. Moreover, the minimum and maximum values of F change, with 0 and $1/2$ representing the extreme cases, for which is discussed later in Section 4.5.

4.4.3 Case of $0 < f_2/f_1 < 1$

A relationship exists between positive rotational frequencies ratios above and below unity. For this discussion, $F_{f_2/f_1}(\theta_{1,0}, \theta_{2,0})$ is used to denote F for two scanners with f_2 / f_1 rotational ratio and $\theta_{1,0}$ and $\theta_{2,0}$ initial angular orientations. Also, let f_2'/f_1' represent the reciprocal of an equivalent rotational frequency ratio of f_2/f_1 such that

$$f_2'/f_1' \equiv f_1/f_2 \tag{19}$$

with reference phases $(\theta_{1,0}', \theta_{2,0}')$, respectively. The equivalent geometric representation between the two scanners with f_2'/f_1' and f_2/f_1 simply represents a rotation of the configuration of the f_2/f_1 scanners by 180° as shown in Figure 11. The result is a new configuration that can be obtained by the translation of $f_2/f_1 \rightarrow f_2'/f_1'$; $\theta_{1,0} \rightarrow \theta_{2,0} + 180°$; and $\theta_{2,0} \rightarrow \theta_{1,0} + 180°$. Therefore, F can be written equivalently between these two configurations as

$$F_{f_2/f_1}(\theta_{1,0}, \theta_{2,0}) = F_{f_2'/f_1'}(\theta_{2,0} + 180°, \theta_{1,0} + 180°) = F_{f_2'/f_1'}(\theta_{1,0}', \theta_{2,0}'). \tag{20}$$

The minimum and maximum values of F are the same between reciprocal pairs of rotational frequencies, but their occurrence is shifted by 180° in evaluation of F. So, the case of $0 < f_2'/f_1' < 1$ is the same as for $1 < f_2/f_1$, except that the values of F are offset with respect to the reference phases.

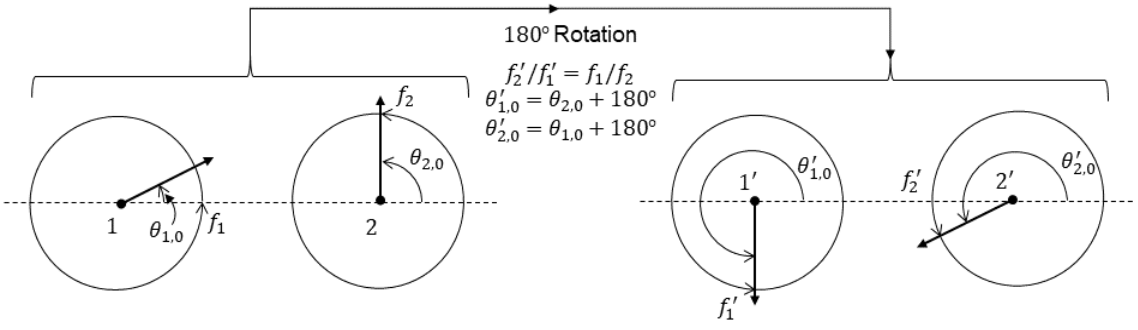

Figure 11 – Relationship between f_2/f_1 and its reciprocal equivalent f_2'/f_1'. The representation of f_2'/f_1' is simply the 180° rotation of the configuration for f_2/f_1.

Figure 12 provides an example of $f_2/f_1 = 1/2$ which is the reciprocal case of Figure 10 when $f_2/f_1 = 2/1$. Over the combined period T, scanner 1 completes two rotations for a total of $720°$ of rotation and scanner 2 completes a single rotation of $360°$. When $\theta_{2,0} = 0°$, the beams do not intersect which is equal to the $180°$ offset equivalent of $F_{2/1}(180°, 180°)$ in Figure 10.

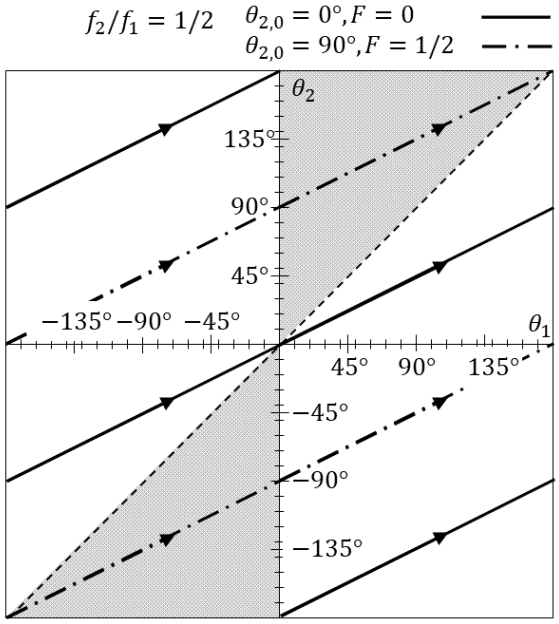

Figure 12 – Representation of rays 1 and 2 in $\boldsymbol{\theta_1, \theta_2}$ space for $\boldsymbol{f_2/f_1 = 1/2}$ and $\boldsymbol{\theta_{2,0} = 0°, 90°}$.

A plot showing F for several special cases of f_2/f_1 is shown in Figure 13 for four different reference phase pairings. Values of F are at a maximum when $(\theta_{1,0}, \theta_{2,0}) = (0°, 0°)$ and $f_2/f_1 > 1$ or $(\theta_{1,0}, \theta_{2,0}) = (180°, 180°)$ and $0 < f_2/f_1 < 1$. Additionally, when $(\theta_{1,0}, \theta_{2,0}) = (0°, 180°)$ and $(\theta_{1,0}, \theta_{2,0}) = (180°, 0°)$, each f_2/f_1 and its reciprocal equivalent are equal. A more detailed explanation of these minimum and maximum values of F are discussed in Section 4.5.

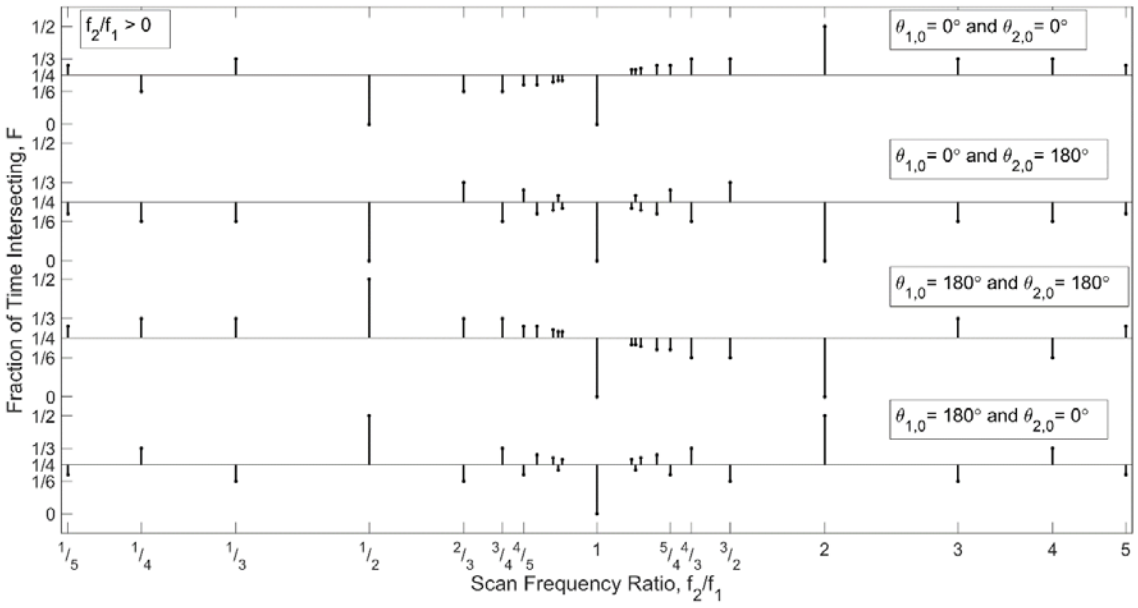

Figure 13 – $F(f_2/f_1)$ for four selected initial angles, $(\theta_{1,0}, \theta_{2,0}) = (0°, 0°)$, $(0°, 180°)$, $(180°, 180°)$, $(0°, 180°)$ when $f_2/f_1 > 0$.

Outside the special cases shown in Figure 13, if given a continuum of rotational frequencies, most evaluations of F have minimum and maximum values that approach $1/4$. Heuristically, when considering the geometry of θ_1, θ_2 space and the relationship of N_2/N_1 to f_2/f_1, incremental changes in f_2/f_1 result in drastic differences in F. In θ_1, θ_2 space, each rotation of scanner 2 is represented by unique, equally spaced line segments as bounded by the upper and lower limits of θ_1, θ_2 and the number of line segments is $\max(|N_1|, |N_2|)$ as shown by [52]. As $N_2 \to \infty$, line segments uniformly fill the plot space and F approaches the fraction of θ_1, θ_2 space that is occupied by the intersection area, which is $1/4$. Similarly, if the rotational frequency ratio is irrational, the number of turns required to evaluate F is infinite and again, F approaches $1/4$. Therefore, outside of the ratios presented in Figure 13, most evaluations of F approach 1/4.

4.4.4 Case of $f_2/f_1 < 0$

If one scanner is rotating clockwise (counter rotation), then the ratio of the scan frequencies f_2/f_1 is negative, thus the trajectory's slope in θ_1, θ_2 space is also negative. Nevertheless, the conditions for intersection do not change, and the rules over which F is evaluated remain the same as when both are scanning with positive rotation. However, the frequency and duration of which intersection occurs is not the same. Additionally, the minimum and maximum values of F and the period of F change between same-direction and counter-direction rotation for a defined rotational frequency ratio, though 0 and $1/2$ remain the extrema. Figure 14 shows an example of counter rotation for two scanners with matched rotational frequencies.

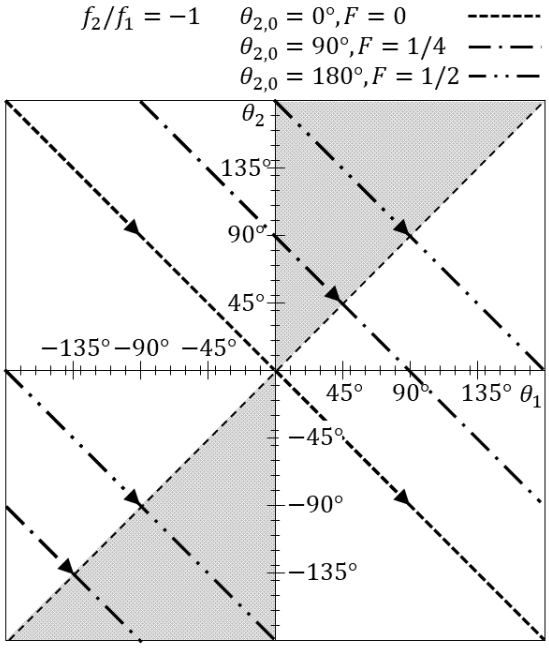

Figure 14 – Representation of rays 1 and 2 in $\boldsymbol{\theta_1, \theta_2}$ space for $\boldsymbol{f_2/f_1 = -1}$ and $\boldsymbol{\theta_{2,0} = 0°, 90°, 180°}$.

The relationship between the line trajectories of rotational ratios with the same absolute value is a horizontal reflection across the θ_1 axis in θ_1, θ_2 space. An example of this reflection is shown in Figure 15 for the case of $|f_2/f_1| = 1/2$. However, since the

intersection area in θ_1, θ_2 space is not symmetric about the θ_1 axis, F is different between these corresponding pairs.

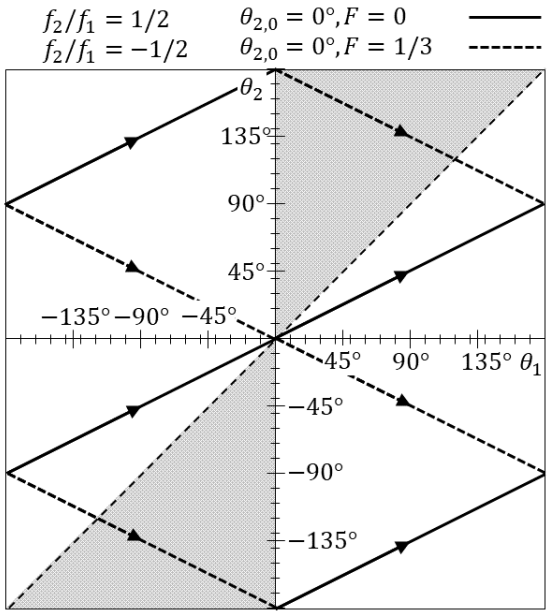

Figure 15 – Representation of rays 1 and 2 in $\boldsymbol{\theta_1, \theta_2}$ space for $\boldsymbol{f_2/f_1 = 1/2, -1/2}$ and $\boldsymbol{\theta_{2,0} = 0°}$.

Figure 16 shows $F(f_2/f_1)$ for several cases of $(\theta_{1,0}, \theta_{2,0})$ when $f_2/f_1 < 0$. When compared to same-direction rotation, F trends closer to $1/4$. The symmetry of F about $f_2/f_1 = -1$ is the same as in Figure 13. Given the translation provided by Equation (20), it is concluded that $(\theta_{1,0}, \theta_{2,0}) = (0°, 0°)$ and $(\theta_{1,0}, \theta_{2,0}) = (180°, 180°)$ are symmetric with each other while $(\theta_{1,0}, \theta_{2,0}) = (0°, 180°)$ and $(\theta_{1,0}, \theta_{2,0}) = (180°, 0°)$ are symmetric with themselves about $f_2/f_1 = -1$. Though it may seem desirable to operate two lidars in counter-direction rotation to avoid mutual interference, there are fewer options to achieve zero intersection.

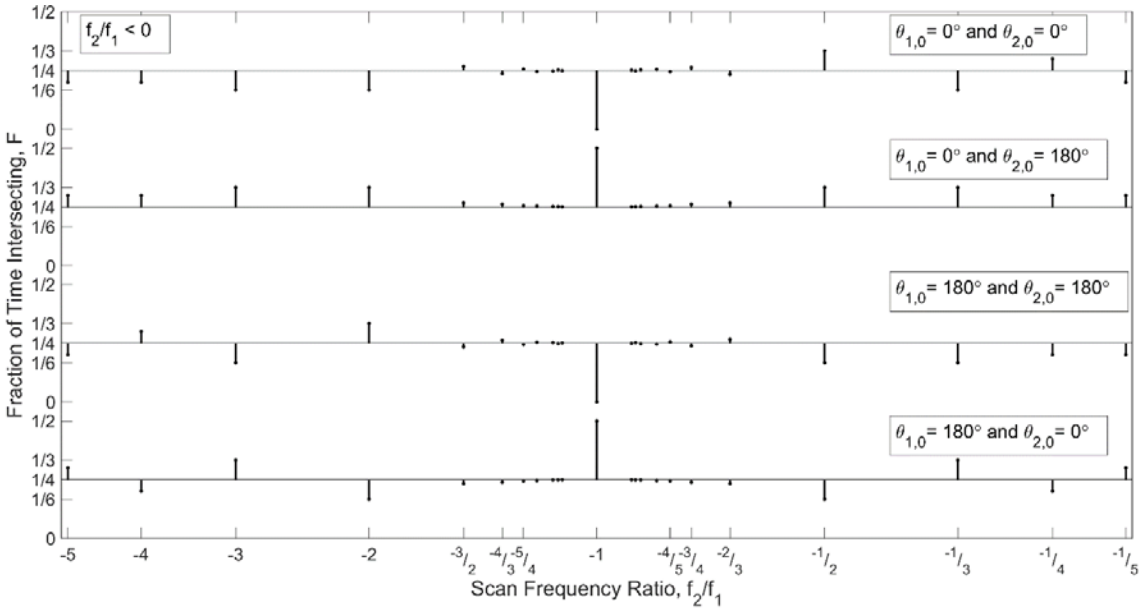

Figure 16 – $F(f_2/f_1)$ for four selected initial angles, $(\theta_{1,0}, \theta_{2,0}) = (0°, 0°)$, $(0°, 180°)$, $(180°, 180°)$, $(0°, 180°)$ when $f_2/f_1 < 0$.

4.5 Conditions for F_{min} and F_{max}

It can be shown analytically that the maximum F for any ratio f_2/f_1 occurs for specific initial angles. To illustrate, let $\tilde{F}_{f_2/f_1}(\theta_{1,n}, \theta_{2,0})$ to be the fraction of intersection occurring over a single rotation of scanner 2, where $\theta_{1,n}$ is the initial angular orientation of scanner 1 on the $n_2{}^{\text{th}}$ rotation of scanner 2 starting at $n_2 = 0$. This can be found as

$$\theta_{1,n} = 360° \frac{n_2 f_1}{f_2} + \theta_{1,0}. \tag{21}$$

Due to the symmetry of the frequency ratio about $|f_2/f_1| = 1$, it is convenient to only discuss the case $|f_2/f_1| > 1$ and then generalize the result to configurations of $0 < |f_2/f_1| < 1$ by symmetry. In this case, given scanner 2 completes N_2 rotations, the trajectory in θ_1, θ_2 space is equally spaced into N_2 line segments. From this, F can be

rewritten as a summation of each of these constituent single rotation values of $\tilde{F}_{f_2/f_1}$ such that

$$\tilde{F}_{f_2/f_1}(\theta_{1,n}, \theta_{2,0}) = \frac{1}{T_2} \int_0^{T_2} s_F(\mathrm{t})\, dt. \tag{22}$$

and

$$F_{f_2/f_1}(\theta_{1,0}, \theta_{2,0}) = \frac{1}{N_2} \sum_{n=0}^{N_2-1} \tilde{F}_{f_2/f_1}(\theta_{1,n}, \theta_{2,0}). \tag{23}$$

$F_{f_2/f_1}(\theta_{1,0}, \theta_{2,0})$ is therefore the average of $\tilde{F}_{f_2/f_1}(\theta_{1,n}, \theta_{2,0})$ and is a periodic function of $\theta_{1,0}$ with period $\frac{360^\circ}{N_2}$.

Figure 17 shows an example of $\tilde{F}$ and F for $f_2/f_1 = 3/1$ and $\theta_{2,0} = -180^\circ$. In Figure 17(a), the trajectory of the two scanners is shown, with the intersection of each constituent rotation of scanner 1, $\tilde{F}_{f_2/f_1}(\theta_{1,n}, \theta_{2,0})$, represented separately. The solid, dashed, and single dotted dashed lines represent the first, second, and third rotations of scanner 1 each starting at $(\theta_{1,0}, \theta_{2,0}) = (0^\circ, -180^\circ)$, $(\theta_{1,1}, \theta_{2,0}) = (120^\circ, -180^\circ)$, and $(\theta_{1,2}, \theta_{2,0}) = (-120^\circ, -180^\circ)$, respectively. Figure 17(b) then shows each of the three rotations' intersection $\tilde{F}_{3/1}(\theta_{1,n}, -180^\circ)$ as a function of scanner 1's initial orientation $\theta_{1,0}$ from which value on the $\theta_{1,0}$-axis all three values of $\tilde{F}_{3/1}(\theta_{1,n}, -180^\circ)$ are read. Each is a periodic, piecewise-linear function with five line segments. The total intersection as a

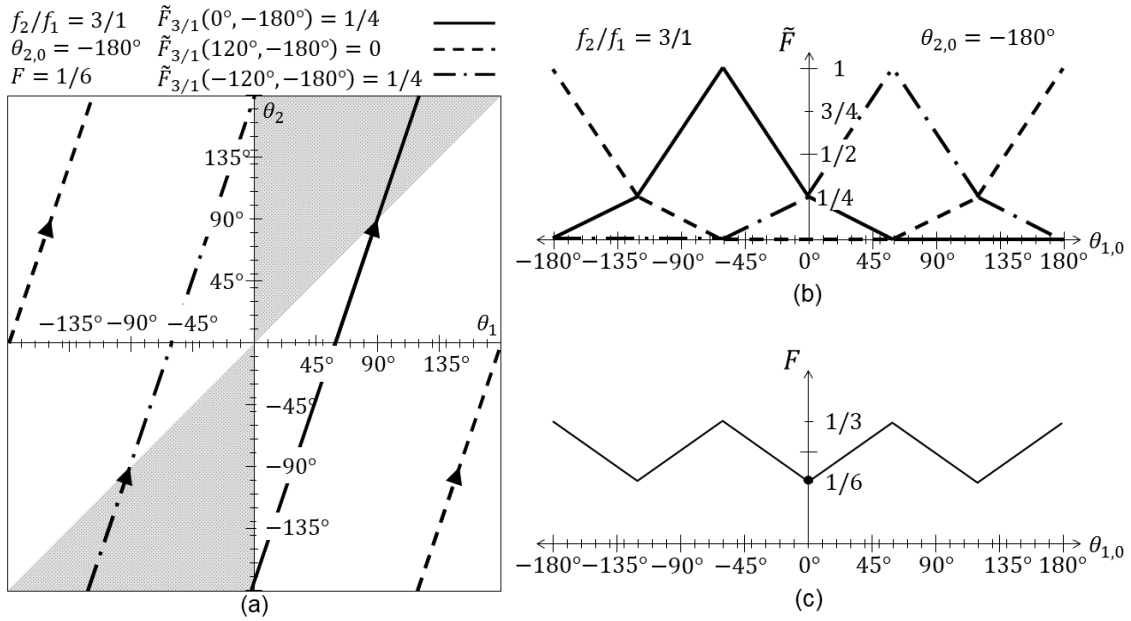

Figure 17 – Representative $\tilde{F}$ and F for $f_2 / f_1 = 3/1$ and $\theta_{2,0} = -180°$. (a) θ_1, θ_2 trajectory of $f_2 / f_1 = 3/1$ and $\tilde{F}$ for each of the three rotations of scanner 1. Scanner 1's first (solid), second (dashed), and third (single dotted dashed) rotations correspond to $\tilde{F}_{3/1}(\theta_{1,0}, -180°)$, $\tilde{F}_{3/1}(\theta_{1,1}, -180°)$, and $\tilde{F}_{3/1}(\theta_{1,2}, -180°)$, respectively. (b) The three functions of $\tilde{F}_{3/1}(\theta_{1,n}, -180°)$ each as a function of the scanner 1's initial orientation $\theta_{1,0}$. (c) The function $F(\theta_{1,0}, -180°)$, which is the average of the previous three functions.

function of scanner 1's initial angle $F(\theta_{1,0}, -180°)$, is the average of these three functions, as shown in Figure 17(c) with the dot marking F for the example in Figure 17(a).

Given the boundaries of the intersection area in θ_1, θ_2 space, the optimization of F and $\tilde{F}$ is a linear programing problem. The corners formed by the lines bounding the intersection area form vertices of the intersection area. The value of $\tilde{F}_{f_2/f_1}(\theta_{1,n}, \theta_{2,0})$ is then a piecewise-linear function. When the initial angle of scanner 1 varies, the value of $\tilde{F}_{f_2/f_1}(\theta_{1,n}, \theta_{2,0})$ can either linearly increase, decrease, or stay the same. A transition point occurs when $\tilde{F}_{f_2/f_1}(\theta_{1,n}, \theta_{2,0})$ changes slope. These transition points correspond to the plotted line segment passing one of the vertices formed by the intersection area in θ_1, θ_2

space. Therefore, a local minimum or maximum can only occur when the line passes a vertex. There are five vertices that form the intersection area: $(0°, 0°)$, $(0°, 180°)$, $(180°, 180°)$, $(0°, -180°)$, $(-180°, -180°)$. In real space, $(0°, 180°)$ and $(0°, -180°)$ are equivalent as well as $(180°, 180°)$ and $(-180°, -180°)$. However, in considering a single line segment of $\tilde{F}$, each needs to be treated separately.

It can also be shown that for the local minima and maxima, F must also pass at least one of the transition points of $\tilde{F}_{f_2/f_1}(\theta_{1,0}, \theta_{2,0})$. Since F is evaluated over the entirety of N_1 rotations of scanner 1 rather than a single rotation (one line segment); $(0°, 180°)$ and $(0°, -180°)$ become equivalent along with $(180°, 180°)$ and $(-180°, -180°)$, so there are only three possible points that may correspond to the minimum or maximum value of F. Therefore, $F(\theta_{m,0})$ is a piecewise-linear function controlled by the values and locations of these three points. Furthermore, it can be shown that there are only two possible values associated with these three points, since two of them must be on the same trajectory. It can be ultimately shown then that $F(\theta_{m,0})$ is a symmetric triangular wave by the proof in [52].

After a rigorous treatment, it is shown that the maximum F value must pass a single special vertex listed below, which is not on the same trajectory as the maximum vertex. The conclusions of these special vertex points are listed as follows and the proof is shown in [52]:

1. If $f_2/f_1 = 1$, the maximum F occurs when $\theta_{2,0} \to \theta_{1,0}$.
   The minimum F occurs when $\theta_{2,0} = \theta_{1,0} + 180°$.
2. If $f_2/f_1 > 1$, the maximum F occurs when $(\theta_{1,0}, \theta_{2,0}) = (0°, 0°)$.
   When N_1 is odd, the minimum F occurs when $(\theta_{1,0}, \theta_{2,0}) = (0°, 180°)$.

When N_1 is even, the minimum F occurs when $(\theta_{1,0}, \theta_{2,0}) = (180°, 180°)$.

3. If $0 < f_2/f_1 < 1$, the maximum F occurs when $(\theta_{1,0}, \theta_{2,0}) = (180°, 180°)$.

   When N_2 is odd, the minimum F occurs when $(\theta_{1,0}, \theta_{2,0}) = (0°, 180°)$.

   When N_2 is even, the minimum F occurs when $(\theta_{1,0}, \theta_{2,0}) = (0°, 0°)$.

4. If $f_2/f_1 < 0$, the maximum F occurs when $(\theta_{1,0}, \theta_{2,0}) = (0°, 180°)$.

   When N_1 is odd, the minimum F occurs when $(\theta_{1,0}, \theta_{2,0}) = (0°, 0°)$.

   When N_1 is even, the minimum F occurs when $(\theta_{1,0}, \theta_{2,0}) = (180°, 180°)$.

The above conclusions are also verified by the plots of F shown in Figure 13 and Figure 16.

4.6 Zero Intersection Cases

4.6.1 Two Scanners

Achieving zero overlap is one way to reduce the risk of scattered interference between two lidar scanners, regardless of the surrounding target geometry. Establishing these fundamental cases for two scanners leads to zero intersection being possible for higher numbers of scanners. For two scanners, $F = 0$ can be satisfied only by these configurations:

a. When $f_2/f_1 = 1$, the trajectory passes $(\theta_1, \theta_2) = (0°, 180°)$, or $\Delta\theta = 180°$.

b. When $f_2/f_1 = -1$, the trajectory passes $(\theta_1, \theta_2) = (0°, 0°)$ and $(180°, 180°)$.

c. When $f_2/f_1 = 2$, the trajectory passes $(\theta_1, \theta_2) = (0°, 180°)$ and $(180°, 180°)$.

d. When $f_2/f_1 = 1/2$, the trajectory passes $(\theta_1, \theta_2) = (0°, 0°)$ and $(0°, 180°)$. This is equivalent to configuration (c).

e. When $f_2/f_1 = 1$, it seems that $\Delta\theta = 0°$ also produces $F = 0$, but it is not a stable case since $\lim_{\Delta\theta \to 0°} F = 1/2$.

However, in the fifth configuration (e), if there is some finite divergence angle for each lidar's laser or FOV, F can be unity. Therefore, for the most part, this case will not be considered, but for completeness, it will be analyzed afterward.

Supporting these claims, manufacturers of devices whose phases are controllable, such as Velodyne, recommend the operation of their devices in the most intuitive of the five cases, (a) [53].

4.6.2 Three Scanners

Zero intersection between three stationary scanners is achievable. To achieve this, pairing combinations of two of the three scanners must satisfy one of the four possible configurations (a through d) for two scanners listed in Section 4.6.1. Therefore, when only considering the three scanners' rotational frequencies, the frequency ratio $f_1 : f_2 : f_3$ can only be $1:1:1$, $1:1:-1$, $1:1:2$ (the same as $1/2:1/2:1$), $2:2:1$ (the same as $1:1:1/2$), or some permutation of these combinations. To consider the arrangement of three scanners, first arrange two scanners with zero intersection then add a third scanner which also satisfies zero intersection with each of the first two scanners. Each combinatory pair of the three scanners then satisfies one of the $F = 0$ conditions. Once all three are considered together, the permutations will be limited to only a few cases and two geometrical configurations.

The geometrical configuration for three scanners is shown in Figure 18. Due to the conditions for zero intersection and initial orientations, the scanners can either be arranged in a right triangle or straight line of which, by convention, scanner 2 forms the apex or center of, respectively. Scanner 3's rotational frequency f_3 and angular orientation are defined the same as scanners 1 and 2 in Section 4.1, except referenced from an imaginary line parallel to the line connecting points 1 and 2 as shown in Figure 18(a). The reference phases can be expressed as $(\theta_{1,0}, \theta_{2,0}, \theta_{3,0})$.

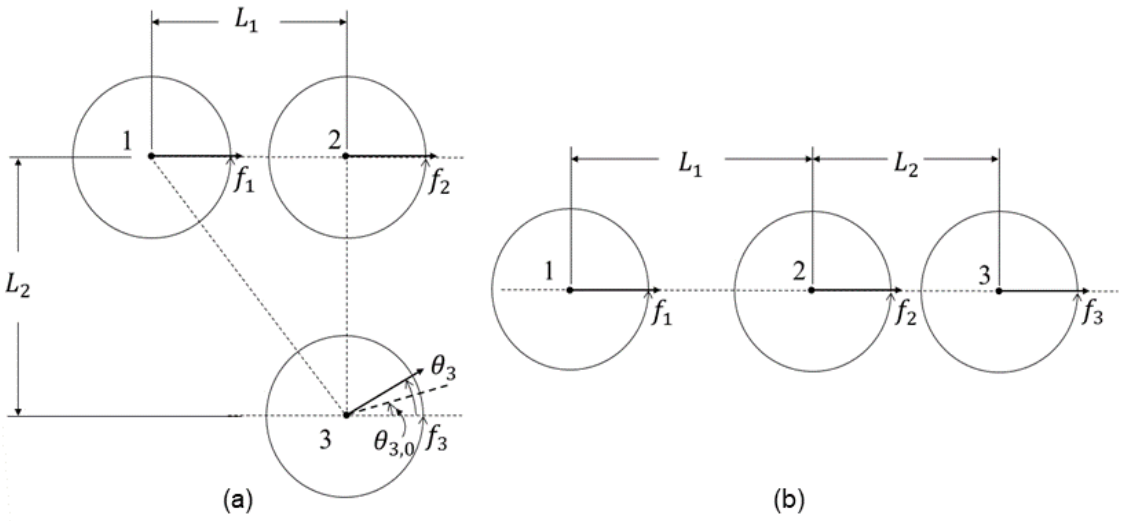

Figure 18 – Definition of three scanners for zero intersection. Three scanners can be arranged in a (a) right triangle configuration or a (b) straight line so that none of the scanner's transmission paths intersect.

When $f_1 : f_2 : f_3 = 1 : 1 : 1$, the three scanners can only be arranged such that they represent the unstable case of no intersection given is 4.6.1(e) and is not viable. When in a right triangle configuration, only $f_1 : f_2 : f_3 = 1 : -1 : 1$ with $(0°, 0°, 180°)$ results in zero intersection. Alternatively, in a straight line, the three scanners can be arranged as $f_1 : f_2 : f_3 = 1 : 1 : 2$ and $(180°, 0°, 180°)$ or $2 : 1 : 2$ and $(0°, 0°, 180°)$ with zero intersection.

4.6.3 Four Scanners

Four stationary scanners may also be arranged such that none of the four beams intersect while scanning. Given four scanners, each group of three scanners should satisfy one of three possible zero intersection configurations discussed in Section 4.6.1 for three scanners. However, in the case of a straight line, to add a fourth scanner requires a combination of the two arrangements ($1:1:2$ and $2:1:2$) therefore, the three possible arrangements become only two and the possible frequency ratios $f_1:f_2:f_3:f_4$ can only be: $1:-1:1:-1$ or $2:1:1:2$. Figure 19 shows the general arrangement of four scanners with the addition of scanner 4's rotational frequency f_4, instantaneous angle θ_4, and reference phase $\theta_{4,0}$.

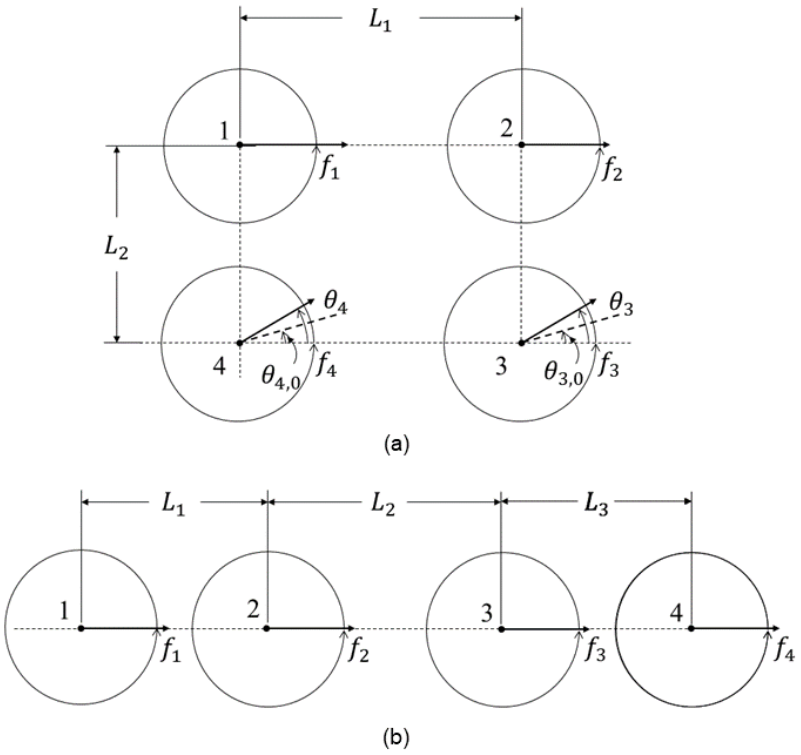

Figure 19 – Definition of four scanners for zero intersection. Four scanners can be arranged in a (a) rectangular configuration or a (b) straight line so that none of the scanner's transmission paths intersect.

If $f_1 : f_2 : f_3 : f_4 = 1 : -1 : 1 : -1$, the four scanners form a rectangle, as shown in Figure 19(a) and initial angular orientations $(0°, 0°, 180°, 180°)$. The two scanners forming a diagonal have the same rotation direction. When Scanners 1 and 3 are pointing at the rectangle's center, Scanners 2 and 4 are pointing away from the center. If $f_1 : f_2 : f_3 : f_4 = 2 : 1 : 1 : 2$, the four scanners are in a line, as shown in Figure 19(b) with initial orientations of $(0°, 0°, 180°, 180°)$.

Zero intersection between scanners is impossible if there are five or more. Under the preface that $f_1 : f_2 : f_3 = 1 : 1 : 1$ is not viable for avoiding intersection, at most two scanners can have the same frequency. Therefore, if there are five scanners or more, there must be three different rotational frequencies among the group, such as $f_1 : f_2 : f_3 = 1 : -1 : 2$, which is not possible. Thus, $F = 0$ is not achievable for five or more scanners.

4.6.4 Other Considerations

If one considers the unstable case (parallel beams) a viable configuration for zero intersection, more configurations are possible. This case may be feasible when considering radiometry and maximum measurable ranges by a lidar, since the divergence may cause the beams to intersect well outside of the range of the two scanners. However, given less than ideal FOVs, this configuration will likely not be the case. Nonetheless, under this configuration, an infinite number of scanners can be arranged in a line with the same frequencies and initial angular orientations to avoid intersection between the devices. Theoretically, one can arrange these scanners in any configuration, as they are hypothetically parallel in all orientations. However, in practice, this arrangement is not expected to be the case.

4.7 Moving Scanners

The analysis of F to this point has assumed that the two lidar sensors are stationary. However, if the two lidars are moving relative to one another, the assessment of F will change. Though a detailed analysis of how is beyond the scope of this work, it is worth illustrating the potential this has on the analysis discussed. To illustrate the difference, consider two vehicles passing each other at highway speeds of approximately 31.3 m/s. At this speed, the two sensors would traverse a radial 300 m maximum range in approximately 4.8 seconds. This transit time allows for approximately 24 to 120 rotations per lidar, given rotational frequencies from 5 Hz to 25 Hz, respectively. As already shown, this can be enough time for F to converge, however, scanner 2's reference phase, which F is a function of, is now a function of the sensors' angular velocity relative to one another. A visual example of this is shown in Figure 20.

Given two vehicles traveling relative to one another, each scanner must rotate further to reach the point when it is looking at the other sensor in the next reference frame. Therefore, at each rotation, the scanner's reference phase changes as the other scanner has moved. Given scanner 1's reference frame on its vehicle, scanner 2's rotational frequency will appear to change relative to scanner 2's position, velocity, and instantaneous angle. Since θ_2 changes as a function of the vehicles' velocity, it is possible that F will be higher than $1/2$.

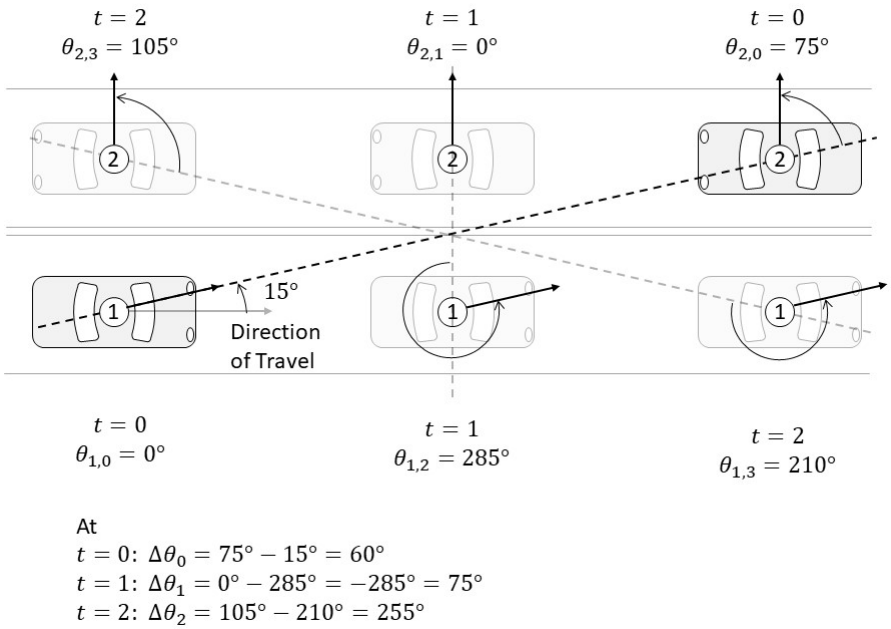

Figure 20 – The change of $\Delta\theta_n$ for two vehicles traveling towards each other which temporally changes the conditions that which F is analyzed.

4.8 Discussion

When two lidars are operating within each other's range, by way of scattering, transmitted energy from one device could be erroneously received by the other, potentially compromising the integrity the collected range data. One condition for this to occur, independent of target geometry, requires that the two lidars' beams intersect. A mathematical model was presented that describes the occurrence of this intersection and forms the upper limit of this potential interference. Graphical tools for evaluating this condition were also introduced that visually represent the angular relationship between these two scanners in θ_1, θ_2 space.

The fraction of time over which two co-planar, circularly scanning lidars have intersecting beam paths is given by the value F which can be extrapolated to the number

or potential points affected in a lidar point cloud. For two stationary, time-invariant scanners, the value of F is deterministic as a function of the two scanners' reference phases $\theta_{m,0}$ and rotational frequencies f_m. It is possible to arrange these scanners such that no intersections occurs between their two beams' paths, thus significantly reducing the risk of scattered interference, regardless of target geometry. Alternatively, the maximum that the two transmission paths can intersect is 50% of the time, $F = 1/2$. However, these represent special cases, outside of which most arrangements between two devices will result in intersection 25% of the time (F approaches $1/4$). Furthermore, it was shown that up to four scanners can be arranged such that none of their beam paths intersect and $F = 0$, thus avoiding scattered interference.

As stated, the values of F only represent an upper theoretical limit to which a lidar's total scan angle may experience scattered interference, while the measured signal interactions are expected to be lower. For scattered interference, it is not just the intersection of a lidar's FOV with another scanner's laser, but also the coincidence of a scattering target capable of returning sufficient energy from the second lidar. Once this is taken into consideration, the amount of scattered interference is expected to be lower. Nonetheless, this model provides a theoretical foundation that is absent in publicly published literature.

The elementary model presented here can serve as the basis for higher-level models that include additional factors such as beam divergence, radiometry, volumetric scattering, non-coplanar scanners, moving scanners, an arbitrary number of scanners, etc. Moreover, the model only examines scattering by way of ray tracing, and therefore ignores multiple

scattering events, transmission medium distortion, direct illumination between the devices, and other propagation phenomenon.

CHAPTER 5. INTERSECTION GEOMETRY

Key Conclusions:

- **The locus of intersection points between two scanners is a function of their rotational frequencies and reference phases.**
- **If $f_2 = f_1$, the locus of intersection points is an arc bounded by the two scanners' locations.**
- **If $f_2 \neq f_1$, the locus of intersection points are arcs with time variant radii bounded by only one scanner.**
- **The superposition of the loci of intersection points, each with deviated rotational frequency and reference phase, can be used to form an intersection density plot.**
- **The intersection density plot can be used to identify target locations at higher risk of scatter interference.**

As stated in Section 3.2.1, beam intersection is only one of the conditions for scattered interference to occur. The intersection of the two beams needs to also be coincident with a scattering target that returns enough laser energy to register as a return. Therefore, it is not just important to quantify the amount of intersection between two lidars but equally as important to understand the geometry formed by the superposition of the two lidar's intersection points. By understanding this geometry, one can overlay target geometry to determine if the second criterion of scattered interference – the signal from the harassing lidar is scattered by a target and received by the victim's receiver – is satisfied.

This confirmation can be achieved by determining if the intersection geometry coincides with a scattering target. In short, the magnitude of F determines the upper limit of *potential* scattered interference, whereas coincidence between intersection geometry and a target determines the *amount* of scattered interference.

5.1 Defining Intersection Geometry

To begin, first consider the geometry formed by the intersection between the rays presented earlier in Figure 6 of Section 4.1. When the two rays are intersecting in the upper half space, a triangle is formed by the rays and the line connecting the rays' origins as shown in Figure 21. If a line $\overline{AB}$ is drawn parallel to the line connecting the two lidars, $\overline{12}$, each scanner's instantaneous angle, θ_1 and θ_2, can easily be projected about the intersection point. It is then clear that the difference between the two angles, $\Delta\theta$, is the

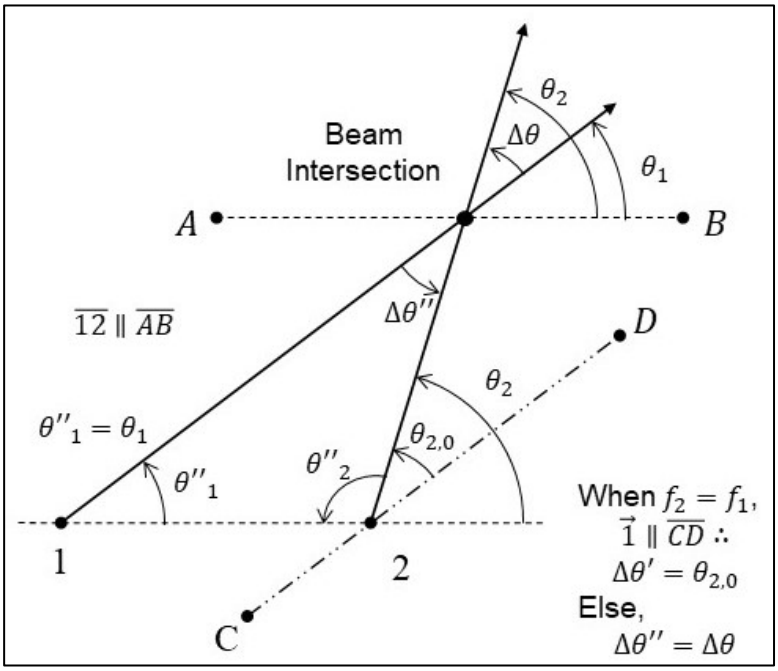

Figure 21 – The triangle formed by the intersection in the upper half space of two rays 1 and 2.

angle formed at the vertex of the two rays' intersection point. The interior vertical angle of $\Delta\theta$ will be called $\Delta\theta''$. When the two lines are intersecting in the upper half space, $\Delta\theta''$ is equal $\Delta\theta$. In the case that the scanning frequencies of the two lidar's are matched ($f_2/f_1 = 1$), the line $\overline{CD}$ that forms the reference phase of scanner 2, $\theta_{2,0}$, with ray 2 remains parallel to ray 1. As such, the $\Delta\theta''$ is the alternate interior angle to scanner 2's reference phase and therefore, $\Delta\theta''$ is also equal to the reference phase, $\theta_{2,0}$.

The second angle of the triangle, θ_1'', is the angle formed at the vertex of ray 1 and line segment $\overline{12}$. When the two rays are intersecting in the upper half space, θ_1'' is equal to scanner 1's instantaneous angle, θ_1. The last angle of the triangle, θ_2'', is the supplementary angle to scanner 2's instantaneous angle, θ_2.

If the intersection occurs in the lower half space, as shown in Figure 22, the angles are similar, but with the following differences. The angle $\Delta\theta''$ is the absolute value of the difference between the two scanner's instantaneous angles $|\Delta\theta|$. When the two scanners are rotating with the same frequency, then $\Delta\theta''$ is the supplementary angle of scanner 2's reference phase, $\theta_{2,0}$. The angle formed at the vertex of scanner 1 and line segment $\overline{12}$, θ_1'', is the explementary angle of scanner 1's instantaneous angle, θ_1. Lastly, the angle formed at the vertex of ray 2 and line segment $\overline{12}$, θ_2'', is the difference of scanner 2's instantaneous angle θ_2 subtracted by $180°$.

The angles making up the triangle formed by the two-beam intersection may be summarized as

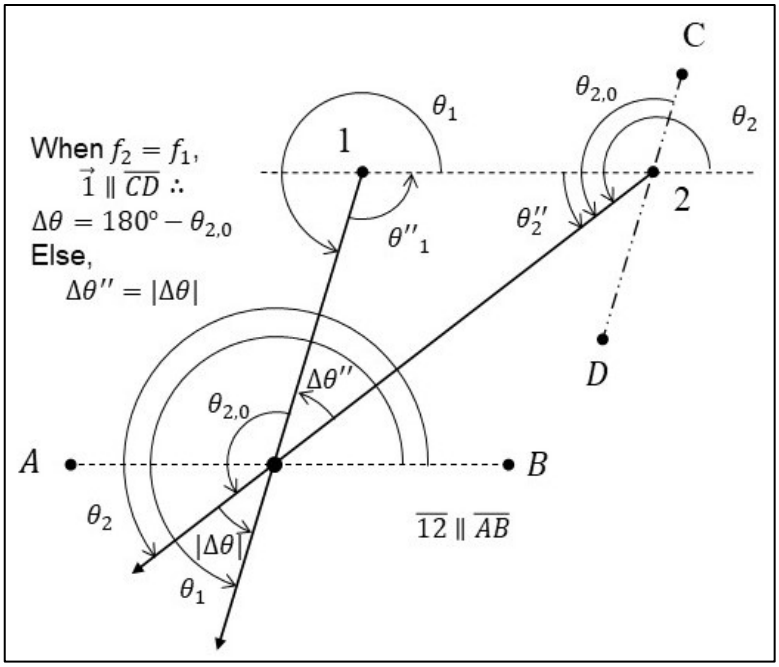

Figure 22 – The triangle formed by the intersection in the lower half space of two rays 1 and 2.

$$\theta_1'' = \begin{cases} \theta_1, & \text{when } \theta_1 < 180° \\ 360° - \theta_1, & \text{when } \theta_1 > 180° \end{cases}, \tag{24}$$

$$\theta_2'' = \begin{cases} 180° - \theta_2, & \text{when } \theta_2 < 180° \\ \theta_2 - 180°, & \text{when } \theta_2 > 180° \end{cases}, \tag{25}$$

and

$$\Delta\theta'' = |\Delta\theta|. \tag{26}$$

5.2 Locus of Intersection Points

The geometry formed by locus of intersection points between rays 1 and 2 through a full period of F, is dependent on the relationship between the two scanners' rotational frequencies, scanner 2's reference phase, and the scanners' separation distance L. In the

case that the two frequencies are equal, the locus of points will form the arc of a circle with the intersection triangle inscribed as shown in Figure 23(a).

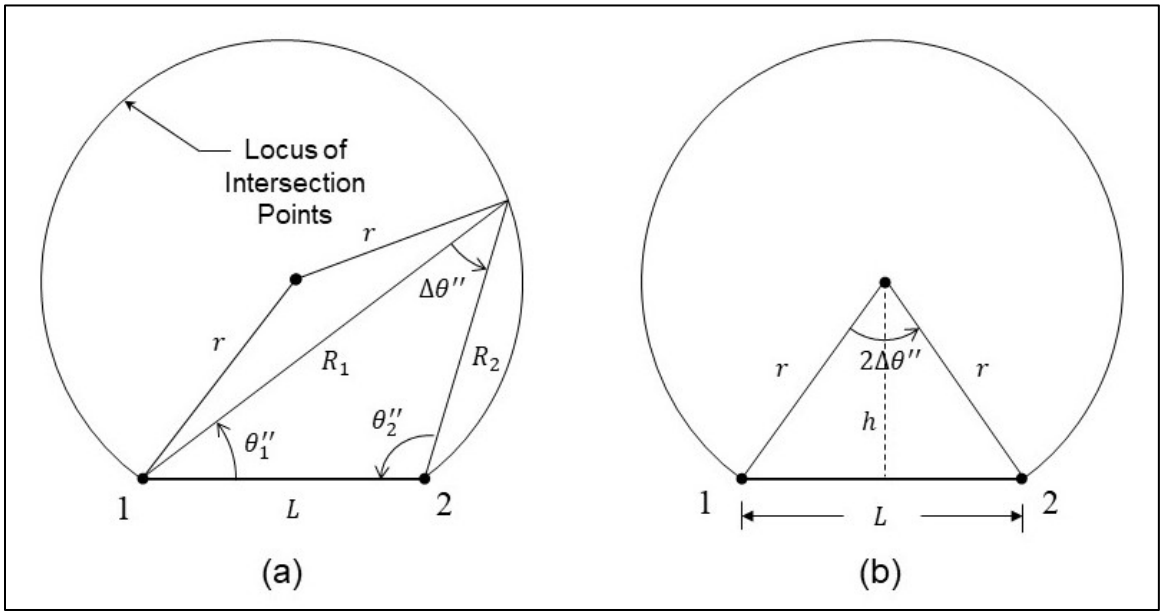

Figure 23 – The arc formed by the locus of intersection points between rotating rays 1 and 2. (a) The triangle formed inscribes the arc of intersection points and is defined by the angles $\Delta\theta''$, θ_1'', and θ_2''. (b) The arc is defined by the cord L, radius r, and distance from the center of the cord to the center of the circle h.

The line segment ($\overline{12}$) between each ray's origin forms a cord in the circle with the length L. The distances from scanners 1 and 2 to the intersection point are represented by R_1 and R_2, respectively, and form the other two legs of the triangle. The circle may be simply characterized by the dimensions shown in Figure 23(b) where the distance between the ray origins L forms the length of the cord, h is the distance from the center of the cord to the center of the circle, and r is the radius of the circle.

The angular separation of lidars 1 and 2 as measured from the center of the arc is the geometric central angle. From the Inscribed Angle Theorem, this central angle is twice $\Delta\theta''$, the angle formed at the intersection of rays 1 and 2. Considering the conditions of

intersection discussed earlier, if intersection between scanners 1 and 2 is occurring in the upper half space, then $\Delta\theta$ must be positive, therefore, in its general form $\Delta\theta''$ is equal to $|\Delta\theta|$. Given this generalization, the radius of this circle can be expressed as a function of the lidar's separation distance L and the difference between the two scanners' angle $\Delta\theta$ as

$$r = \frac{L}{2\sin(|\Delta\theta|)}. \tag{27}$$

Furthermore, the perpendicular distance of the cord from the center of the circle h can be expressed as

$$h = \frac{L}{2\tan(|\Delta\theta|)}. \tag{28}$$

Assuming the distance L between the lidars is constant, then the radius of the arc R becomes a function of $\Delta\theta$.

5.2.1 Locus of Points for $f_2/f_1 = 1$

Figure 24 shows the locus of intersection points for two scanners with matched scan frequencies ($f_2/f_1 = 1$) and varied reference phases of scanner 2. The figure was generated by a computer model that tests for intersection between two rotating line rays and stores the coordinates of intersection points when found. In Figure 24 the spatial measurements are normalized to L. As scanner 2's reference phase is varied from 1° to 170°, the arcs transition from major to minor. When scanner 2's reference phase approaches 0° from above, the radius of the arc goes to positive infinity. Between 0° and 90°, major arcs are formed between points 1 and 2 of decreasing radius as $\theta_{2,0}$ increases. When $\theta_{2,0}$ equals

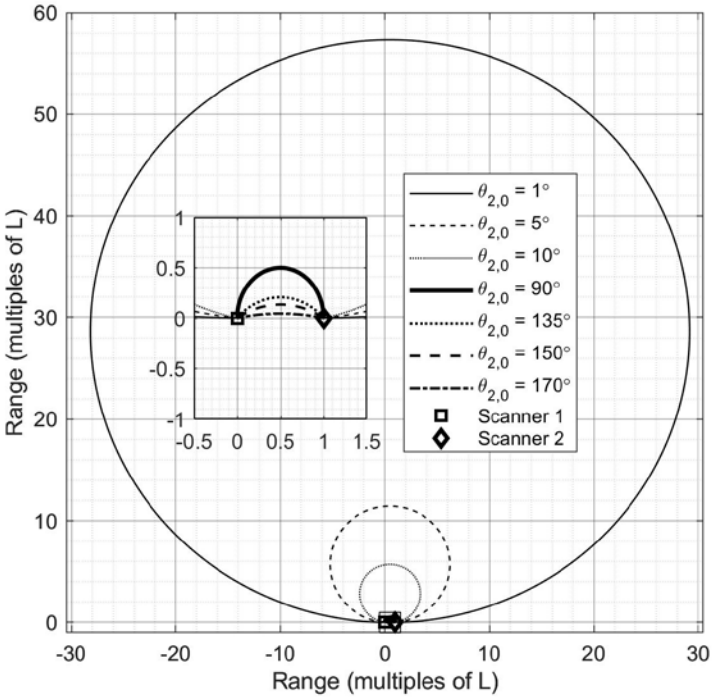

Figure 24 – The locus of points intersecting between two rotating line rays with matched rotational frequency shown with varying differences in reference phases of scanner 2 form internally tangential arcs.

90°, the cord L is the diameter of the circle and a semi-circular arc is formed. As scanner 2's reference phase increases from 90° to 180°, h is now negative (the center of the circle is in the lower half space) and minor arcs of increasingly greater radii are formed between points 1 and 2. Lastly, as scanner 2's reference phase approaches 180°, the radius again approaches infinity, however, h approaches negative infinity (located in lower half space), thus the limit of the locus of intersection points is a line between the victim and harassing lidars.

If control over the two scanners' reference phases is achievable, target locations should be considered prior to choosing an $F = 0$ configuration to minimize scattered interference as presented in Section 4.6.1. When also considering the intersection geometry

(the locus of intersection points), the choice to offset the two scanner's reference phases by 0° or 180° should not just consider minimizing F, but must also consider *where* targets are likely to be encountered relative to the two scanners.

As concluded in Section 4.6.1, when only considering F, it is logical to choose a 180° reference phase of scanner 2 to minimize incidental intersection when considering the real possibility of rotational frequency drift and beam divergence. This choice may be logical if target integrity is critical to the exterior of the two scanners since some minimal reference phase drift will incur intersection spatially between the scanners (consider $\theta_{2,0} = 170°$ in Figure 24). Therefore, scattered interference may occur between the scanners.

However, if target integrity is critical spatially between the scanners, then choosing 0° for $\theta_{2,0}$ may be logical since intersection occurs to the exterior of the two scanners with any perturbation of the reference phases (consider $\theta_{2,0} = 1°$ in Figure 24). Therefore, scattered interference may occur at exterior azimuths to the two scanners. Moreover, once the radiometric limits of the lidars are considered, it is possible that much of the intersection geometry when $F \rightarrow 1/2$ for deviation about $\theta_{2,0} = 0°$, may lay outside of the maximum range of the scanners further mitigating the risk of scattered interference.

5.2.2 Locus of Points for $f_2/f_1 \neq 1$

When the rotational frequencies are not matched, as in the case of Figure 25, the geometry formed is different than when f_1 equals f_2. The radius of the loci is now time dependent as given by Equation (27) with a time variant $\Delta\theta(t)$. As time progresses, the

radius of the arc can go to either positive infinity, negative infinity, or stay the same. The result are sets of spirals that have some asymptotically limit.

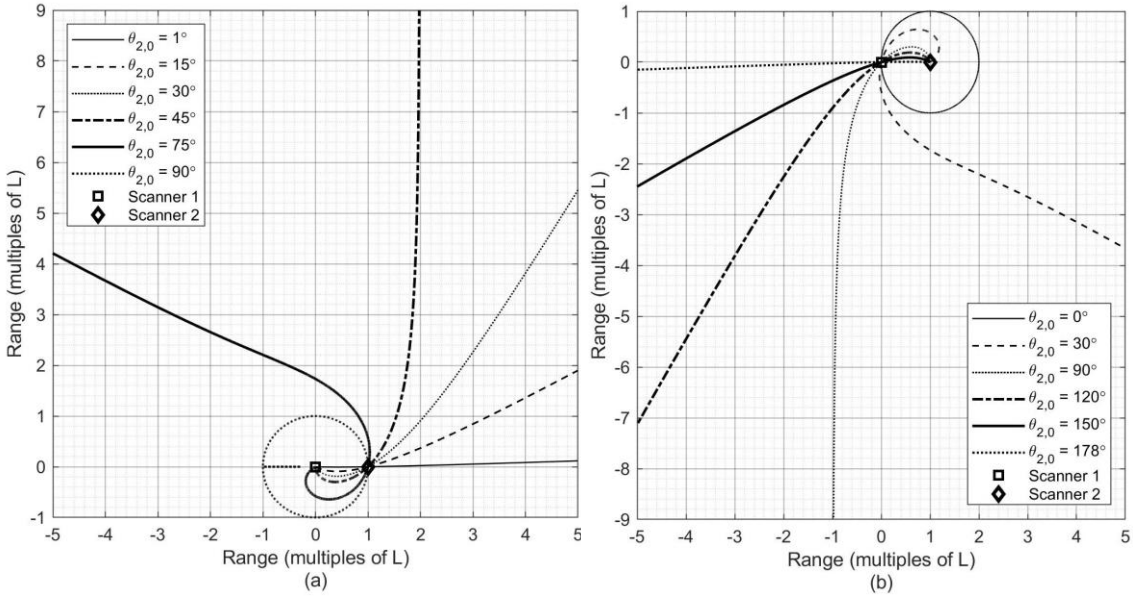

Figure 25 – The locus of points intersecting between two rotating line rays when (a) $f_2/f_1 = 1/2$ and (b) $f_2/f_1 = 2$ and various reference phases of scanner 2. The resulting geometry forms various patterns where the intersection spirals out or terminates into each of the scanners.

Figure 25(a) shows an example for these spirals for when the victim is rotating at twice the speed of the harasser and Figure 25(b) represents when the harasser rotates twice as fast as the victim. As discussed in Section 4.4.4, the reciprocal rotational frequencies ratio counterpart represents 180° rotation about scanner 2. Figure 25(a) and (b) provide a graphical example of this rotational symmetry. When $F = 1/2$, the two scanners have complete intersection over a single rotation of scanner 1, ($\tilde{F} = 1$) followed by a rotation absent of intersection ($\tilde{F} = 0$) which averages to $F = 1/2$. This is shown in Figure 25(a) when $\theta_{2,0} = 90°$ and in Figure 25(b) when $\theta_{2,0} = 0°$

5.3 Density of Intersection Points

When considering the practical application of lidar, a scanner's rotational frequency is not constant, but rather drifts as a result of engineering tolerances associated with beam steering. Moreover, given the current constraints of vehicle-to-vehicle communications, control of the scan frequencies between two lidar-enabled vehicles is not realistic. As a result, through the course of normal operation, the rotational frequencies should drift about some mean frequency if not controlled. It follows that the scanners' reference phases will also change. Given independent drift, when using rotations of scanner 1 as a reference, scanner 2's reference phases should not prefer one angle over another. This independent drift would also be the case for two vehicles passing each other as discussed in Section 4.7. When the number of rotations of the scanners is large, this change can be extrapolated to be simply the result of changing scanner 2's reference phase with every rotation of scanner 1 and observing the change in intersection loci each rotation. As a result, for each rotation, the locus of intersection points will transition between the discrete cases shown earlier in Figure 24 and Figure 25.

Figure 26 shows the theoretical density of intersection points for two scanners with match mean rotational frequencies equal to 50 Hz and rotational drift. To account for rotational drift, a normal distribution of the two scanners' rotational frequencies with standard deviations both equal to 0.25 Hz was used to vary their rotational frequencies upon every rotation of scanner 1. To account for changes in scanner 2's reference phase, $\theta_{2,0}$ was varied every rotation with a uniform distribution from $0°$ to $360°$. $10{,}000$ rotations of scanner 1 were executed and the intersection loci were recorded. The density of intersection points was then calculated at a resolution of $1°$ of θ_1 and $0.1\,L$ of range, then normalized over the total number of discrete intersection points recorded.

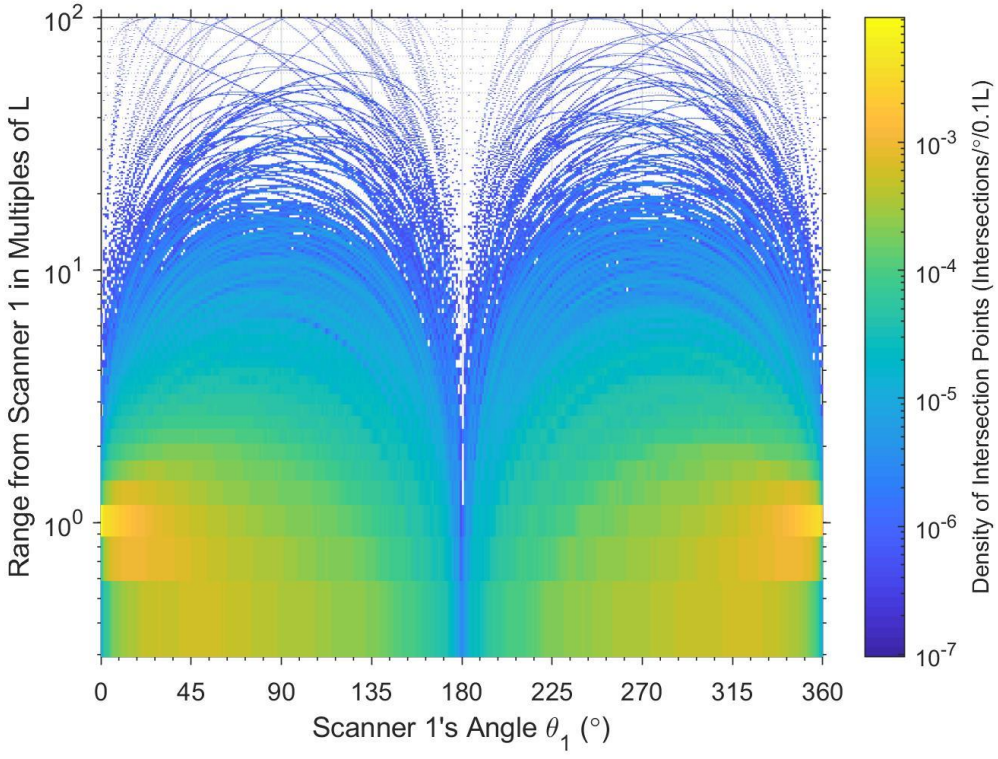

Figure 26 – The density of intersection occurrences per degree of scan angle θ_1 per $0.1L$ for two scanners with matched scan frequency and a uniform distribution of reference phases from 0° and 360° after $10,000$ rotations.

Given this projection, it is evident that the highest concentration of intersection points occurs near the line connecting the two scanners (near $\theta_1 = 0°$). This fact is intuitive when considering the convergence of intersection points at each scanner in Figure 24 in analogous form to magnetic field lines with the two scanners as poles. Therefore, a target of the same angular size located near $\theta_1 = 0°$, at a distance L (with line of sight to both scanners) should result in higher scattered interference than a target located at 180° and equal distance. The same is generally true for targets located at the same angle, but of increasing range starting from a range equal to the lidar's separation distance L.

5.4 Extension to Interference

By itself, this geometry does not represent interference. However, if a target's scattering surface is tangential to intersection point, then the potential for scattered interference exists. Radiometry will further limit this risk as power from potential harassing lidars degrades under different conditions. Additionally, the type of scattering surface will determine the amount of energy scattered and in what directions. However, assuming a Lambertian surface and ray tracing, these locations can be simply extrapolated.

Figure 27 shows an example of conditions that could result in scattered interference. Here the intersection geometry for a victim scanner rotating at twice the frequency as the harassing scanner is shown in a four-sided room. The coincidence of the intersection geometry with a target – in this case the wall – then creates the conditions that which

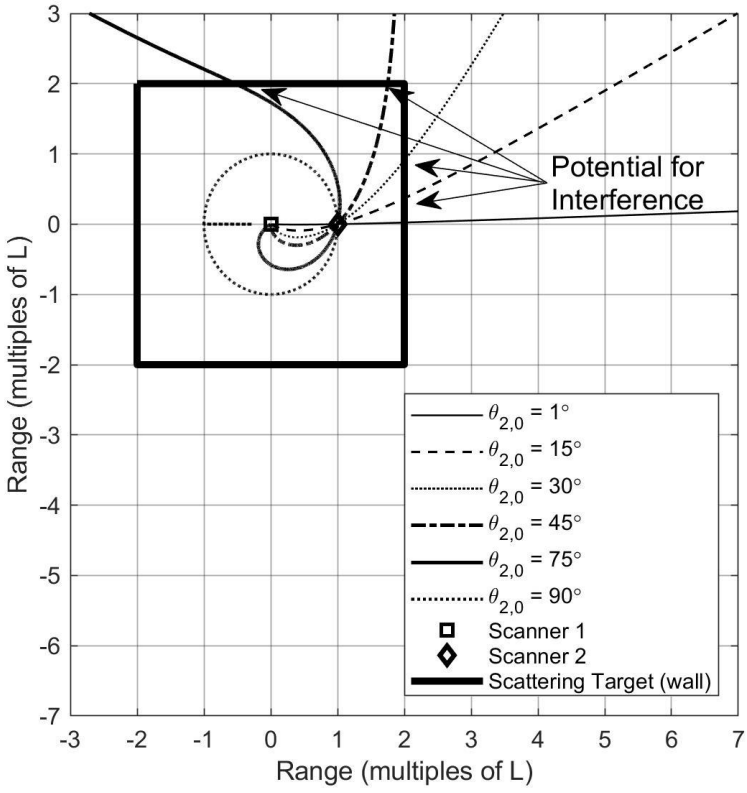

Figure 27 – Conditions for scattered interference between two scanners whose ratio of rotational frequencies $f_2/f_1 = 1/2$.

scattered interference may occur. Interference could then manifest itself as a near or far sided ranging error along the azimuth of intersection between the target and victim scanner.

Given the practical reality of rotational drift, the intersection geometry would transition between the discretely illustrated projections of various $\theta_{2,0}$ conditions in Figure 27. As such, the point at which the intersection geometry coincides with the target will changes over time. This means that scattered interference should not be expected at only a single azimuth, but over the range of its scanning limits. However, given the differences in the rate of change of intersection geometry's radius r, the relationship between the two scanners, and the target geometry's location, the occurrence of scatter interference should vary angularly as seen from scanner 1. In other words, the angular distribution of scattered interference around scanner 1 will likely not be uniform.

CHAPTER 6. AN EXPERIMENT TO TEST INTERFERENCE

Key Conclusions:

- **An experiment is described that places up to four scanners in a room to test theoretical conditions of interference.**
- **The experiment replicated three test cases reported by [17] and introduces two new test cases.**
- **In the absence of interference, multi-target returns were found to occur along scan angles containing abrupt range transitions.**
- **A statistical method was used to identify interference events based on interfered ranging data of the room taken in the absence of interference and five sigma standard deviation tolerances.**
- **The comparison of the statistical method and method reported by [17] for interference identification show that the statistical method identifies outliers with statistical expectation while the [17] method falsely identified second range return as interference.**
- **Interference occurrences were higher than those reported by [17] which is hypothesized to be the result of using a greater scan angle in this work and supports the theorized geometric interpretation of interference.**

To test the proposed theory, an experiment was devised to simulate conditions under which interference should occur as predicted by the model's criteria. The experiment placed coplanar, circularly scanning lidars in a room with simple target geometry and

recorded the ranging data. The ranging data was analyzed to find outliers which would have statistically resulted from interference between the devices. Iterations of the experiment were performed for five test cases with permutations of arrangements between the two lidar scanners. The fifth arrangement employed 4 lidar scanners.

6.1 Experimental Design

The experiment was designed to achieve several goals. The first was to replicate the results of [17] in order to extend the analysis of the reported findings. The second was to create an environment to test the proposed theoretical conditions for lidar interference. The third was to gather data to better identify and distinguish between modes of interference. Lastly, the experiment was designed to facilitate simple replication in a Monte Carlo simulation to compare theoretical and experimental results.

6.1.1 Equipment

All iterations of the experiment utilized the SICK LMS531-11100 Lite lidar scanner while fifth iteration also employed the Velodyne VLP-16 lidar scanner. All measurements were made using a SICK LMS531 which will be referred to as scanner 1 and represents the victim scanner, while the second LMS531 will be referred to as scanner 2 – the harassing scanner. The two VLP-16 scanners were used in the last test and will be referred to as scanners 3 and 4, also representing harassing scanners.

6.1.1.1 SICK LMS531

The SICK LMS531-11100 Lite lidar scanner was selected because it employs a single laser and rotating mirror to circularly scan a laser about a horizontal plane which

allows for the two scanners to operate coplanar [54]. Moreover, the LMS531 is a multi-return lidar capable of recording two returns for every transmitted pulse. This capability was important for the experiment to ensure an accurate count of potential interference pulses. Consider the case when an interference pulse's timing is such that it succeeds scanner 1's return from an actual target (far side ranging error). If scanner 1 can only record a single return, the second interference pulse would go undetected. However, this point does not provide a simple solution to eliminate interference since a nearside ranging error would prevent the detection of an actual target given a single return lidar.

The LMS531 features a total scan angle $\Theta_{m,total}$ of $190°$. This feature allowed for portions of the lidars' scan plane to be isolated from beam intersection with the other scanner, thus allowing for the isolation of direct and scattered interference depending on the arrangement. Furthermore, these scanners were similar in design to the two scanners used by [17], offering the ability to closely replicate the experiment performed by the research team. A detailed table of performance specification for the LMS531 as reported by the manufacturer and the device's operating modes for the experiment are shown in Table 2.

The LMS531 device packaging is shown in Figure 28. The scanner body featured a curved forward face with a recessed, curved plastic laser housing (dark glossy plastic). The curved side of the detector is the emitting side, out of which the scanning laser is transmitted. The plastic housing acts as a bandpass filter to reduce optical noise on the receiver and is opaque to visible wavelengths as indicated by its dark color. In Figure 28(b), it is shown that this housing only extends approximately 3/4 of the way around the detector's body from which the remaining portion of the body is non-emitting. The laser

housing plastic is a partially reflective surface and tappers slightly to the bottom which may redirect incident laser energy.

Table 2 – Performance and operating specifications of SICK LMS531-111000 Lite lidar scanners used for the experiment as reported by the manufacturer [54, 55].

Performance Specification Description	Value
Manufacturer	SICK
Model	LMS531-11100 Lite
Wavelength, λ	905 nm
Number of Laser-Emitter Pairs	1
Total Scanning Angle, Θ	190°
Rotational Frequency, f	25 Hz, 35 Hz, 50 Hz*, 75 Hz
Angular Step	0.25°, 0.5°*, 1°
Pulse Repetition Frequency, PRF	36 kHz
Ranging ability	0.7 m – 80 m
Max Range with 10% Reflectivity	40 m
Standard Ranging Resolution	$\pm$25 mm
Systematic Range Resolution Error	$\pm$25 mm (1 m – 10 m)* $\pm$35 mm (10 m – 20 m) $\pm$50 mm (20 m – 30 m)
Statistical Range Resolution Error (1σ)	$\pm$6 mm (1 m – 10 m)* $\pm$8 mm (10 m – 20 m) $\pm$14 mm (20 m – 30 m)
Dimensions (l × w × h)	160 mm × 155 mm × 185 mm
* indicates the mode or conditions the scanners were operated at if multiple operating modes exist	

(a) (b) (c) (d)

Figure 28 – Device packaging of the SICK LMS531 Lite lidar scanner used in the experiment shown from the (a) front, (b) side, (c) top, and (d) oblique prospective.

6.1.1.2 Velodyne VLP-16

Two Velodyne VLP-16 lidar scanners were used in the last test of the experiment. The scanners utilize 16 independent lasers emitter-receiver pairs aligned along unique polar angles to the scan plane. None of these laser channels were arrayed along the 0° polar angle, which allowed for the testing of interference between out-of-plane devices. Additionally, the scanners featured a 360° scan angle which permitted iterations to be performed that attempted to saturate the amount of interference. A detailed summary of the performance specifications of the VLP-16 scanners a presented in Table 3.

The VLP-16 uses a laser source with a 903 nm wavelength, while the LMS531 uses a wavelength of 905 nm. Given precise enough filtering, the two could be considered out-of-band and, therefore, not at risk of interference. However, the experimental results showed that the LMS531's bandpass filter was not narrow enough to sufficiently attenuate the VLP-16's laser source below detection threshold, therefore, the VLP-16 was still considered to operate in-band with the LMS531.

The VLP-16 features a cylindrical body with 360° curved surface glass as shown in Figure 29. This glass acts as a bandpass filter to reduce optical noise but is also a partially reflective surface. In contrast to the LMS531, the device circularly scans, emitting and receiving along the entirety of cylindrical body's circumference.

Table 3 – Performance and operating specifications of the Velodyne VLP-16 lidar scanners used for the experiment as reported by the manufacturer [56].

Performance Specification Description	Value
Manufacturer	Velodyne LiDAR
Model	VLP-16
Wavelength, λ	903 nm
Number of laser emitter-receiver pairs	16
Polar angles of each laser pair relative to a 0° plane $(1-16)$	$-15°, -13°, -11°, -9°, -7°, -5°, -3°, -1°, 1°, 3°, 5°\ 7°, 9°, 11°, 13°, 15°$
Total Scanning Angle, Θ	360°
Vertical FOV	$-15°$ to 15° (30°)
Rotational Frequency, f	5 Hz* – 20 Hz in 1 Hz increments
Angular Step	$0.1° - 0.4°$ (rotational frequency dependent)
Pulse Repetition Frequency, PRF	~ 300 kHz (combined)
Maximum Range	100 m
Range Accuracy	Up to $\pm$30 mm
Dimensions (h × dia)	73 mm × 103 mm
* indicates the mode or conditions the scanners were operated at if multiple operating modes exist	

6.1.2 Translation from θ_1 to Θ_1 Reference Frame

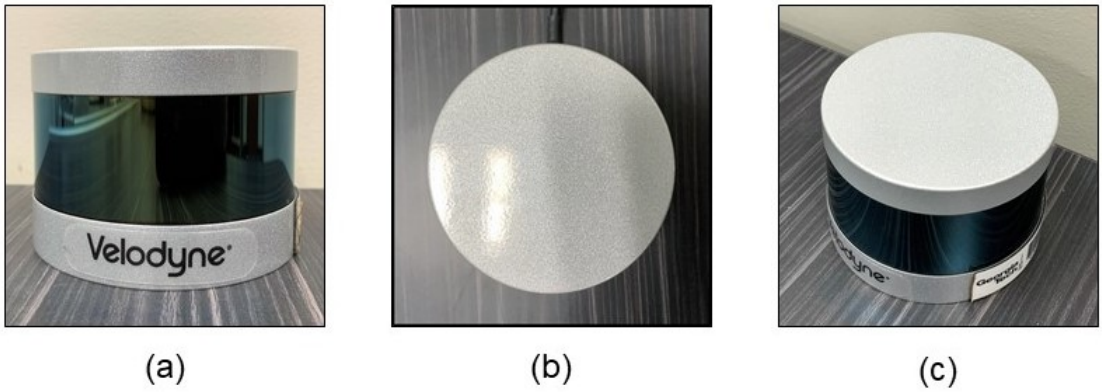

Figure 29 – Device packaging of the Velodyne VLP-16 lidar scanner used in the experiment shown from the (a) front, (b) top, and (c) oblique prospective.

In Section 4.1, the two-scanner system is defined in terms of the spatial relationship between two lidars. A scanner's angular orientation was defined by the angle θ_m referenced from the line joining the two devices. This geometry is convenient for theoretical discussion but does not support practical application. When collecting ranging data, lidars use their own reference frame defined by a scan angle Θ_m, reference from 0° and designated by the manufacturer. Lidars that do not scan a complete 360°, such as the LMS531, further constrain their scan angle with maximum and minimum values given as $\Theta_{m,max}$ and $\Theta_{m,min}$, respectively. The total scan angle's range may extend beyond $\Theta_m = 0°$. In the case of the LMS531, the device begins scanning at a scan angle of $\Theta_{m,min} = -5°$ and ends at a maximum of $\Theta_{m,max} = 185°$ for a total scan angle of $\Theta_{m,total} = 190°$. The centered orientation is taken to be the scanner's azimuth of scan. When describing multiple lidars with unique orientations, this paper will identify their azimuths of scan referenced from scanner 1's 0° scan angle with unit circle angular convention.

The relation between the two-scanner reference frame (θ_m) and the single-scanner reference frame (Θ_m) is shown Figure 30. The translation between the two reference frames uses a translation angle $\Delta\Theta_\theta$. The translation angle $\Delta\Theta_\theta$ is defined as scanner 1's scan angle that which is oriented directly at scanner 2's rotational axis given as

$$\Delta\Theta_\theta \equiv \Theta_1 = \text{Scanner } 2'\text{s Angular Location.} \tag{29}$$

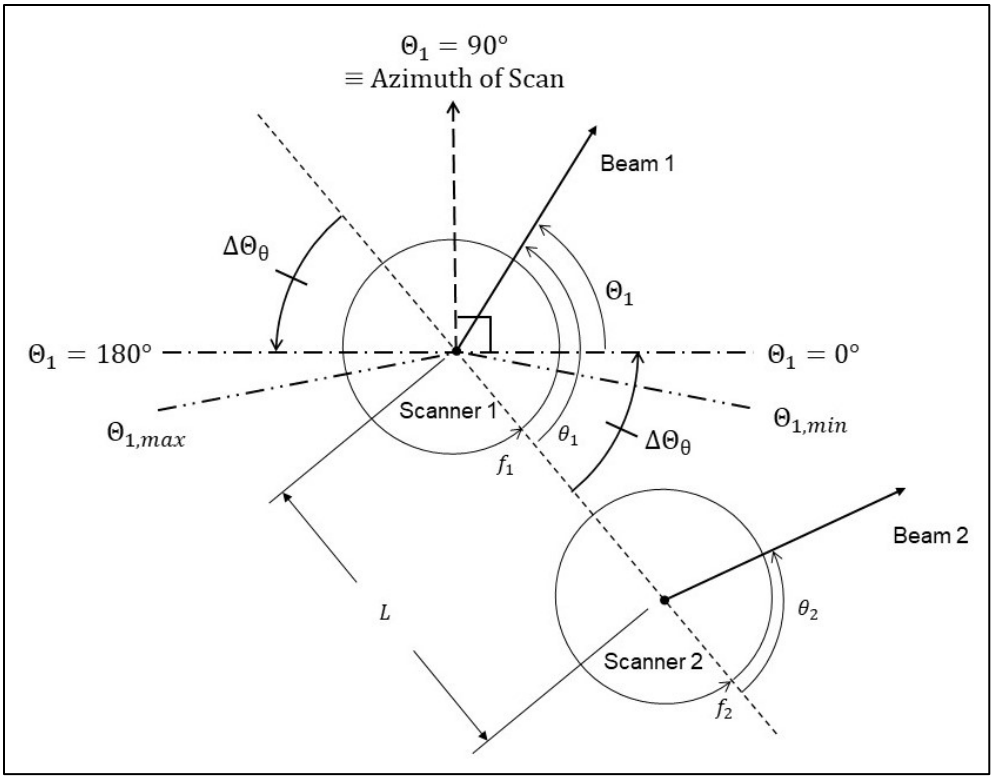

Figure 30 – Relation of the two-scanner reference frame (θ_1) to the one scanner reference frame (Θ_1) using the addition or subtraction of the translation angle $\Delta\Theta_\theta$.

The translation angle $\Delta\Theta_\theta$ is then applied to either reference frame to obtain the other reference frame as either

$$\Theta_1 = \theta_1 - \Delta\Theta_\theta \tag{30}$$

or

$$\theta_1 = \Theta_1 + \Delta\Theta_\theta. \tag{31}$$

If it is desired to calculate for scanner 2, by definition, scanner 2 becomes scanner 1 and the same angle relative to the new scanner orientations can be applied.

6.1.3 Experimental Setup

A basic schematic of the experimental setup is shown in Figure 31. This design closely resembles the setup reported by [17]. The two SICK LMS531 scanners were placed in a staged rectangular room with matte finished walls. Except for test case 4, Scanner 1 remained in the position shown in Figure 31 for the duration of the experiment. Scanner 2 was positioned with measurements made relative to scanner 1 in five separate arrangements. The back wall of the room was constructed of unpainted cinderblock while the side walls were composed of two unpainted, overlapping, 2.4 m long plywood boards each. Other than the walls and scanners, no targets were placed within the scanning plane of the lidars. The arranged room was in the basement of a building, therefore, any returns identified in or outside the limits of the walls represent erroneous target ranges. Scanner

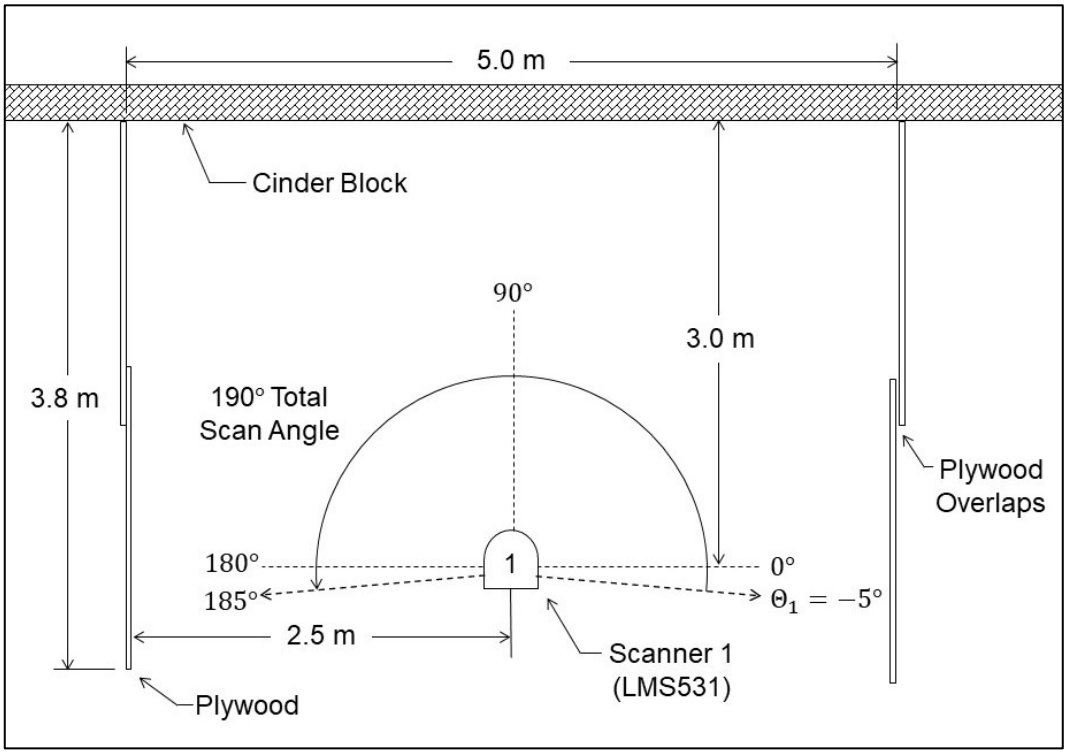

Figure 31 – Basic experimental setup and positioning of scanner 1.

1's scan angle Θ_1 and azimuth of scan are indicated in Figure 31. Scanner 1 was oriented directly at and perpendicular to the back-concrete wall for all five iterations.

The three test cases of the two scanners reported by [17] were closely replicated with two additional test cases added for supplemental investigation. This setup facilitated validation of the previous work while allowing for an extension of [17]'s analysis. Moreover, the experiment provided simple cases to isolate and combine the hypothesized lidar interference types – direct and scattered interference. Lastly, the configurations provided target geometry that allowed for a relatively simple reconstruction with a simulation.

6.1.3.1 Case 1: Side-by-side arrangement #1

The first test case, Case 1, is shown in Figure 32. The two scanners were arranged abreast and oriented in the same direction. This arrangement would test both direct and scattered interference. Scattered interference was hypothesized along mutual scan angles between scanners 1 and 2 which comprised the majority of scanner 1's $190°$ scan FOV. Direct interference was hypothesized to be observable in the portion of scanner 1's scan angle that was occupied by the emitting portion of scanner 2. Since the emitting window from the LMS531 only extend approximately 3/4 of the length of the device, this would leave a small portion of scan angles at a low risk of interference since neither beam intersection nor direct illumination would be possible over these limits. Of note, this arrangement differs from [17] since scanner 2 is directly visible from scanner 1 due to the use of a $190°$ scan angle as opposed to [17]'s use of only $160°$.

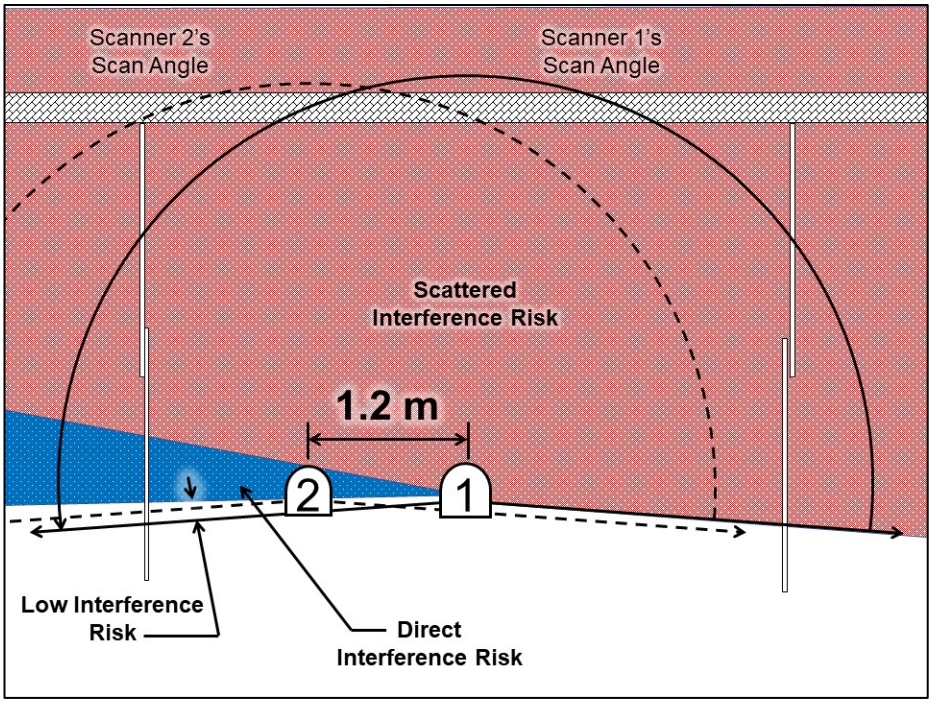

Figure 32 – Case 1: side-by-side arrangement #1 used for testing both direct and scattered interference.

6.1.3.2 Case 2: Side-by-side arrangement #2

The second test case, Case 2, is shown in Figure 33. It too represented a side-by-side configuration, however, scanner 2 was not visible from within scanner 1's scan FOV. This arrangement isolated scattered interference since scanner 2 was not directly visible from scanner 1. Additionally, this tested how the angular distribution of interference occurrences changed given a new relationship to targets by changing the spatial configuration of scanners relative to the walls.

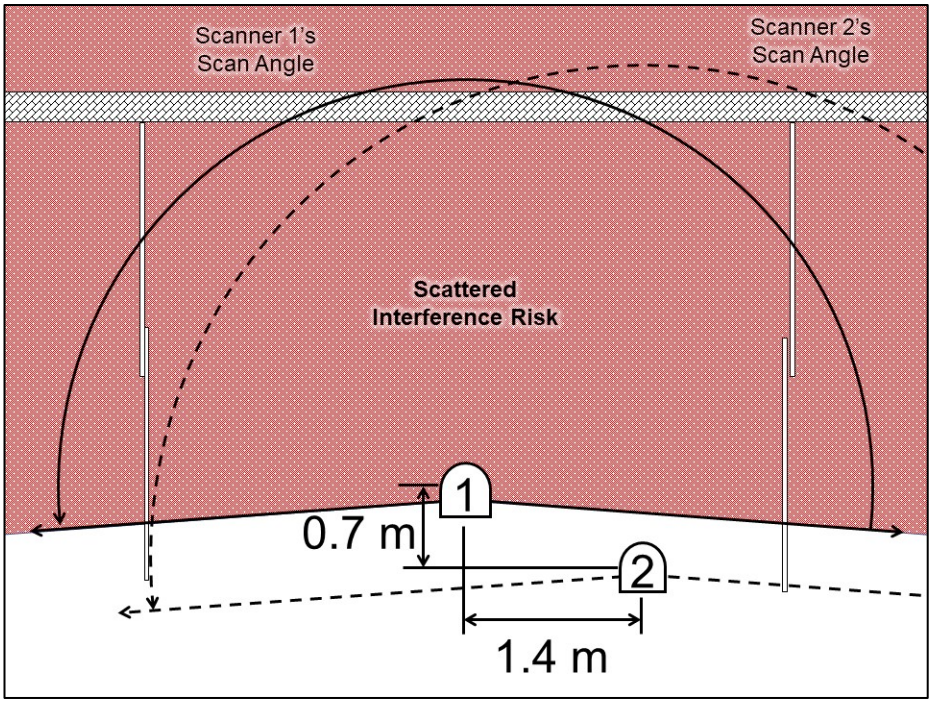

Figure 33 – Case 2: side-by-side arrangement #2 configuration used for testing scattered interference only.

6.1.3.3 Case 3: Face-to-face arrangement

The third arrangement, Case 3, is shown in Figure 34. Case 3 arranged the scanners in a face-to-face configuration such that both scanner's azimuths of scan were directly oriented at the other. This setup allowed for the isolation of scattered and direct interference such that their occurrences were not over contiguous scan angles. Scattered interference should only occur across two bands of scanner 1's scan angle that over lapped with scanner 2's while the center of scanner 1's scan angle should be absent of scattered interference since the two scanner's beams cannot intersect at a target. However, there should be a distinct narrow band of direct interference in the center of scanner 1's scan FOV that which was occupied by scanner 2. Interference should not be observed outside these interference regions.

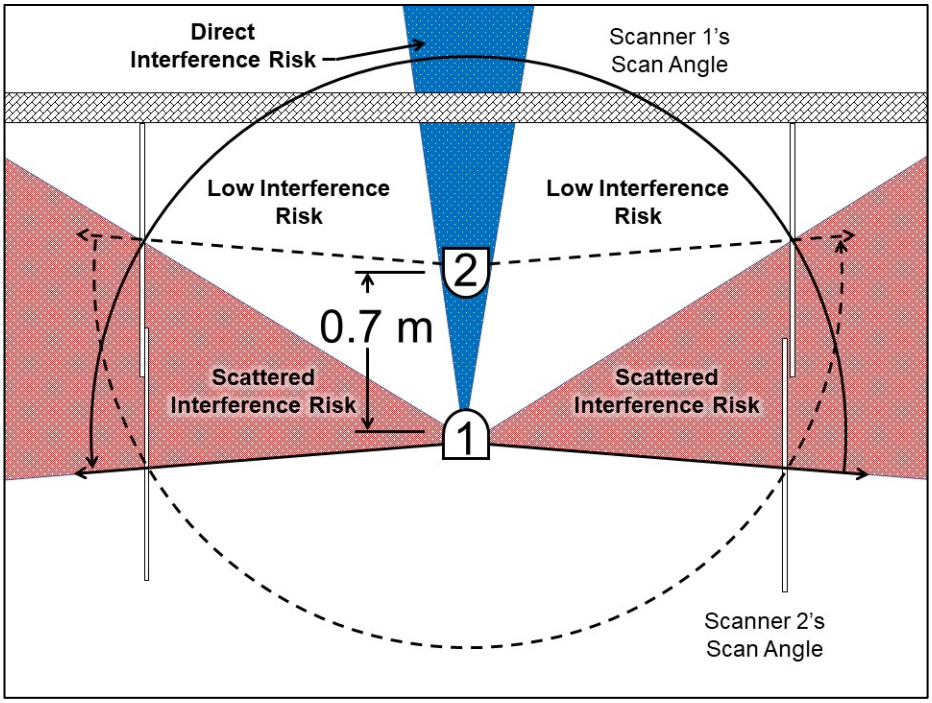

Figure 34 – Case 3: face-to-face configuration used for isolating direct and scattered interference.

6.1.3.4 Case 4: Side-by-side arrangement #3

The fourth test case, Case 4, is shown in Figure 35. Case 4 was one of two arrangements that extended beyond the analysis previously reported by [17]. This

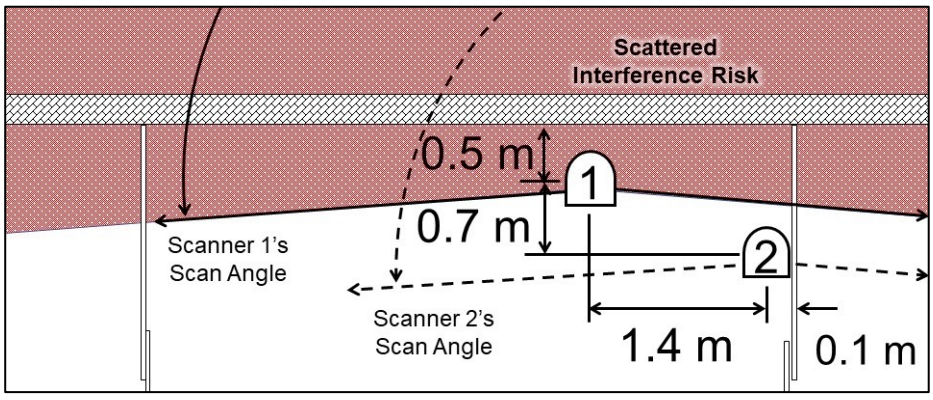

Figure 35 – Case 4: modification of Case 2 with same relative distances between the scanners, but closer to the walls to test the relationship of intersection density to scattered interference occurrences.

arrangement modified Case 2 by maintaining the same relative distance between the two scanners as in Case 2 but arranging them closer to surrounding targets. The purpose of this arrangement was test scattered inference as a function of target location and intersection density. As proposed in Section 5.3, occurrences of reflected interference should increase as a target's location approaches scan angles near the line connecting the two devices and at distances approaching the two devices' separation (in this arrangement approximately 1.6 m). The hypothesis was that Case 4 would result in a higher number of scattered interference occurrences than in Case 2 because targets were in areas of greater intersection point density.

Case 4 was also repeated four times to determine the variance in interference events over multiple observation periods. Given rotational drift and independent pulse transmissions from the two scanners, interference occurrences should be stochastic. However, it is hypothesized that given enough observation, the rate of interference occurrences should have some convergence.

6.1.3.5 Case 5: Multiple Lidar Arrangement

The fifth test case, Case 5, is shown in Figure 36. Case 5 also was a test beyond [17]'s reported results and a modification of Case 2. Using the basic arrangement of Case 2, two VLP-16 scanners (scanners 3 and 4) were added into scanner 1's scanning FOV. This experiment allowed a configuration that tested the risk of signal interference between out-of-plane devices. Additionally, it was a cursorily look at interference between groups of scanners greater than two. This arrangement could then represent a possible scenario of vehicles in a parking garage.

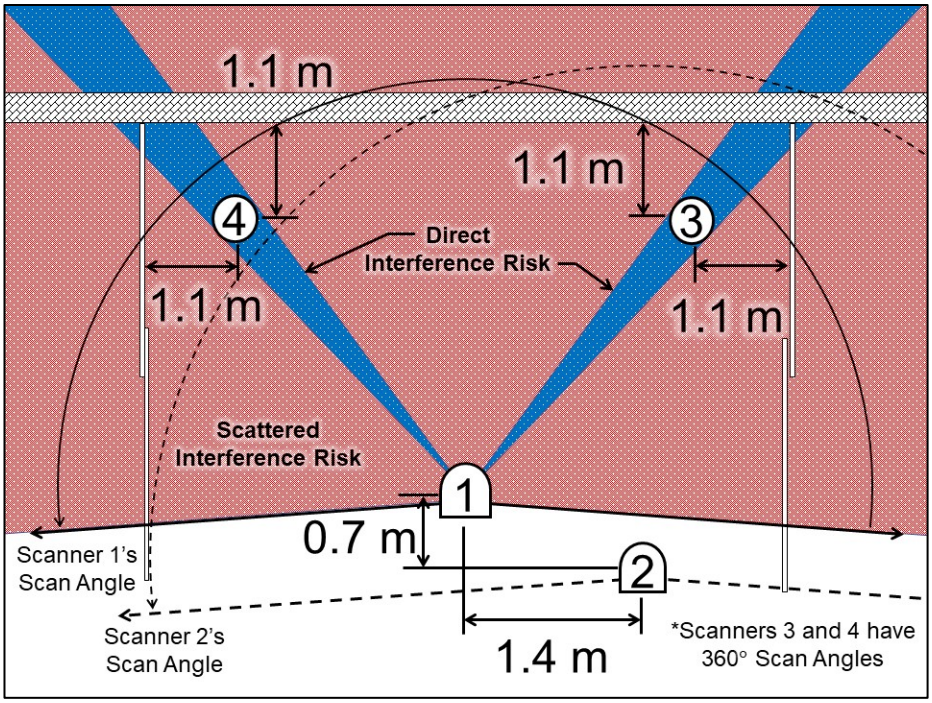

Figure 36 – Case 5: modification of Case 2 with the introduction of two VLP-16 lidars (scanners 3 and 4) added into scanner 1's scan field of view to test out-of-plane interference and interference saturation.

A summary of the five test cases is given in Table 4.

Table 4 – Summary of test cases performed and the test's intended purpose.

Case	Purpose
1. Side-by-side arrangement #1	Tests contiguous direct and scattered interference scan angles
2. Side-by-side arrangement #2	Tests scattered interference only
3. Face-to-face arrangement	Isolates direct and scattered interference conditions with non-contiguous scan angles
4. Side-by-side arrangement #3	Tests the intersection-interference dependency and variance of interference occurrences
5. Multiple lidar arrangement	Tests the susceptibility of interference from out-of-plane scanners and interference saturation

6.1.4 Measurements between devices

For consistency and repeatability, all distances between LMS531 scanners were measured from the contamination indicator sticker on the top of the scanner shown in Figure 37(a). This provided a universal reference on all LMS531 devices that was spatially the closest to the scanner's axis of rotation. However, this was not the rotational axis of the rotating mirror which was likely offset by approximately 5 cm but offered no distinguishable reference.

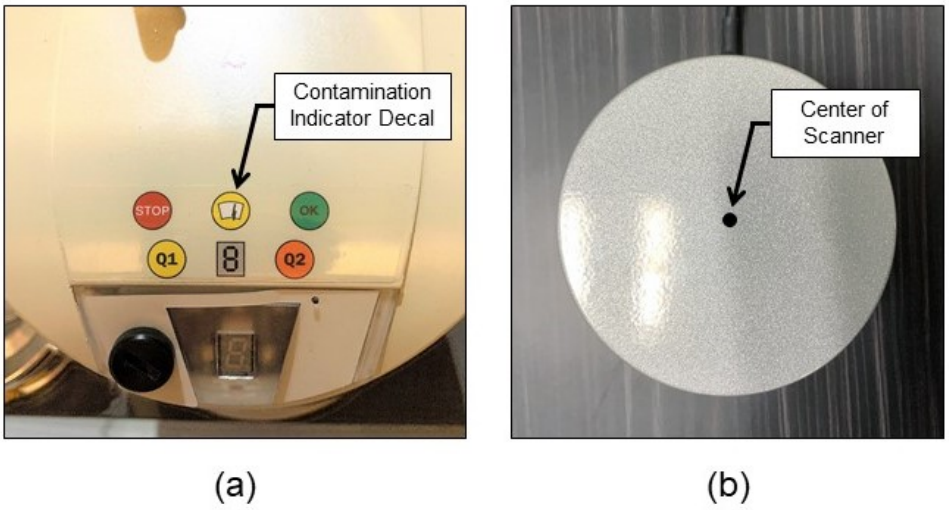

Figure 37 – Measurement references between devices were the (a) contamination indicator decal on the SICK LMS531 and (b) center of the Velodyne VLP-16 lidar scanner were used for all spatial measurements between devices.

The VLP-16 measurements were reference to the center of the scanner, shown in Figure 37(b), which were aligned with the rotational axis of the device. Measurements between devices were made with a standard tape measure and precision carried to 0.01 m. However, due to warping in the plywood walls, the room measurements are not consistent nor perpendicular throughout.

For continuity between tests, after scanner 1 was positioned in the center of the room as shown earlier in Figure 31, Cases 1 through 3 and 5 were carried out without moving scanner 1's positions. Then scanner 1 was repositions and Case 4 was conducted.

6.1.4.1 Differences from Previous Experimental Setups

Though emphasis was placed on replicating the conditions reported by [17] for Cases 1 – 3, some differences existed between the experiments. It was assessed that these differences would not prevent qualitative extrapolation and comparison between the two. A summary of these differences is shown in Table 5.

Table 5 – Summary of difference between experimental setup of [17] and this paper.

Conditions that differ	Kim, 2015	This paper
Lidar Model	SICK LMS511	SICK LMS531
Rotational Frequency	25 Hz	50 Hz
Angular Step	0.25°	0.5°
Scan Angle	160°	190°
Scanner 1's positions from left, front, and right walls	2.5 m, 2.8 m, 2.8 m	2.5 m, 3.0 m, 2.5 m
Run time per iteration	24 hours	Equivalent to 6 minutes

One difference between the two experiments with the potential to disrupt comparability was the use of a total scan angle of 190° as a result of equipment performance, which contrasts to the 160° scan angle used by [17]. This difference could affect the number of recorded interference events. However, when considering interference as a percentage of transmitted pulses, assuming there is a linear relationship, this change should be extrapolatable for reflected interference in Cases 2 and 3. Case 1, however, was expected to result in a higher percentage of interference since direct interference would now be included where it previously was not.

6.2 Procedure

The evaluation of each test case included a training period and a testing period. The training period recorded the ranging data for each configuration, absent of interference source transmissions, to identify the normal operating tolerances of scanner 1 in each test case. The testing period immediately followed the training period and recorded ranging data with the interference source(s) transmitting. The testing period ranging data was compared to the training period data, outliers where identified, and the results were analyzed.

Each period was run for 2.5 hours. By comparison, this was equivalent to 6 minutes of evaluation under the conditions used by [17]. This difference was due to communications constraints of the LMS531 LITE, which only reports scan data at a rate of 1 Hz, despite the device's 50 Hz rotational frequency [57]. This reporting frequency means the device reports one complete scan line of 381 scan angles (0.5° increments over 190°) once per second. Therefore, 2.5 hours, with 1 rotation reported per second is equivalent to 6 minutes at 25 Hz with every rotation reported. As a result, the temporal resolution of the collected data was constrained. However, this setup still provides a regular sampling interval and allowed for a controlled collection of ranging data. Nonetheless, the limits of the temporal resolution were taken into consideration during analysis.

6.2.1 Scan Plane Alignment

At the beginning of each period, the beam scanning planes of the devices were verified to ensure the two scanners were coplanar. A digital camera sensitive to the near infrared (NIR) spectrum was used to perform this alignment. Due to the lower responsivity

of the digital camera in the NIR and the highly collimated nature of the devices' lasers, a laser was visible in the camera display within a narrow angular deviation from the beam's axis. Therefore, the camera could serve as an alignment tool for the beams' projections when using the walls.

The lidars' scan planes were aligned by viewing both lidars simultaneously with the camera from one corner of the room (farthest point from the two scanners) and adjusting scanner 2's pitch and elevation until both lasers were visible in the camera, indicating overlapping projection at that corner. The process was carried out at the other corner of the room and repeated until both lasers were visible in both corners without adjustment between observations. Since the corners of the room were not diametrically opposing points with respect to the scanners' axis of elevation, their simultaneous overlap indicated scan plane alignment between the two. The alignment view from the digital camera is shown in Figure 38.

In Case 5, the VLP-16s were elevated until their bodies were visible in the scan view of scanner 1. Their 0° scan planes were then aligned by using an electronic level. The use of an electronic level was not viable for the LMS531's alignment due to the curved sloping faces of the device.

6.2.2 Training Period

To establish the deviation of ranging points under normal operating conditions (absent of interference energy), a training period was conducted for each test case. For this, the room was mapped at the beginning of each new arrangement for equal duration to the

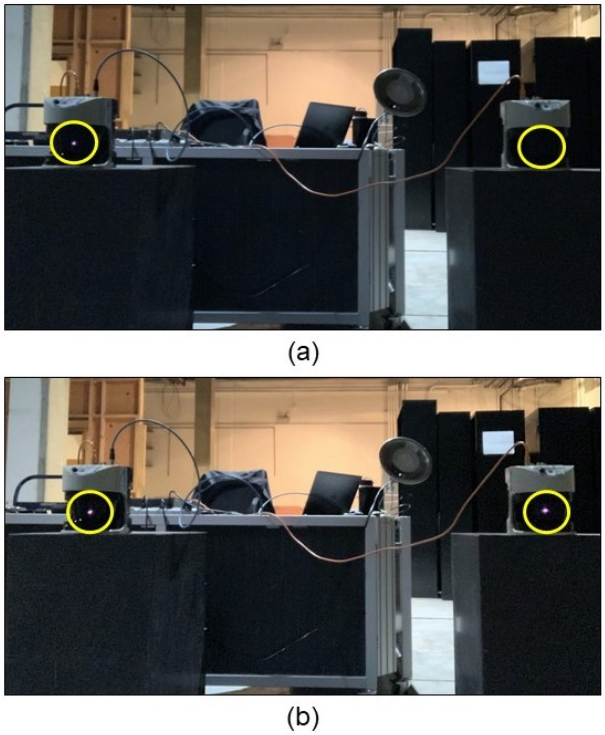

Figure 38 – Alignment of lidar scan plane using a NIR sensitive digital camera. (a) The scan plane between the two lidars is not aligned since only one laser is visible (outlined by yellow circle). (b) The scan plane is aligned and both lasers are visible at the camera.

testing period. Once the room was arranged, scanner 1 collected ranging data for 2.5 hours while scanner 2 remained off but in its designated position for the subsequent testing period. For Case 4, only one initial training period was conducted for the four testing periods.

6.2.3 Testing Period

Following the completion of the training period, scanner 2 was turned on. The scan plane alignment was verified again, and data was collected over another 2.5-hour period. For Case 4, this was repeated four times.

6.2.4 Data Collection and Processing

The data was collected using SICK's SOPAS Engineering Tool version 2018.3. The program's data recorder was used to record the ranging data. The data recording settings were set to a sample period of 1,000 ms and "ScanData" results were selected in the filtering selection. Once recorded, the results were exported using the data recorder's export feature to a comma-separated value file for processing in MATLAB. MATLAB 2018b was used to analyze the recorded data. MATLAB scripts used for this analysis are presented in Appendix B.

6.3 Identification of Interference

In post processing, the training period point cloud data was analyzed for each test case to establish ranging limits at each scan angle for normal operation of scanner 1. Ranging data from the testing periods were compared to these limits. Returns that fell outside of the calculated limits were identified as erroneous ranging data resulting from interference.

Two methods were used to calculate these range limits. The first method followed the procedure prescribed by [17] to facilitate a cursory comparison between the studies. The second used a rigorous statistical method to establish statistical confidence in the identification of interference points.

6.3.1 Kim, 2015 Method

The method for interference identification prescribed by [17] was used to facilitate a cursory comparison between the collected data and the other research team's published

results. The method used the minimum, maximum, and average values of the training data at each scan angle to establish lower and upper ranging limits.

From the training data, at each scan angle of scanner 1, the average $\bar{R}(\Theta_1)$, minimum $R_{min}(\Theta_1)$, and maximum $R_{max}(\Theta_1)$ ranges were calculated or identified. The upper and lower range tolerance limits, $R_{upper}(\Theta_1)$ and $R_{lower}(\Theta_1)$, were calculated as

$$R_{upper}(\Theta_1) = R_{max}(\Theta_1) + \{R_{max}(\Theta_1) - \bar{R}(\Theta_1)\} \times 0.1 \quad (32)$$

and

$$R_{lower}(\Theta_1) = R_{min}(\Theta_1) + \{R_{min}(\Theta_1) - \bar{R}(\Theta_1)\} \times 0.1. \quad (33)$$

Upper and lower tolerances were calculated for both first and second returns.

However, this method does not consider the statistical or mechanical error of the scanner. As reported by the manufacture, under similar experimental conditions the systematic error of the device is reported to be $\pm$ 25 mm with statistical error (1σ) another $\pm$ 6 mm for first returns [56]. Moreover, no justification was provided by [17] for the use of the 0.1 multiplication factor of the extrema's deviation from the average. It was found that using this method resulted in numerous limits well below this statistical error. Additionally, this method ignores the significance of the sample size from which these limits are calculated. Therefore, a second method was used for further analysis of the data to quantify the certainty of false positives and negatives.

6.3.2 Statistical Method

The statistical approach calculated ranging tolerances based on analysis of the training data and distribution fitting. From the training data, it was observed that range returns for a single scan angle in the absence of interference follow a Gaussian distribution as shown in Figure 39. The mean range $\bar{R}(\Theta_1)$ and standard deviation $R_\sigma(\Theta_1)$ were calculated for each scan angle Θ_1 for both first and second returns, as applicable. Upper and lower ranging limits were calculated using five $R_\sigma(\Theta_1)$ deviations from the mean range $\bar{R}(\Theta_1)$ as given by

$$R_{upper}(\Theta_1) = \bar{R}(\Theta_1) + 5R_\sigma(\Theta_1) \tag{34}$$

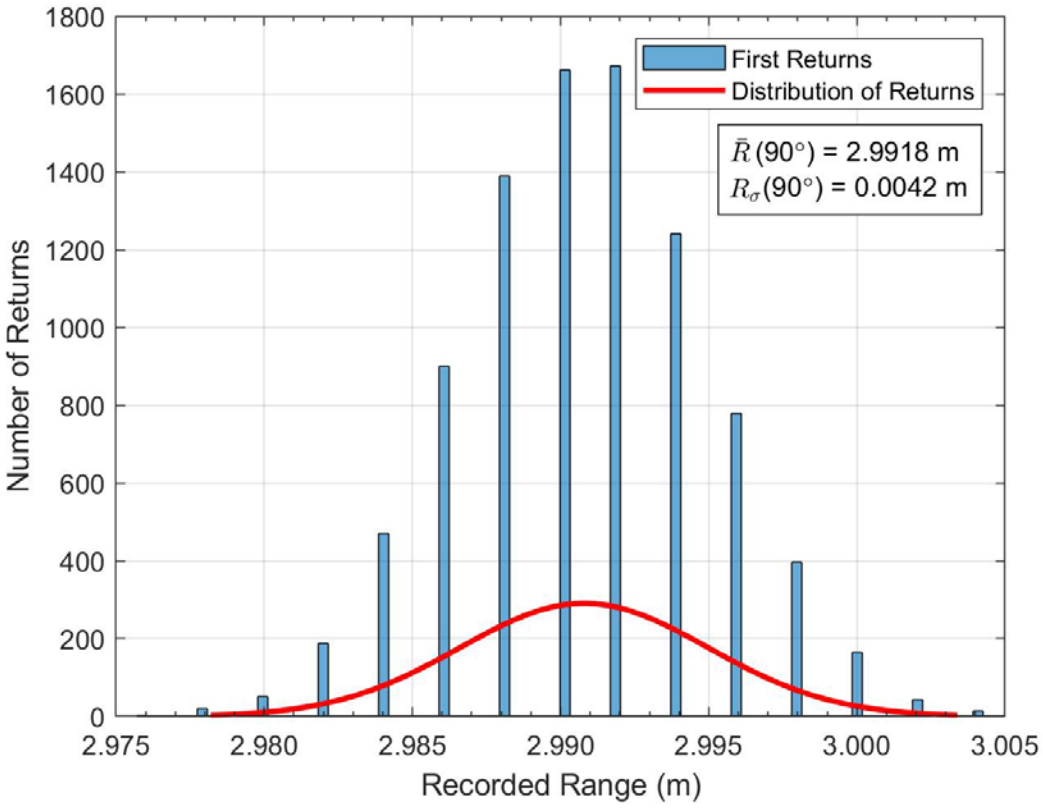

Figure 39 – Gaussian distribution of first returns along a scan angle of 90° collected during training period for Case 1.

and

$$R_{lower}(\Theta_1) = \bar{R}(\Theta_1) - 5R_{\sigma}(\Theta_1)\ . \tag{35}$$

Statistically, only 1 in $1{,}744{,}287$ returns or 5.733×10^{-5} % should fall outside of the upper and lower limits. Therefore, even if every transmitted pulse resulted in two returns, with 381 scan angles per rotation, and approximately $8{,}995$ rotations per test for a total of $6{,}854{,}190$ potential returns per test; less than 4 should be statistically out-of-tolerance.

6.3.2.1 Multi-target Observations

From observation of the training data several multi-target range distributions were observed in Cases 1, 3, and 5. In all these cases, the scan angles with multi-target range distributions corresponded with another scanner's location. The multi-target distributions likely resulted from the partial transmission of the ranging pulse across the other scanners' edges or through scanner 2's laser enclosure.

An example of a dual-target distribution observed in Case 1 is shown in Figure 40. Dual-target ranges for first and second returns were recorded at the first scan angle ($\Theta_1 = 179.5°$) at which scanner 2 was observable by scanner 1. At this scan angle and during this training period, a second return was detected for every transmitted pulse. This parity between first and second returns suggests that at this scan angle scanner 1's beam spot was likely partially clipped by the edge scanner 2 allowing enough laser energy to reach the back wall and scatter a detectable return.

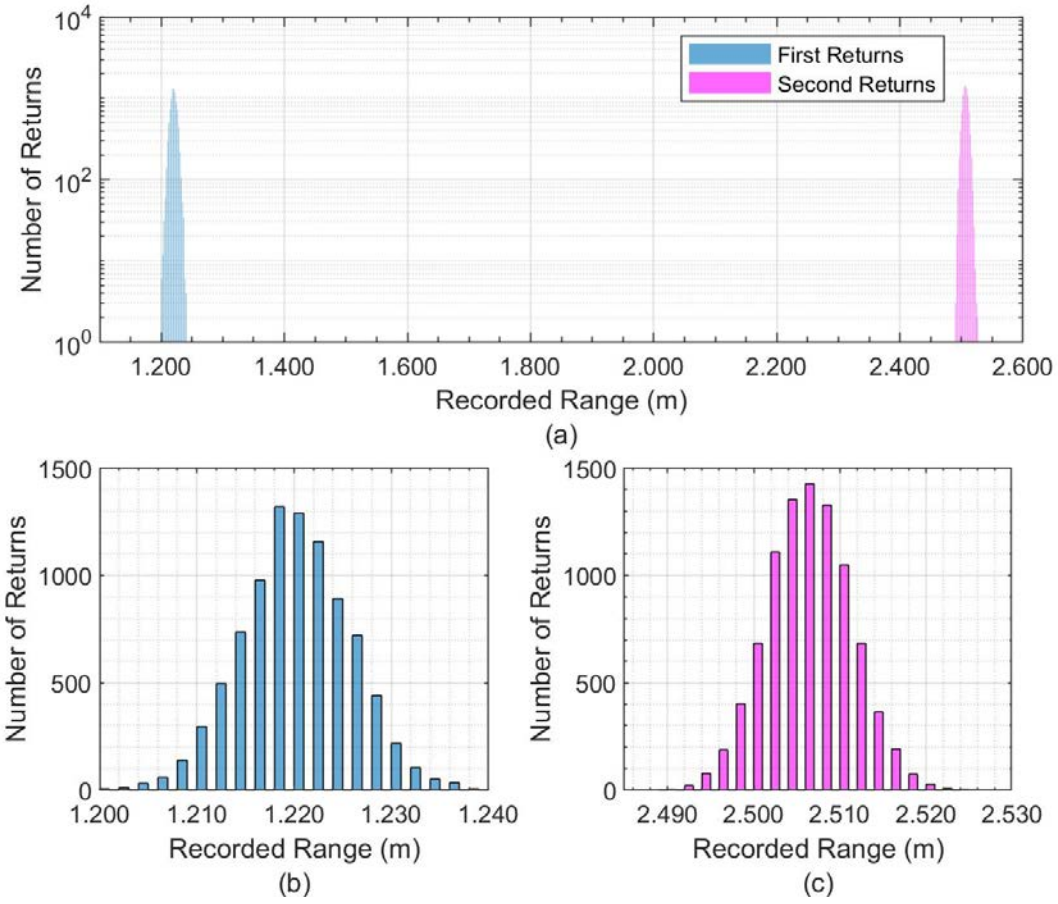

Figure 40 – Histograms showing (a) dual-target returns observed between (b) first returns corresponding to scanner 2's range and (c) second returns corresponding to the backside wall at a scan angle ($\Theta_1 = 179.5°$) in training period of Case 1.

Figure 41 shows the distribution of ranging returns for the next subsequent scan angle ($\Theta_1 = 180.0°$) after the angle shown in Figure 40 for Case 1. Three distributions were observed (Figure 41(a)) with the two larger distributions between 1.200 m and 1.400 m, corresponding to scanner 2's location. A third smaller distribution was observed around 2.450 m, which corresponded to the far-left side wall. The first set of returns (left distribution in Figure 41(b)) had an average range equal to 1.223 m and likely corresponded with a first reflection off scanner 2's plastic laser enclosure. The downward tapering of the enclosure may explain the lower number of returns from this reflection. The

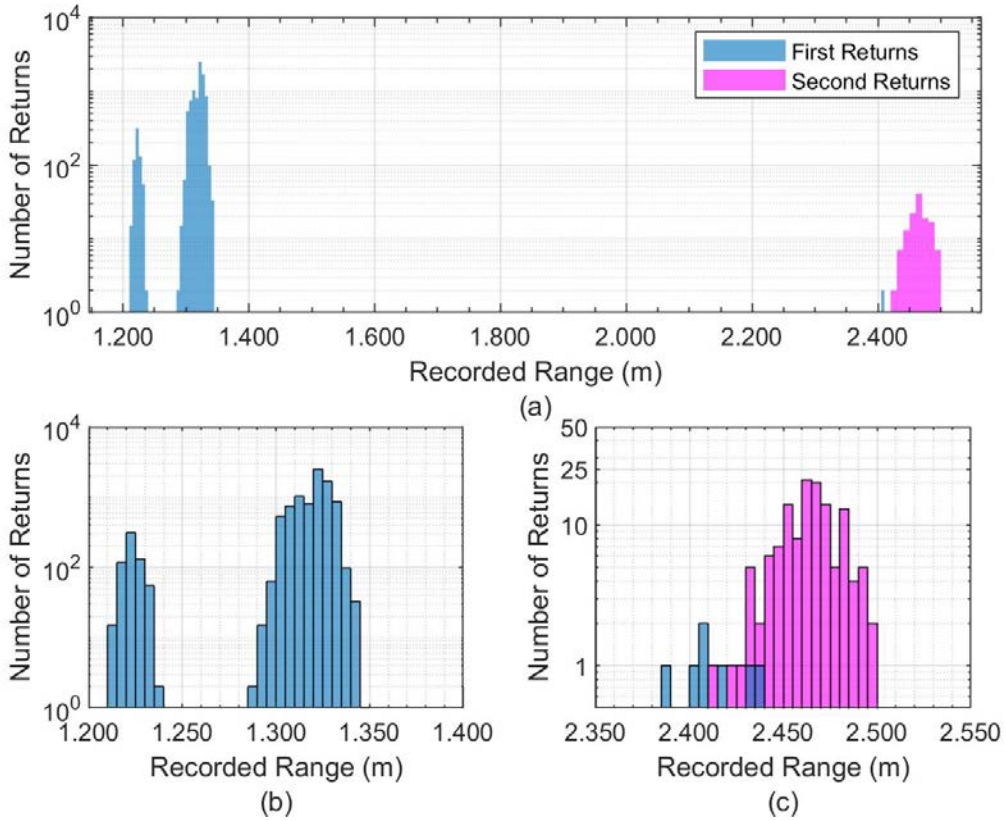

Figure 41 – Histograms showing (a) triple-target returns observed at scan angle ($\Theta_1 = 180.0°$) corresponding with the edge of scanner 2 in training period of Case 1 (b) with returns registering near at scanner 2's range and (c) at the wall on the far side of scanner 2.

second, larger set of returns had an average range of 1.320 m. The distance between these two average ranges roughly equals to 0.097 m, which is slightly less than the width of scanner 2, given by the manufacture as 0.155 m [56]. This correspondence suggests that the second distribution is associated with another reflection occurring within the width of scanner 2. It is hypothesized that this corresponded with another reflection from the laser housing plastic as the beam exited the other side of scanner 2's laser enclosure. Furthermore, the width of the enclosure was less than that of the overall width of the scanner. The distribution in Figure 41(c) then corresponds with the wall on the opposite side of scanner 2 from scanner 1. Figure 42 illustrates this hypothesis, however, the internal

structure of the housing would need to be inspected to substantiate this hypothesis and a nondestructive examination was not possible.

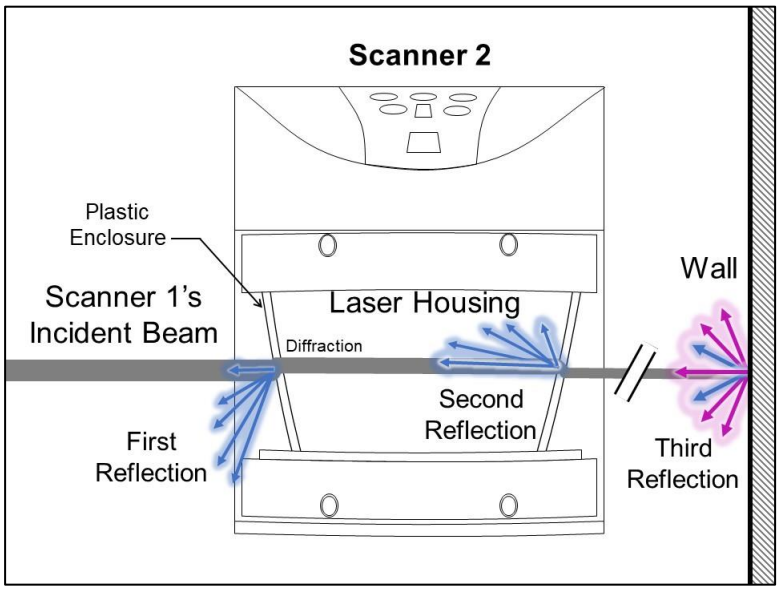

Figure 42 – Hypothesis of triple-target return distribution observed in Case 1 at scan angle 180° with two partial reflections off scanner 2's laser housing and the last return from the back wall.

Most of returns that corresponded with the back wall were from second returns. However, a total of seven first returns were recorded at this range. This distribution was compared to the distribution at the same scan angle observed during the training period of Case 2. Case 2's data provided an uninhibited ranging measurement of the wall at this scan angle since scanner 2 was not intervening in this arrangement. The average range observed in Case 2's training period was found to be 2.453 m which corresponds with the distribution of the second returns in Case 1's training data. Therefore, it appears the first returns observed at this angle are nearside biased. However, the number of observations is small and further investigation would be needed to understand why. These two instances were the only two scan angles that observed multi-target range distributions and second returns in Case 1's training data.

Triple-target and dual-target range distributions with similar characteristics were observed in Case 3's training period data and are shown in Figure 43. These were observed at the scan angles corresponding with the right and left edges, respectively, of scanner 2 as observed from scanner 1 ($\Theta_1 = 88.5°$ and $93.5°$). As expected, even after treating each target distribution individually, scan angles corresponding with multi-target range distributions contained the highest standard deviations when calculated. This was likely due to the lower sample size in each distribution since first returns were divided between two (or three) target ranges.

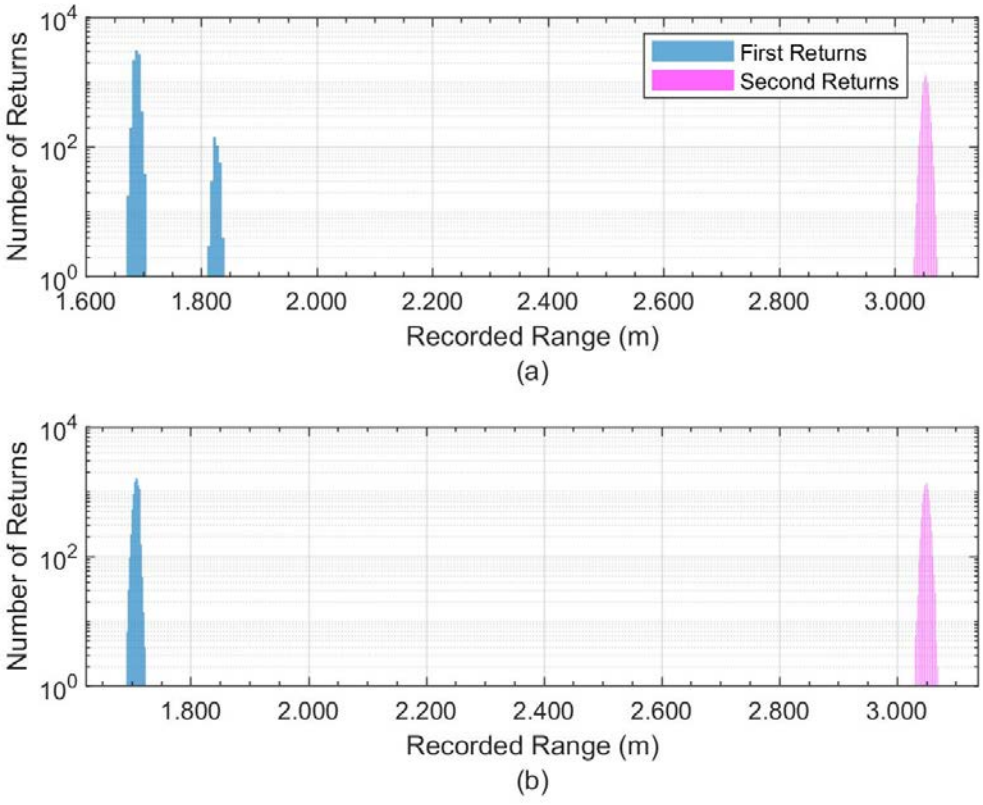

Figure 43 – Histograms showing (a) triple-target and (b) dual-target range returns at scan angles corresponding with the right ($\Theta_1 = 88.5°$) and left ($\Theta_1 = 93.5°$) edges of scanner 2 in training period of Case 3.

No multi-target ranges distributions were observed from Case 2 or Case 4's training data which further supported the hypothesis that this was caused by features with abrupt range changes such as scanner 2's edge. These features were absent in Cases 2 and 4. However, multi-target distributions were observed again in Case 5 around the edges of scanners 3 and 4. A summary of the standard deviations by test case are shown in Table 6.

Table 6 – Summary of standard deviations calculated for each training period.

Parameter	**Case 1**	**Case 2**	**Case 3**	**Case 4**	**Case 5**
Total Pulses	3,427,095	3,428,238	3,427,857	3,428,238	3,428,238
First Returns					
Total	3,427,095	3,428,238	3,427,857	3,428,238	3,428,238
Maximum Standard Deviation (Scan Angle Observed)	0.0197 m (180.0°)*	0.0045 m (130.5°)	0.0047 m (132.0°)	0.0068 m (1710°)	0.0080 m (128.0°)
Average Standard Deviation	0.0043 m	0.0042 m	0.0043 m	0.0042 m	0.0041 m
Minimum Standard Deviation (Scan Angle Observed)	0.0036 m (180.0°)	0.0038 m (182.0°)	0.0038 m (178.5°)	0.0037 m (−2.5°)	0.0036 m (53.5°)
Second Returns					
Total	9,124	0	17,650	0	2,282
Maximum Standard Deviation (Scan Angle Observed)	0.0197 m (180.0°)*	–	0.0054 m (88.0°)	–	0.0194 m (127.5°)
Average Standard Deviation	0.0043 m	–	0.0053 m	–	0.0134 m
Minimum Standard Deviation (Scan Angle Observed)	0.0049 m (179.5°)	–	0.0053 m (93.5°)	–	0.0045 m (128.0°)

* Both correspond to the same distribution. The distribution included both first and second returns from the back wall.

6.3.2.2 Evaluating Interference in Multi-target Cases

Multi-target distributions were identified and treated on a case by case basis when establishing upper and lower range limits for interference identification. Although this phenomenon may degrade the overall precision of ranging measurements, for this investigation, their occurrence was not considered to be interference. Therefore, since the number of returns in each range distribution represented a significant sample size, the upper and lower limits were calculated for each range distribution separately.

When evaluating the test period data, returns along multi-target scan angles were tested against all sets of upper and lower range limits. If within tolerance of any, the point was considered within normal observable limits. However, if a return's range did not fall within any set, the return was considered the result of interference. Additionally, second returns were compared to both the calculated first and second return limits. Only if a testing period return was out-of-tolerance with both, was it considered to be interference. The reasoning for this decision considers that if a nearside ranging error had occurred due to interference, this would be registered as the first return. A subsequent return would still be expected from the true target along that scan angle corresponding to what would have been the first return without interference.

6.3.2.3 Distinguishing Between Direct and Scattered Interference

Since this work is the first to distinguish between types of lidar interference, simple filtering methods were employed to begin analysis. Modes of interference were distinguished by separating out-of-tolerance returns by scan angle. The original hypothesis postulated that out-of-tolerance points returned from within the angular limits of scanner 2

were the result of direct interference while those returns from outside the scanner's angular limits would have to be the result of scattered interference.

Case 3 provided an arrangement to test this hypothesis since direct and scattered interference should be isolated due exclusivity of scan angles between scanners 1 and 2 along the back wall. While further discussion is included later, it was found that the effects of direct interference could be observed outside these limits. Therefore, because it was trivial to distinguish between direct and scattered interference in Case 3, the scan angle filtering criteria was adjusted to accommodate this observation. However, due to the difficulty in distinguishing between interference returns in Cases 1 and 5, the strict angular limits of scanners 2, 3, and 4 were used. Therefore, the direct interference numbers reported for Cases 1 and 5 are likely conservative while the scattered interference is likely liberal. However, the total out-of-tolerance points recorded for these cases is not affected by these filtering criteria. Subsequent analysis as to the occurrences per scan, by interference mode, and relation to first or second returns was then conducted.

6.3.3 Evaluation of Training Data

The training data was first analyzed against the calculated range tolerance using the two methods to see how known in-tolerance data performed against each method. Under normal operating conditions, some deviation in the recorded ranges should be expected. Ideally, the upper and lower ranging limits should be broad enough to include these natural fluctuations but narrow enough as to not overlook interference induced degradations in ranging accuracy. Moreover, if the limits are too constrained, they will misidentify returns as interference that represent legitimate targets and thus bias the results.

The analysis of the training data using both methods is shown in Table 7. In general, the method use by [17] falsely categorized second returns from real targets as points out-of-tolerance. Overall, the method identified 26,774 second returns as out-of-tolerance when they corresponded with real targets. Therefore, this method would over count the number of interference occurrences when used in an environment that normally produces multiple returns such as Cases 1, 3, and 5.

Table 7 – Comparison of methods used to identify interference (out-of-tolerance) points analyzing training spatial data that was absent of interference sources.

	Case 1		**Case 2**		**Case 3**	
	Kim, 2015 Method	**Statistical Method**	**Kim, 2015 Method**	**Statistical Method**	**Kim, 2015 Method**	**Statistical Method**
Total Pulses	3,427,095		3,428,238		3,427,857	
Total Returns	3,436,219		3,428,238		3,445,507	
Total Out-of-tolerance Returns	8,995	1	0	4	17,650	5
First Returns	3,427,095		3,428,238		3,427,857	
First Returns Out-of-tolerance	0	1	–	4	0	5
Second Returns	9,124		0		17,650	
Second Returns Out-of-tolerance	8,995	0	–	-	17,650	0

Alternatively, the number of returns identified as out-of-tolerance by the second method were statistically expected. Using five standard deviations as upper and lower limits for recorded ranging data that follow a Gaussian distribution should results in only 1 in 1,744,287 observations outside the limits. Given the observed sample size, it would be expected to see approximately 2 first returns and less than 1 second return out-of-

tolerance for each Case. This trend was generally observed. However, all out-of-tolerance points identified using the statistical method were found to be over the upper ranging limits. This result suggests that the distribution about the mean target range is not exactly Gaussian. Nonetheless, the method identified out-of-tolerance points with statistical expectation. A detailed discussion of each Case's results is presented next.

6.3.3.1 Case 1 Comparison

In Case 1, the Kim, 2015 method identified a majority of the second returns as out-of-tolerance. These returns corresponded with the left side wall and were observed at $\Theta_1 = 179.5°$ which aligned with the right edge of scanner 2 as seen from scanner 1. Since this method considers each set of first or second returns for a scan angle as a homogenous distribution, it calculated the upper and lower limits between and 2.550 m and 1.200 m, respectively. Therefore, this method would consider any return identified between scanner 2's location and the left side wall, which was absent of targets at this scan angle, as within tolerance. Erroneous returns recorded between scanner 2 and the wall would then have been overlooked.

Alternatively, the statistical method identified only one first return as out-of-tolerance by a difference of -2.5×10^{-4} m (short of the wall) along a scan angle of $168.0°$. Statistically, this result met expatiations.

6.3.3.2 Case 2 Comparison

In Case 2, the Kim, 2015 method identified all training points as within tolerance. This trend was expected since the target geometry did not include any abrupt range

transitions and all returns were for a single range. The statistical method identified four training points out-of-tolerance at four separate azimuths. The greatest of which was over its upper limit by 0.0045 m and corresponded near the back-left corner as observed from scanner 1. The four points were all over the upper limit which suggests that the distribution about the wall is not perfectly Gaussian, but slightly biased to greater ranges. However, four out-of-tolerance returns still agrees well with the statistical distribution.

6.3.3.3 Case 3 Comparison

In Case 3, the Kim, 2015 method identified all 17,650 second returns as out-of-tolerance. These points corresponded with returns from the back wall and represented a real target. Moreover, the returns identified as out-of-tolerance corresponded with the left and right angular limits of scanner 2 as observed from scanner 1.

The statistical method identified only 5 first returns as out-of-tolerance. One of these points corresponded to the back wall just right of scanner 2 as seen from scanner 1. No distinguishable pattern was observed in the other four points. The highest deviation from the upper limit was 0.002 m seen in two of the points, while the other three were over the upper limit by less than 0.001 m.

6.4 Comparison of Testing Results to Previous Work

A cursory comparison of the data from the testing period was compared to the results reported by [17] to assess the reproducibility of the work. As a comparison, both tolerance methods were used to analyze the testing data. The results of this comparison are shown in Table 8.

Table 8 – Comparison of Kim, 2015 results to observed results.

Case 1			
Average	**Kim, 2015 Results [17]**	**Kim, 2015 Method (this work)**	**Statistical Method (this work)**
Total Pulses	1,384,560,000	3,428,238	
Interference Points	41,031	35,825	30,194
Percent Interference	2.96×10^{-3} %	1.04 %	0.881 %
Case 2			
Total Pulses	1,384,560,000	3,428,238	
Interference Points	228,271	1,332	771
Percent Interference of Transmitted	0.0165 %	0.0389 %	0.0224 %
Case 3			
Total Pulses	1,384,560,000	3,428,238	
Interference Points	34,167	20,279	794
Percent Interference of Transmitted	2.47×10^{-3} %	0.592 %	0.0232 %

As discussed earlier in Section 6.3.3, the Kim, 2015 method likely resulted in an over identification of interference events. Nonetheless, the method was used to facilitate a comparison of this work's experimental data with the results reported by the method's authors in [17]. For this comparison, the percent interference of transmitted pulses was calculated. This is given by the percentage of total interference points observed over total pulses transmitted or

$$\%\ \text{Interference of Transmitted} = \frac{\text{Total Interference Observations}}{\text{Total Pulses Transmitted}} \times 100. \quad (36)$$

This equation was used for this comparison because the number of returns was not reported by [17], but rather the total number of transmitted pulses. However, the number of pulses was only reported to the nearest ten thousand. Nonetheless, assuming this is a rounded value, the difference in the resulting percent interference for the most sensitive case (Case

3, which contained the least interferences pulses) would be less than one billionth of a percent when considering $\pm 5{,}000$ pulses. Therefore, this is a sufficient metric to facilitate a simple comparison between the two studies. However, this method of quantifying interference has its shortcomings. Namely, this does not consider the number of returns, which may be higher (or lower) than the number transmitted pulses. Assuming interference corrupts the recorded ranging data, it is more significant to discuss interference in terms of the fraction of one's point cloud that may be corrupted which is representative of the number of returns, not the transmitted pulses. Therefore, later analysis will focus on the percent interference relative to returns which is more relevant when considering point cloud integrity.

In general, the observed instances of interference were higher than those reported by [17] using both methods for the same experiments. An initial explanation is the use $190°$ of total scan angle as compared to the previous study's use of only $160°$. As a result, in Case 1, scanner 2 was directly observable from scanner 1 where as in the experiment performed by [17] it was not. Therefore, one would expect an increase in the observed interference as direct interference is now included.

When the results of Case 2 were compared, the observed percent interference was on the same order of magnitude, which was expected since this test only included reflected interference. Despite the increased scan angle, Case 2's conditions are nearly analogous between the two experiments. However, the results were still nearly two to three-fold higher than previously observed, depending on the method of interference identification.

Several explanations could explain observed increases in interference. The first of which could be a result of differences in scan plane alignment techniques between the two experiments. Kim [17] did not report the method used for scan plane alignment, so this is unknown. The second explanation could be from differences in how the two scanner models detected and recorded returns. Though both scanners are from the same product line and family, differences may still exist between them. Another explanation could include the higher scan angle. As calculated, the percent interference is relative to the number of transmitted pulses. Therefore, this suggests that interference does not occur uniformly by scan angle. This observation partially supports the hypothesis of geometric influence on interference since the density of intersection points is not uniform by scan angle either (see Figure 26 from Section 5.3).

Case 3's results using the previous study's method identified occurrences of interference at a rate three orders magnitude higher than previously reported. Again, the increased scan angle likely contributed, but it does not provide a satisfactory explanation. However, the unknowns of the previous experiment's conduct prevent further substantive explanation.

CHAPTER 7. EXPERIMENT RESULTS

Key Conclusions:

- **Direct and scattered interference distinguished themselves by angular and spatial density.**
- **Direct interference was characterized by at least an order of magnitude higher intensity of occurrences than scattered interference, however, resulted in lower average ranging errors – on average between 0.003 m and 2.482 m of error.**
- **Scattered interference was characterized by a more diffuse angular and spatial occurrence, however, resulted in higher average ranging errors – on average between 31.087 m and 38.344 m of error.**
- **Direct interference likely has two modes – diffuse-direct and coupled-direct – each depending on the coupling efficiency between the scanners and characterized by different ranging error.**
- **Direct interference is likely more sensitive to beam alignment than scattered interference based off the hypothesis that the Case 3 results were compromised due to poor beam alignment.**
- **The angular distribution of scattered interference events correlated well to the distribution predicted by considering intersection point density and target location.**
- **In-tolerance ranging points were not observed over some direct interference scan angles which suggests that interference may also compromise the integrity of the point cloud in addition to adding erroneous spatial data.**

- **The variance of interference occurrences was found to have a standard deviation of roughly 10% of the mean value of scattered interference occurrences in Case 4.**

A thorough analysis of the results was conducted to identify patterns in the interference occurrences that may suggest distinguishing characteristics and mechanisms between the two modes. For this analysis, only the statistical method was used to identify occurrences of interference. An overview of the results is presented first with a comparative analysis in the subsequent sections.

7.1 Overview of Results

7.1.1 Case 1: Side-by-Side Arrangement #1

The in- and out-of-tolerance points recorded in Case 1 are plotted in Figure 44. Overall, of the nearly 3.5 million returns, just over 27,500 returns (1.04% of the total returns) were identified as out-of-tolerance. The majority of these, 33,661 returns, were identified to be as a result of direct interference as opposed to the 2,164 returns identified as scattered interference. Interference points were recorded out to the maximum range of the scanner 1 (80 m). This quantitative distinction between angular regions supports the hypothesis that direct and scattered interference are distinct phenomenon from one another. Moreover, these regions of varying interference intensity correspond with the hypothesized interference risks discussed in Section 6.1.2.

Qualitatively, the density of interference points was higher in the left half of the observable target space (scanner 2's side), even outside of the angular limits of direct

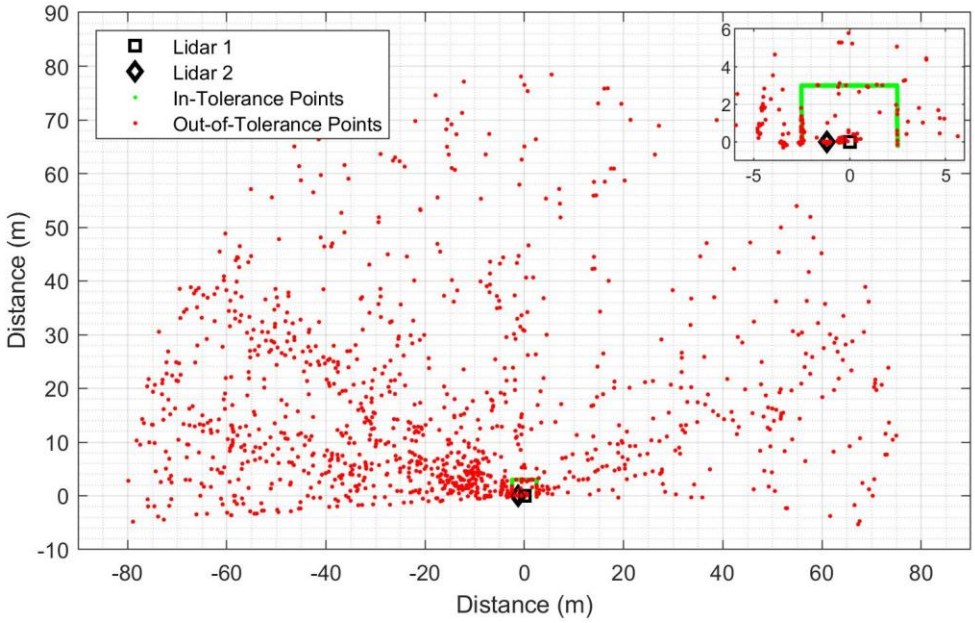

Figure 44 – Case 1: ranging points recoded during the testing period of the first side-by-side arrangement.

interference. This trend was qualitatively observable in [17]'s results and is hypothesized to be a result of the intersection geometries' coincidence with the targets geometries in areas of higher intersection density. A more detailed quantitative analysis that support this is given in the following sections.

A summary of the testing results is given in Table 9. Here, the percentage of interference is presented in two ways – relative to the number of returns, by type and relative to the total observed interference, by type.

Table 9 – Case 1: Side-by-side arrangement #1 results analysis.

Parameter	Total	First Returns	Second Returns
Pulses	3,428,238	–	–
Returns	3,438,411	3,428,233	10,178
Total Interference	35,825	29,442	6,383
Direct Interference	33,661	28,321	5,340
Scattered Interference	2,164	1,121	1,043
% Total Interference of Returns	1.04%	0.859%	62.7%
% Direct Interference of Returns	0.979%	0.826%	52.5%
% Scattered Interference of Returns	0.0629%	0.0327%	10.2%
% Direct Interference of Interference	94.0%	96.2%	83.7%
% Scattered Interference of Interference	6.04%	3.81%	16.3%

7.1.2 Case 2: Side-by-Side Arrangement #2

The ranging points from Case 2's testing period are shown in Figure 45. This case only included scattered interference and accordingly, the density of out-of-tolerance points was mostly diffuse and absent of high intensity pockets of interference when compared to Case 1 with direct interference. Instances of interference were also lower than Case 1, with only 771 out-of-tolerance events recorded from the nearly 3.5 million returns. This difference is hypothesized to result from the change in the target geometry's position relative to the intersection geometry. Accordingly, the number of scattered interference events was expected to change in each case, given a new relationship of the two scanners and the surrounding target geometry. To a lesser extent, this decrease may also result from the lack of direct interference coupling that may occur outside of the strict angular limits of scanner 2 that occurred in Case 1. This difference is discussed further in Section 7.2.2.

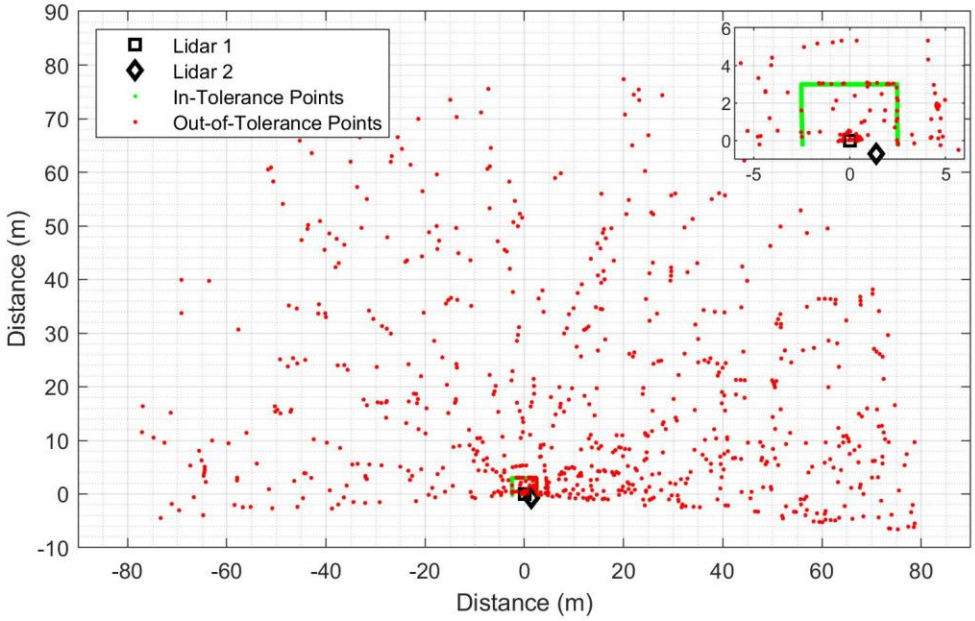

Figure 45 – Case 2: ranging points recoded during the testing period of the second side-by-side arrangement.

Of the 697 second returns, 695 returns were identified out-of-tolerance, thus the result of interference. The two in-tolerance, second returns were likely still the result of interference but just happened to register within tolerance since this configuration did not produce any second returns during the training period.

Not as distinguishable, but still qualitatively evident is the higher density of out-of-tolerance points on the side of the plot (right side) that which scanner 2 occupies. A summary of the testing results is given in Table 10.

Table 10 – Case 2: Side-by-side arrangement #2 results analysis.

Parameter	Total	First Returns	Second Returns
Pulses	3,428,238	–	–
Returns	3,428,932	3,428,235	697
Total Interference	771	76	695
Direct Interference	0	0	0
Scattered Interference	771	76	695
% Total Interference of Returns	0.0225%	0.00222%	99.7%
% Direct Interference of Returns	0%	0%	0%
% Scattered Interference of Returns	0.0225%	0.00222%	99.7%
% Direct Interference of Interference	0%	0%	0%
% Scattered Interference of Interference	100%	100%	100%

7.1.3 Case 3: Face to Face

The results of Case 3's testing period are shown in Figure 46. In this arrangement, the distinction between areas of hypothesized direct and scattered interference risk were easily observable. However, only 794 points were identified as out-of-tolerance, the

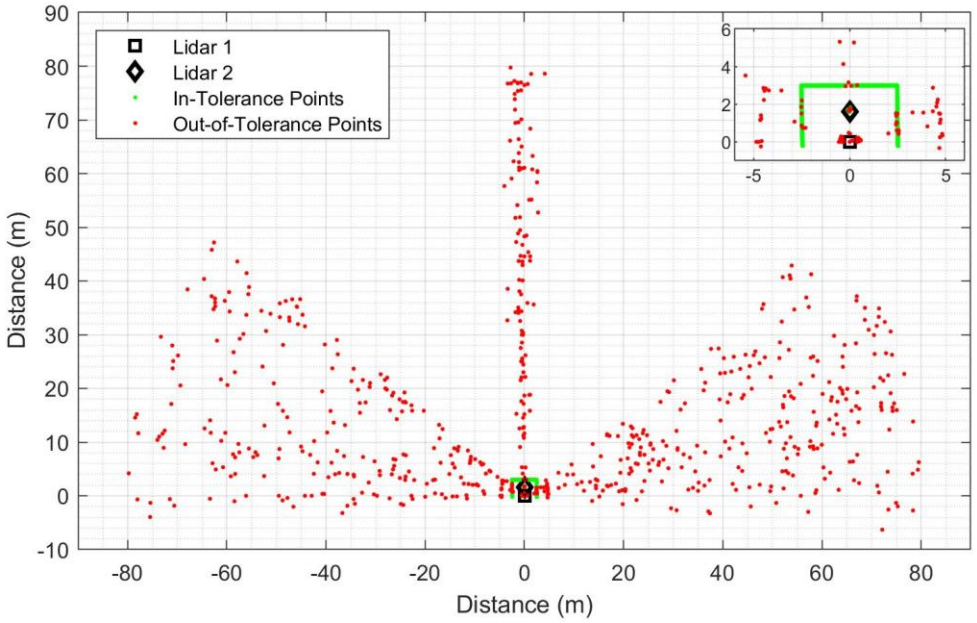

Figure 46 – Case 3: ranging points recoded during the testing period the face-to-face.

majority of which (581) identified as a result of scattered interference. While only 213 were identified as the result of direct interference.

The lower observations of scattered interference when compared to Cases 1 and 2 is broadly explainable due to the lower number of mutual shared scan angles between scanners 1 and 2. In this arrangement, approximately only 85° out of scanner 1's 190° scan angle was shared with scanner 2 as opposed to the near and full 190° in Cases 1 and 2, respectively. As a result of this decrease, the occurrences of scattered interference were expected to be lower.

This test was also the lowest producing interference test from [17]'s results. However, the lower number of direct interference events is not as readily explainable and will be analyzed further in the subsequent analysis in Section 7.5.3. Nonetheless, it suggests that the beam alignment procedure for Case 3 may have been inadequate. A summary of the testing results is given in Table 11.

Table 11 – Case 3: Face-to-face results analysis.

Parameter	**Total**	**First Returns**	**Second Returns**
Pulses	3,428,238	–	–
Returns	3,446,541	3,428,238	18,303
Total Interference	794	161	633
Direct Interference	213	106	107
Scattered Interference	581	55	526
% Total Interference of Returns	0.0230%	0.00470%	3.46%
% Direct Interference of Returns	0.00618%	0.00309%	0.585%
% Scattered Interference of Returns	0.0169%	0.00160%	2.87%
% Direct Interference of Interference	26.8%	65.8%	16.9%
% Scattered Interference of Interference	73.2%	34.2%	83.1%

Case 4: side-by-side arrangement #3

The testing results from the first of four iterations of Case 4 are plotted in Figure 47. The first purpose of this case was to test the proposed dependency of scattered interference on target geometry by moving the scanners closer to the wall such that the wall coincides with areas of theorized higher intersection density as discussed earlier in Section 5.3. As hypothesized, the number of out-of-tolerance points increased from that observed in Case 2 with 771 points, to a total of 1,076 points for the first iteration. As with Case 2, most of the out-of-tolerance points were recorded as second returns with only one other second return registered in-tolerance. Again, the density of out-of-tolerance points is higher on the half of the plot that scanner 2 occupies which is consistent with the hypothesized function of the intersection geometry. A summary of the results from Case 4 are presented in Table 12.

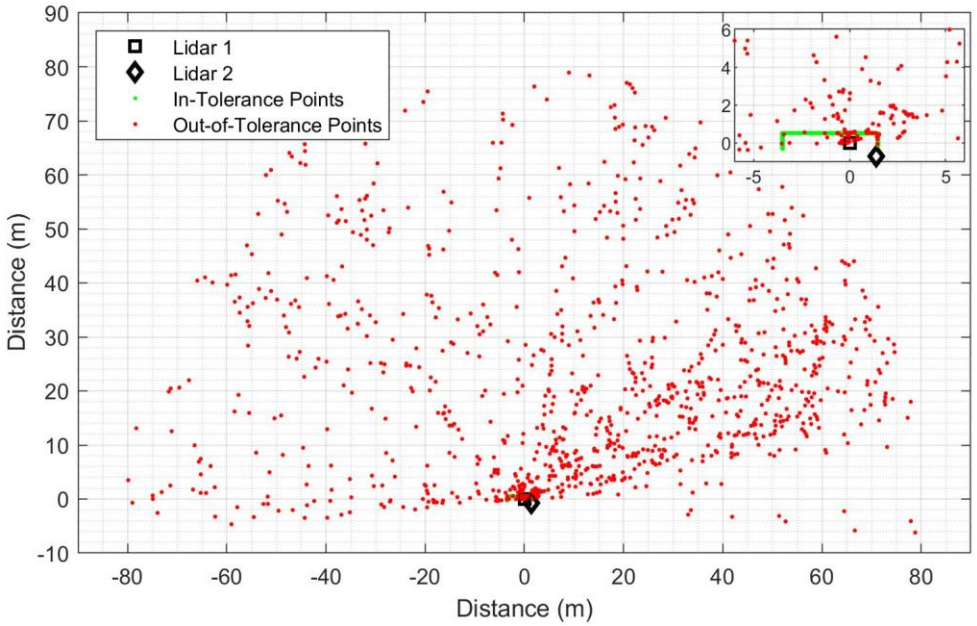

Figure 47 – Case 4: ranging points recoded during the testing period the third side-by-side arrangement.

Table 12 – Case 4: Side-by-side arrangement #3 results analysis.

Parameter	Total	First Returns	Second Returns
Pulses	3,427,857	–	–
Returns	3,438,846	3,427,852	994
Total Interference	1,076	83	993
Direct Interference	0	0	0
Scattered Interference	1,076	83	993
% Total Interference of Returns	0.0313%	0.00242%	99.9%
% Direct Interference of Returns	0%	0%	0%
% Scattered Interference of Returns	0.0313%	0.00242%	99.9%
% Direct Interference of Interference	0%	0%	0%
% Scattered Interference of Interference	100%	100%	100%

7.1.4 Case 5: multi-lidar arrangement

The recorded ranging data from Case 5 are shown in Figure 48. The data demonstrated out-of-tolerance points resulting from both direct and scattered interference. A total of 33,290 out-of-tolerance points were recorded during this test period which

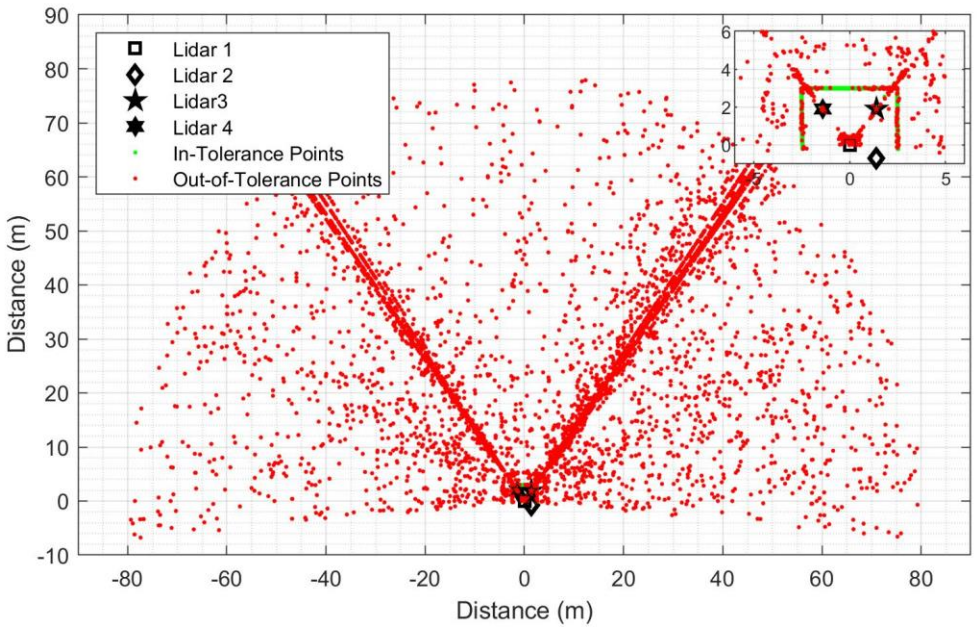

Figure 48 – Case 5: ranging points recoded during the testing period with multiple lidar scanners.

accounted for just under 1% of all returns. Over 90% of these were attributed to direct interference, while 2,965 were attributed to scattered interference. Two modes of high density, out-of-tolerance points coincided with the angular locations of the two VLP-16 lidar scanners demonstrating a distinguishable density difference in interference events. In notable contrast to Cases 1 and 3, these modes appear to contain a higher density of points out to the maximum range of scanner 1. In Cases 1 and 3, these errors appeared in greater concentration at scanner 2's location. This greater dispersion of error is hypothesized to have been the result of increased coupling efficiency between the scanners and will be discussed further in Section 7.5.1.3. A summary of the testing results is given in Table 13.

Table 13 – Case 5: Multiple lidar scanner results analysis.

Parameter	Total	First Returns	Second Returns
Pulses	3,427,857	–	–
Returns	3,448,725	3,427,814	20,911
Total Interference	33,290	20,632	12,658
Direct Interference	30,325	20,359	9,966
Scattered Interference	2,965	273	2,692
% Total Interference of Returns	0.965%	0.602%	60.5%
% Direct Interference of Returns	0.879%	0.594%	47.7%
% Scattered Interference of Returns	0.0860%	0.00796%	12.9%
% Direct Interference of Interference	91.1%	98.7%	78.7%
% Scattered Interference of Interference	8.91%	1.32%	21.3%

7.2 Interference by Scan Angle

Analyzing the occurrence of out-of-tolerance points as a function of scan angle provided a significant distinction between direct and scattered interference events. Scan angles corresponding with direct interference totaled interference events several orders of magnitude higher than those scan angles associated with scattered interference.

Furthermore, scan angles associated with scattered interference showed a dependency between the scan angle and the number of interference events. As the scan angle Θ_1 approached the two-scanner reference frame angle of $\theta_1 = 0°$, the density and number of out-of-tolerance points by scan angle generally increased. This supported the hypothesized relationship between beam intersection and scattered interference since the flux of intersection points converges near $\theta_1 = 0°$ (and 180°) when scan frequencies are match, $f_1 = f_2$.

7.2.1 Evaluation of Case 1

Returns plotted as a function of scan angle and range are shown in Figure 49 for Case 1. Figure 49(a) spatially shows the returns' range by scan angle while Figure 49(b) shows the number of out-of-tolerance returns recorded at each scan angle. Overlaid onto the histogram in Figure 49(b) is the normalized cross section of theoretical density points corresponding to the walls location, which was initially presented in Figure 26 in Section 5.3. The density map has been translated into the single-scanner reference frame and distance between the scanners calculated for in terms of their normalized separation *L*. This overlay facilitates a cursory comparison of the fluctuations in observed interference events to those hypothesized by the theoretical intersection density to qualitative evaluate the proposed theory. However, this only is for comparing trends in relative fluctuations and does not predict the number of interference events.

What was initially evident was the two orders of magnitude difference between returns within angular limits of direct interference versus those returned from scattered

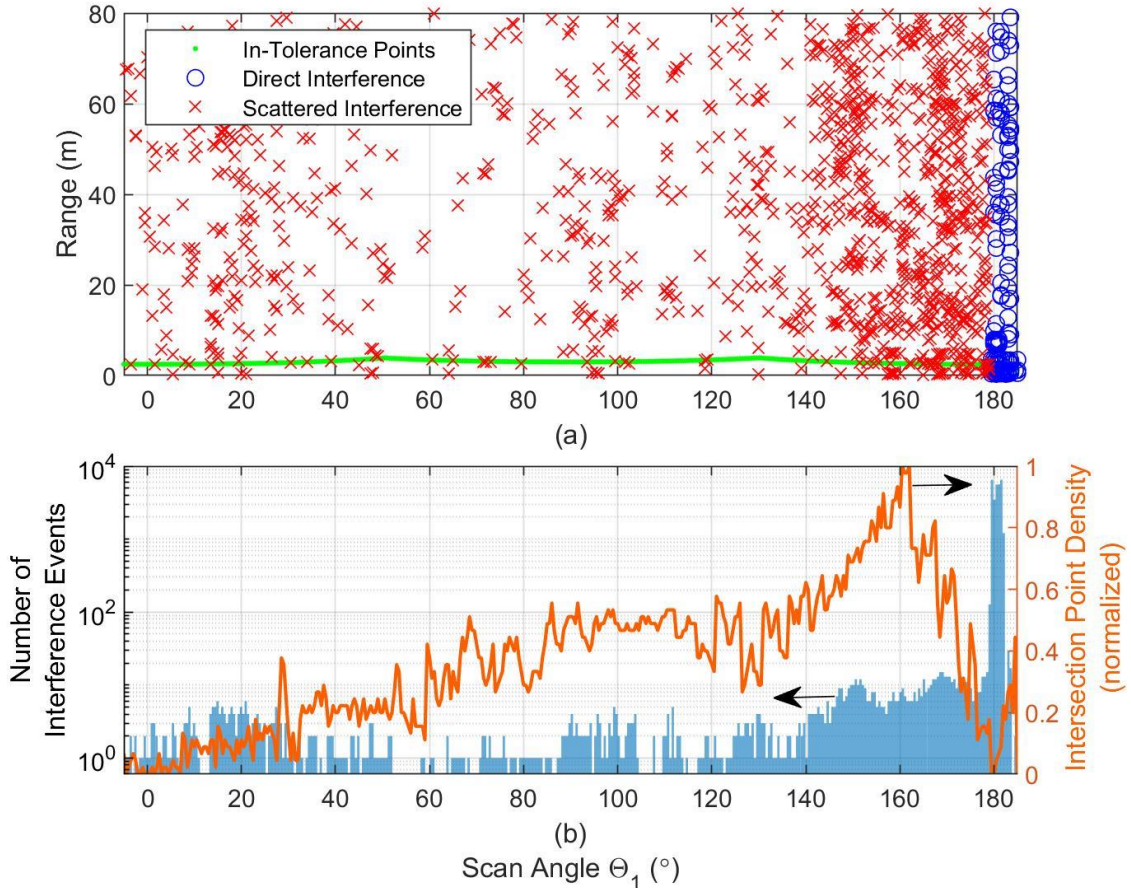

Figure 49 – The (a) spatial and (b) total occurrences of returns as a function scan angle for Case 1 with theoretical intersection density overlaid.

interference. However, the adherence of the scattered interference to the density of intersection point is also apparent and supports the interference theory of intersection.

In Case 1, Scanner 2's angular scan limits extended from 179.5° to 185°. Within these bounds, the out-of-tolerance returns totaled two orders of magnitude higher angle than the remaining angles of the scanning FOV. Notably, this was not uniform across the entire angular width of scanner 2. From 179.5° to 182.0°, returns totaled over 1,000 per scan angle, while the returns from 182.5° to 185° mostly totaled in the single digits. Furthermore, no out-of-tolerance returns were recorded at 184.0°. This discontinuity in direct interference occurrences was hypothesized in the experimental setup (Figure 32) due

to the limits of the emitting window of scanner 2 when compared to the scanner's entire body length. Therefore, these scan angles correspond to the opaque portions of scanner 2's body which precluded beam intersection and direct illumination – thus reducing interference. However, the single digit number of out-of-tolerance events identifies that some effects of direct interference are observable outside of the direct angular limits of an emitter, likely due to the detector's FOV.

Scattered interference also appears to possess distinguishable characteristics by scan angle. In Figure 49(b), from 140.0° to the beginning of the direct interference events, there was a higher angular density interference events than in scan angles before 140.0°. Direct interference points resulting from coupling outside of the angular limits of scanner 2 may account for some of these points. However, from observing the angular limits of direct interference later presented in Case 3, it was found that these instances were not observable outside of 2.5° beyond the angular limits of scanner 2. Moreover, by extrapolating the instances of direct interference observed over the non-emitting potions of scanner 2's body in this case (182.5° to 185°), these would only account for single digit increases of interference events per scan angle. Therefore, it appears that this increase of interference represents an increase in the number of scattered interference events.

This increase in scattering interference is also qualitatively observable in the results reported by [17]. When compared to the fluctuations of the intersection point density in Figure 49(b), these changes are consistent with the hypothesized relationship between scattered interference and the coincidence of intersection density with targets. Though it does not represent as significant an impact as direct interference, it provides heuristic evidence of interference as a function of intersection geometry.

For a cursory comparison to the theory, the cross-section of interference density points is presented in Figure 50 in similar form to its presentation earlier in Section 5.3. Here, the bivalent histogram showing intersection density as a function of distance, normalized to the scanners' separation L (in this case 1.2 m), has be translated into scanner 1's scan angle Θ_1. The wall's range is then superimposed, which traces the intersection density plot overlaid in Figure 49(b). This overlay provides a visualization for the coincidence of the wall with the intersection density. The cross section of the intersection density along the wall's path is then the projection overlaid in Figure 49(b). This is not exact given the approximations made in generating the density plot. Moreover, it is hypothesized that the high frequency fluctuations of the interference events in both the

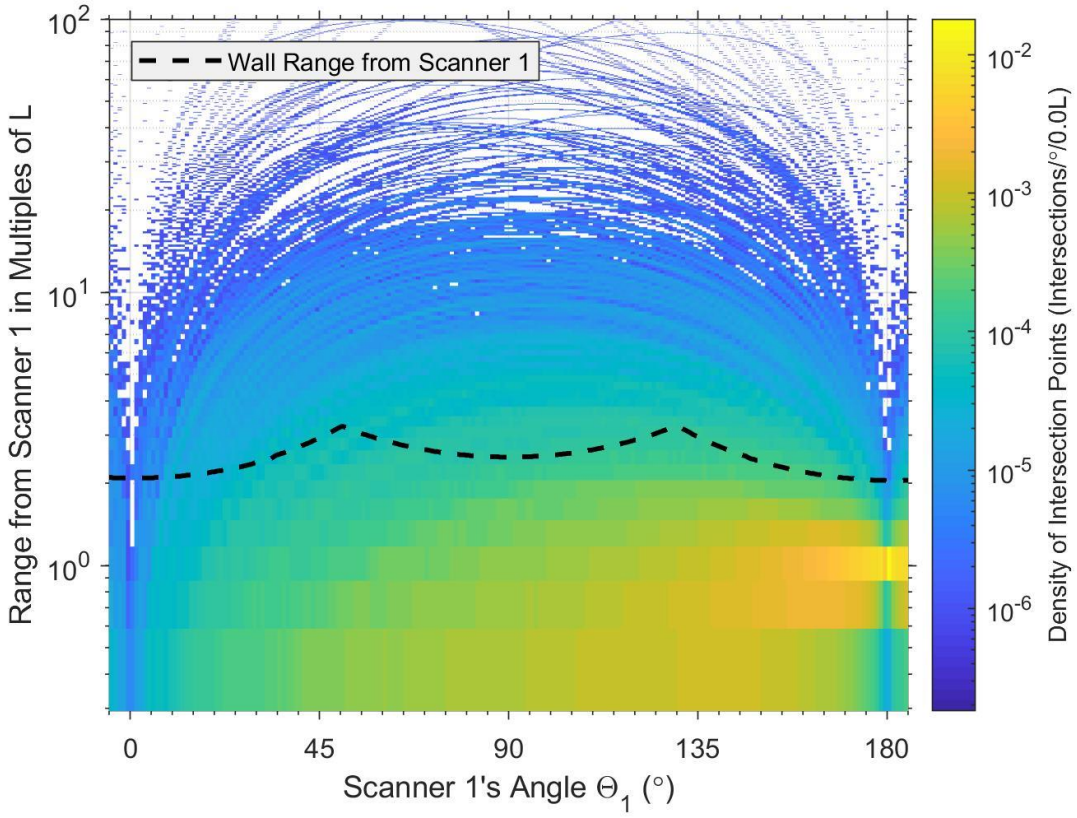

Figure 50 – Intersection density as a function of scan angle Θ_1 with the wall's range in terms of scanner separation distance *L* for Case 1.

experimental and theoretical results will converge to a general point given sustained observation. Therefore, what is important in comparing the results is the general trend of the occurrences. However, further investigation would be required to confirm this hypothesis.

7.2.2 Evaluation of Case 2

Returns plotted by range and scan angle for Case 2's testing data is shown in Figure 51. Given the lack of direct interference sources, all out-of-tolerance points can be assumed to be the result of scattered interference. In Case 2, interference events were generally under

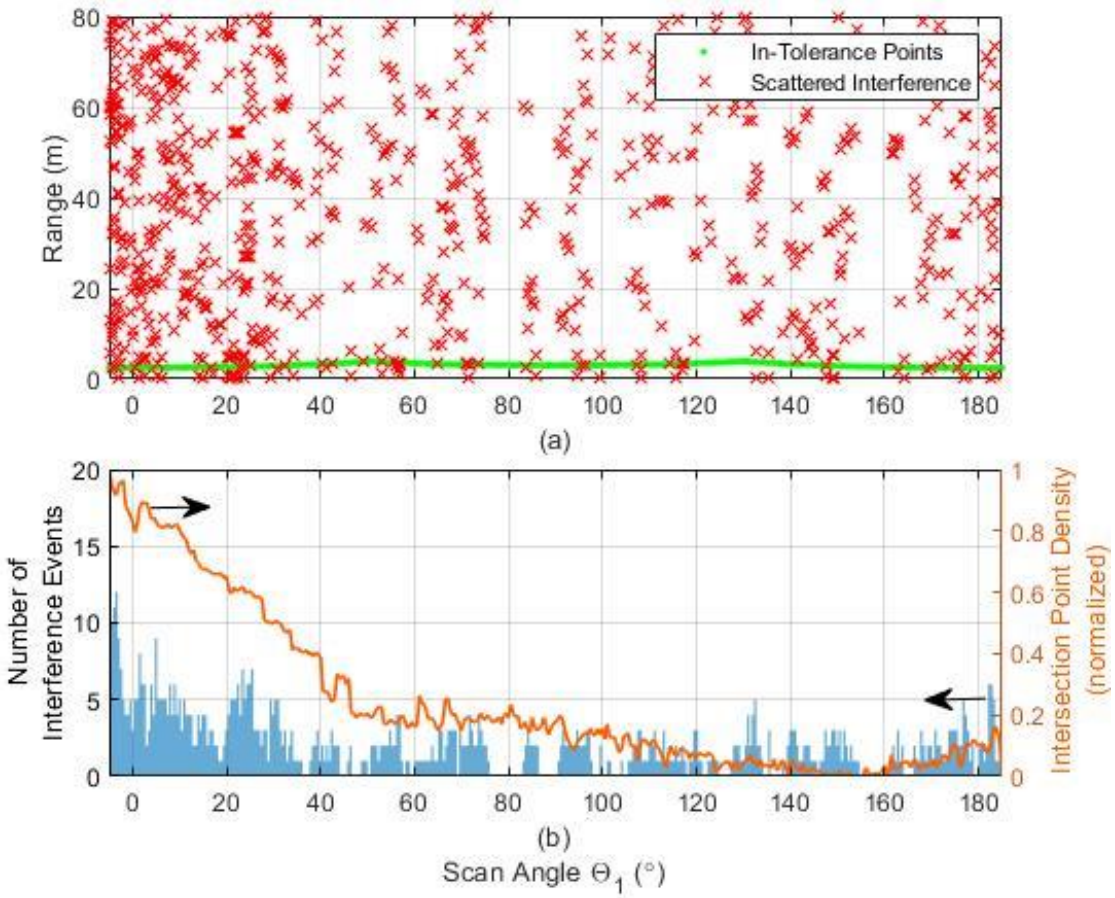

Figure 51 – The (a) spatial and (b) total occurrences of interference events as a function scan angle for Case 2 with theoretical intersection density overlaid.

10 per $0.5°$ scan angle which were far lower than the instances for direct interference seen in Case 1, but consistent with Case 1's scatter interference events.

In this arrangement, Scanner 2 is located out of the scanner 1's scanning FOV at a scan angle of roughly $-26.5°$. Once more, the density of interference events was observed to generally increase as the scan angle approached scanner 2's angular location. This increase was independent of direct interference since there was no line of sight between the emitters. And again, the general adherence to the trends of the intersection density was generally consistent. This continuity is continued evidence supporting the relationship between beam intersection and scattered interference.

The gap seen in the observed interference events in Figure 51(b) between roughly $155°$ and $160°$ was likely attributed to the obscuration of scanner 2's laser by the non-emitting portion of scanner 1's body. It is hypothesized that this obscuration resulted in the eclipsing of scanner 2's interference energy along the wall over these scan angles in the shadow of scanner 1. Therefore, in the absence of scanner 2's beam spot, no intersection was achievable, and in turn, no interference took place.

The peak in out-of-tolerance events around $\Theta_1 = 26.5°$, noticeably departed from the trend predicted by the overlaid cross-section of intersection density points. However, the likely explanation represents another interesting phenomenon. In this configuration, scanner 2 is located roughly at $-26.5°$ in reference to scanner 1's scan angle. Therefore, this local maximum of interference events is consistent with the angle of reflectance complementary to scanner 2's laser's angle of incidence. It is hypothesized that this increase in events is due to the partial reflection of scanner 2's laser off scanner 1's laser

housing, subsequently then scattering from the wall at $\theta_1 = 26.5°$. From this reflection, the concentration of interference events with small ranging errors along this scan angle may be partially explained by additional mechanisms of interference discussed in Section 7.5.2. However, further investigation is warranted to completely explain the result of the phenomenon.

For additional reference, the translation of intersection points with Case 2's scanner arrangement is presented in Figure 52. The relationship of the intersection and target geometries again show general adherence to the instances of interference experimental observed for Case 2. The most notable deviation between the comparison occurs around 26°, however, once the reflection of scanner 2's laser along is accounted for the, the

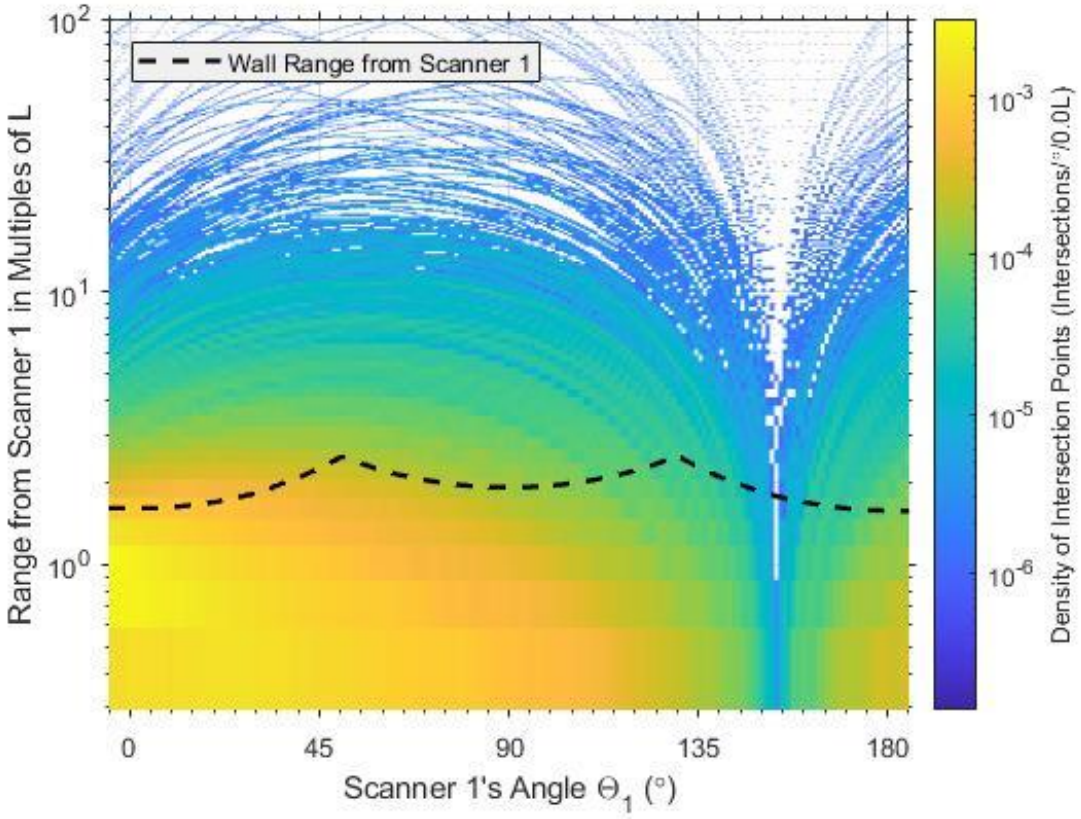

Figure 52 – Intersection density as a function of scan angle Θ_1 with the wall's range in terms of scanner separation distance *L* for Case 2.

experimental results show relatively strong qualitative correlation. The difference in the general trends of angular interference occurrences is explainable when considering the difference in intersection point densities between Cases 1 and 2. However, the magnitude of interference densities is not as readily explainable. This may require further consideration of radiometry to fully explain and would need continued inquiry to determine.

7.2.3 Evaluation of Case 3

Returns plotted by range and scan angle from Case 3's testing data are shown in Figure 53. The evaluation of Case 3 provided the most compelling evidence to support the identification of direct and scattered interference with scan angle limits. Case 3 facilitated an arrangement that allowed for the isolation of direct and scattered interference. In this case, scanner 2 occupied approximately $5.5°$ of scanner 1's total scan angle centered around $\Theta_1 = 90°$. However, the original hypothesis stating that direct interference would be constrained to these scan angles needed to be amended.

From observation, interference returns resulting from direct interference were received over a total $9°$ of which was nearly evenly distributed on either side of scanner 2's angular limits. Only one return fell outside of these limits. It is hypothesized that this extended observation of direct interference was the result of scanner 2's extended laser coupling into scanner 1's receiver due to beam divergence and a less than ideal receiver FOV, which is discussed further in Section 7.5.1. However, of the 213 direct interference events observed in Case 3, 90% of these occurred within the angular limits of scanner 2 as

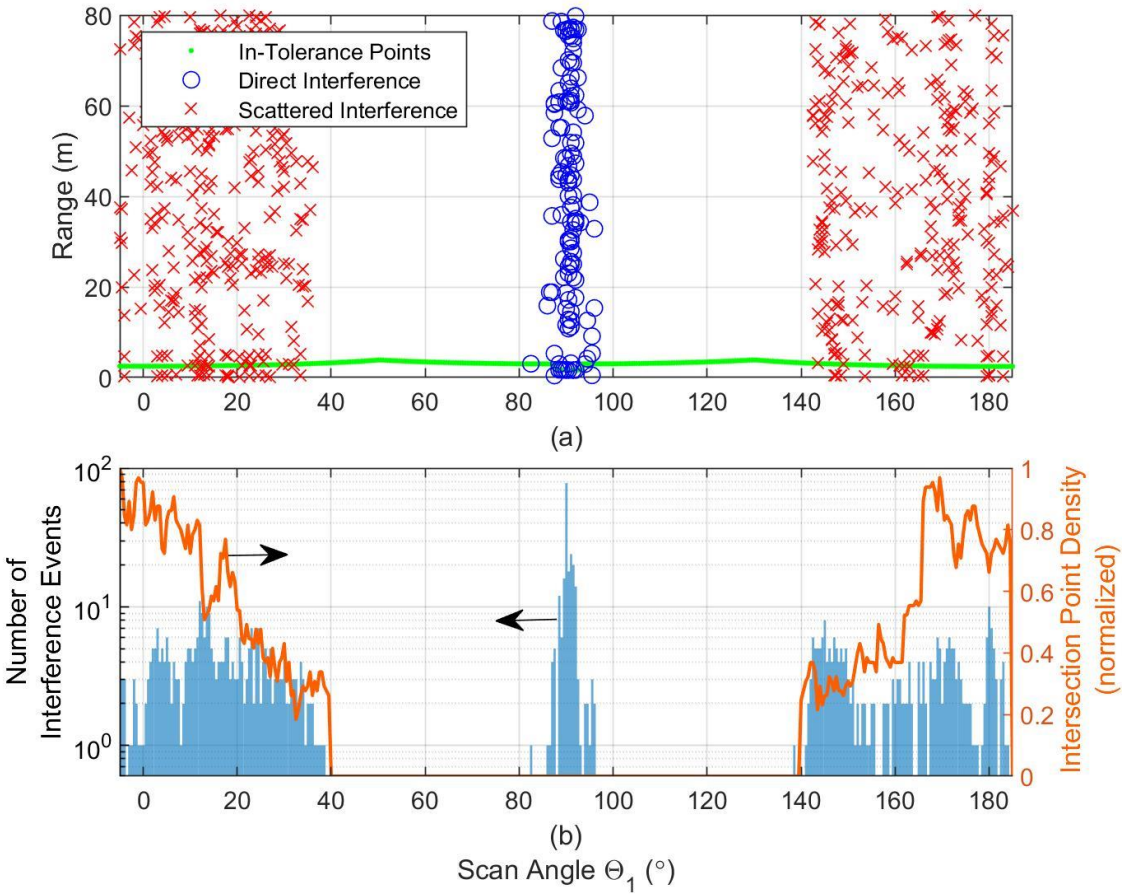

Figure 53 – The (a) spatial and (b) total occurrences of interference events as a function scan angle for Case 3 with theoretical intersection density overlaid.

seen from scanner 1. This concentration of events provides evidence that the coupling is not as significant as the direct exposure to the harassing laser as one would intuitive infer.

Furthermore, Case 3 provided additional evidence to support the proposed theory of scattered interference. Since portions of scanner 1's scan angle were mutually exclusive to scanner 2's scan angle, it provided a control to test whether scattered interference would be constrained to areas where beam intersection was possible (mutually shared scan angles). The results provided confirmation of this partitioning as shown in Figure 53(b). Other than direct interference, from approximately $\Theta_1 = 35°$ to nearly $145°$ no interference was observed. These angles roughly corresponded with the projection of

scanner 2's minimum and maximum scan limits along the back wall as identified in the experimental setup.

Though fewer scan angles were available for comparison, those with reflected interference continued to show general adherence when compared to the extrapolated density of intersection points overlaid in Figure 53(b), though not a full explanation. This may be partially due to the low sample size of scattered interference points given the fewer number of scan angles over which the phenomenon occurred.

When viewing the intersection density plot in Figure 54 and following the wall projection, if the scan angles were to have continued to overlap between 40° and 140°, it

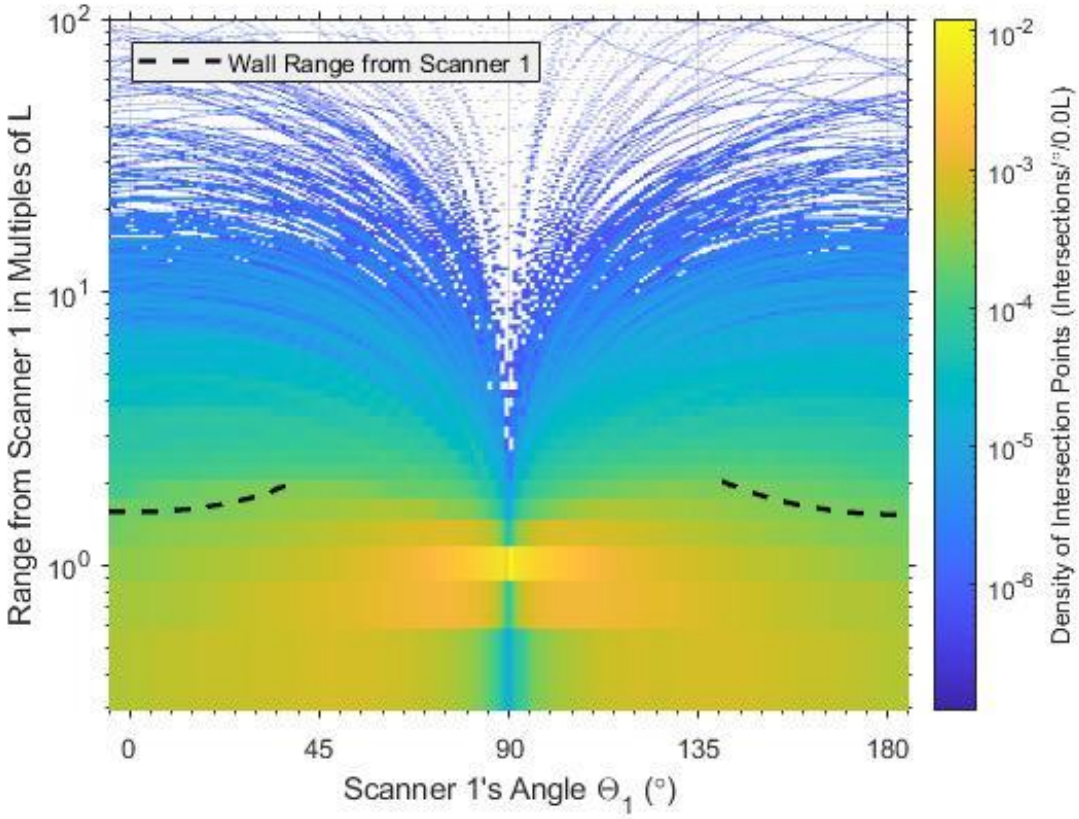

Figure 54 – Intersection density as a function of scan angle Θ_1 with the wall's range in terms of scanner separation distance *L* for Case 3.

is hypothesized that the occurrences of scattered interference would have significantly decreased in compliance with the intersection geometry. However, further testing would be required to verify this extrapolation.

7.2.4 Evaluation of Case 4

The experimental results for the first iteration of Case 4 are presented in Figure 55. In general, the data continued to show adherence between theoretical intersection occurrences and scatter interference. However, a notable discrepancy between the intersection density overlay and the observable instances of interference are seen around the 26.5° scan angle in Figure 55(b). Again, this discrepancy is explainable by considering

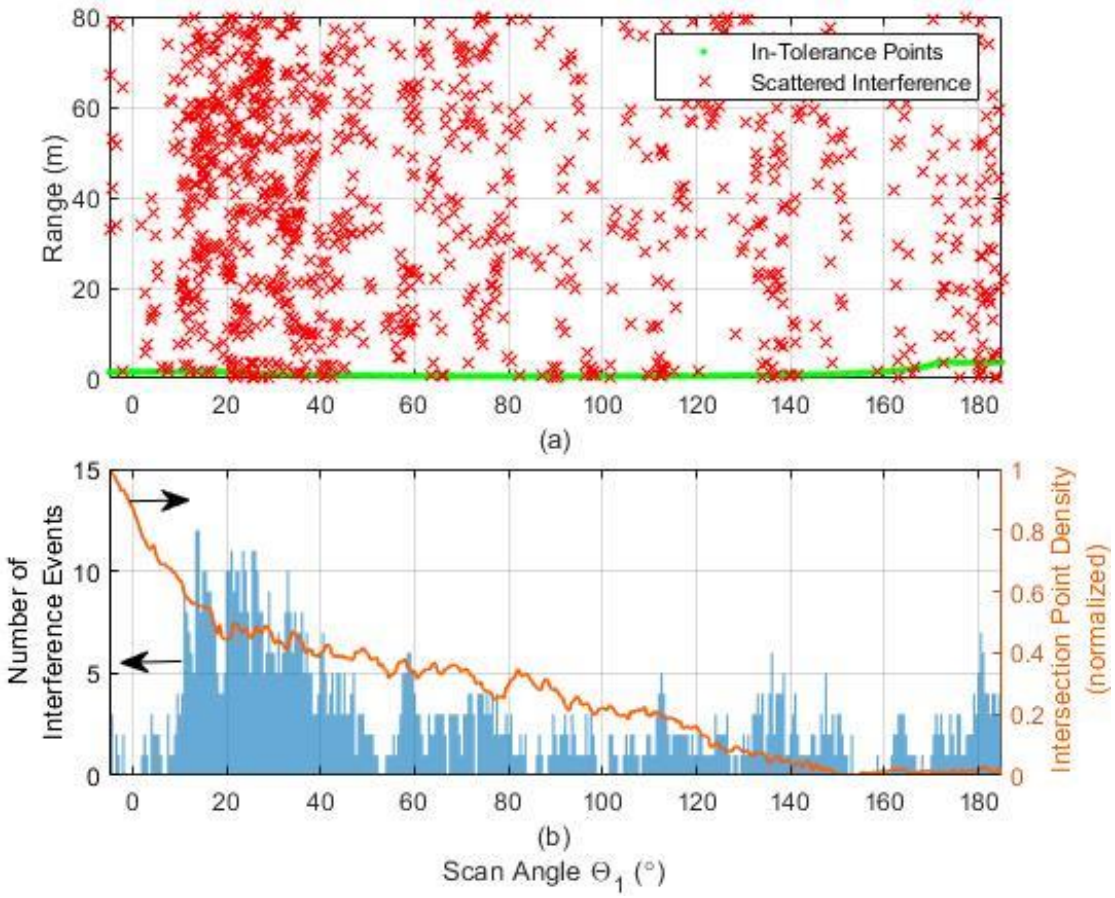

Figure 55 – The (a) spatial and (b) total occurrences of interference events as a function scan angle for Case 4 with theoretical intersection density overlaid.

scanner 2's angle of incidence and reflection, which are the same as in Case 2 due to the maintained spacing between the scanners in both test cases. The change in angular width of these event's occurrences may be due to the closure proximity of the scanners to the wall, therefore, reducing pathlength losses of the reflected laser or increasing the angular width of the event's observation. However, further testing would be required to ascertain this hypothesis.

Aside from experimentally testing the variance of interference occurrences, Case 4 intended to explicitly test the theory connecting intersection and target geometry to observed interference. To test this hypothesis, the relative arrangement between the scanners in Case 2 was maintained to preserve the two-scanner reference frame distance *L*,

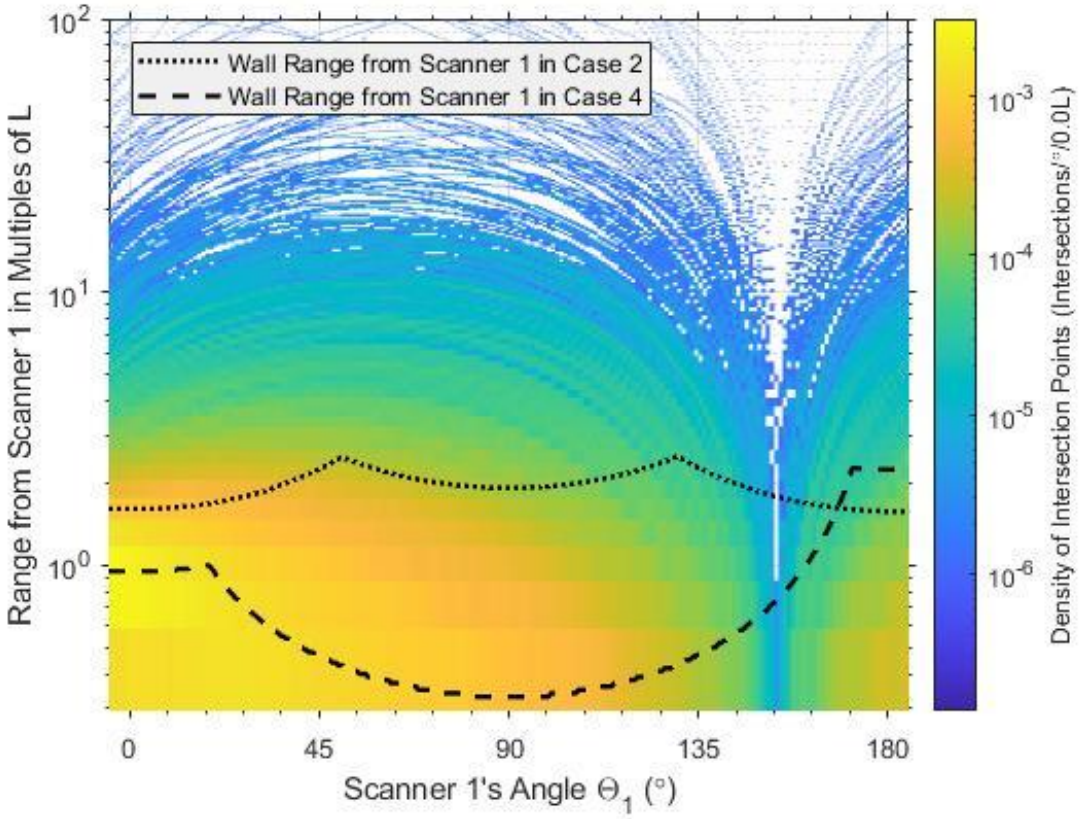

Figure 56 – Intersection density as a function of scan angle Θ_1 with the wall's distances in terms of scanner separation distance *L* for Case 4.

however, the scanners were moved closer to the wall such that the target geometry coincided with areas of greater intersection density. The hypothesized result was that the occurrence of interference should increase. Consistent with the theory, the occurrence of interference did increase from 771 events in Case 2 to 1,076 in Case 4. The transition of the wall relative to the intersection geometry showing this increase intersection density around the wall is shown in Figure 56.

7.2.5 Evaluation of Case 5

The recorded returns for Case 5 are shown in Figure 57. Overall the occurrences of interference were greater and with higher spatial and angular density than in the previous 4 cases. Overall the direct interference from the two VLP-16 scanners (scanners 3 and 4) produced ranging errors with greater range distribution along the entirety of scanner 1's ranging ability. This is shown by the two deeply saturated lines of direct interference out to 80 m in Figure 57(b). Additionally, a higher angular density of scatter interference was recorded throughout scanner 1's total scan angle.

For the three scanners in Case 5, the density of intersection points presented in Figure 57(b) was calculated by finding the cross-section of intersection density points for each scanner individually but relative to scanner 1, then summing their totals. However, due to the independent distances to the three scanners, a simple projection of the wall over the bivariant histogram is not readily achievable since that projection uses the normalized two-scanner distance L as unit of measure.

The variations of observed scattered interference by scan angle partially agreed with the intersection point density for Case 5. However, the theory appears to depart from that

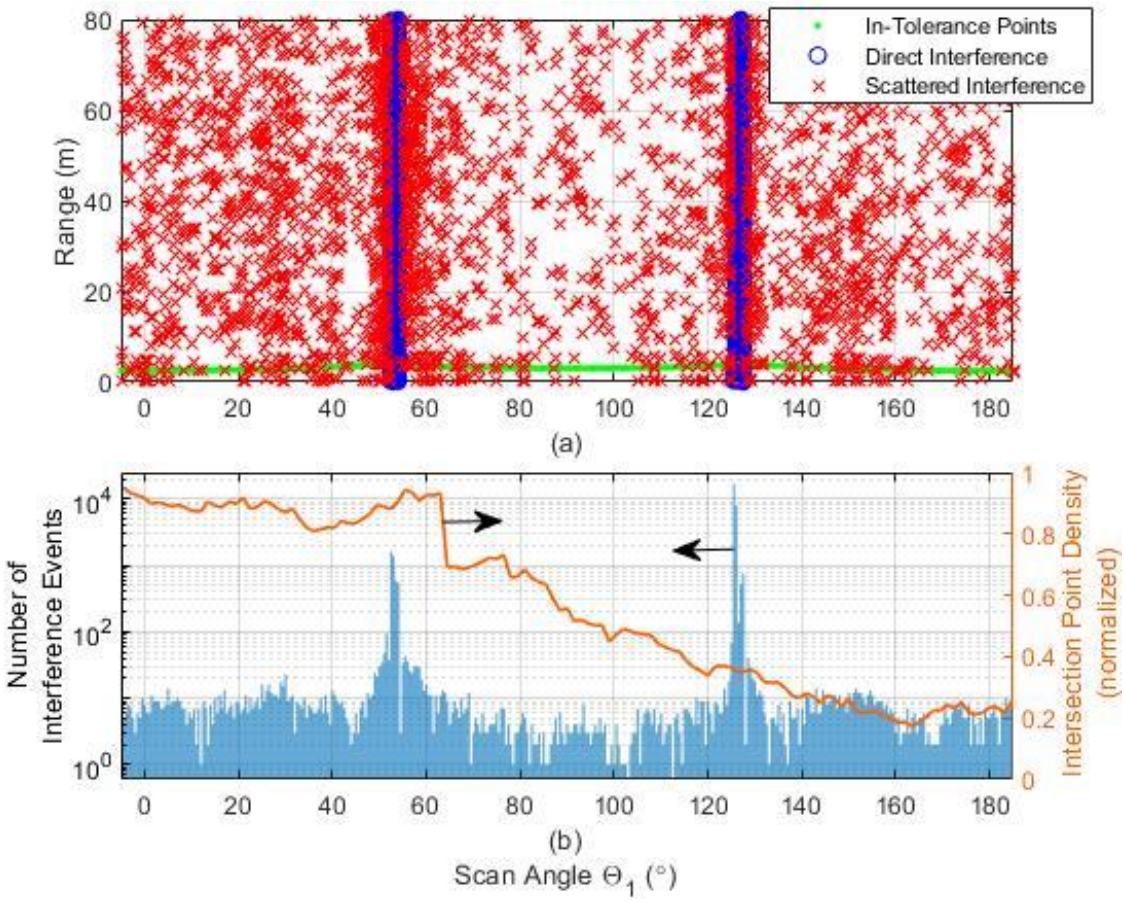

Figure 57 – The (a) spatial and (b) total occurrences of interference events as a function scan angle for Case 5 with theoretical intersection density overlaid.

observed above 120°. This deviation may be partially expected since the theory of intersection was developed for co-planer scanners and scanners 3 and 4 scan out-of-plane. Moreover, scanners 3 and 4 employ multiple ranging channels that further complicate the lidar's signal interactions. Therefore, the theoretical extension of intersection point density to out-of-plane scanners does not appear to hold.

7.3 Ranging Errors

The ranging error R_{error} associated with interference events was analyzed for all cases. The ranging error of an interference event along a scan angle Θ_1 was calculated by

taking the difference of the interference event's erroneous range and the average in-tolerance range calculated from the training data. This error is given as

$$R_{error} = R_{out\ of\ tolerance} - \bar{R}(\Theta_1). \tag{37}$$

As a result, far side errors were positive and near side errors were negative.

If a multi-target range distribution existed along the scan angle, the difference was calculated for all average ranges associated with the scan angle. Since it could not be known which of the multiple targets the range error was associated with, the smallest range error of the group was selected as R_{error}.

A summary of the ranging errors observed in all five cases is presented in Table 14. The ranging errors produced by direct and scattered interference appear to distinguish themselves by magnitude. Though direct interference occurred with greater frequency, the ranging errors resulting from its occurrences were on average only between 0.0027 m and 2.482 m. This error was two to four orders of magnitude less than the errors resulting from scattered interference, which were on average between 31.087 m and 38.344 m. Therefore, though it may seem that by occurrence direct interference is more detrimental to the faithful representation of targets, scattered interference has greater impact on the error associated with the erroneous ranging data. As it pertains to autonomous vehicles, reflected interference could have the potential for greater risk by producing errors on the order of tens of meters rather than on the order of tens or less of centimeters in the case of direct interference.

Table 14 – Near and far side ranging errors for each test case.

Parameter	Case 1	Case 2	Case 3	Case 4	Case 5
Total Interference Points	30,194	771	794	1,076	33,290
Average Range Error from All Sources (m)	1.739	34.300	32.841	38.344	5.377
Total Near Side Ranging Errors	2,662	53	43	37	16,415
Total Far Side Ranging Errors	2,753	718	751	1,039	16,875
Direct Interference Points	28,966	–	213	–	30,325
Average Direct Interference Range Error (m)	0.584		0.0027	–	2.482
Direct Near Side Ranging Errors	2,521	–	3	–	16,253
Direct Far Side Ranging Errors	26,445	–	210	–	14,072
Scattered Interference Points	1,228	771	581	1,076	2,965
Average Scattered Interference Range Error (m)	31.087	34.300	36.654	38.344	35.014
Scattered Near Side Ranging Errors	141	53	40	37	162
Scattered Far Side Ranging Errors	1,087	718	540	1039	2,803

Errors were observed over a span equal to the maximum range of scanner 1 – a total of 80 m. In most cases, direct interference appeared evenly distributed between near and far side ranging errors, despite the walls' short range between 2.5 m and 3.0 m of the total 80 m span of errors. This even distribution on either side of the target is in contrast with ranging errors associated with scattered interference events, which appeared to have a ratio of near to far side ranging errors closer to the ratio of scanner 1's ranging capability as partitioned by the wall. In other words, scattered interference errors appeared to be evenly distributed along the total 80 m range of scanner 1. Therefore, the amount of nearside errors (at ranges short of the room's walls) was roughly proportional to the number of far side errors (at ranges outside the room's walls) at a ratio given by

$$\text{Ratio of Scattered Range Errors} = \frac{\text{Near Side Errors}}{\text{Far Side Errors}} \approx \frac{\text{Average Wall Range}}{80\text{ m} - \text{Average Wall Range}}. \quad (38)$$

However, direct interference events were more likely to occurs near the wall with relative even distribution on either side.

Originally hypothesized, the erroneous range of an interference point should follow a uniform distribution since the arrival time of an interference pulse was assumed to be stochastic, given its independent transmission and path to scanner 1. However, direct interference did not follow such a hypothesis, which suggests another mechanism is influencing the occurrence of direct interference. A revised hypothesis of direct interference is discussed further in Section 7.5.1.

It should be noted that this analysis of the ranging error distribution is partially subjective due to the range error calculation method. Because the least ranging error was selected for multi-target range distributions, which were almost exclusively along scan angles corresponding to direct interference, the actual near or far side nature of the error cannot be determined in most cases. Considering the dual-target return distributions associated with another scanner's edge, errors that fall between these distributions could be either near or far side depending on which target they are associated with. However, by virtue of selecting the least error, a side was assigned that may not reflect how the error was derived.

7.3.1 Direct Interference Ranging Errors

A histogram of the ranging errors from direct interference events in Cases 1, 3, and 5 are shown in Figure 58. Each histogram bin width is equal to 0.1 m of ranging error. In Cases 1 and 5, direct interference events were an order of magnitude greater than scattered interference events, however, most of these occurrences carried a ranging error within ± 0.2 m of a target. This relatively low error is important to take into consideration. Despite the high number of detected direct interference events, the majority of these would not represent error with a significance that one would expect to result in catastrophic navigation influence for an autonomous vehicle.

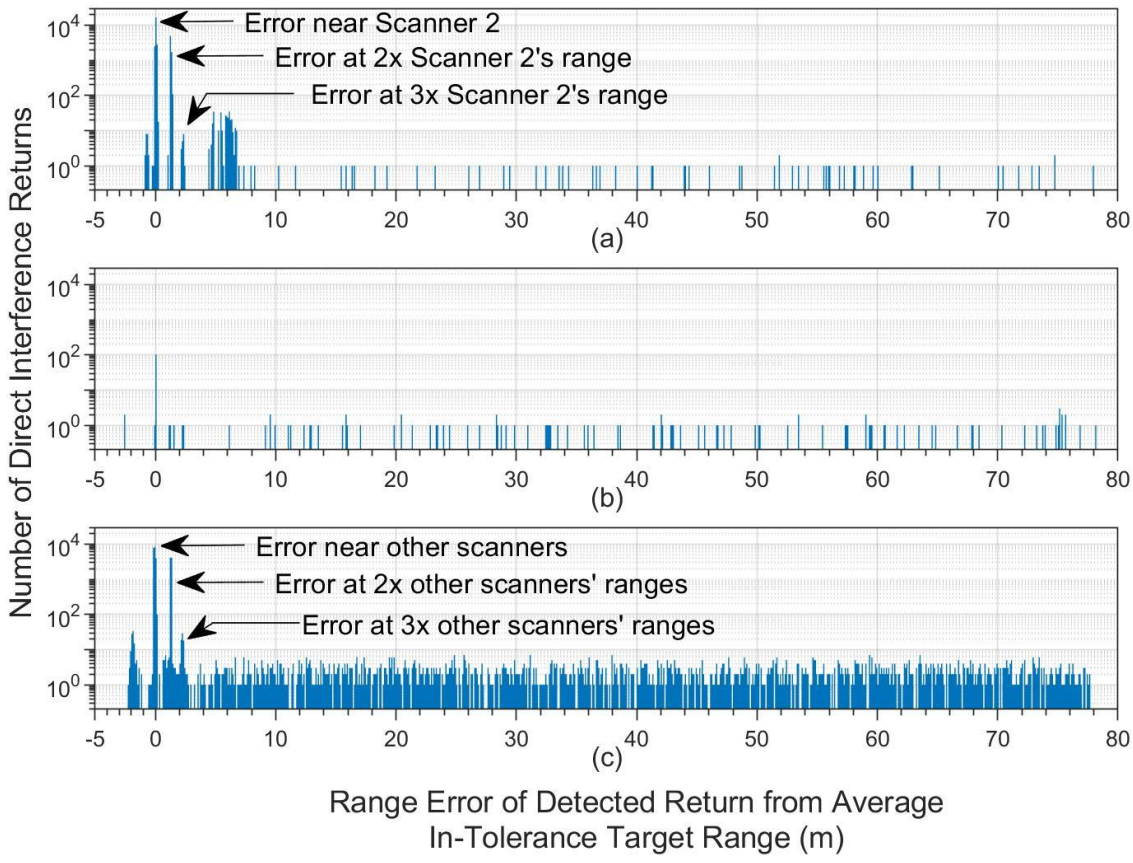

Figure 58 – Recorded ranging errors of as a result of direct interference for (a) Case 1, (b) Case 3, and (c) Case 5 as deviated from the average in-tolerance range.

Given direct interference's unexpected ranging error features, it is likely the mode of interference is more nuanced than initially hypothesized. It is then amended that in most instances of direct interference not all energy from an interference source is coupled into the device. As a result, the diffuse coupling only induces minor changes in the leading edge of scanner 1's detected pulse. Only when enough energy is coupled into the scanner does a bold ranging error register, which could be understood to occur with less frequency. Further discussion explaining this hypothesis is provided in Section 7.5.1.

Outside of ± 0.2 m error, the next highest occurrence of ranging errors in Cases 1 and 5 was observed around $+1.2$ m. This ranging error in both cases roughly corresponded with the distance between scanner 1 and the other scanner(s) (twice the range to the other scanner(s)). Therefore, it is hypothesized that error corresponds with the formation of an optical cavity between the scanners' reflective plastic/glass laser housings or internal structure. Supporting this assessment is the appearance of another distinct peak roughly observed around 2.2 m of error (three times the range to other scanner(s)) with even fewer detected occurrences. This error pattern was not observed in Case 3 and it is assessed that the scanners were not properly aligned during testing. However, further investigation would be needed to confirm this. These error peaks and their range multiples are annotated in Figure 58.

7.3.2 Scattered Interference Ranging Errors

The ranging errors resulting from scattered interference in Cases 1 through 5 are shown in Figure 59. In contrast to direct interference, the ranging errors associated with

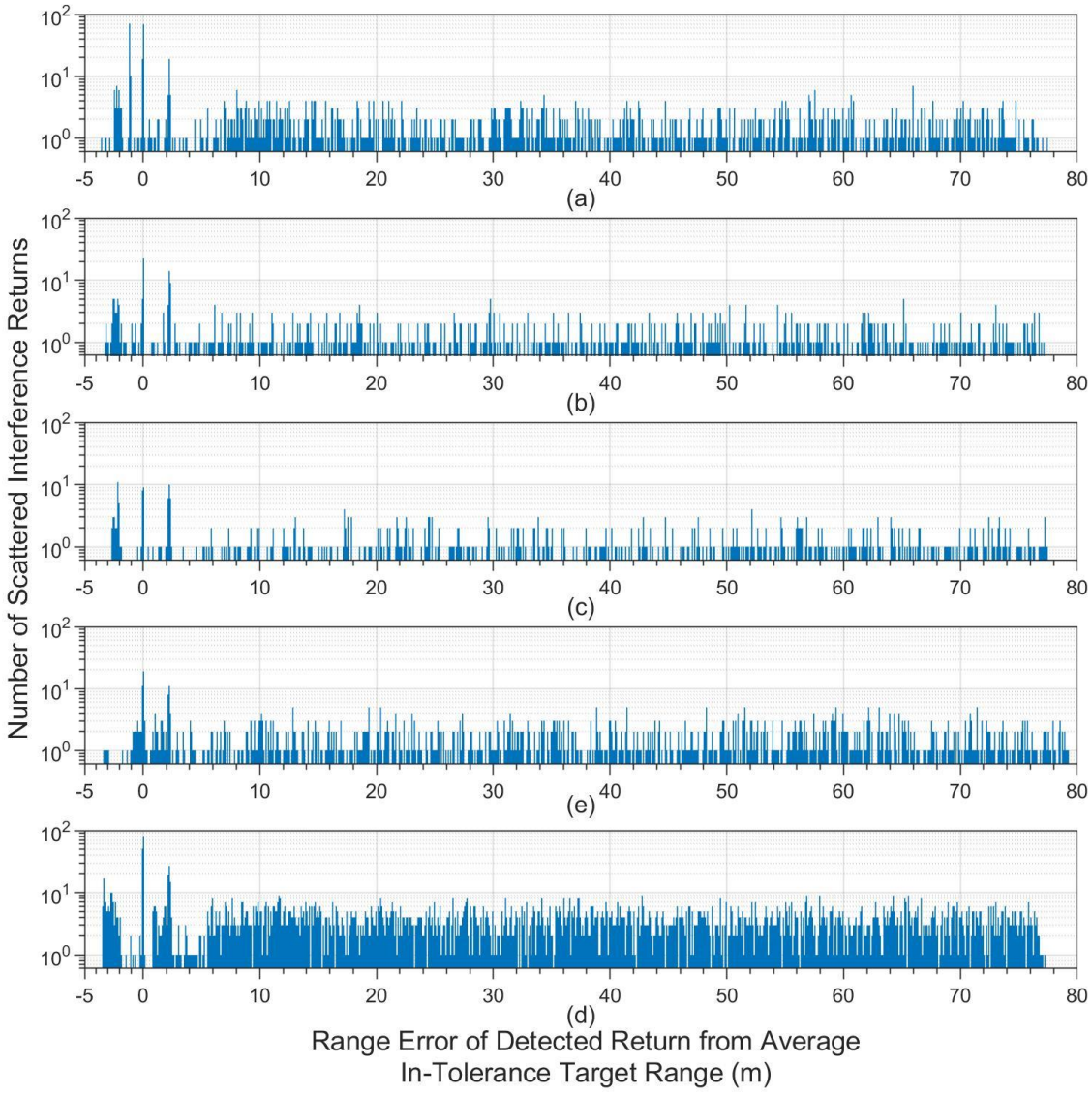

Figure 59 – Recorded ranging errors of as a result of scattered interference for (a) Cases 1 through (e) Case 5 as deviated from the average in-tolerance range.

scattered interference followed a more uniform distribution. This distribution is consistent with the assumption of stochastic arrival times for interference pulses made earlier.

Despite following a more uniform distribution, there is still a significant peak of errors observed within ± 0.1 m. Though not of the same prominence as in direct interference, this concentration of small range errors may support the hypothesis of a third

distinct case of interference – indirect interference. Indirect interference may occur when an interference source illuminates the victim scanner, but the victim scanner's FOV is not directly oriented at the interference source. A more detail discussion of indirect interference is given in Section 7.5.2.

Complementing the error peak between $\pm$ 0.1 m were a pair of peaks seen generally around -2.2 m and 2.2 m, respectively, in Cases 1-3 and 5. In Case 4 the -2.2 m peak was noticeably absent. The mechanisms for this pattern are currently unknown. The 2.2 m peak did not show a readily available association with target location since it was invariant in all 5 cases while the relative locations of targets were not. However, the -2.2 m peak may be spatially related to scanner 1 since it did not appear in Case 4 when scanner 1 was moved. Due to the two peaks' symmetry about the average in-tolerance range, it would seem likely that they were related. The peaks also did not appear to be a function of the harassing scanners' location since the harassing scanner(s) were spatially difference throughout. However, the distance between scanners 1 and 2 only varied between 1.2 m and 1.6 m. Therefore, this may still be a possible mechanism if the phenomenon has a low sensitivity to this spatial relationship.

7.4 Variance of Interference Events

Four iterations of Case 4 were performed to determine the variance of interference counts from one observation period to the next, with identical conditions. A summary of results from all four iterations of testing is given in Table 15. The interference events ranged from 1,076 to 1,364, which showed relative consistency between the sample observations. The sample mean of these observations was found to be 1,208.5 interference

events. Under an assumption that the event totals follow a normal distribution, the sample standard deviation was found to be equal to 122.7 returns or approximately 10% of the mean. This relationship shows reasonably consistent repeatability of interference events. Moreover, deviation was expected since the underlying occurrences of events were hypothesized to be temporally stochastic. However, it is further hypothesized that the standard deviation of these occurrences will decrease as the observation time increases.

Table 15 – The results of the four repeated trials of Case 4 to determine the variance of interference observations.

Parameter	Iteration 1	Iteration 2	Iteration 3	Iteration 4
Pulses	3,427,857	3,424,428	3,427,857	3,427,857
Returns	3,438,846	3,425,267	3,428,647	3,428,619
Scattered Interference	1,076	1,157	1,237	1,364
% Interference of Returns	0.031%	0.034%	0.036%	0.040%
First Returns	3,427,852	3,424,424	3,427,854	3,427,855
First Return Interference	83	314	444	600
% of Interference	7.714%	27.139%	35.893%	43.988%
Second Returns	994	843	793	764
Second Return Interference	993	843	793	764
% of Interference	92.286%	72.861%	64.107%	56.012%
Sample Mean	1,208.5			
Sample Standard Deviation	122.7			

Though the data from the four test cases show a steady increase of approximately 100 interference events between each successive iteration, it is likely a coincidental pattern since no testing conditions changed from one iteration to the next. Additionally, more than 76 hours transpired between the first and second iteration of measurements, while iterations two through four were taken successively with less than 10 minutes between sample

periods. Therefore, though a linearly increasing pattern seems apparent, the temporal relation between the measurements is not linear. However, further evaluation would be needed to definitively determine that this pattern was a chance occurrence.

7.5 Discussion

7.5.1 Direct Interference

7.5.1.1 Angular Extent of Direct Interference

It was originally hypothesized that direct interference would be constrained to the angular limits containing a harassing scanner. However, from observation of the results of Case 3, this was found to not be the case. While the angular limits containing actively emitting interference likely do represent sources of direct interference, it was found that the effects were observable several degrees outside of these angular limits. It is hypothesized that this increased observation results from coupling between the harassing lidar's laser and the victim's receiver just outside direct viewing and with enough energy to register a return. Therefore, the angular limits of this effect should be a function of the victim lidar receiver's FOV. Devices with a narrower FOV would likely experience this effect over fewer scan angles than a device with a higher FOV.

Because strict angular limits between direct and scattered interference are not supported by the data, angle filtering is likely not the best method to distinguish between the two cases when their occurrences are angularly contiguous such as in Case 1. Albeit, the use of strict angular limits to distinguish interference will prevent the false identification of scattered interference (scattered interference should not occur within the

angular limits of the other scanner), it does not prevent the misidentification of direct interference (direct inference can be observed outside the angular limits). Therefore, further investigation is required to better understand the angular distribution of direct interference about an interference source. With a refined distribution, more sophisticated filtering techniques may be applied to improve the distinguishability of interference types.

7.5.1.2 Modes of Direct Interference

From the data, it also appears that direct interference is more nuanced than previously hypothesized. Previously it was assumed the erroneous ranging errors resulting from all interference would observe a nearly uniform distribution between the minimum and maximum range of the victim detector since the arrival time of an interference pulse was assumed to be stochastic. However, the data suggest the mechanisms are more nuanced than that. As a result, it is hypothesized that there are two distinct forms of direct interference – what will be referred to as diffuse-direct interference and coupled-direct interference – which are shown in Figure 60.

Coupled-direct interference, Figure 60(a), represents the original hypothesis for direct interference occurrences. In this mode, enough energy from the harassing scanner is coupled into the victim's receiver to exceed the detection threshold, thus registering a return. This would occur as originally hypothesized, at stochastic intervals, thus bold ranging errors are observed out to the victim's maximum range.

By contrast, diffuse-direct interference, Figure 60(b), occurs when the energy from the interference source is not fully coupled into the victim device. The defuse light that is coupled is not enough to trigger the device's detection threshold independently, as shown

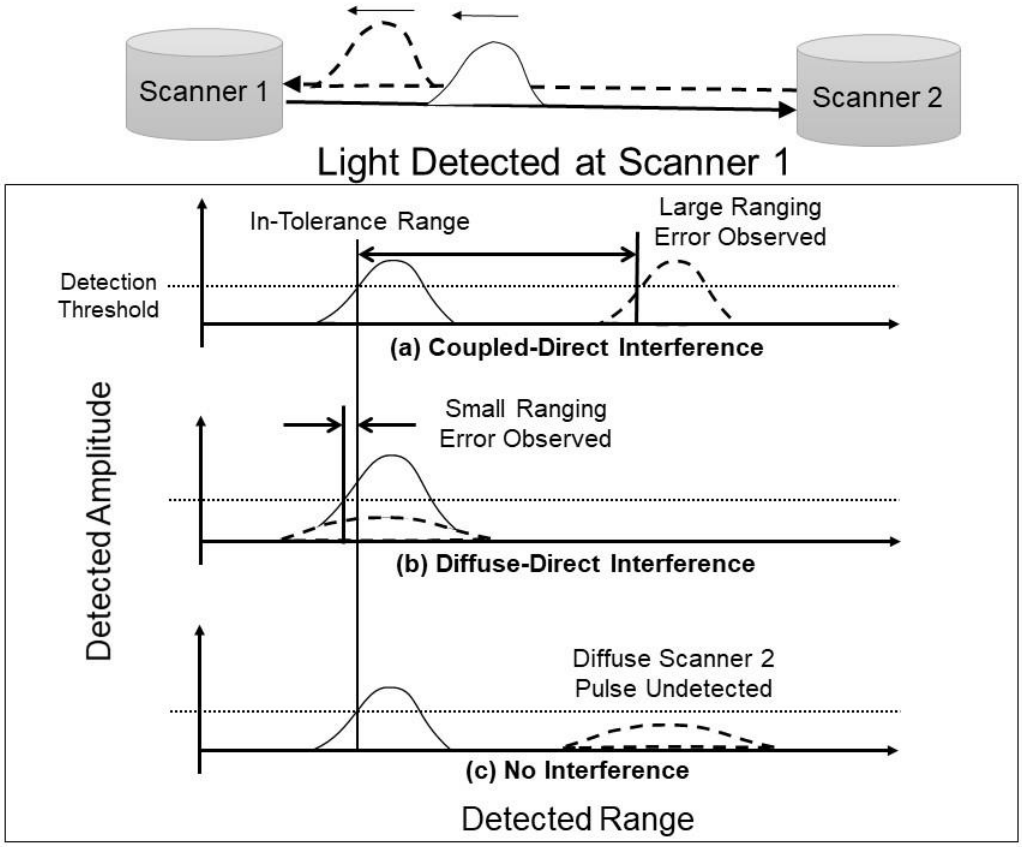

Figure 60 – Hypothesis of two distinct direct interference modes – (a) coupled-direct interference and (b) diffuse-direct – alongside a (c) no interference occurrence to explain ranging errors of direct interference events.

in Figure 60(c). However, when coinciding with scanner 1's return, the additive amplitude causes a slight deviation in the leading edge of scanner 1's return, thus resulting in minor ranging errors. Diffuse-direct interference is hypothesized to occur with greater frequency than coupled-direct interference since the conditions for diffuse coupling should be less stringent.

However, to validate this theory would require greater knowledge of the scanner's time-to-digital converter (TDC) and ranging (threshold) decision process, which was unknown. In the absence of this knowledge and under the assumption of the illustration in Figure 60, if this theory is true, small ranging errors should be near side biased due to the

early detection of scanner 1's perturbed pulse. This range error bias was not fully observed. However, inobservance may be a result of the subjectivity in determining near and far side errors as discussed in Section 7.3. As a result, near and far side errors are indistinguishable for multi-target returns, which were exclusively observed over direct interference scan angles. Therefore, by using the least error to demine the near or far side nature of the ranging error, this near side biasing pattern may have been lost. In any case, further investigation would be required to confirm this hypothesis.

7.5.1.3 Coupling of Multi-Channel Scanners

In Case 5, a higher number of direct interference events were observed with a greater number of bold ranging errors. This trend could be explained by several factors. First, the number of combined pulses per VLP-16 scanner (PRF = ~ 300 kHz) increased the number of chances that which an interference pulse may be directly coupled. Second, though not every channel of the VLP-16 was aligned with scanner 1, more than one channel could have been diffusely coupled into the device. Moreover, if the theory of diffuse coupling is correct, between the two scanners, the combined occurrences of diffuse-direct interference may have cumulatively exceeded the detection threshold, allowing for these more frequent coupling events to be registered independent of the reception of scanner 1's return. This increased coupling, in turn, increased the observation of bold ranging errors.

7.5.2 Indirect Interference

It is possible that a third distinct form of interference has been observed that could be described as indirect interference. This form of interference would occur under similar circumstances to that of diffuse-direct interference in Figure 60(b), except that scanner 1 is

not directly oriented at scanner 2. Despite this angular offset, enough light is coupled into scanner 1 such that in conjunction with reception of scanner 1's own return, the diffuse interference energy induces small ranging errors as shown earlier in Figure 60(b).

A higher occurrence of small ranging errors (< 0.1 m) were observed for scattered interference in all test cases, as shown earlier in Figure 59. This trend may be explained by extending the theory of diffuse-direct interference to a greater number of scan angles. This theory is also supported by [21] who suspected the ability to couple interference energy into a victim lidar from sources outside of the lidar's FOV by way of diffraction and reflection of the victim lidar's curved reception glass.

However, evidence against this theory may found in the results of Case 3. If this mechanism of interference exists, then it would be expected to have seen some forms of it manifest between the noncontiguous scan angles for direct and scattered interference. Yet the data was absent of any out-of-tolerance occurrences over these scan angles. However, the observed data for Case 3 does depart from the results reported by [17]. In their published results, some interference events were recorded over these scan angles. This inconstancy also further supports the idea that the experimental setup in this present work's execution Case 3 may have incurred error, which constrained the observation of potential interference events.

7.5.3 Case 3 Results

It is hypothesized that the results in Case 3 may not accurately reflect the intended set up due to misalignment between the devices. In the results reported by [17], this case also produced the least amount of detected interference, however, the occurrences of direct

interference in the present work were two orders of magnitude less than those in Case 1, which indicate a possible discrepancy.

Though alignment procedures where completed for Case 3 consistent to the other test cases, it is likely that the laser transmitter from scanner 2 was not completely coupled into scanner 1. This is hypothesized due to the significantly lower number of direct interference cases observed in Case 3 as compared to Cases 1 and 5. This occurrence, despite the alignment procedures, may be explainable when considering the scan plan alignment procedures applied to Case 3.

In Case 3 the scan alignment was checked using the method described earlier in Section 6.2.1. However, because no common corner between the scanners with a viewable projection of both scanners' lasers existed for this arrangement, the alignment was conducted from two near diametrically opposing points to the scanners' sides. As a result, it would have been possible to confirm observation of both lasers at each of these points without actually achieving the alignment of the scan planes. The projections of this false alignment are shown in Figure 61.

However, the discrepancy overserved between Cases 1 and 3 may also be explained by the orientation of the scanners' bodies relative to each other. That is, by its design, Case 1 may be more susceptible to interference returns given that scanner 2's laser housing is in profile relative to scanner 1 such that it forms a partially transmissive target surface. This orientation contrasts with the arrangement in Case 3 since the scanners are face to face and transmissions from scanner 1 into scanner 2's housing will terminate into the back side of the housing rather than continuing through to another scattering surface. This frontal

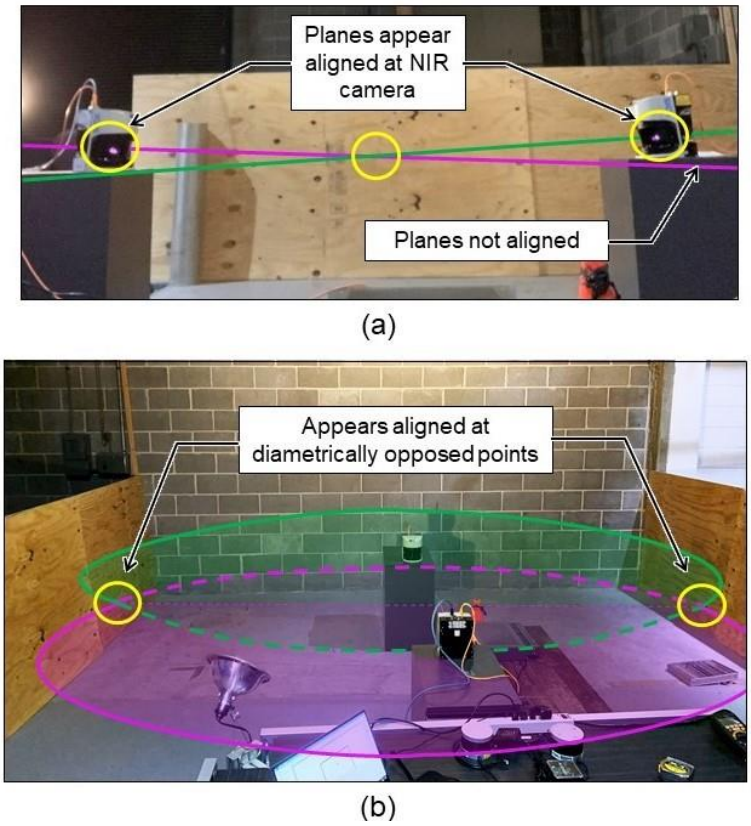

Figure 61 – Possibility of false alignment in Case 3's setup which could have contributed to the fewer recorded instances of direct interference.

orientation may result in less diffusion events since a second reflection of the high gloss scanner housing glass is not taking place. Moreover, the termination into the backside of the housing, may be beyond the mirror which directs returns to the receiver. However, the internal structure of the housing would need to be inspected to substantiate this hypothesis, and a nondestructive examination was not possible.

If the disparity in direct interference events was the result of misalignment between the devices, these results could suggest the sensitivity of direct interference to beam alignment. As a result, despite direct interferences' causal significance in the number of interference events, it may be a less probable mode of interference resulting between two scanners affixed to moving vehicles on the roadway. The results also would suggest that

scattered interference may be more robust in prevailing despite naturally occurring misalignment between to coincidental vehicle meetings on the road.

7.5.4 Loss of Intolerance Points

A loss of in-tolerance returns was observed in both Cases 1 and 5 over scan angles that corresponded with direct interference. In other words, in addition to the erroneous ranging points detected over direct interference scan angles, targets that were present were also not identified within tolerance by the scanner. Outside of these two cases all other scan angles recorded at least one in-tolerance return for each ranging pulse transmitted (plus or minus a few returns).

A histogram showing the in-tolerance returns for Cases 1 and 5 between the scan angles where loss was observed are shown in Figure 62(a) and (c). In Case 1, this loss of in-tolerance points was observed between 179.5° to 182.0°, which angularly contained scanner 2. A total of 8,998 pulses were transmitted at each scan angle and uniformly received on all scan angles except those in this span. Therefore, over these angles a total of 19,855 returns were not recorded as in-tolerance and identified as missing (including the net gain of ranging pulses observed at 180.0°). Out-of-tolerance points observed at these scan angles totaled 29,910. Of those found to be out-of-tolerance, 7,077 had ranging errors exceeding 1 m, while 269 of those exceeded 5 m, and 30 of those exceeded 10 m. Therefore, it is possible that the missing out-of-tolerance returns can be accounted for in those errors of less than 1 m. Though still significant, this possibility may mitigate the severity of the loss. A histogram of the ranging errors observed for out-of-tolerance returns between the scan angles of 179.5° to 182.0° in Case 1 is shown in Figure 62(b).

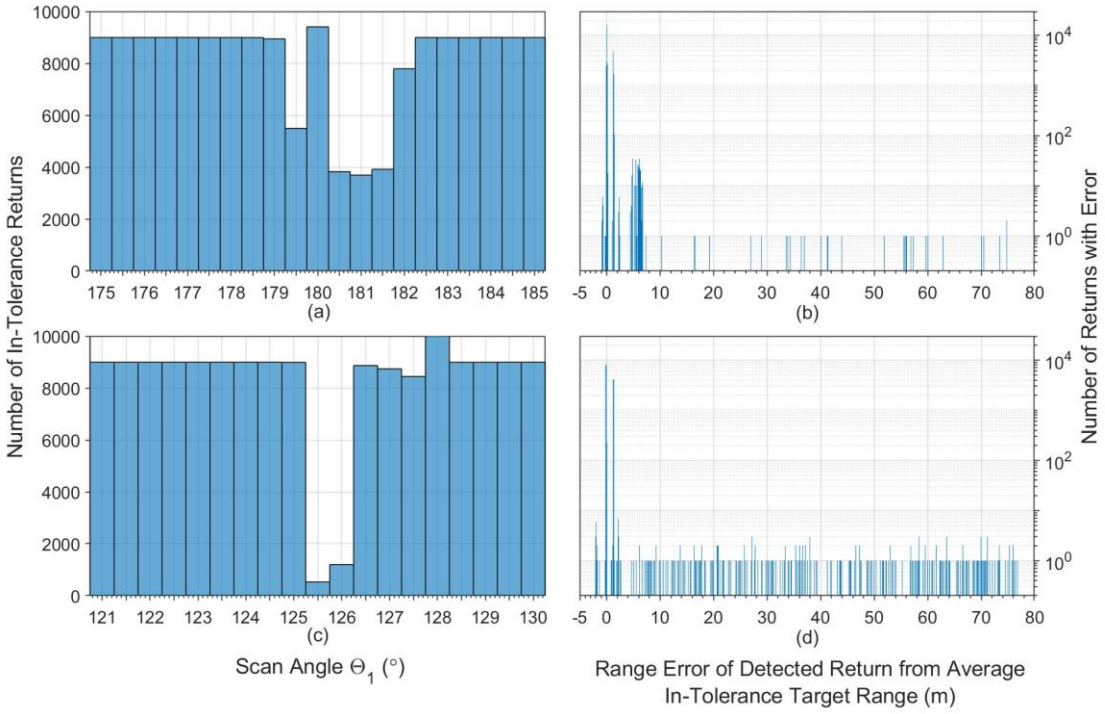

Figure 62 – Loss of in-tolerance points observed in (a) Case 1 and (c) Case 5's data over scan angles which corresponded with direct interference. The number of ranging errors over these windows by magnitude of error are shown for (b) Case 1 and (d) Case 5.

The loss of in-tolerance points observed in Case 5 occurred over two consecutive scan angles, 125.5° and 126.0°, which is shown in Figure 62(c). In Case 5 every scan angle transmitted 8,997 ranging pulses, with all recording generally uniform detection of at least one return per pulse transmitted, except these two angles. Using the measure of one return per pulse observed, a total of 16,270 ranging pulses were not observed as in-tolerance at these two scan angles. Out-of-tolerance points between these two scan angles totaled 24,775. Of these, 8,526 were found to have ranging errors greater than 1 m, with 253 of those greater than 5 m, and 253 of these returns exceeding 10 m of error. Again, the missing in-tolerance points could be mostly accounted for in the ranging errors of less than 1 m. However, this degradation of target data requires consideration for software-based approaches to interference mitigation.

Both these instances show that lidar signal interference does not just additively impose erroneous ranging data to a foundationally valid point cloud, but rather, it has the potential to degrade the accuracy of what may have been previously thought of as a foundation of accurate data.

This degradation in point cloud accuracy introduces certain challenges for software-based approaches to mitigate lidar interference. In the method proposed by [19], lidar returns are filtered with a spatio-temporal filtering algorithm to remove outliers. As it relates to autonomous vehicles, if these algorithms are too aggressive, outlier elimination could result in a loss of target identification over scan angles that would correspond with another lidar enabled autonomous vehicle (direct interference). Therefore, these algorithmic approaches need to account for the degradation in ranging accuracy for legitimate targets to find a balance between aggressively filtering interference and retaining slightly compromised but legitimate target data – which the current understanding of lidar interference does not identify.

7.5.5 Double Out-of-tolerance Returns

To a lesser extent but of unique nature, double out-of-tolerance points were observed in all test cases. Double out-of-tolerance points were events which both the first and second returns were found to be out-of-tolerance. It was originally hypothesized that no more than one out-of-tolerance point should be found along a single scan angle for every transmitted pulse. This hypothesis was arrived to by considering the matching PRFs between scanners (in Cases 1-4) and the expectation that a legitimate target should follow a near side error,

or a far side error could follow a legitimate target, notwithstanding receiver deadtime. However, this was found not to be the case.

Double out-of-tolerance points were observed over both scattered and direct interference angles; however, higher concentrations were observed in conjunction with direct interference. In general, and in each of the cases, these pairs of points followed a pattern in which the first and second returns were uniformly distributed as near and far side errors with equal and opposite ranging error, respectively. In other words, the pairs of interference events appeared on either side of the actual target with generally equidistant range from the target.

An example of this pattern is shown in Figure 63 for those double out-of-tolerance pairs observed in Case 2. The relationship of these double out-of-tolerance points to actual target locations suggests that this was the distortion of scanner 1's ranging signal rather than the sole misinterpretation of an interference source's independent ranging pulse. The errors on either side of the targets did not appear to deviate as a function of the scanners' locations. Additionally, in Case 2, a higher concentration of errors was observed at a scan angle equal to the angle of reflectance θ_r complementing an angle of incidence θ_i made with scanner 2 as annotated in Figure 63. However, the phenomenon also occurred outside of this angle with generally uniform distribution. Moreover, it does not seem to be dependent on this reflection since the phenomenon is observed over scan angles $180°$ opposite to scanner 2's location.

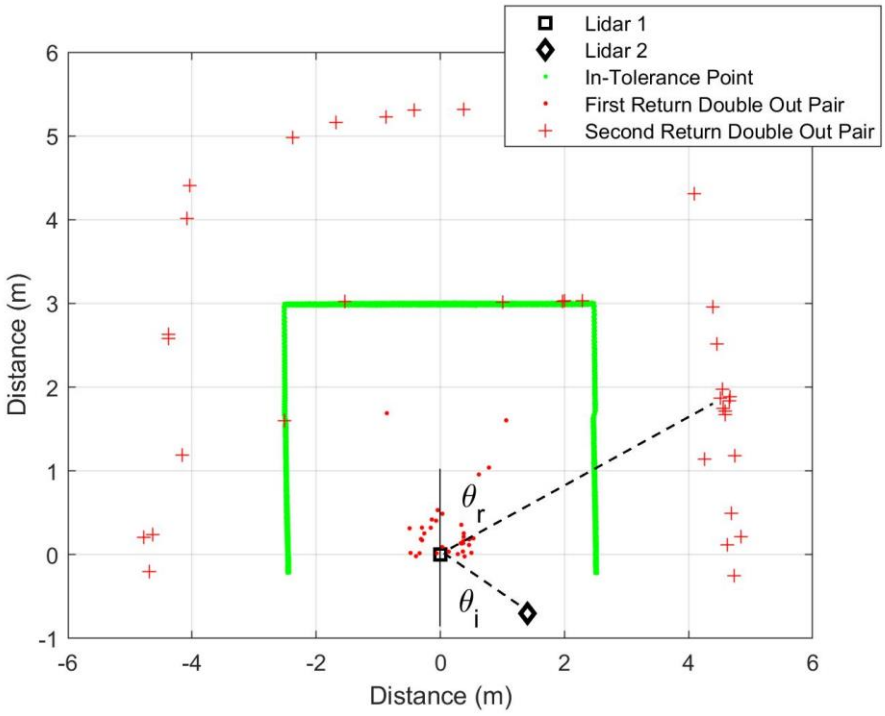

Figure 63 – Observed pairs of first and second returns that were both found to be out-of-tolerance during Case 2's testing. Though unexplained, a higher concentration of the points is found at a scan angle roughly equal to the angle of reflection θ_r for an angle of incidence θ_i reference to scanner 2's location.

A similar relationship to the angle of incidence was also observed in Case 4 and is shown in Figure 64. Again, despite the apparent change in shape of the pair's location, their general displacement about the wall remained fairly uniform when measured from scanner 1's location.

Table 16 provides the statistics for the occurrences of double out-of-tolerance points observed in all test cases. Higher occurrences of double out-of-tolerances points were observed in Cases 1 and 5, which are hypothesized to be the result of direct interference. However, much remains unknow about this phenomenon warranting further investigation.

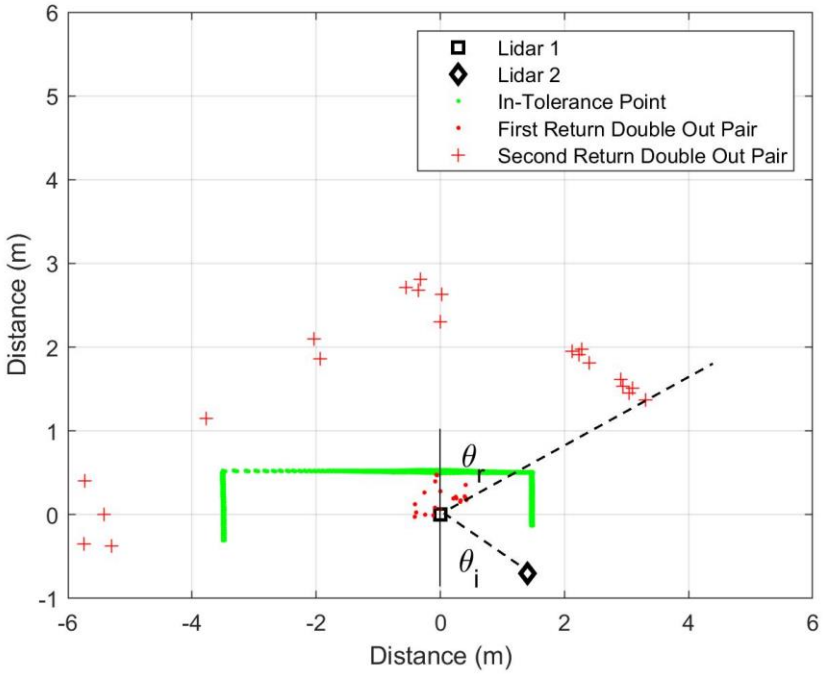

Figure 64 – Observed pairs of first and second returns that were both found to be out-of-tolerance during Case 4's testing. Though unexplained, a higher concentration of the points is found at a scan angle roughly equal to the angle of reflection θ_r for an angle of incidence θ_i reference to scanner 2's location.

Table 16 – Statistics of double out-of-tolerance points observed in all test cases.

Parameter	Case 1	Case 2	Case 3	Case 4	Case 5
Total Interference Points	30,194	771	794	1,076	33,290
Number of Double Out-of-tolerance Pairs	722	35	26	21	8,997
Maximum Range Difference Between Pairs (m)	74.402	5.542	4.858	5.356	77.094
Average Range Difference Between Pairs (m)	3.368	4.239	4.5112	3.170	3.0104
Minimum Range Difference Between Pairs	1.188	1.502	4.269	2.2240	0.878
Most Occurring Scan Angle	181.0°	N/A	180°	N/A	125.5°
Number of Occurrences at Mode Scan Angle	259	–	2	–	8,244

CHAPTER 8. MONTE CARLO SIMULATIONS

Key Conclusions:

- **A simulation was developed to model interference between two lidar scanners using the theoretical conditions of interference presented in Chapters 3-5 and experimental setup of Cases 1-4.**
- **Other than the scanners' maximum ranges, the model did not consider radiometry in order to isolate the dependency of interference on geometry.**
- **The simulation uses Monte Carlo techniques to account for rotational frequency drift between the two scanners.**
- **With each rotation of scanner 1, the two scanners' rotational frequencies are redefined from a normal distribution of frequencies, and scanner 2's reference phase is redefined from a uniform distribution.**
- **If an interference event is conditionally met, an erroneous range is determined along the interference event's scan angle.**
- **For direct interference, a log-normal distribution was used to generate the erroneous ranging data, while for scattered interference, a uniform distribution was used.**
- **Qualitatively, the overview of results produced similar characteristics to the experimentally observed test cases.**

A simulation was developed to compare the theory proposed in Chapters 3-5 with the experimental results in Chapter 7. The simulation uses the underlaying theoretical assumptions for the conditions of lidar interference as outlined in Section 3.2.1. The

simulation was compared to the experimental results and by way of extension, tested the theory's underlaying assumptions for interference. The results of that comparison are then presented in Chapter 9.

8.1 Simulation Fundamentals

The simulation modeled the rotation of two line segments about their origins as depicted in Chapter 4 by Figure 6 to simulate two rotational scanning lidars. The beams were constrained to line segments to account for the maximum range of the scanners. Input parameters were set to account for the scanning relationship between the devices as needed. These parameters included the rotational frequency f_m, reference phase $\theta_{m,0}$, and total scan angle $\Theta_{m,total}$ among others. Scanner 1 was used as a reference from which the model looped for every rotation of the lidar. As the line segments angularly incremented, a series of logic tests were performed to determine if conditions for direct or scattered interference had been met. If conditions had been met, then the state of the scanners was recorded, and an erroneous ranging point was generated for qualitative comparison to the experimental results.

8.2 Input Parameters

8.2.1 Scanner Parameterization

The conduct of each scanner was defined by several parameters that are shown in Table 17. Parameters were either defined by the equipment manufacturer's specifications, experimental setup, or observationally fit. In accordance with the experiment, the model used scanner 1 a reference for interference. The duration of the simulation was defined by the number of rotations n_1 that scanner 1 completed. The number of rotations was defined for each simulated test case to match the number of rotations scanner 1 completed during the associated experimental trial. The scanners' maximum range $R_{m,max}$, mean rotational

frequency $f_{m,\mu}$, pulse repetition frequency PRF_m, total scan angle Θ_{total}, and body width were selected using the manufacturer's specifications. The devices' PRFs and mean rotational frequencies determined the scanners' angular increment between successive pulse iterations to simulate a discreet pulse as defined in Chapter 4 by Equation (10). The scanners' widths and locations were used to determine the angular limits of direct interference. The devices' location and azimuth of scan were determined by the experimental setup for each test case. Other than the scanners' maximum range, the model ignored radiometric parametrization in order to isolate the relationship of interference and beam intersection.

Table 17 – Scanner input parameters of the Monte Carlo Simulation.

Parameter	Constant	Case 1	Case 2	Case 3	Case 4
Number of Rotations of Scanner 1, n_1	–	8,998	8,998	8,998	8,997
	Lidar 1	**Lidar 2**			
Location, $(x_{m,1}, y_{m,1})$ (m)	(0, 0)	$(-1.2, 0)$	(1.4, -0.7)	(0, 1.6)	(1.4, -0.7)
Azimuth of Scan (°)	90°	90°	90°	270°	90°
Lidar Width	155 mm	0.075 mm*	155 mm		
Maximum Range, $R_{m,max}$	80 m	80 m			
Mean of Rotational Frequency, $f_{m,\mu}$	50 Hz	50 Hz			
Standard Deviation of Rotational Frequency, $f_{m,\sigma}$	0.1 Hz	0.1 Hz			
Pulse Repetition Frequency, PRF_m	36 kHz	36 kHz			
Scan Angle	190°	190°			
*Scanner 2's width was taken to be smaller in Case 1 because the width of the laser housing facing scanner 1 was less than the width of the scanner from head on (Case 3).					

8.2.2 Monte Carlo Parameterization

Monte Carlo techniques were used to account for drift in the scanners' rotational frequencies. For each test case, a normal distribution of scan frequencies f_1 and f_2 with a sample size defined by the number of simulated rotations of scanner 1 was calculated. The distribution was defined by the rotational frequency standard deviation $f_{m,\sigma}$ approximated from experimental observation. From the distribution, the rotational frequencies were redefined upon each new rotation of scanner 1 to simulate the scanners' drift. From the assumption that the scanners' rotational drift occurs independently, a uniform distribution was used to account for the subsequent drift in reference phase between the devices. Because the model was defined by rotations of scanner 1, only scanner 2's scan angle reference phase $\Theta_{2,0}$ was redefined for each rotation. A uniform distribution of reference phases from $0°$ to $360°$ was used to vary $\Theta_{2,0}$ every rotation based on the assumption that the rotational drift is not periodic. Therefore, the scanners should not favor any set of reference phases.

8.2.3 Target Parameterization

A summary of the input target parameters is presented in Table 18. The arrangement of walls around the scanners was defined as the target geometry in each case of the simulations. The walls were defined with polar coordinates. Because beam divergence and receiver FOV were not parameterized, a tolerance was taken around the walls to uniformly account for these parameters. In each simulated test case, the wall tolerance was calibrated by using the output number of scattered interference events as a metric. The tolerance was adjusted until this parameter fell within 10% of the experimental value, which roughly represented one standard deviation as calculated by Case 4's experimental data. Additionally, scanner 2's body was not modeled as a target, due to

complexities in the scanner's laser housing. However, for a complete explanation of all phenomenon, all targets should be taken into consideration.

Table 18 – Obstacle input parameters for the Monte Carlo simulation.

Parameter	Case 1	Case 2	Case 3	Case 4
Wall Tolerance	0.022	0.0055	0.0055	0.0018
Target	Wall 1	Wall 2	Wall 3	(Wall 1); (Wall 2); (Wall 3)
	Obstacles constant in Cases 1 through 3			
Start Location	$(-0.8, -2.5)$	$(-2.5, 3.0)$	$(2.5, 3.0)$	$(-3.5, -1.0)$; $(-3.5, 0.5)$; $(1.5, 0.5)$
Orientation	90°	0°	270°	No Change
Wall Length	3.8 m	5.0 m	3.8 m	No Change

8.3 Simulation Conduct

A block diagram showing the sequence of logic events for the simulation is shown in Figure 65. With the input parameters defined for the desired test case, the simulation was initialized. The simulation executed a loop for each of the n_1 rotations of scanner 1. Within this, a nested loop incremented for every pulse transmitted for scanner 1. The scanners' angular orientations were incremented within this loop as defined by the relation of the two scanners' PRFs and rotational frequencies. Each increment represented a sequential pulse transmitted by the two scanners.

At each increment of scanner 1, a series of logic tests were performed to determine if interference was occurring and of what nature. The first test checked to see if both scanners were oriented within their scan angle limits. This test was performed since the scanners rotate $360°$, but only emit and collect within their scan angle limits. If one or neither of the scanners were within their angular limits, interference was determined infeasible since only one or neither of the scanners would have been transmitting. The loop then incremented for another orientation of the two beams. Otherwise, if both scanners

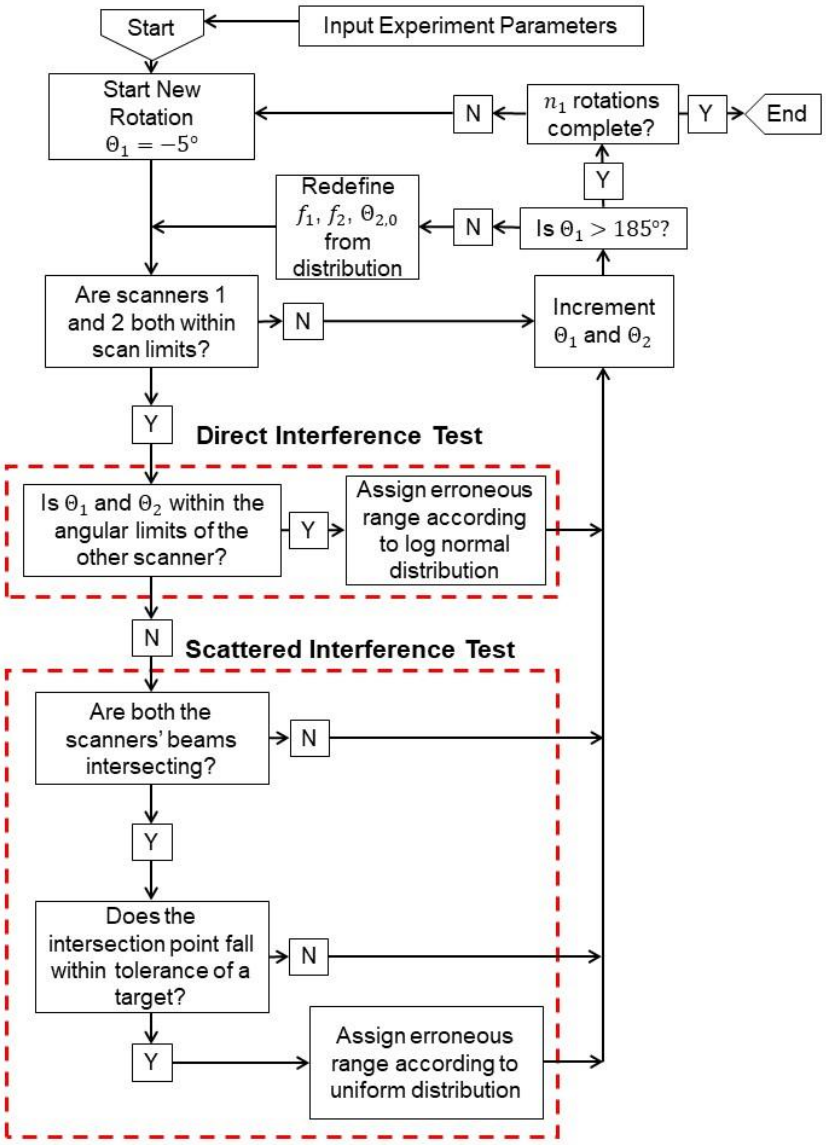

Figure 65 – Block diagram of simulation logic sequence to determine lidar interference.

were within their scan angle limits, the loop proceeded with the direct interference logic test.

If both scanners were within their scan limits, direct interference was logically tested for next. From the user defined scanner widths and locations, the angular limits were calculated and used to check for the conditions of direct interference. If both scanners where oriented within the angular limits of the other, a direct interference event was

recorded. An erroneous ranging point was then generated using a log-normal distribution of ranges fit from experimental observations of direct interference range errors in Cases 1 and 3. The log-normal distribution was selected due to the strong skewedness of the distribution towards scanner 2's location observed in both cases. If the direct interference test was logically true, the simulation exited the interference logic tests and incremented another pulse. If the direct interference test was logically false, then the scattered interference test was performed.

The scattered interference logic test began by using the conditions in Equation (17) in Chapter 4 to test if the two beams were intersecting. If beam intersection was occurring, the Cartesian coordinate of the intersection point was recorded and then tested against the target geometry. If the point was found within the tolerance of the target geometry, a scattered interference event was recorded, and an erroneous ranging point was generated using a uniform distribution out to the maximum range of scanner 1. If any of the scattered interference logic tests were false, the simulation exited the loop and incremented another sequential scan angle.

The angular orientations of scanner's 1 and 2 were looped and incremented until scanner 1's angular orientation exceeded its scan limit of $185°$. The rotational loop then incremented, and the tests repeated until the user defined number of rotations of scanner 1 n_1 was completed. With each iteration of the rotation loop, f_1 and f_2 were redefined from the user defined normal distribution of rotational frequencies. Scanner 2's scan angle reference phase $\Theta_{2,0}$ was also redefined from the uniform distribution of reference phases from $0°$ to $360°$. The simulation script can be found in Appendix B.

8.4 Simulation Results

An overview of simulation results is first presented to spatially show the model's interpretation of lidar interference for each test case. In Chapter 9, the results are then compared to their respective test case's experimental data to facilitate assessment of the theory's assumptions.

8.4.1 Case 1

The simulations results using the parameters for Case 1 are shown in Figure 66. On a macroscale, the spatial distribution of interference points shows similarity to the experimental results presented earlier in Figure 44. However, the simulation results show greater uniformity in dispersion of points than those observed in the experimental data. Nonetheless, a higher density of points can be observed to the side on which the scanner 2 was located. This density was noted in the experimental results and attributed to the relationship of target geometry and intersection density. Because of the absence of

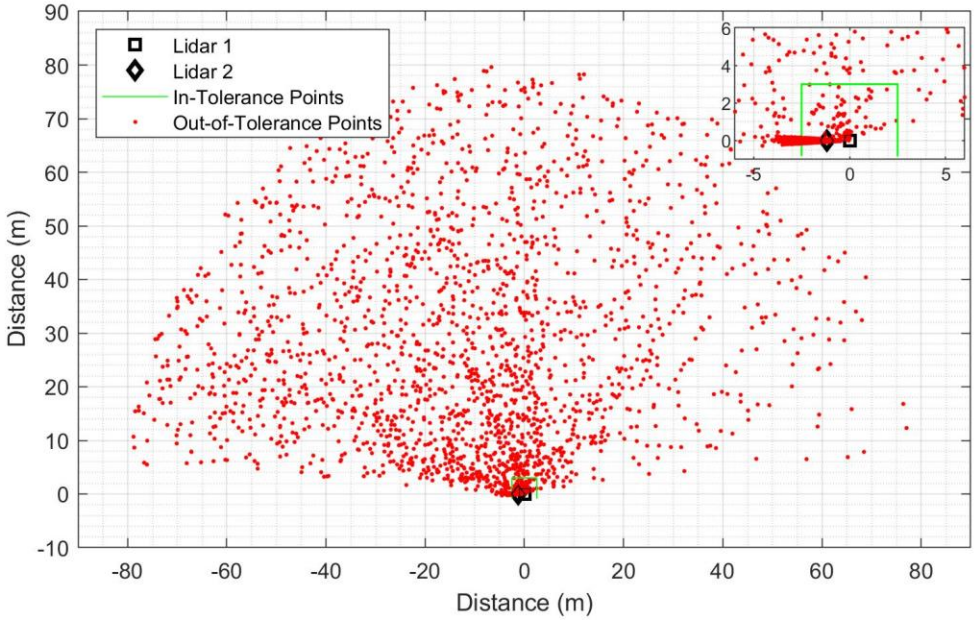

Figure 66 – Interference points from simulation results using Monte Carlo methods with input parameters of Case 1.

radiometric considerations in the simulation, this demonstrates that this phenomenon is a function of beam intersection and target location.

8.4.2 Case 2

The simulations results showing spatially plotted interference points for Case 2 are shown in Figure 67. Qualitatively, a stronger similarity in the distribution of ranging points is seen when compared to the Case 2 experimental results shown earlier in Figure 45. Again, a higher density of points can also be observed to the scanner 2 side of the target space which continues to support the intersection hypothesis. Cases 2 and 4 also provided arrangements to isolate the manifestation of scattered interference. Therefore, the comparison of these simulations to their experimental counterpart are important in establishing the validity of the scattered interference theory.

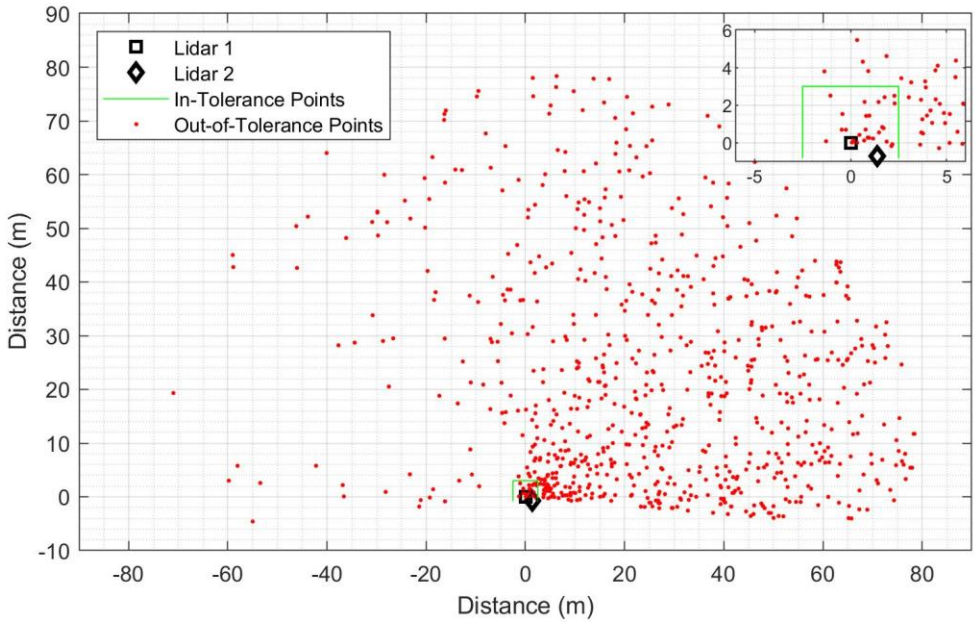

Figure 67 – Interference points from simulation results using Monte Carlo methods with input parameters of Case 2.

8.4.3 Case 3

The Case 3 simulation results are presented in Figure 68. In these results, the signature non-contiguous interference patterns are clearly visible as seen earlier in Case 3's test results presented in Figure 46. It is also initially evident that the number of direct interference events occurring in the simulation outnumbered those observed experimentally. However, the manifestation of these ranging errors as a function of scan angle is nearly identical. On a macro scale, the spatial distribution of scattered interferences points shows similar characteristics as well.

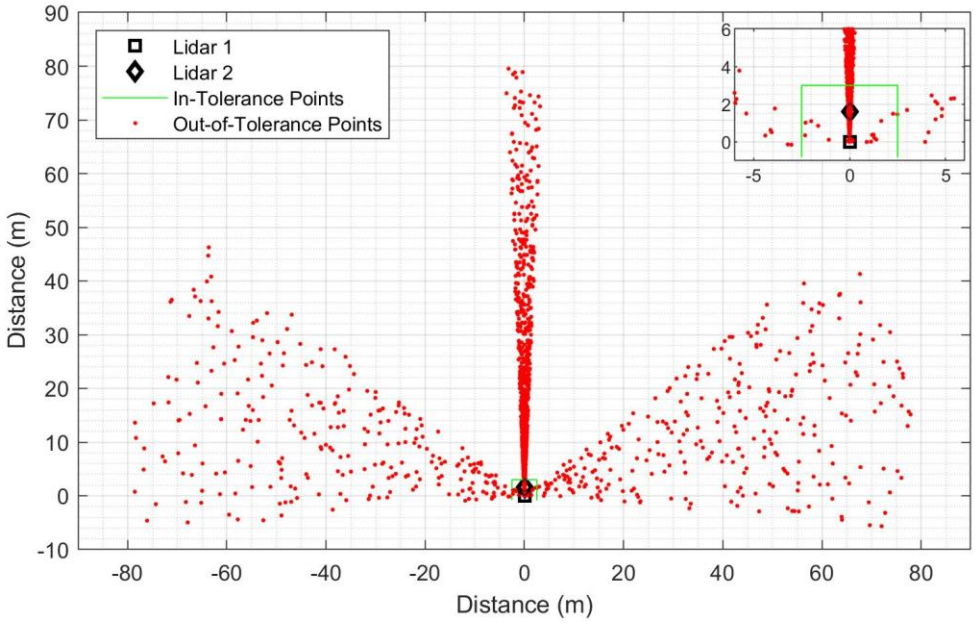

Figure 68 – Interference points from simulation results using Monte Carlo methods with input parameters of Case 3.

8.4.4 Case 4

The results of the simulation for Case 4 are shown in Figure 69. Just as with Case 2's results, a similarity can be seen between the spatial distribution of points on the macroscale

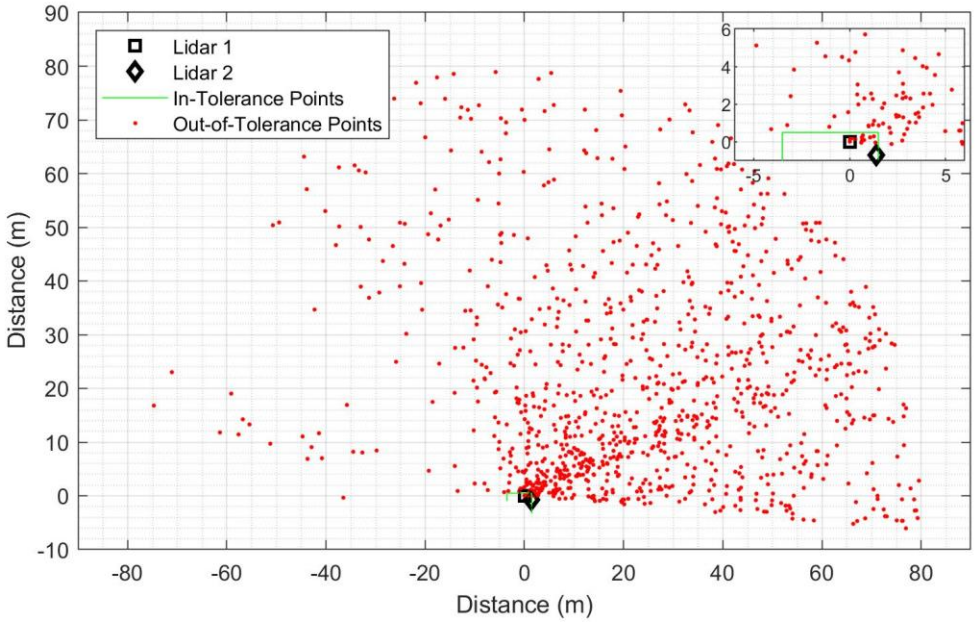

Figure 69 – Interference points from simulation results using Monte Carlo methods with input parameters of Case 4.

when compared to the experimental results presented earlier in Figure 47. And again, a higher concentration of interference points developed on scanner 2's side of the plot as experimentally observed in Cases 1, 2, and 4. This suggests that the experimental results for these cases are consistent with the intersection theory for scatter interference.

CHAPTER 9. COMPARISON OF MODEL TO EXPERIMENTAL RESULTS

Key Conclusions:

- **The angular distribution of interference events was explained well by the theoretical conditions proposed in Chapters 3-5.**
- **The spatial distribution of ranging errors was explain well using the uniform distribution for scattered interference but was not explained well using the log-normal distribution for direct interference ranging errors.**
- **Radiometric considerations such as transmission pathlength and reflectivity may provide additional refinement but did not explain the general angular fluctuations of the interference as well as geometric modeling.**

The simulated results for Case 1 through 4 were compared to the experimentally observed data. Qualitatively the model showed correlation to the experimental results, which given the model's sole dependency on geometry, supports the geometric theory of lidar interference. The model performed best in explaining the angular and spatial distribution of scattered interference events, along with explaining drastic transitions for direct interference occurrences. However, the model did not explain all characteristics observed from the experimental results. Namely, the number of direct interference points showed significant deviation between Cases 1 and 3 for the simulated and observed results. Moreover, for a complete model, it is likely that the radiometric parameterizing is needed. Nonetheless, the theory of interference as a function of beam intersection appears to be supported and a critical factor in describing lidar interference.

To satisfy speculation into the radiometric impacts on interference, each comparison of the simulated and experimental results was overlaid with the normalized inverse pathlength squared between the two detectors by way of the surrounding walls. The pathlength is the distance between the scanners by way of their beam intersection with the wall as a function of scanner 1's scan angle. Since laser irradiance is a function of its transmission distance inversely squared, this overlay provided some context to visually assess if radiometric considerations may further explain experimental observation. Though it is a cursory extension beyond beam intersection, its intent is to direct further inquiry.

The percent difference between the simulated and experimental observations was calculated for comparison between the two results using the formula

$$\%\ \text{Difference} = \left|\frac{\text{Observed} - \text{Expected}}{\text{Expected}}\right| \times 100\%. \tag{39}$$

The experimental data were taken to be the expected, while the simulated results were used as the observed values. This quantity provided some measure of the magnitude of the difference between the results.

9.1 Case 1 Comparison

A comparison of the simulated and experimental statistics for Case 1 are presented in Table 19. Despite a strong calibration of scattered interference events, the direct interference events identified by the model were an order of magnitude below what was experimentally observed. This disparity is likely attributed to the absence of multiple returns as a constraint of the simulation. Furthermore, the model does not consider the complex optical structures associated with scanner 2's laser housing during the experiment.

Table 19 – Quantitative comparison of Case 1 between experimentally measured and simulation results.

Parameter	Experimental Results	Monte Carlo	% Difference
Pulses	3,428,238	3,414,698	0.40%
Total Interference	35,825	4,657	87.00%
Direct Interference	33,661	2,586	92.32%
Scattered Interference	2,164	2,071	4.30%
% Interference of Pulses	1.05%	0.14%	86.95%
% Direct Interference of Interference	93.96%	55.53%	40.90%
% Scattered Interference of Interference	6.04%	44.47%	636.21%

When comparing the spatial results by scan angle, greater similarity can be drawn between the model and experimental results. Figure 70 shows the comparison between experimentally observed, Figure 70(a) and (c), and simulated, Figure 70(b) and (d), results

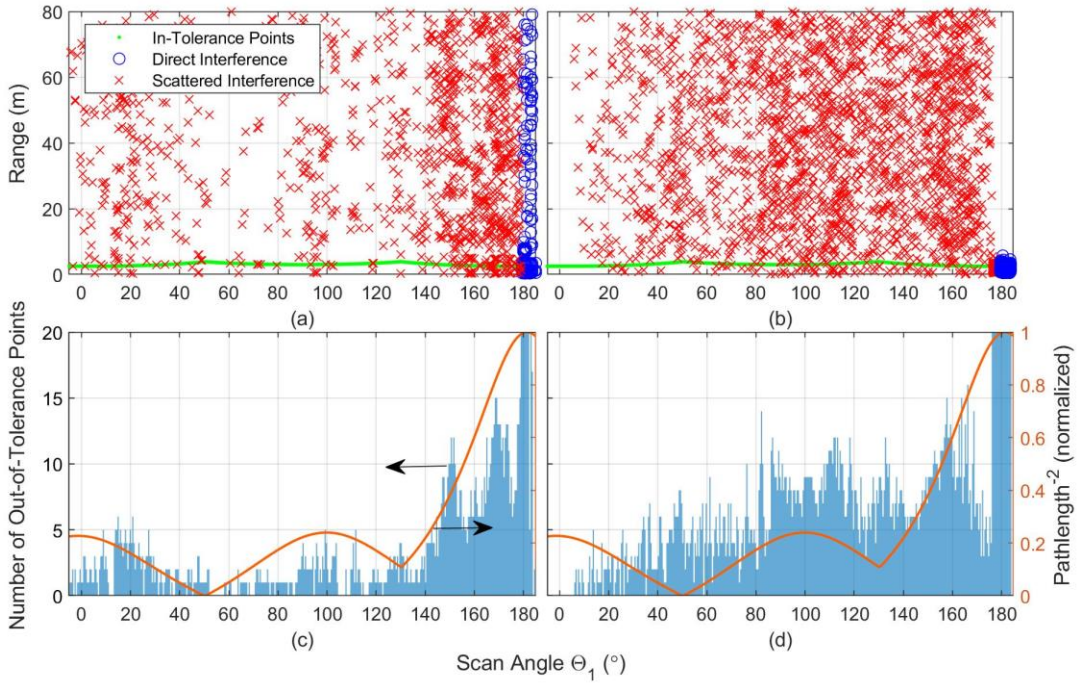

Figure 70 – Comparison of Case 1 between (a and c) experimentally observed and (b and d) simulated interference results. (a and b) Spatial and (c and d) total occurrences of interference events as a function scan angle. The normalized inverse pathlength squared between scanners and the wall by scan angle is overlaid on (d) to facilitate comparison for radiometric considerations.

by scan angle Θ_1. Similarities between the two results include the local maxima of interference points between $150°$ and $160°$, the tapering of interference points as Θ_1 approached $0°$ from above, and the distinct increase in interference events around $180°$ associated with direct interference. Moreover, the overlay of the pathlength provided additional context that supports its use in further refinement of the interference model.

However, in Case 1 the model and experimental results departed in several areas. The first was the noticeable set of interference maxima identified by the model between $80°$ and $120°$. Though a small peak is observed over these scan angles in the experimental results, it is not representative of the model. In this case, radiometric considerations may provide some refinement since the experimental distribution appears to show a strong relationship to the pathlength over these scan angles.

Additionally, another local maxima of experimentally observed interference occurred between $160°$ and $180°$ but was noticeably absent in the simulation results. Although the experimental presence adheres to the proportionality of the inverse pathlength squared, its occurrence as a local maximum is not well explained by transmission distance alone. It may be possible that this maxima could be the result of coupling by way of the earlier proposed indirect interference due to the scan angles' proximity to the line formed by the two scanners. However, this theory does not provide a satisfactory explanation as to its distinct angular separation from the direct interference events. Moreover, this theory does not explain why this was the second highest occurring group of out-of-tolerance points after direct interference.

The simulated ranging errors for direct interference did not replicate the experimentally observed results well using the log-normal distribution calculated from Case 1's experimental data. One likely explanation is that sample size for computing this distribution was nearly 36,000 events – many of which were errors of less than < 1 m.

Since the model identified just under 6,000 direct interference events, the probability of generating a ranging error of greater than 1 m with the distribution was small. It could also suggest that these errors do not follow a log-normal distribution, warranting further investigation.

9.2 Case 2 Comparison

The quantitative comparison for Case 2 is shown in Table 20. A close calibration of the scattered interference results was achieved. This successful calibration provided a good comparative result between the model and experimental results as Case 2 allowed for the isolation of scattered interference events.

Table 20 – Quantitative comparison of Case 2 between experimentally measured and simulation results.

Parameter	Experimental Results	Monte Carlo	% Difference
Pulses	3,428,238	3,414,711	0.39%
Total Interference	771	770	0.13%
Direct Interference	0	0	–
Scattered Interference	771	770	0.13%
% Interference of Pulses	0.02%	0.02%	0.27%
% Direct Interference of Interference	0.00%	0.00%	–
% Scattered Interference of Interference	100.00%	100.00%	0.00%

The comparison of Case 2's interference by scan angle is shown in Figure 71. The trend between the model and experimental results was generally well synchronized. Though some deviation existed between the two results, it may be partially explained by optical phenomena.

The trend of interference points started with a maximum near $-5°$ then generally reduced as the scan angle advanced toward $185°$. Some over assessments of interference

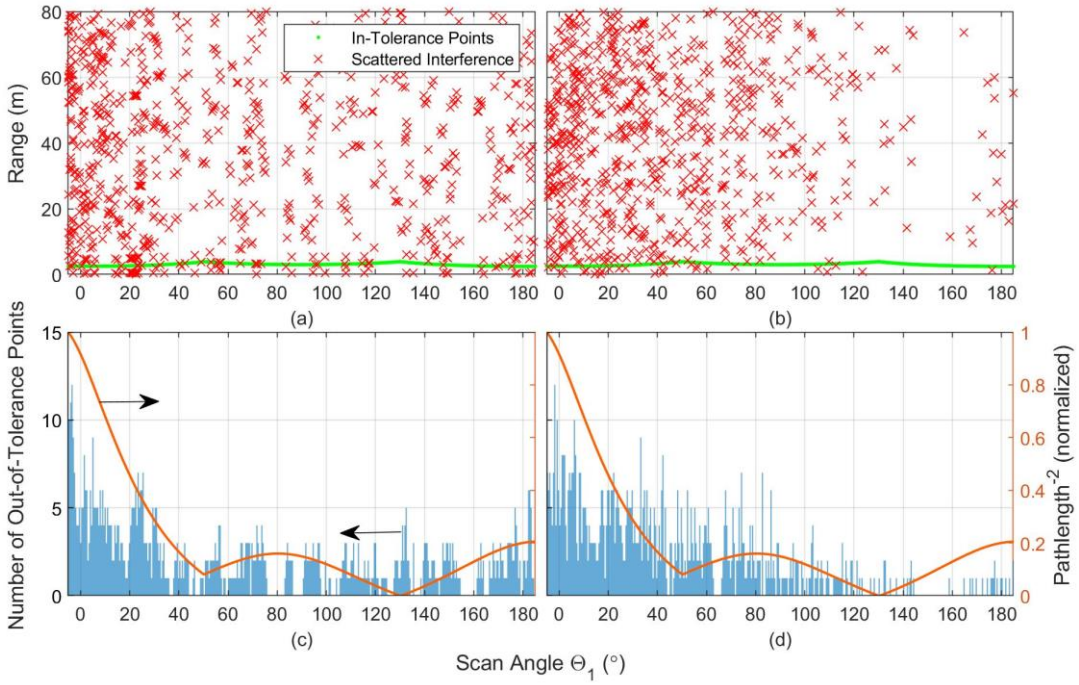

Figure 71 – Comparison of Case 2 between (a and c) experimentally observed and (b and d) simulated interference results. (a and b) Spatial and (c and d) total occurrences of interference events as a function scan angle. The normalized inverse pathlength squared between scanners and the wall by scan angle is overlaid on (d) to facilitate comparison for radiometric considerations.

by the simulation occurred between 40° and 90° which may be further refined by considering radiometry as shown by the relation of the pathlength.

A distinct gap of interference points existed in the simulated results around a scan angle of 65° that was not as readily observable in the experimental results. In the two-scanner reference frame, this corresponds with $\theta_1 = 90°$ and in combination with this arrangement of target geometry appears to produce a theoretical dead spot for scattered interference. Two distinct gaps can be observed in the experimental results around the scan angles of 80° and 85°. However, given the difference in scan angle occurrences, it is difficult to assess whether the simulated result corresponded with this distinct absence of experimentally observed interference points.

One deviation between the model and experimental observation can be accounted for based on the analysis of Case 2's results in Section 7.2.2. The local maximum in interference points experimentally observed around 26.5° corresponded with the angle of reflectance complimentary to scanner 2's angle of incidence with scanner 1's laser housing. This reflection was not included by the simulation, though it should be considered for future refinement.

9.3 Case 3 Comparison

The comparison of simulated and experimental results for Case 3 are shown in Table 21. A close comparison was achieved between the occurrences of scattered interference for the two data sets. However, in contrast to the under representation of direct interference events observed in Case 1, the simulation in Case 3 over evaluated the instances of direct interference. This discrepancy may be explained by the consistent evidence suggesting that the experimental setup of Case 3 failed to accurately align the two scanners' scan planes. Of course, this discrepancy could also be due to the failure of the model to accurately account for all mechanisms, to include complex scanner geometry, when assessing direct interference. This uncertainty only contributes to the case that further investigation is needed to fully understand this phenomenon.

The comparison of interference occurrences by scan angle for Case 3 is shown in Figure 72. The isolation of the two forms of interference – direct and scattered – were represented well by the simulation. Over the two bands that which scattered interference was experimentally observed, qualitative similarities existed with the simulation's account of the events' angular distribution. The pathlength squared of the two scanners may also provide some refinement. However, the fluctuations of scattered interference occurrences appeared to be well represented by geometric intersection alone.

Table 21 – Quantitative comparison of Case 3 between experimentally measured and simulation results.

Parameter	Experimental Results	Monte Carlo	% Difference
Pulses	3,428,238	3,414,848	0.39%
Total Interference	794	2,118	166.75%
Direct Interference	213	1,547	626.29%
Scattered Interference	581	571	1.72%
% Interference of Pulses	0.02%	0.06%	167.80%
% Direct Interference of Interference	26.83%	73.04%	172.27%
% Scattered Interference of Interference	73.17%	26.96%	63.16%

The model deviated from the experimental observation primarily with regards to direct interference. First, the model did not account for coupling of direct interference outside the angular limits of the interference scanner. As a result, a sharp boundary existed

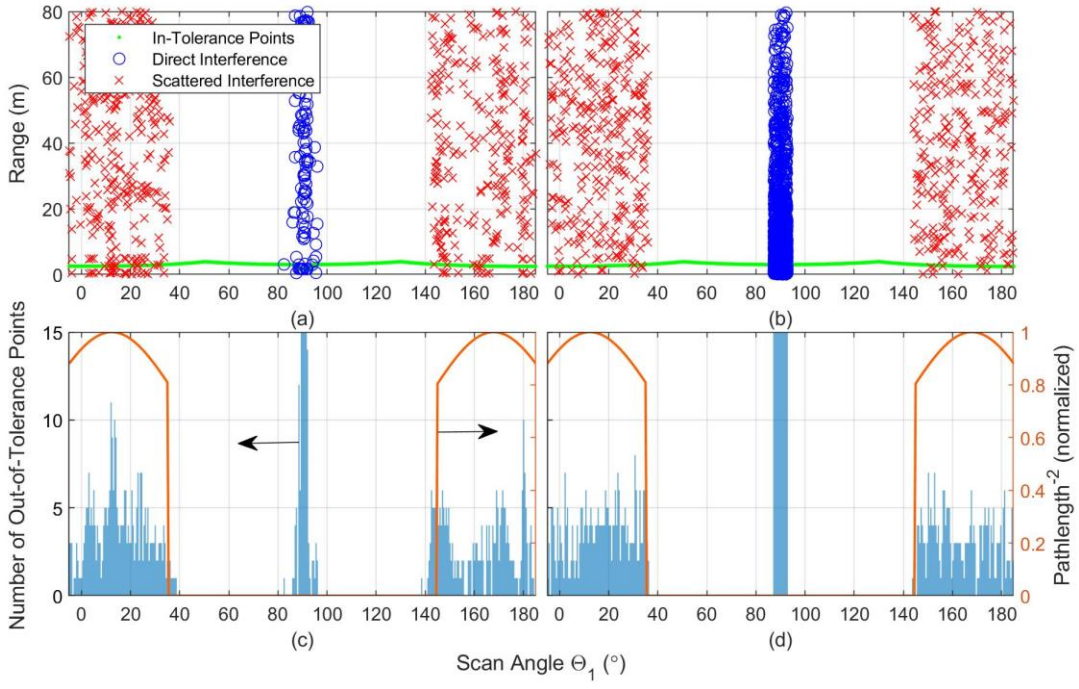

Figure 72 – Comparison of Case 3 between (a and c) experimentally observed and (b and d) simulated interference results. (a and b) Spatial and (c and d) total occurrences of interference events as a function scan angle. The normalized inverse pathlength squared between scanners and the wall by scan angle is overlaid on (d) to facilitate comparison for radiometric considerations.

about scanner 2's angular location, outside of which no direct interference was assessed. By contrast, several cases of direct interference were experimentally observed outside of these strict limits – though they were of a lesser extent.

Secondly, the range distribution failed again to accurately account for ranges of direct interference points using the log-normal distribution fitted from Case 3's experimental data. This failure further supports that the manifestation of range errors as a result of direct interference cannot simply be modeled using this distribution.

Outside of direct interference, the use of a uniform distribution to assign range errors of scattered interference occurrences worked well. Though as observed earlier in Section 7.3, the occurrence of near ranging errors (< 1 m) will likely require additional parameterization to accurately simulate.

9.4 Case 4 Comparison

The comparative results between statistics from Case 4 are given in Table 22. As with Case 2, it was relatively simple to achieve a close representation of the total interference since scattered interference was the only mode of interaction.

Table 22 – Quantitative comparison of Case 4 between experimentally measured and simulation results.

Parameter	Experimental Results	Monte Carlo	% Difference
Pulses	3,427,857	3,414,360	0.39%
Total Interference	1,076	1,054	2.04%
Direct Interference	0	0	–
Scattered Interference	1,076	1,054	2.04%
% Interference of Pulses	0.03%	0.03%	1.66%
% Direct Interference of Interference	0.00%	0.00%	–
% Scattered Interference of Interference	100%	100%	0.00%

The comparison of interference distributions is presented in Figure 73 for both results of Case 4. As before, in Case 2, the model showed general adherence to the distribution of experimentally observed interference points. Though the pathlength also showed some similarities, it failed to account for the interference cases above 120°. Albeit, the model's account of these occurrences is not as robust as experimentally observed either.

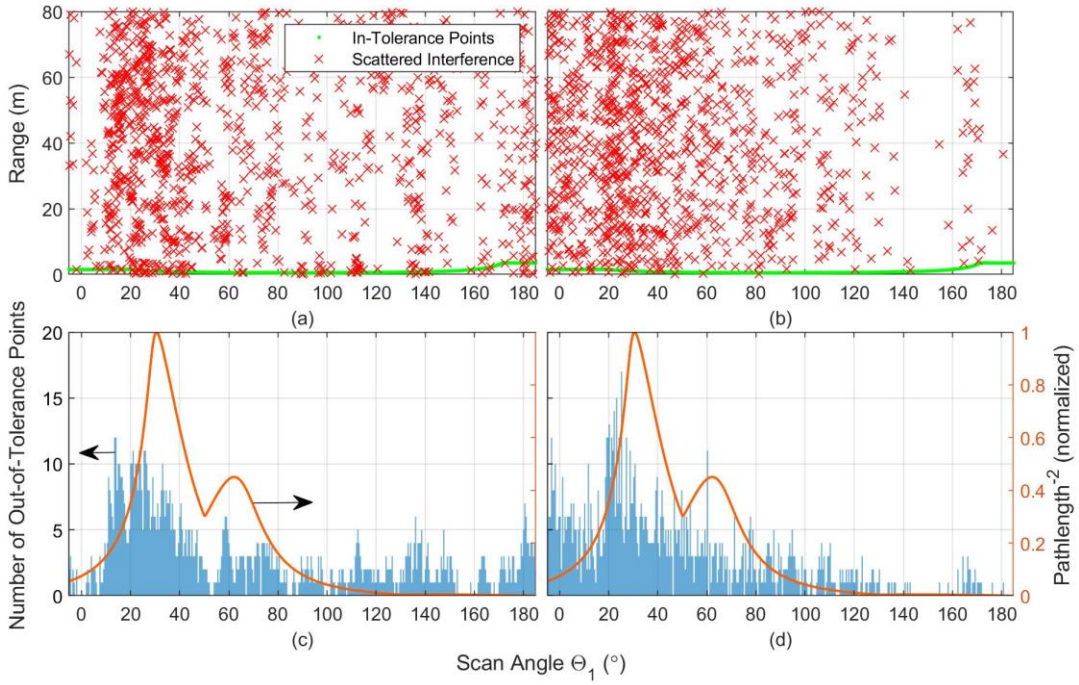

Figure 73 – Comparison of Case 4 between (a and c) experimentally observed and (b and d) simulated interference results. (a and b) Spatial and (c and d) total occurrences of interference events as a function scan angle. The normalized inverse pathlength squared between scanners and the wall by scan angle is overlaid on (d) to facilitate comparison for radiometric considerations.

As discussed in Section 7.5.5, the concentration of interference points experimentally observed around the 26.5° scan angle is partially attributed to the reflection of scanner 2's laser at its angle of reflectance. Excluding this extraordinary occurrence, the local maxima experimental observed between 10° and 40° were generally identified by the model. The local maxima experimentally observed at 60° may be partially accounted for by the single scan angle peak at 60° in the model. This occurrence may have been experimentally measured with some angular deviation thus spreading the occurrences over

several scan angles. However, further evaluation would be required to ascertain this angular deviation.

Additionally, the absences of experimentally observed interference from roughly 150° to 160° is represented by the model. However, the model fails to account for the general increase in interference points beyond 170°, making it difficult to assess the predictive nature of the model in this region.

9.5 Discussion

Overall the simulation showed general consistency with explaining the occurrences of scattered interference and the angular transition of events for direct interference. It can be concluded that beam intersection and angular limits offer a substantial explanation for the occurrences of interference between lidar devices. The account of these occurrences would appear to partially benefit from increased parameterization to account for radiometry. However, radiometry did not appear to solely explain interference events as well as intersection did. The complexities of target geometry would also further refine these explanations. Baring these refinements, it is supported that significant analysis of lidar interference can be gleaned by solely accounting for geometry between the devices.

Given the nature of the simulation, further consideration should be accounted for when comparing the simulated and experimental results. These considerations are presented next.

9.5.1 Methods of Assessing Ranging Errors

Except for the maximum range, the model does not consider radiometry. Therefore, some scattering phenomenon should be expectedly absent. Ranging errors hypothesized to be the result of diffuse-direct interference as described in Section 7.5.1 were not directly

modeled. To qualitatively replicate these errors, the simulation used a log-normal distribution fitted from the experimental observations of direct interference in Cases 1 and 3. However, these distributions consistently failed to replicate the experimentally observed results. This failure suggests that these manifestations are likely the result of more complicated mechanisms as hypothesized earlier in Chapter 7.

9.5.2 Multiple Range Returns

Multiple returns were also not assessed by the simulation. Therefore, complex multi-target returns observed along scan angles containing scanner 2 did not reflect the true nature of their multi-target distribution. This omission should not affect the identification of scattered interference since the wall tolerance was calibrated by matching the experimental and simulated scattered interference totals. However, the absence of double out-of-tolerance returns (Section 7.5.5) was expected to affect direct interference results in the simulation since these scan angles accounted for the highest number of double out-of-tolerance returns and were not accounted for.

9.5.3 Coupling of Direct Interference Outside of Strict Limits

As identified in the assessment of Case 3's experimental data, direct interference points could be observed up to 2.5° outside of the angular width of scanner 2 from scanner 1. This increased observation suggests that direct interference was not strictly confined to an interference source's angular limits. Since the factors of this phenomenon are still widely unknown, the model did not account for this. As a result, since this coupling should occur independent of intersection, the experimentally observed distribution of interference points near direct interference limits may further differ from the simulated results.

9.5.4 Experimental Error

Another factor that may account for discrepancies between experimentally observed and simulated results include experimental error. Direct interference results in Case 3 were likely impacted due to poor scan plane alignment. The model assumes ideal beam alignment between the two scanners. Therefore, in Case 3, the higher assessment of direct interference events by the simulation could be expected.

9.5.5 Precision of Experimentally Measured Scan Angles

In all cases, the models' angular location of maxima and minima may have deviated slightly from the experimental results. This deviation should be expected due to the precise definition of target geometry in the model when compared to the achievable precision that which was used to arrange the scanners and construct the walls for the experiment. Moreover, the LMS531 scanner does not report the scan angle of returns with any precision, but rather just reports them by bin associated with the scan angle. Therefore, actual deviation of the scan angle is unknown in the reported results. This unknown scan angle deviation could further compound shifts in the experimentally measured distributions when compared to the simulated results.

CHAPTER 10. CONCLUSION

Key Conclusions:

- **Theory was proposed that outlined the occurrences of direct and scattered lidar interference.**
- **Direct interference occurs when two lidar scanners are oriented/emitting directly at one another and the energy from one device is coupled into the other.**
- **Scattered interference occurs when the ranging signal from a harassing lidar is scattered from a target and received by a victim scanner.**
- **A mathematical model was introduced to assess the upper limit of scattered interference which is quantified by the fraction of time two lidar beams intersect.**
- **The superposition of intersection points between two lidar beams was analyzed to describe the intersection geometry.**
- **The coincidence of intersection geometry and scattering target surfaces can inform the occurrences of scattered interference.**
- **An experiment was conducted to assess the occurrence of both types of lidar interference.**
- **When preset, direct interference was found to occur with generally greater frequency than scattered interference but resulted in a lower average ranging error.**
- **Scattered interference occurred with less frequency than direct interference but manifested with a greater average ranging error.**
- **A Monte Carlo simulation was developed to model lidar interference between two lidar scanners using the proposed theory.**

- **The simulation results provided a general explanation for fluctuations in scattered interference events as a function of scan angle and distinction between frequency occurrences of direct and scattered interference.**
- **Further work is required to better explain the manifestation of direct interference ranging errors and interference phenomena which may be explained through radiometry.**

The use of lidar to enable future autonomous vehicle navigation has raised the potential of the technology's ubiquitous use. However, a widespread deployment will challenge the technology in ways not fully understood. One potential threat to lidar's safe and accurate employment includes signal interference. However, the phenomenon has been largely unstudied and as a result, a lack of theory exists to inform engineering to contend with this vulnerability.

10.1 Summary of Results

A theory of lidar interference was presented that intended to codify and classify the occurrences of the phenomenon. It was proposed that lidar interference has at least two distinct forms – direct interference and scattered interference – each with their own unique characteristics and considerations. With this theory, conditions were proposed to explain the occurrences of each mode.

10.1.1 Theoretical Model

Direct mutual illumination of each scanner conditionally establishes the occurrence direct interference. The occurrence of scattered interference can be conditionally partitioned into beam intersection between two lidar scanners and the coincidence of a scattering target. A mathematical description for beam intersection was presented that

which established the lower and upper limits of scattered interference to be between 0% and 50% of scanning time or angles, with an average of most occurrences around 25% of a scanner's rotational time. This relatively large percentage is further reduced once the coincidence of a scattering target is considered.

The intersection geometry was described which provides a visualization of the temporal transition of intersection points. By modeling this intersection geometry and accounting for small perturbations in the two scanner's rotational frequencies, an intersection density map can be generated from the resulting intersection points. This map along with the knowledge of target geometry can facilitate analysis to identify locations with the greatest risks of scattered interference between the devices.

10.1.2 Experimental Observation

An experiment was conducted to replicated conditions for lidar interference. The experiment set to validate the work of [17] while extending its analysis. Five different test cases were used to collect data and isolate the occurrences of lidar interference. The two forms of theorized interference – direct and scattered – were observed to have characteristically different behavior.

When present, direct interference was generally found to be the dominant form of interference by occurrence. However, depending on the efficiency of the lidars' beam coupling, its erroneous interpretation of ranging data was found to mostly manifest itself with small ranging errors of less than 1 m. Based on the observations of direct interference, it was further proposed that this interference comes in two forms – diffuse-direct and coupled-direct interference – which account for the small and large ranging errors, respectively.

Scattered interference was observed with less frequency, however, its erroneous interpretation resulted in the larger of average ranging errors, centered near the middle of the lidar's ranging capability. Furthermore, the comparison of intersection point density maps with the angular distribution of observed reflected interference events showed significant correlation between the two, supporting the theory of scatter interference.

10.1.3 Comparison to Theory

A simulation that used the underlying assumptions of the proposed theory was developed to test the theory through the comparison of the simulated and observed data. The simulation used only beam intersection, target location, and angular limits of the scanners to analyze interference occurrences between the two lidars. Monte Carlo techniques were used to account for drift between the lidars' scanning progressions. Four of the test cases were compared qualitatively and quantitatively. In the absence of radiometric consideration, the simulated results showed a general adherence to the experimentally observed events, which supports the proposed geometric theory. However, some refinement is required to better model the manifestation of direct interference ranging errors and optical phenomenon such as multiple surface reflections.

10.2 Possible Solutions

Given the potential threat of lidar interference, there are several cursorily recommendations that can be made to mitigate its occurrences based on these results. As proposed by the mathematical framework, phase locking and frequency control may be utilized to reduce the occurrences of scattered interference between devices. The most intuitive of these cases ($f_2/f_1 = 1$ and $\theta_{2,0} = 180°$) are already recommended by

manufactures, such as Velodyne, to avoid interference between their devices [53]. However, this is not completely feasible given multiple uncoordinated vehicles on a roadway unless vehicle to vehicle communication advances enough for real-time control.

Though it is not feasible to completely control the scan plane of devices on a roadway, vehicleborne lidars should avoid the employment of 0° scan planes. The polar angle offset of the scanner has the potential to significantly reduce the occurrences of direct interference. The misalignment of scan planes is also recommended by manufactures, such as SICK, for employment of more than one sensor [54]. However, out of plane scanners (other than 0° polar angle alignment with respect to rotational axis) follow a conical shape, which should have less risk of both scattered (beam intersection) and direct interference. Moreover, Case 3's abnormal results suggest that direct interference is more sensitive to beam plane alignment than scattered interference. Therefore, effort should be made to misalign scan planes so to reduce the probability of inter-scanner coupling. This misalignment may be further supported between vehicles by variations in vehicle heights and placement on the vehicle's body.

Retroreflective automotive paint could also be used to reduce angular dispersion of laser energy for vehicle lidar. This application would both improve the desired return's intensity (potentially extending range or improving ranging precision) while reducing the lateral scattering to other scanners, in turn, reducing the risk of scattered interference. Consideration of scattering targets along roadways would also need to be considered. Highly reflective urban environments such as city roadways flanked by mirrored glass buildings may further complicate the scattering environment. Therefore, the application of

these paints should not just be considered for vehicles, but all targets within the line-of-sight of a roadway which does carry a significant challenge for infrastructure modification.

As discussed earlier, laser encoding and data filtering techniques are other methods currently pursued by other research teams to reduce interference [22-27]. Each has their merit, however, only addresses the risk of scattered interference. As such, the mitigation of lidar interference will likely not come in the form of a single technology, but rather in the consorted effort of technological design, data processing techniques, and best practices.

10.3 Future Work

The work presented in this thesis leaves many new questions about lidar interference. The theory was intended as a starting point from which the direction of future research could be guided. With this guidance, further work could be done towards extending this thesis' theoretical, experimental, and simulated work.

Regarding the mathematical description of beam intersection, future work could include an extension of the theory to out of plane scanners, moving scanners, and time variant scanning frequencies. Furthermore, the application of beam divergence and FOV would improve the model's functionality. In addition, much work can still be done to develop an understanding of intersection geometry. Finally, from the theory, the zero intersection scanner configurations proposed in Chapter 4 should also be experimentally tested.

Experimentally, observations posed more questions than answered. Future approaches to the work could investigate serval interesting phenomena observed in or

hypothesized from the experimental work. With regard to general interference phenomena, future investigations could analyze the spatial-temporal occurrence of interference events by analyzing how interference events manifest as a function of time. Additionally, much work can be done into explaining the mechanisms of double out-of-tolerance events observed in Section 7.5.5 and explaining their unique pattern. Finally, further understanding could be developed into the variance of interference occurrences. The current investigation of interference variance only analyzed a sample size of four iterations, of which only contained scattered interference events. Increasing the sample size (both in the number of iterations and rotations) and extending the analysis to direct interference would improve the understanding of this phenomenon.

Regarding direct interference, further investigation would be warranted into confirming or denying the hypothesis for direct interference's ranging error manifestation. Additionally, further investigation could analyze the angular distribution of direct interference events about an interference source to improve future models. An extension of this analysis could determine direct interference's sensitivity to beam alignment and may offer future solutions to deconflicting inter-lidar interference of autonomous vehicles.

With regard to scattered interference, further investigation is warranted into confirming the hypothesis posed in Section 7.2.1 that assumes the high frequency fluctuations of scattered interference occurrences will converged given longer observation. Additionally, rotational drift of the scanners should be experimentally measured to improve modelling parameters. And in all test cases, experimental iterations could also be performed by maintaining target geometry but modifying target reflectivity to observe potential radiometric effects on scattered interference.

In all cases, unaccounted for biases and abnormalities may have been imposed on the experimental results from the manufacturer's hardware design and data processing techniques. As a result, interpretation of the data may be manufacturer specific, rather than physically universal. To overcome this potential limitation, the use of a purpose build custom lidar with waveform resolution is recommended for future experiments. This would enable the analysis to identify how interference manifests at the waveform level and propose theories and solutions with the greatest ubiquity in application.

A Monte Carlo simulation that included beam divergence, detector FOV, and pathlength in addition to beam intersection was developed beyond the work presented. However, as more factors were included, experimental and simulated observations became less coordinated. Though individually, each of these are grounded in sound optical theory, their collective use requires additional consideration that remains to be developed. This disagreement suggests that despite the hypothesis for each of these factor's significance in explaining lidar interference, their complete and concurrent application remains to be explained.

10.4 Concluding Remarks

Lidar offers a promising technology for the autonomous vehicle industry. Its development over more than half a century has proven the technology an accurate form of remote sensing. However, its historic uses have not tested it in ways that widespread commercial autonomous vehicle deployments will. As a result, the lidar, autonomous vehicle, and transportation safety industries will have to contend with the technology's safety considerations. Therefore, further published explanation of lidar interference should be pursued to facilitate lidar's safe application in a world relying on its guidance. This

thesis intended to lay the foundation for this continued study. And it is the hope that this leads to fruitful and innovative solutions so that society may continue to develop technology for the safety of its users.

APPENDIX A. EQUIVALENT EXPRESSION FOR *F*

The expression for s_F given by Equation (17) can be written in Boolean logical conditional form as

$$s_F(t) = \{s[\theta_1(t)] = s[\theta_2(t)] = s[\Delta\theta(t)] = 1\} + \{s[\theta_1(t)] = s[\theta_2(t)] = s[\Delta\theta(t)] = 0\}, \tag{40}$$

where "+" represents the OR operation. A similar equivalent conditional equation is

$$s_F(t) = \{S[\theta_1(t)] = S[\theta_2(t)]\} \cdot \{S[\theta_2(t)] = S[\Delta\theta(t)]\}, \tag{41}$$

where "·" represents the AND operation and an alternative Boolean logic expression. A further similar equivalent equation is

$$s_F(t) = \{s[\theta_1(t)] \odot s[\theta_2(t)]\} \cdot \{s[\theta_2(t)] \odot s[\Delta\theta(t)]\}, \tag{42}$$

where "⊙" represents the EXCLUSIVE NOR operation (EXNOR) which is also called the Boolean EQUALITY operation since it produces a 1 when the two inputs match.

APPENDIX B. MATLAB CODE

The following scripts were written for compatibility for MATLAB R2018b.

B.1 Training Analysis

The script used to analyze the experimental training data and output the range limits is presented below.

```
function [] = SICK_LMS531_Training()
%Calculates average and maximum standard deviation of ranges from
training
%portion of interference experiment.

% Input: INTEX#_Train.mat file with n length corresponding to the
number of
% rotations of scanner 1. Variables include:
    %DTG_Stamp: n x 1 string array of date time group stamps of each
    %rotation
    %ElapsedTime: n x 1 array of the elapsed time in milliseconds from
    %the star of recording. (*Note: each INTEX recording is
    %concatenated from 5 min recordings, so the elapsed time is
    %relative to the beginning of the 5 minute recording)
    %Returns: n x 361 x 2 matrix return ranges measured at 0.5 degree
    %intervals staring at -5^deg to 185^deg (measured like a unit
    %circle). Returns(n,361,1) are first returns while
    % Returns(n,361,2) are second returns
%
%Output:
  %RangeLimits: 5x381x2 array with the following ((:,:,1) are first
  %returns and (:,:,2) are second returns):
    %RangeLimits(1,:,1): average range of first returns by scan
    %angle
    %RangeLimits(2,:,1): max range of first returns by scan
    %angle
    %RangeLimits(3,:,1): min range of first returns by scan
    %angle
    %RangeLimits(4,:,1): upper limit of range of first returns by
    %scan angle to be consider in tolerance
    %RangeLimits(5,:,1): lower limit of range of first returns by
    %scan angle to be consider in tolerance

  %ReturnsCart: 4 x n matrix with the first two col

TestNumber = 6;  % 6 = INTEX6; 7 = INTEX7; 8 = INTEX8; etc to 11
NumberSigma = 5;   % The number of sigma deviations to calculate the
limits of normal operation.
```

```
INTEX_Directory = 'C:\InputYourFileDirectoryLocation';


TestName = string(['INTEX',num2str(TestNumber),'_Train']);

if TestNumber == 6 || TestNumber == 7 || TestNumber == 8

  % load Kim Distance Analysis

load(strcat(INTEX_Directory,'INTEX',num2str(TestNumber),'\INTEX',num2st
r(TestNumber),'_KimDistanceAnalysis.mat'))
end

% load Train file
load(strcat(INTEX_Directory,'INTEX',num2str(TestNumber),'\INTEX',num2st
r(TestNumber),'_Train.mat'))


VariablesSaveName =
strcat('INTEX',num2str(TestNumber),'_',num2str(NumberSigma),'sigma_Dist
anceAnalysis.mat');
RangeLimitsSaveName =
strcat('INTEX',num2str(TestNumber),'_',num2str(NumberSigma),'sigma_Rang
eLimits.mat');


n = length(ElapsedTime);
Returns(Returns==0) = NaN;        %replaces zero returns to NaN
AngleArrayDeg = [-5:0.5:185];    %Angle array in degrees from -5deg to
185deg in 0.5deg increments in radians
AngleArray = deg2rad(AngleArrayDeg);

%% Tolerance Analysis

RangeLimits = zeros(5,381,2);


for i = 1:2
  for ii =1:381
    if sum(~isnan(Returns(:,ii,i)),'all') ~= 0
      pd = fitdist(Returns(:,ii,i),'Normal');
      RangeLimits(1,ii,i) = pd.mu;
      RangeLimits(2,ii,i) = pd.sigma;
      RangeLimits(3,ii,i) = AngleArrayDeg(ii);
      RangeLimits(4,ii,i) =
RangeLimits(1,ii,i)+NumberSigma*RangeLimits(2,ii,i);
      RangeLimits(5,ii,i) = RangeLimits(1,ii,i)-
NumberSigma*RangeLimits(2,ii,i);
    end
  end
end

if TestNumber == 6
  RangeLimits(:,371,:) = NaN;
  DistributionRanges = sort(Returns(:,371,1));
```

```
  DistributionRange1 = DistributionRanges(1:634);
  DistributionRange2 = DistributionRanges(635:8988);
  DistributionRange3 =
vertcat(DistributionRanges(8989:8995),Returns(:,371,2));

  TriDistINTEX6_Bin371 = NaN(5,3);

  pd = fitdist(DistributionRange1,'Normal');
  TriDistINTEX6_Bin371(1,1) = pd.mu;
  TriDistINTEX6_Bin371(2,1) = pd.sigma;
  TriDistINTEX6_Bin371(3,1) = 180;
  TriDistINTEX6_Bin371(4,1) =
TriDistINTEX6_Bin371(1,1)+NumberSigma*TriDistINTEX6_Bin371(2,1);
  TriDistINTEX6_Bin371(5,1) = TriDistINTEX6_Bin371(1,1)-
NumberSigma*TriDistINTEX6_Bin371(2,1);

  pd = fitdist(DistributionRange2,'Normal');
  TriDistINTEX6_Bin371(1,2) = pd.mu;
  TriDistINTEX6_Bin371(2,2) = pd.sigma;
  TriDistINTEX6_Bin371(3,2) = 180;
  TriDistINTEX6_Bin371(4,2) =
TriDistINTEX6_Bin371(1,2)+NumberSigma*TriDistINTEX6_Bin371(2,2);
  TriDistINTEX6_Bin371(5,2) = TriDistINTEX6_Bin371(1,2)-
NumberSigma*TriDistINTEX6_Bin371(2,2);


  pd = fitdist(DistributionRange3,'Normal');
  TriDistINTEX6_Bin371(1,3) = pd.mu;
  TriDistINTEX6_Bin371(2,3) = pd.sigma;
  TriDistINTEX6_Bin371(3,3) = 180;
  TriDistINTEX6_Bin371(4,3) =
TriDistINTEX6_Bin371(1,3)+NumberSigma*TriDistINTEX6_Bin371(2,3);
  TriDistINTEX6_Bin371(5,3) = TriDistINTEX6_Bin371(1,3)-
NumberSigma*TriDistINTEX6_Bin371(2,3);

elseif TestNumber == 8
  RangeLimits(:,187,1) = NaN;

  DistributionRanges = sort(Returns(:,187,1));

  DistributionRange1 = DistributionRanges(1:8653);
  DistributionRange2 = DistributionRanges(8654:8995);


  TriDistINTEX8_Bin187 = NaN(5,2);

  pd = fitdist(DistributionRange1,'Normal');
  TriDistINTEX8_Bin187(1,1) = pd.mu;
  TriDistINTEX8_Bin187(2,1) = pd.sigma;
  TriDistINTEX8_Bin187(3,1) = 88;
  TriDistINTEX8_Bin187(4,1) =
TriDistINTEX8_Bin187(1,1)+NumberSigma*TriDistINTEX8_Bin187(2,1);
  TriDistINTEX8_Bin187(5,1) = TriDistINTEX8_Bin187(1,1)-
NumberSigma*TriDistINTEX8_Bin187(2,1);

  pd = fitdist(DistributionRange2,'Normal');
  TriDistINTEX8_Bin187(1,2) = pd.mu;
```

```
  TriDistINTEX8_Bin187(2,2) = pd.sigma;
  TriDistINTEX8_Bin187(3,2) = 88;
  TriDistINTEX8_Bin187(4,2) =
TriDistINTEX8_Bin187(1,2)+NumberSigma*TriDistINTEX8_Bin187(2,2);
  TriDistINTEX8_Bin187(5,2) = TriDistINTEX8_Bin187(1,2)-
NumberSigma*TriDistINTEX8_Bin187(2,2);

elseif TestNumber == 9
  RangeLimits(:,267,1) = NaN;
  DistributionRanges = sort(Returns(:,267,1));

  DistributionRange1 = DistributionRanges(1:178);
  DistributionRange2 = DistributionRanges(179:8998);

  TriDistINTEX9_Bin267 = NaN(5,3);

  pd = fitdist(DistributionRange1,'Normal');
  TriDistINTEX9_Bin267(1,1) = pd.mu;
  TriDistINTEX9_Bin267(2,1) = pd.sigma;
  TriDistINTEX9_Bin267(3,1) = 128;
  TriDistINTEX9_Bin267(4,1) =
TriDistINTEX9_Bin267(1,1)+NumberSigma*TriDistINTEX9_Bin267(2,1);
  TriDistINTEX9_Bin267(5,1) = TriDistINTEX9_Bin267(1,1)-
NumberSigma*TriDistINTEX9_Bin267(2,1);

  pd = fitdist(DistributionRange2,'Normal');
  TriDistINTEX9_Bin267(1,2) = pd.mu;
  TriDistINTEX9_Bin267(2,2) = pd.sigma;
  TriDistINTEX9_Bin267(3,2) = 128;
  TriDistINTEX9_Bin267(4,2) =
TriDistINTEX9_Bin267(1,2)+NumberSigma*TriDistINTEX9_Bin267(2,2);
  TriDistINTEX9_Bin267(5,2) = TriDistINTEX9_Bin267(1,2)-
NumberSigma*TriDistINTEX9_Bin267(2,2);

  RangeLimits(:,120,1) = NaN;
  DistributionRanges = sort(Returns(:,120,1));

  DistributionRange1 = DistributionRanges(1:124);
  DistributionRange2 = DistributionRanges(125:8998);

  TriDistINTEX9_Bin120 = NaN(5,3);

  pd = fitdist(DistributionRange1,'Normal');
  TriDistINTEX9_Bin120(1,1) = pd.mu;
  TriDistINTEX9_Bin120(2,1) = pd.sigma;
  TriDistINTEX9_Bin120(3,1) = 54.5;
  TriDistINTEX9_Bin120(4,1) =
TriDistINTEX9_Bin120(1,1)+NumberSigma*TriDistINTEX9_Bin120(2,1);
  TriDistINTEX9_Bin120(5,1) = TriDistINTEX9_Bin120(1,1)-
NumberSigma*TriDistINTEX9_Bin120(2,1);

  pd = fitdist(DistributionRange2,'Normal');
  TriDistINTEX9_Bin120(1,2) = pd.mu;
  TriDistINTEX9_Bin120(2,2) = pd.sigma;
  TriDistINTEX9_Bin120(3,2) = 54.5;
  TriDistINTEX9_Bin120(4,2) =
TriDistINTEX9_Bin120(1,2)+NumberSigma*TriDistINTEX9_Bin120(2,2);
```

```
  TriDistINTEX9_Bin120(5,2) = TriDistINTEX9_Bin120(1,2)-
NumberSigma*TriDistINTEX9_Bin120(2,2);


end


h(1) = figure(1);
polarplot(AngleArray,RangeLimits(1,:,1),'.')  %Average First Returns
title('Average Range of First Returns')

h(2) = figure(2);
polarplot(AngleArray,RangeLimits(1,:,2),'.')  %Average Second Returns
title('Average Range of Second Returns')

if TestNumber == 6
  h(3) = figure(3);
  subplot(2,1,1)
  plot(RangeLimits(3,:,1),RangeLimits(1,:,1),'k',...
    RangeLimits(3,:,1),RangeLimits(4,:,1),'--k',...
    RangeLimits(3,:,1),RangeLimits(5,:,1),':k',...
    TriDistINTEX6_Bin371(3,:,1),TriDistINTEX6_Bin371(1,:,1),'k',...
    TriDistINTEX6_Bin371(3,:,1),TriDistINTEX6_Bin371(4,:,1),'--k',...
    TriDistINTEX6_Bin371(3,:,1),TriDistINTEX6_Bin371(5,:,1),':k')
  title('First Returns Average \mu and Upper and Lower Limits')
  legend('\mu', 'Upper Limit', 'Lower Limit')
  xlim([-5 185])
  xlabel('Scan Angle \theta_1')
  ylabel('Range (m)')

  subplot(2,1,2)
  plot([-5:0.5:185],RangeLimits(2,:,1),'k')
  title('Standard Deviation \sigma')
  legend('\sigma')
  xlim([-5 185])
  xlabel('Scan Angle \theta_1')
  ylabel('Range (m)')

elseif TestNumber == 8
  h(3) = figure(3);
  subplot(2,1,1)
  plot(RangeLimits(3,:,1),RangeLimits(1,:,1),'k',...
    RangeLimits(3,:,1),RangeLimits(4,:,1),'--k',...
    RangeLimits(3,:,1),RangeLimits(5,:,1),':k',...
    TriDistINTEX8_Bin187(3,:,1),TriDistINTEX8_Bin187(1,:,1),'k',...
    TriDistINTEX8_Bin187(3,:,1),TriDistINTEX8_Bin187(4,:,1),'--k',...
    TriDistINTEX8_Bin187(3,:,1),TriDistINTEX8_Bin187(5,:,1),':k')
  title('First Returns Average \mu and Upper and Lower Limits')
  legend('\mu', 'Upper Limit', 'Lower Limit')
  xlim([-5 185])
  xlabel('Scan Angle \theta_1')
  ylabel('Range (m)')

  subplot(2,1,2)
  plot([-5:0.5:185],RangeLimits(2,:,1),'k')
  title('Standard Deviation \sigma')
  legend('\sigma')
```

```
  xlim([-5 185])
  xlabel('Scan Angle \theta_1')
  ylabel('Range (m)')

elseif TestNumber == 9
  h(3) = figure(3);
  subplot(2,1,1)
  plot(RangeLimits(3,:,1),RangeLimits(1,:,1),'k',...
    RangeLimits(3,:,1),RangeLimits(4,:,1),'--k',...
    RangeLimits(3,:,1),RangeLimits(5,:,1),':k',...
    TriDistINTEX9_Bin120(3,:,1),TriDistINTEX9_Bin120(1,:,1),'k',...
    TriDistINTEX9_Bin120(3,:,1),TriDistINTEX9_Bin120(4,:,1),'--k',...
    TriDistINTEX9_Bin120(3,:,1),TriDistINTEX9_Bin120(5,:,1),':k',...
    TriDistINTEX9_Bin267(3,:,1),TriDistINTEX9_Bin267(1,:,1),'k',...
    TriDistINTEX9_Bin267(3,:,1),TriDistINTEX9_Bin267(4,:,1),'--k',...
    TriDistINTEX9_Bin267(3,:,1),TriDistINTEX9_Bin267(5,:,1),':k')
  title('First Returns Average \mu and Upper and Lower Limits')
  legend('\mu', 'Upper Limit', 'Lower Limit')
  xlim([-5 185])
  xlabel('Scan Angle \theta_1')
  ylabel('Range (m)')

  subplot(2,1,2)
  plot([-5:0.5:185],RangeLimits(2,:,1),'k')
  title('Standard Deviation \sigma')
  legend('\sigma')
  xlim([-5 185])
  xlabel('Scan Angle \theta_1')
  ylabel('Range (m)')

else

  h(3) = figure(3);
  subplot(2,1,1)
  plot(RangeLimits(3,:,1),RangeLimits(1,:,1),'k',...
    RangeLimits(3,:,1),RangeLimits(4,:,1),'--k',...
    RangeLimits(3,:,1),RangeLimits(5,:,1),':k')
  title('First Returns Average \mu and Upper and Lower Limits')
  legend('\mu', 'Upper Limit', 'Lower Limit')
  xlim([-5 185])
  xlabel('Scan Angle \theta_1')
  ylabel('Range (m)')

  subplot(2,1,2)
  plot([-5:0.5:185],RangeLimits(2,:,1),'k')
  title('Standard Deviation \sigma')
  legend('\sigma')
  xlim([-5 185])
  xlabel('Scan Angle \theta_1')
  ylabel('Range (m)')
end

h(5) = figure(4);
subplot(2,1,1)
plot([-5:0.5:185],RangeLimits(1,:,2),'k',...
  [-5:0.5:185],RangeLimits(4,:,2),'--k',...
  [-5:0.5:185],RangeLimits(5,:,2),':k')
```

```
title('Second Returns Average \mu and Upper and Lower Limits')
legend('\mu', 'Upper Limit', 'Lower Limit')
xlim([-5 185])
xlabel('Scan Angle \theta_1')
ylabel('\Delta Range (m)')

subplot(2,1,2)
plot([-5:0.5:185],RangeLimits(2,:,2),'k')
title('Standard Deviation \sigma')
legend('\sigma')
xlim([-5 185])
xlabel('Scan Angle \theta_1')
ylabel('Range (m)')

if TestNumber == 6 || TestNumber == 7 || TestNumber == 8
  %% Compare to Kim, 2015 Method
  DeltaMethods = NaN(3,381,2);
  DeltaMethods(1,:,:) = RangeLimits(1,:,:)-KimDistanceAnalysis(1,:,:);
  DeltaMethods(2,:,:) = RangeLimits(4,:,:)-KimDistanceAnalysis(4,:,:);
  DeltaMethods(3,:,:) = RangeLimits(5,:,:)-KimDistanceAnalysis(5,:,:);

  h(5) = figure(5);
  subplot(3,1,1)
  plot([-5:0.5:185],DeltaMethods(1,:,1),'-k',...
    [-5:0.5:185],DeltaMethods(1,:,2),'--k')
  title('Our Method \mu - Kim \mu')
  xlim([-5 185])
  xlabel('Scan Angle \theta_1')
  ylabel('\Delta Range (m)')
  legend('First Returns','Second Returns')

  subplot(3,1,2)
  plot([-5:0.5:185],DeltaMethods(2,:,1),'-k',...
    [-5:0.5:185],DeltaMethods(2,:,2),'--k')
  title('Our Method Upper Limit - Kim Upper Limit')
  xlim([-5 185])
  xlabel('Scan Angle \theta_1')
  ylabel('\Delta Range (m)')
  legend('First Returns','Second Returns')

  subplot(3,1,3)
  plot([-5:0.5:185],DeltaMethods(3,:,1),'-k',...
    [-5:0.5:185],DeltaMethods(3,:,2),'--k')
  title('Our Method Lower Limit - Kim Lower Limit')
  xlim([-5 185])
  xlabel('Scan Angle \theta_1')
  ylabel('\Delta Range (m)')
  legend('First Returns','Second Returns')
end

clear h
clear SaveName
clear pd
clear ii
clear i
clear DTG_Stamp
clear ElapsedTime
```

```
save(VariablesSaveName)
if TestNumber == 6
  save(RangeLimitsSaveName,'RangeLimits','TriDistINTEX6_Bin371')

elseif TestNumber == 7
  save(RangeLimitsSaveName,'RangeLimits')

elseif TestNumber == 8
  save(RangeLimitsSaveName,'RangeLimits','TriDistINTEX8_Bin187')

elseif TestNumber == 9

save(RangeLimitsSaveName,'RangeLimits','TriDistINTEX9_Bin120','TriDistI
NTEX9_Bin267')

elseif TestNumber == 11
  save(RangeLimitsSaveName,'RangeLimits')
end

end
```

B.2 Interference Identification

The script used to analyze the experimental testing data and identify occurrences of interference base on the testing data is presented below.

```
function [] = SICK_LMS531_Interference()
%Find point out of tolerance and given by RangeLimits vector for a
%SICK LMS531 detector

%Outputs:
  % Inst_f: n x 1 vector of the instantaneous rotational frequency
  % (n=number of scans)
    %C1: instantaneous rotational frequency (Hz)

  % Avg_f: scalar of the average rotational frequency (Hz)

  % StdDev_f: scalar of the standard deviation of the rotational
frequency (Hz)

  % OutOfToleranceCounter: 2 x 381 matrix that counts of the number of
return
  %out of tolerance by angle (rows) for first returns (1st column) and
second
  %returns (2nd column)

  % OutOfTolerancePoints: nn x 3 x 2 matrix of out of tolerance points.
  %The first and second pages are the first and second returns (nn =
  %number of out of tolerance points)
    %C1: erroneous target range
```

```
    %C2: scanner 1's angle to target
    %C3: rotation number


TestNumber = 6;  % 6 = INTEX6; 7 = INTEX7; 8 = INTEX8
NumberSigma = 5;   % The number of sigma deviations to calculate the
limits of normal operation.


INTEX_Directory = 'C:\InputYourFileDirectoryLocation';

if TestNumber == 6
     % Lidar 1 location
  x11 = 0;          %Lidar 1 x position (meters)
  y11 = 0;          %Lidar 1 y position (meters)
  % Lidar 2 (harassing lidar) Parameters
  x21 = -1.2;         %Origin x-axis coordinate of lidar 2 relative to
lidar 1 (meters)
  y21 = 0;         %Origin y-axis coordinate of lidar 2 relative to
lidar 1 (meters)

elseif TestNumber == 7
    % Lidar 1 location
  x11 = 0;          %Lidar 1 x position (meters)
  y11 = 0;          %Lidar 1 y position (meters)
  % Lidar 2 (harassing lidar) Parameters
  x21 = 1.4;         %Origin x-axis coordinate of lidar 2 relative to
lidar 1 (meters)
  y21 = -0.7;         %Origin y-axis coordinate of lidar 2 relative to
lidar 1 (meters)

elseif TestNumber == 8
    % Lidar 1 location
  x11 = 0;          %Lidar 1 x position (meters)
  y11 = 0;          %Lidar 1 y position (meters)
  % Lidar 2 (harassing lidar) Parameters
  x21 = 0;         %Origin x-axis coordinate of lidar 2 relative to
lidar 1 (meters)
  y21 = 1.6;         %Origin y-axis coordinate of lidar 2 relative to
lidar 1 (meters)

elseif TestNumber == 9 || TestNumber == 10
    % Lidar 1 location
  x11 = 0;          %Lidar 1 x position (meters)
  y11 = 0;          %Lidar 1 y position (meters)
  % Lidar 2 (harassing lidar) Parameters
  x21 = 1.4;         %Origin x-axis coordinate of lidar 2 relative to
lidar 1 (meters)
  y21 = -0.7;         %Origin y-axis coordinate of lidar 2 relative to
lidar 1 (meters)
      % Lidar 3 location
  x31 = 1.4;          %Lidar 3 x position (meters)
  y31 = 1.9;          %Lidar 3 y position (meters)
  % Lidar 4 (harassing lidar) Parameters
  x41 = -1.4;         %Origin 4-axis coordinate of lidar 2 relative to
lidar 1 (meters)
```

```
  y41 = 1.9;         %Origin 4-axis coordinate of lidar 2 relative to
lidar 1 (meters)


elseif TestNumber == 11 || TestNumber == 12 || TestNumber == 13 ||
TestNumber == 14
    % Lidar 1 location
  x11 = 0;          %Lidar 1 x position (meters)
  y11 = 0;          %Lidar 1 y position (meters)
  % Lidar 2 (harassing lidar) Parameters
  x21 = 1.4;         %Origin x-axis coordinate of lidar 2 relative to
lidar 1 (meters)
  y21 = -0.7;          %Origin y-axis coordinate of lidar 2 relative to
lidar 1 (meters)


end


  % load Distance Analysis
load(strcat(INTEX_Directory,'INTEX',num2str(TestNumber),'\INTEX',num2st
r(TestNumber),'_',num2str(NumberSigma),'sigma_DistanceAnalysis.mat'))


  % load Live file
load(strcat(INTEX_Directory,'INTEX',num2str(TestNumber),'\INTEX',num2st
r(TestNumber),'_Live.mat'))

SaveName =
string(['INTEX',num2str(TestNumber),'_',num2str(NumberSigma),'sigma_Int
erferenceAnalysis.mat']);
SaveFigName =
string(['INTEX',num2str(TestNumber),'_',num2str(NumberSigma),'sigma.fig
']);
ExperimentName = string(['INTEX',num2str(TestNumber)]);


AngleArray = deg2rad([-5:0.5:185].');    %Angle array in degrees from
0deg to 190deg in 0.5deg increments in radians
n = length(ElapsedTime);
ReturnsStats = Returns;
Returns(Returns==0) = NaN;        %replaces zero returns to NaN

%% Out of Tolerance Check

FirstInds = NaN(n,381);   %Indecies of points that are out of tolerance
SecondInds = NaN(n,381);
RangeLimitsTest = RangeLimits; %Prevents NaN values for second range
from preventing identification of out of tolerance points in test
RangeLimitsTest(isnan(RangeLimitsTest)) = 0; %Prevents NaN values for
second range from preventing identification of out of tolerance points
in test

if TestNumber == 6
  for ii = 1:381
    if ii == 371
      %Checks if the return is any of the trimodal distributions
```

```
      FirstInds(:,ii) = abs(sign(sign(TriDistINTEX6_Bin371(5,1) -
Returns(:,ii,1)) +...
        sign(TriDistINTEX6_Bin371(4,1) - Returns(:,ii,1))))...
        .*abs(sign(sign(TriDistINTEX6_Bin371(5,2) - Returns(:,ii,1))
+...
        sign(TriDistINTEX6_Bin371(4,2) - Returns(:,ii,1))))...
        .*abs(sign(sign(TriDistINTEX6_Bin371(5,3) - Returns(:,ii,1))
+...
        sign(TriDistINTEX6_Bin371(4,3) - Returns(:,ii,1))));

      SecondInds(:,ii) = abs(sign(sign(TriDistINTEX6_Bin371(5,1) -
Returns(:,ii,2)) +...
        sign(TriDistINTEX6_Bin371(4,1) - Returns(:,ii,2))))...
        .*abs(sign(sign(TriDistINTEX6_Bin371(5,2) - Returns(:,ii,2))
+...
        sign(TriDistINTEX6_Bin371(4,2) - Returns(:,ii,2))))...
        .*abs(sign(sign(TriDistINTEX6_Bin371(5,3) - Returns(:,ii,2))
+...
        sign(TriDistINTEX6_Bin371(4,3) - Returns(:,ii,2))));

    else
      FirstInds(:,ii) = abs(sign(sign(RangeLimitsTest(5,ii,1) -
Returns(:,ii,1)) +...
        sign(RangeLimitsTest(4,ii,1) - Returns(:,ii,1))));

      SecondInds(:,ii) = abs(sign(sign(RangeLimitsTest(5,ii,2) -
Returns(:,ii,2)) +...
        sign(RangeLimitsTest(4,ii,2) - Returns(:,ii,2))))...
        .*abs(sign(sign(RangeLimitsTest(5,ii,1) - Returns(:,ii,2)) +...
        sign(RangeLimitsTest(4,ii,1) - Returns(:,ii,2))));   %Checks if
the second return is within tolerance of the first or second return
average
    end
  end

elseif TestNumber == 7 || TestNumber == 11 || TestNumber == 12 ||
TestNumber == 13 || TestNumber == 14
  for ii = 1:381
    FirstInds(:,ii) = abs(sign(sign(RangeLimitsTest(5,ii,1) -
Returns(:,ii,1)) +...
      sign(RangeLimitsTest(4,ii,1) - Returns(:,ii,1))));

    SecondInds(:,ii) = abs(sign(sign(RangeLimitsTest(5,ii,2) -
Returns(:,ii,2)) +...
      sign(RangeLimitsTest(4,ii,2) - Returns(:,ii,2))))...
      .*abs(sign(sign(RangeLimitsTest(5,ii,1) - Returns(:,ii,2)) +...
      sign(RangeLimitsTest(4,ii,1) - Returns(:,ii,2))));   %Checks if
the second return is within tolerance of the first or second return
average
  end

elseif TestNumber == 8
  for ii = 1:381
    if ii == 187
      %Checks if the return is any of the bimodal distributions of
      %first returns and trimodal of second returns
```

```
      FirstInds(:,ii) = abs(sign(sign(TriDistINTEX8_Bin187(5,1) -
Returns(:,ii,1)) +...
        sign(TriDistINTEX8_Bin187(4,1) - Returns(:,ii,1))))...
        .*abs(sign(sign(TriDistINTEX8_Bin187(5,2) - Returns(:,ii,1))
+...
        sign(TriDistINTEX8_Bin187(4,2) - Returns(:,ii,1))));

      SecondInds(:,ii) = abs(sign(sign(TriDistINTEX8_Bin187(5,1) -
Returns(:,ii,2)) +...
        sign(TriDistINTEX8_Bin187(4,1) - Returns(:,ii,2))))...
        .*abs(sign(sign(TriDistINTEX8_Bin187(5,2) - Returns(:,ii,2))
+...
        sign(TriDistINTEX8_Bin187(4,2) - Returns(:,ii,2))))...
        .*abs(sign(sign(RangeLimitsTest(5,ii,2) - Returns(:,ii,2)) +...
        sign(RangeLimitsTest(4,ii,2) - Returns(:,ii,2))));

    else
      FirstInds(:,ii) = abs(sign(sign(RangeLimitsTest(5,ii,1) -
Returns(:,ii,1)) +...
        sign(RangeLimitsTest(4,ii,1) - Returns(:,ii,1))));

      SecondInds(:,ii) = abs(sign(sign(RangeLimitsTest(5,ii,2) -
Returns(:,ii,2)) +...
        sign(RangeLimitsTest(4,ii,2) - Returns(:,ii,2))))...
        .*abs(sign(sign(RangeLimitsTest(5,ii,1) - Returns(:,ii,2)) +...
        sign(RangeLimitsTest(4,ii,1) - Returns(:,ii,2))));   %Checks if
the second return is within tolerance of the first or second return
average
    end
  end

elseif TestNumber == 9 || TestNumber == 10
  for ii = 1:381
    if ii == 120
      %Checks if the return is any of the trimodal distributions
      FirstInds(:,ii) = abs(sign(sign(TriDistINTEX9_Bin120(5,1) -
Returns(:,ii,1)) +...
        sign(TriDistINTEX9_Bin120(4,1) - Returns(:,ii,1))))...
        .*abs(sign(sign(TriDistINTEX9_Bin120(5,2) - Returns(:,ii,1))
+...
        sign(TriDistINTEX9_Bin120(4,2) - Returns(:,ii,1))))...
        .*abs(sign(sign(TriDistINTEX9_Bin120(5,3) - Returns(:,ii,1))
+...
        sign(TriDistINTEX9_Bin120(4,3) - Returns(:,ii,1))));

      SecondInds(:,ii) = abs(sign(sign(TriDistINTEX9_Bin120(5,1) -
Returns(:,ii,2)) +...
        sign(TriDistINTEX9_Bin120(4,1) - Returns(:,ii,2))))...
        .*abs(sign(sign(TriDistINTEX9_Bin120(5,2) - Returns(:,ii,2))
+...
        sign(TriDistINTEX9_Bin120(4,2) - Returns(:,ii,2))))...
        .*abs(sign(sign(RangeLimitsTest(5,ii,2) - Returns(:,ii,2)) +...
        sign(RangeLimitsTest(4,ii,2) - Returns(:,ii,2))));

      FirstDeltaInds(:,ii) = sign(sign(TriDistINTEX9_Bin120(5,1) -
Returns(:,ii,1)) +...
        sign(TriDistINTEX9_Bin120(4,1) - Returns(:,ii,1)))...
```

```
        .*sign(sign(TriDistINTEX9_Bin120(5,2) - Returns(:,ii,1)) +...
        sign(TriDistINTEX9_Bin120(4,2) - Returns(:,ii,1)));

      SecondDeltaInds(:,ii) = sign(sign(TriDistINTEX9_Bin120(5,1) -
Returns(:,ii,2)) +...
        sign(TriDistINTEX9_Bin120(4,1) - Returns(:,ii,2)))...
        .*sign(sign(TriDistINTEX9_Bin120(5,2) - Returns(:,ii,2) +...
        sign(TriDistINTEX9_Bin120(4,2) - Returns(:,ii,2))))...
        .*sign(sign(RangeLimitsTest(5,ii,2) - Returns(:,ii,2)) +...
        sign(RangeLimitsTest(4,ii,2) - Returns(:,ii,2)));   %Checks if
the second return is within tolerance of the first or second return
average

    elseif ii == 267
      %Checks if the return is any of the trimodal distributions
      FirstInds(:,ii) = abs(sign(sign(TriDistINTEX9_Bin267(5,1) -
Returns(:,ii,1)) +...
        sign(TriDistINTEX9_Bin267(4,1) - Returns(:,ii,1))))...
        .*abs(sign(sign(TriDistINTEX9_Bin267(5,2) - Returns(:,ii,1))
+...
        sign(TriDistINTEX9_Bin267(4,2) - Returns(:,ii,1))))...
        .*abs(sign(sign(TriDistINTEX9_Bin267(5,3) - Returns(:,ii,1))
+...
        sign(TriDistINTEX9_Bin267(4,3) - Returns(:,ii,1))));

      SecondInds(:,ii) = abs(sign(sign(TriDistINTEX9_Bin267(5,1) -
Returns(:,ii,2)) +...
        sign(TriDistINTEX9_Bin267(4,1) - Returns(:,ii,2))))...
        .*abs(sign(sign(TriDistINTEX9_Bin267(5,2) - Returns(:,ii,2))
+...
        sign(TriDistINTEX9_Bin267(4,2) - Returns(:,ii,2))))...
        .*abs(sign(sign(RangeLimitsTest(5,ii,2) - Returns(:,ii,2)) +...
        sign(RangeLimitsTest(4,ii,2) - Returns(:,ii,2))));

      FirstDeltaInds(:,ii) = sign(sign(TriDistINTEX9_Bin267(5,1) -
Returns(:,ii,1)) +...
        sign(TriDistINTEX9_Bin267(4,1) - Returns(:,ii,1)))...
        .*sign(sign(TriDistINTEX9_Bin267(5,2) - Returns(:,ii,1)) +...
        sign(TriDistINTEX9_Bin267(4,2) - Returns(:,ii,1)));

      SecondDeltaInds(:,ii) = sign(sign(TriDistINTEX9_Bin267(5,1) -
Returns(:,ii,2)) +...
        sign(TriDistINTEX9_Bin267(4,1) - Returns(:,ii,2)))...
        .*sign(sign(TriDistINTEX9_Bin267(5,2) - Returns(:,ii,2) +...
        sign(TriDistINTEX9_Bin267(4,2) - Returns(:,ii,2))))...
        .*sign(sign(RangeLimitsTest(5,ii,2) - Returns(:,ii,2)) +...
        sign(RangeLimitsTest(4,ii,2) - Returns(:,ii,2)));   %Checks if
the second return is within tolerance of the first or second return
average

    else
      FirstInds(:,ii) = abs(sign(sign(RangeLimitsTest(5,ii,1) -
Returns(:,ii,1)) +...
        sign(RangeLimitsTest(4,ii,1) - Returns(:,ii,1))));

      SecondInds(:,ii) = abs(sign(sign(RangeLimitsTest(5,ii,2) -
Returns(:,ii,2)) +...
```

```
        sign(RangeLimitsTest(4,ii,2) - Returns(:,ii,2))))...
        .*abs(sign(sign(RangeLimitsTest(5,ii,1) - Returns(:,ii,2)) +...
        sign(RangeLimitsTest(4,ii,1) - Returns(:,ii,2))));   %Checks if
the second return is within tolerance of the first or second return
average

      FirstDeltaInds(:,ii) = sign(sign(RangeLimitsTest(5,ii,1) -
Returns(:,ii,1)) +...
        sign(RangeLimitsTest(4,ii,1) - Returns(:,ii,1)));

      SecondDeltaInds(:,ii) = sign(sign(RangeLimitsTest(5,ii,2) -
Returns(:,ii,2)) +...
        sign(RangeLimitsTest(4,ii,2) - Returns(:,ii,2)))...
        .*sign(sign(RangeLimitsTest(5,ii,1) - Returns(:,ii,2)) +...
        sign(RangeLimitsTest(4,ii,1) - Returns(:,ii,2)));   %Checks if
the second return is within tolerance of the first or second return
average
    end
  end
end

Inds = cat(3,FirstInds,SecondInds);

Inds(isnan(Inds)) = 0;
InterferencePointCount = sum(Inds, 'all');
NotInterferenceCount = sum(Inds == 0,'all');
Check = InterferencePointCount + NotInterferenceCount - n*381*2;
% Should be equal to zero

OutOfTolerancePoints = Inds.*Returns;
OutOfTolerancePointsStats = OutOfTolerancePoints;
OutOfTolerancePoints(OutOfTolerancePoints==0) = NaN;        %replaces
zero returns to NaN
InTolerancePoints = (~Inds).*Returns;
InTolerancePointsStats = InTolerancePoints;
InTolerancePoints(InTolerancePoints==0) = NaN;        %replaces zero
returns to NaN

% Convert to Cartesian
TempOutOfTolerancePointsCart = NaN(381,4,n);
OutOfTolerancePointsCart = NaN(n*381,4);
TempInTolerancePointsCart = NaN(381,4,n);
InTolerancePointsCart = NaN(n*381,4);

for i = 1:n


[TempOutOfTolerancePointsCart(:,1,i),TempOutOfTolerancePointsCart(:,2,i
)] = pol2cart(AngleArray,OutOfTolerancePoints(i,:,1)');

[TempOutOfTolerancePointsCart(:,3,i),TempOutOfTolerancePointsCart(:,4,i
)] = pol2cart(AngleArray,OutOfTolerancePoints(i,:,2)');
  [TempInTolerancePointsCart(:,1,i),TempInTolerancePointsCart(:,2,i)] =
pol2cart(AngleArray,InTolerancePoints(i,:,1)');
  [TempInTolerancePointsCart(:,3,i),TempInTolerancePointsCart(:,4,i)] =
pol2cart(AngleArray,InTolerancePoints(i,:,2)');
```

```
end

OutOfTolerancePointsCart =
num2cell(TempOutOfTolerancePointsCart,[1,2]);
OutOfTolerancePointsCart = vertcat(OutOfTolerancePointsCart{:});
InTolerancePointsCart = num2cell(TempInTolerancePointsCart,[1,2]);
InTolerancePointsCart = vertcat(InTolerancePointsCart{:});

TempFirstOutOfTolerancePointsPol = NaN(n,3,381);
TempSecondOutOfTolerancePointsPol = NaN(n,3,381);
TempFirstInTolerancePointsPol = NaN(n,3,381);
TempSecondInTolerancePointsPol = NaN(n,3,381);

% Convert to Polar (radians on 1st column, degrees in third column
for i = 1:381


TempFirstOutOfTolerancePointsPol(:,:,i)=[ones(n,1).*AngleArray(i),OutOf
TolerancePoints(:,i,1),ones(n,1).*AngleArrayDeg(i)];
  TempSecondOutOfTolerancePointsPol(:,:,i) =
[ones(n,1).*AngleArray(i),OutOfTolerancePoints(:,i,2),ones(n,1).*AngleA
rrayDeg(i)];
  TempFirstInTolerancePointsPol(:,:,i) =
[ones(n,1).*AngleArray(i),InTolerancePoints(:,i,1),ones(n,1).*AngleArra
yDeg(i)];
  TempSecondInTolerancePointsPol(:,:,i) =
[ones(n,1).*AngleArray(i),InTolerancePoints(:,i,2),ones(n,1).*AngleArra
yDeg(i)];

end

FirstOutOfTolerancePointsPol =
num2cell(TempFirstOutOfTolerancePointsPol,[1,2]);
FirstOutOfTolerancePointsPol =
vertcat(FirstOutOfTolerancePointsPol{:});
SecondOutOfTolerancePointsPol =
num2cell(TempSecondOutOfTolerancePointsPol,[1,2]);
SecondOutOfTolerancePointsPol =
vertcat(SecondOutOfTolerancePointsPol{:});
OutOfTolerancePointsPol =
cat(3,FirstOutOfTolerancePointsPol,SecondOutOfTolerancePointsPol);

FirstInTolerancePointsPol =
num2cell(TempFirstInTolerancePointsPol,[1,2]);
FirstInTolerancePointsPol = vertcat(FirstInTolerancePointsPol{:});
SecondInTolerancePointsPol =
num2cell(TempSecondInTolerancePointsPol,[1,2]);
SecondInTolerancePointsPol = vertcat(SecondInTolerancePointsPol{:});
InTolerancePointsPol =
cat(3,FirstInTolerancePointsPol,SecondInTolerancePointsPol);


% Distance Analysis Points
RangeLimitsCart = NaN(381,4);
[RangeLimitsCart(:,1),RangeLimitsCart(:,2)] =...
  pol2cart(AngleArray,RangeLimits(1,:,1)');
[RangeLimitsCart(:,3),RangeLimitsCart(:,4)] =...
```

```
  pol2cart(AngleArray,RangeLimits(1,:,2)');

if TestNumber == 9 || TestNumber == 10

  figure(1)

  plot(x11,y11,'bo',x21,y21,'ko',x31,y31,'mo',x41,y41,'co',...
    InTolerancePointsCart(:,1),InTolerancePointsCart(:,2),'g.',...

OutOfTolerancePointsCart(:,1),OutOfTolerancePointsCart(:,2),'r.',...

OutOfTolerancePointsCart(:,3),OutOfTolerancePointsCart(:,4),'r.',...
    x11,y11,'bo',x21,y21,'ko',x31,y31,'mo',x41,y41,'co')
  legend('Lidar 1','Lidar 2')
  xlabel('Distance (m)')
  ylabel('Distance (m)')
  xlim([-6 6])
  ylim([-1 6])


else
  figure(1)

  plot(x11,y11,'bo',x21,y21,'ko',...
    InTolerancePointsCart(:,1),InTolerancePointsCart(:,2),'g.',...

OutOfTolerancePointsCart(:,1),OutOfTolerancePointsCart(:,2),'r.',...

OutOfTolerancePointsCart(:,3),OutOfTolerancePointsCart(:,4),'r.',...
    x11,y11,'bo',x21,y21,'ko')
  legend('Lidar 1','Lidar 2')
  xlabel('Distance (m)')
  ylabel('Distance (m)')
  xlim([-6 6])
  ylim([-1 6])

end

% % Uncomment to plot upper and lower limits by angle
% RangeLimitsCartMin = NaN(381,4);
% [RangeLimitsCartMin(:,1),RangeLimitsCartMin(:,2)] =...
%   pol2cart(AngleArray,RangeLimits(5,:,1)');
% [RangeLimitsCartMin(:,3),RangeLimitsCartMin(:,4)] =...
%   pol2cart(AngleArray,RangeLimits(5,:,2)');
%
% RangeLimitsCartMax = NaN(381,4);
% [RangeLimitsCartMax(:,1),RangeLimitsCartMax(:,2)] =...
%   pol2cart(AngleArray,RangeLimits(4,:,1)');
% [RangeLimitsCartMax(:,3),RangeLimitsCartMax(:,4)] =...
%   pol2cart(AngleArray,RangeLimits(4,:,2)');
%
% plot(RangeLimitsCartMax(:,1), RangeLimitsCartMax(:,2),'b.',...
%   RangeLimitsCartMax(:,3), RangeLimitsCartMax(:,4),'m.',...
%   RangeLimitsCartMin(:,1), RangeLimitsCartMin(:,2),'b.',...
%   RangeLimitsCartMin(:,3), RangeLimitsCartMin(:,4),'m.')
```

```
%% Interference Analysis
ReturnsTotal = sum(~isnan(Returns), 'all');
FirstReturnsTotal = sum(~isnan(Returns(:,:,1)), 'all');
SecondReturnsTotal = sum(~isnan(Returns(:,:,2)), 'all');
FirstReturnsTotalByRow = sum(~isnan(Returns(:,:,1)), 2);
SecondReturnsTotalByRow = sum(~isnan(Returns(:,:,2)), 2);


% DirectInterferenceAngles =
% sign(sign(diff(RangeLimits(1,:,1))-.05)+1); %Tool for finding
% direct interference limits
OutOfTolerancePointsCountByRow = sum(~isnan(OutOfTolerancePoints), 2);
TotalFirstInterference = sum(~isnan(OutOfTolerancePoints(:,:,1)),
'all');
TotalSecondInterference = sum(~isnan(OutOfTolerancePoints(:,:,2)),
'all');
OutOfTolerancePointsCountByRowFirst =
sum(~isnan(OutOfTolerancePoints(:,:,1)), 2);
OutOfTolerancePointsCountByRowSecond =
sum(~isnan(OutOfTolerancePoints(:,:,2)), 2);

if TestNumber == 6
  DirectInterferencePoints = OutOfTolerancePoints(:,370:381,:);
  ReflectedInterferencePoints = OutOfTolerancePoints(:,1:369,:);

elseif TestNumber == 7 || TestNumber == 11 || TestNumber == 12 ||
TestNumber == 13 || TestNumber == 14
  DirectInterferencePoints = NaN(1,1,2);
  ReflectedInterferencePoints = OutOfTolerancePoints;

elseif TestNumber ==8
  DirectInterferencePoints = OutOfTolerancePoints(:,183:203,:);
  ReflectedInterferencePoints = OutOfTolerancePoints(:,[1:182
204:381],:);

elseif TestNumber == 9 || TestNumber == 10
  DirectInterferencePoints = OutOfTolerancePoints(:,[116:120
262:266],:);
  ReflectedInterferencePoints = OutOfTolerancePoints(:,[1:115 121:261
267:381],:);

end

% Direct Interference Analysis
DirectInterferenceCount = sum(~isnan(DirectInterferencePoints),'all');
DirectInterferenceCountByRow =
sum(~isnan(DirectInterferencePoints(:,:,1)), 2)...
  +sum(~isnan(DirectInterferencePoints(:,:,2)), 2);
DirectInterferenceCountByRowFirst =
sum(~isnan(DirectInterferencePoints(:,:,1)), 2);
DirectInterferenceCountByRowSecond =
sum(~isnan(DirectInterferencePoints(:,:,2)), 2);

% Reflected Interference Analysis
ReflectedInterferenceCount =
sum(~isnan(ReflectedInterferencePoints),'all');
```

```
ReflectedInterferenceCountByRow =
sum(~isnan(ReflectedInterferencePoints(:,:,1)), 2)...
  +sum(~isnan(ReflectedInterferencePoints(:,:,2)), 2);
ReflectedInterferenceCountByRowFirst =
sum(~isnan(ReflectedInterferencePoints(:,:,1)), 2);
ReflectedInterferenceCountByRowSecond =
sum(~isnan(ReflectedInterferencePoints(:,:,2)), 2);

%Average Statistics
AvgPulsePerRotation = 381;   %Gives the average number of pulses per
rotation
AvgReturnsPerRotation = ReturnsTotal/n;   %Gives the average number of
pulses per rotation
AvgFirstReturnsPerRotation = FirstReturnsTotal/n;   %Gives the average
number of pulses per rotation
AvgSecondReturnsPerRotation = SecondReturnsTotal/n;   %Gives the
average number of pulses per rotation


AvgDirectInterference = mean(DirectInterferenceCountByRow);  %Gives the
average direct interfering pulses
AvgDirectInterferenceFirst = mean(DirectInterferenceCountByRowFirst);
%Gives the average direct interfering pulses
AvgDirectInterferenceSecond = mean(DirectInterferenceCountByRowSecond);
%Gives the average direct interfering pulses

AvgReflectInterferece = mean(ReflectedInterferenceCountByRow);  %Gives
the average fraction of reflection interference pulse
AvgReflectInterfereceFirst =
mean(ReflectedInterferenceCountByRowFirst);  %Gives the average
fraction of reflection interference pulse
AvgReflectInterfereceSecond =
mean(ReflectedInterferenceCountByRowSecond);  %Gives the average
fraction of reflection interference pulse

AvgInterference = mean(OutOfTolerancePointsCountByRow); %Gives the
average fraction of all interference pulses
AvgInterferenceFirst = mean(OutOfTolerancePointsCountByRowFirst);
%Gives the average fraction of all interference pulses
AvgInterferenceSecond = mean(OutOfTolerancePointsCountByRowSecond);
%Gives the average fraction of all interference pulses

AvgFractionInterference =
mean(OutOfTolerancePointsCountByRow)/AvgPulsePerRotation; %Gives the
average fraction of all interference pulses
AvgFractionInterferenceFirst =
mean(OutOfTolerancePointsCountByRowFirst)/AvgPulsePerRotation; %Gives
the average fraction of all interference pulses
AvgFractionInterferenceSecond =
mean(OutOfTolerancePointsCountByRowSecond)/AvgPulsePerRotation; %Gives
the average fraction of all interference pulses

AverageStatistics = table(ExperimentName, NumberSigma,
AvgPulsePerRotation,...
  AvgReturnsPerRotation,
AvgFirstReturnsPerRotation,AvgSecondReturnsPerRotation,...
```

```
  AvgDirectInterference,AvgDirectInterferenceFirst,
AvgDirectInterferenceSecond, ...
  AvgReflectInterferece, AvgReflectInterfereceFirst,
AvgReflectInterfereceSecond,...
  AvgInterference, AvgInterferenceFirst, AvgInterferenceSecond,...
  AvgFractionInterference, AvgFractionInterferenceFirst,
AvgFractionInterferenceSecond);

%Total Statistics
TotalPulses = n*381;                %Total Number of pulses
TotalInterference = sum(OutOfTolerancePointsCountByRow,'all');
TotalDirect = DirectInterferenceCount;       %Total Number of pulses
TotalDirectFirst = sum(DirectInterferenceCountByRowFirst,'all');
TotalDirectSecond = sum(DirectInterferenceCountByRowSecond,'all');

TotalReflectionInterference = ReflectedInterferenceCount;
TotalReflectedFirst = sum(ReflectedInterferenceCountByRowFirst,'all');
TotalReflectedSecond =
sum(ReflectedInterferenceCountByRowSecond,'all');

FactionDirect = TotalDirect/ReturnsTotal;
FractionTotalReflected = TotalReflectionInterference/ReturnsTotal;
FractionTotalInterference =
(TotalReflectionInterference+TotalDirect)/ReturnsTotal;

TotalStatistics = table(ExperimentName, NumberSigma, TotalPulses, ...
  ReturnsTotal, FirstReturnsTotal, SecondReturnsTotal,...
  TotalInterference,TotalFirstInterference,TotalSecondInterference, ...
  TotalDirect, TotalDirectFirst, TotalDirectSecond, ...
  TotalReflectionInterference, TotalReflectedFirst,
TotalReflectedSecond, ...
  FactionDirect, FractionTotalReflected, FractionTotalInterference);


save(SaveName)
savefig(SaveFigName)

end
```

B.3 Monte Carlo

The script for the Monte Carlo simulation of lidar interference is presented below. Additionally, this script was used to generate the intersection point density by increasing the two scanners' maximum range to 10^9 and plotting a bivariate histogram of the intersection points.

```
function [] = Interference_Monte_Carlo()
% v4 designed for parallel computing

%Intersection of two lines
%  Ref: https://blogs.mathworks.com/loren/2011/08/29/intersecting-
lines/?s_cid=fb_wall_10-21-11_loren_lines
% Addition of adjustable scan limits, direct interference
% Updated logic to ensure within scan limits

% Output:
  %Statistics: matrix with the following columns:
    %C1: The number of pulses transmitted per rotation with each row a
    %new rotation
    %C2: The number of direct interference events per rotation with
each row a
    %new rotation
    %C3: The number of discrete angular orientations of scanner 1 that
    %both beams are intersecting
    %C4: The number of reflected interference events
    %C5: The number of reflected interference events less those that
    %fall in deadspace due to detector response time
    %C6: Fraction of direct interference events over total pulses
    %C7: Fraction of reflected interference events over total pulses
    %C8: Fraction of total interference events over total pulses

  %IntersectonPoints: matrix of intersection points that occurred
between
  % beams 1 and 2 with the following columns:
    %C1: X coordinate of intersection point
    %C2: y coordinate of intersection point
    %C3: Scanner 1 rotation
    %C4: sequential pulse number for the rotation

  %ReflectedInterferentPoints: matrix of reflected interference points
  %which are defined as intersection points that fall within the
  %tolerance of a target's geometry that with columns:
    %C1: X coordinate of intersection point
    %C2: y coordinate of intersection point
    %C3: Scanner 1 rotation
    %C4: sequential pulse number for the rotation

  %DirectErroneousPoints: matrix of erroneous ranging points that
  %are generated from a random range (unknown when scanner 2's pulse
  %transmitted) within the scanner's radiometric limits and azimuth of
  % a direct interference event with columns:
    %C1: X coordinate of erroneous point
    %C2: y coordinate of erroneous point
    %C3: Scanner 1 rotation
    %C4: sequential pulse number for the rotation

  %ReflectedErroneousPoints: matrix of erroneous ranging points that
  %are generated from a random range (unknown when scanner 2's pulse
  %transmitted) within the scanner's radiometric limits and azimuth of
  % a reflected interference event with columns:
    %C1: X coordinate of erroneous point
    %C2: y coordinate of erroneous point
    %C3: Scanner 1 rotation
```

```
    %C4: sequential pulse number for the rotation

  %ReflectedDeadspacePoints: matrix of erroneous ranging points that
  %are generated from a random range (unknown when scanner 2's pulse
  %transmitted) within the scanner's radiometric limits and azimuth of
  % a reflected interference but would go undetected due to the
  % receiver's temporal resolution limits event with columns:
    %C1: X coordinate of erroneous point
    %C2: y coordinate of erroneous point
    %C3: Scanner 1 rotation
    %C4: sequential pulse number for the rotation

%% Save as name

TestNumber = 8;
ExperimentName = string(['Monte_Carlo_INTEX',num2str(TestNumber)]);
VariablesName =
string(['Monte_Carlo_INTEX',num2str(TestNumber),'.mat']);
FigName = string(['Monte_Carlo_INTEX',num2str(TestNumber),'.fig']);
GraphicName =
string(['Monte_Carlo_INTEX',num2str(TestNumber),'.jpeg']);

if TestNumber == 6

  n = 8998;
  % Experiment Specific
  x11 = 0;          %Lidar 1 x position (meters)
  y11 = 0;          %Lidar 1 y position (meters)
  azimuth_of_scan_1 = deg2rad(90);  %Direction the lidar is facing

  % Experiment Specific
  x21 = -1.2;       %Origin x-axis coordinate of lidar 2 relative to
lidar 1 (meters)
  y21 = 0;        %Origin y-axis coordinate of lidar 2 relative to
lidar 1 (meters)
  azimuth_of_scan_2 = deg2rad(90);  %Direction the lidar is facing
  % Experimentally Fit
  tolerance = 0.022;    %Tolerance +/- around walls for intersections
  width_lidar_2 = .075;  %Width of lidar 2 (m)

elseif TestNumber == 7

  n = 8998;
  % Experiment Specific
  x11 = 0;          %Lidar 1 x position (meters)
  y11 = 0;          %Lidar 1 y position (meters)
  azimuth_of_scan_1 = deg2rad(90);  %Direction the lidar is facing
  width_lidar_2 = .155;  %Width of lidar 2 (m)

  % Experiment Specific
  x21 = 1.4;       %Origin x-axis coordinate of lidar 2 relative to
lidar 1 (meters)
  y21 = -0.7;        %Origin y-axis coordinate of lidar 2 relative to
lidar 1 (meters)
  azimuth_of_scan_2 = deg2rad(90);  %Direction the lidar is facing
  % Experimentally Fit
  tolerance = 0.0055;    %Tolerance +/- around walls for intersections
```

```
  width_lidar_2 = .155;  %Width of lidar 2 (m)

elseif TestNumber == 8

  n = 8998;
  % Experiment Specific
  x11 = 0;          %Lidar 1 x position (meters)
  y11 = 0;          %Lidar 1 y position (meters)
  azimuth_of_scan_1 = deg2rad(90);  %Direction the lidar is facing

  % Experiment Specific
  x21 = 0;       %Origin x-axis coordinate of lidar 2 relative to lidar
1 (meters)
  y21 = 1.6;        %Origin y-axis coordinate of lidar 2 relative to
lidar 1 (meters)
  azimuth_of_scan_2 = deg2rad(270);  %Direction the lidar is facing
  % Experimentally Fit
  tolerance = 0.0055;    %Tolerance +/- around walls for intersections
  width_lidar_2 = .155;  %Width of lidar 2 (m)

  elseif TestNumber == 11

  n = 8997;
  % Experiment Specific
  x11 = 0;          %Lidar 1 x position (meters)
  y11 = 0;          %Lidar 1 y position (meters)
  azimuth_of_scan_1 = deg2rad(90);  %Direction the lidar is facing

  % Experiment Specific
  x21 = 1.4;       %Origin x-axis coordinate of lidar 2 relative to
lidar 1 (meters)
  y21 = -0.7;        %Origin y-axis coordinate of lidar 2 relative to
lidar 1 (meters)
  azimuth_of_scan_2 = deg2rad(90);  %Direction the lidar is facing
  % Experimentally Fit
  tolerance = 0.022;    %Tolerance +/- around walls for intersections
  width_lidar_2 = .155;  %Width of lidar 2 (m)

end


%% Constants
c = 2.998*10^8;         %Speed of light (m/s)

%% Lidar 1 (victim lidar) Parameters
% Experimentally Fit
f_scan_1_std = .1;    %Standard deviation
reciever_delay_time = 1.66*10^-9;  %Delay before receiver can detect a
second pulse (seconds)

% Manufacturer Specific
R_1max = 80;        %Max range of lidar 1 [victim lidar] (meters)
PRF_1 = 36000;       %Pulse repetition frequency of lidar 1(Hz)
f_scan_1_mu = 50;      %Mean of f_scan, assuming normal distribution of
f_scan drift
scan_angle_1 = deg2rad(190);    %Scanning angle of lidar receiver
width_lidar_1 = .155;   %Width of lidar 1 (m)
```

```
%Calculated
f_scan_1 = (randn(n,1)*f_scan_1_std)+f_scan_1_mu;  %Distribution of
f_scan_1 frequencies
number_of_scan_points_1 = PRF_1./f_scan_1;     %Number of points
scanned by lidar 1 in a rotation **Set lidar 1's scan freq here by
chosing index value
theta_inc1 = 2*pi()./number_of_scan_points_1;    %Increment of
theta_1_prime for each look
reciever_delay_distance = c*reciever_delay_time;

%% Lidar 2 (harassing lidar) Parameters
% Experimentally Fit
f_scan_2_std = .1;  %Standard deviation

% Manufacturer Specific
R_2max = 80;      %Max range of lidar 2 (meters)
PRF_2 = 36000;     %Pulse repetition frequency of lidar 2(Hz)
f_scan_2_mu = 50;    %Mean of f_scan, assuming normal distribution of
f_scan drift
scan_angle_2 = deg2rad(190);  %Scanning angle of lidar receiver
width_lidar_2 = .155;  %Width of lidar 2 (m)

%Calculated
f_scan_2 = (randn(n,1)*f_scan_2_std)+f_scan_2_mu;  %Distribution of
f_scan1 frequencies
number_of_scan_points_2 = PRF_2./f_scan_2;
theta_inc2 = 2*pi()./number_of_scan_points_2;    %Increment of
theta_2_prime for each look
ratio_PRF2_1 = PRF_2/PRF_1;   %Ratio of PRF 2 to PRF 1

% theta_2_prime_0 for each rotation is assumed to be a uniform
distribution due to
% drift is scanner 2's rotational frequency
theta_2_prime_0_min = 0;
theta_2_prime_0_max = 2*pi();
theta_2_prime_0 = theta_2_prime_0_min+rand(n,1)*(theta_2_prime_0_max-
theta_2_prime_0_min);

%% Obstacles


if TestNumber == 11
  % Experiment Dependent
  % Wall 1 is the western vertical wall
  startW1 = [-3.5, -1]; %Start point for wall
  thetaW1 = pi()/2;    %Direction wall runs measured as on a unit
circle
  lengthW1 = 1.5;     %Length of wall (meters)

  % Wall 2 is the northern horizontal wall
  startW2 = [-3.5, 0.5]; %Start point for wall
  thetaW2 = 0;      %Direction wall runs measured as on a unit circle
  lengthW2 = 5.0;     %Length of wall (meters)

  % Wall 3 is the eastern vertical wall
```

```
  startW3 = [1.5, 0.5];  %Start point for wall
  thetaW3 = 3*pi()/2;   %Direction wall runs measured as on a unit
circle
  lengthW3 = 3.8;     %Length of wall (meters)

  % Wall 4 is the southern horizontal wall (input 0 for length if not
used)

  startW4 = [1.5, -1]; %Start point for wall
  thetaW4 = pi();     %Direction wall runs measured as on a unit circle
  lengthW4 = 0;      %Length of wall (meters)

else
  % Experiment Dependent
  % Wall 1 is the western vertical wall
  startW1 = [-2.5, -0.8]; %Start point for wall
  thetaW1 = pi()/2;    %Direction wall runs measured as on a unit
circle
  lengthW1 = 3.8;     %Length of wall (meters)

  % Wall 2 is the northern horizontal wall
  startW2 = [-2.5, 3.0]; %Start point for wall
  thetaW2 = 0;      %Direction wall runs measured as on a unit circle
  lengthW2 = 5.0;     %Length of wall (meters)

  % Wall 3 is the eastern vertical wall

  startW3 = [2.5, 3.0];  %Start point for wall
  thetaW3 = 3*pi()/2;   %Direction wall runs measured as on a unit
circle
  lengthW3 = 3.8;     %Length of wall (meters)

  % Wall 4 is the southern horizontal wall (input 0 for length if not
used)

  startW4 = [2.5, -0.8]; %Start point for wall
  thetaW4 = pi();     %Direction wall runs measured as on a unit circle
  lengthW4 = 0;      %Length of wall (meters)
end
% Calculated
%  Wall 1
[startW1rt(1), startW1rt(2)] = pol2cart(thetaW1+pi(),tolerance);
%Relative start point corrected for with tolerance
startW1t = [startW1rt(1)+startW1(1), startW1rt(2)+startW1(2)];   %Start
point corrected for with tolerance

[endW1r(1), endW1r(2)] = pol2cart(thetaW1,lengthW1+2*tolerance);
%Relative end point with tolerance

[W1r(1,1) , W1r(2,1)] = pol2cart(thetaW1+pi()/2,tolerance); %Relative
coordinates of corner of wall
[W1r(1,2) , W1r(2,2)] = pol2cart(thetaW1+pi()/2,tolerance); %Relative
coordinates of corner of wall
[W1r(1,3) , W1r(2,3)] = pol2cart(thetaW1-pi()/2,tolerance); %Relative
coordinates of corner of wall
[W1r(1,4) , W1r(2,4)] = pol2cart(thetaW1-pi()/2,tolerance); %Relative
coordinates of corner of wall
```

```
wall1(:,1) = [W1r(1,1)+startW1t(1) W1r(1,2)+endW1r(1)+startW1t(1) ...
       W1r(1,3)+endW1r(1)+startW1t(1) W1r(1,4)+startW1t(1)];
wall1(:,2) = [W1r(2,1)+startW1t(2), W1r(2,2)+endW1r(2)+startW1t(2), ...
       W1r(2,3)+endW1r(2)+startW1t(2), W1r(2,4)+startW1t(2)];

% line_wall1 = [wall1(1,1) wall1(1,2); wall1(2,1) wall1(2,2)];

%  Wall 2
[startW2rt(1), startW2rt(2)] = pol2cart(thetaW2+pi(),tolerance);
%Relative start point corrected for with tolerance
startW2t = [startW2rt(1)+startW2(1) startW2rt(2)+startW2(2)];   %Start
point corrected for with tolerance

[endW2r(1), endW2r(2)] = pol2cart(thetaW2,lengthW2+2*tolerance);
%Relative end point with tolerance

[W2r(1,1) , W2r(2,1)] = pol2cart(thetaW2+pi()/2,tolerance); %Relative
coordinates of corner of wall
[W2r(1,2) , W2r(2,2)] = pol2cart(thetaW2+pi()/2,tolerance); %Relative
coordinates of corner of wall
[W2r(1,3) , W2r(2,3)] = pol2cart(thetaW2-pi()/2,tolerance); %Relative
coordinates of corner of wall
[W2r(1,4) , W2r(2,4)] = pol2cart(thetaW2-pi()/2,tolerance); %Relative
coordinates of corner of wall

wall2(:,1) = [W2r(1,1)+startW2t(1) W2r(1,2)+endW2r(1)+startW2t(1) ...
       W2r(1,3)+endW2r(1)+startW2t(1) W2r(1,4)+startW2t(1)];
wall2(:,2) = [W2r(2,1)+startW2t(2), W2r(2,2)+endW2r(2)+startW2t(2), ...
       W2r(2,3)+endW2r(2)+startW2t(2), W2r(2,4)+startW2t(2)];

% line_wall2 = [wall2(1,1) wall2(1,2); wall2(2,1) wall2(2,2)];

%  Wall 3
[startW3rt(1), startW3rt(2)] = pol2cart(thetaW3+pi(),tolerance);
%Relative start point corrected for with tolerance
startW3t = [startW3rt(1)+startW3(1) startW3rt(2)+startW3(2)];   %Start
point corrected for with tolerance

[endW3r(1), endW3r(2)] = pol2cart(thetaW3,lengthW3+2*tolerance);
%Relative end point with tolerance

[W3r(1,1) , W3r(2,1)] = pol2cart(thetaW3+pi()/2,tolerance); %Relative
coordinates of corner of wall
[W3r(1,2) , W3r(2,2)] = pol2cart(thetaW3+pi()/2,tolerance); %Relative
coordinates of corner of wall
[W3r(1,3) , W3r(2,3)] = pol2cart(thetaW3-pi()/2,tolerance); %Relative
coordinates of corner of wall
[W3r(1,4) , W3r(2,4)] = pol2cart(thetaW3-pi()/2,tolerance); %Relative
coordinates of corner of wall

wall3(:,1) = [W3r(1,1)+startW3t(1) W3r(1,2)+endW3r(1)+startW3t(1) ...
       W3r(1,3)+endW3r(1)+startW3t(1) W3r(1,4)+startW3t(1)];
wall3(:,2) = [W3r(2,1)+startW3t(2), W3r(2,2)+endW3r(2)+startW3t(2), ...
       W3r(2,3)+endW3r(2)+startW3t(2), W3r(2,4)+startW3t(2)];

% line_wall3 = [wall3(1,1) wall3(1,2); wall3(2,1) wall3(2,2)];
```

```
%  Wall 4
[startW4rt(1), startW4rt(2)] = pol2cart(thetaW4+pi(),tolerance);
%Relative start point corrected for with tolerance
startW4t = [startW4rt(1)+startW4(1) startW4rt(2)+startW4(2)];   %Start
point corrected for with tolerance

[endW4r(1), endW4r(2)] = pol2cart(thetaW4,lengthW4+2*tolerance);
%Relative end point with tolerance

[W4r(1,1) , W4r(2,1)] = pol2cart(thetaW4+pi()/2,tolerance); %Relative
coordinates of corner of wall
[W4r(1,2) , W4r(2,2)] = pol2cart(thetaW4+pi()/2,tolerance); %Relative
coordinates of corner of wall
[W4r(1,3) , W4r(2,3)] = pol2cart(thetaW4-pi()/2,tolerance); %Relative
coordinates of corner of wall
[W4r(1,4) , W4r(2,4)] = pol2cart(thetaW4-pi()/2,tolerance); %Relative
coordinates of corner of wall

wall4(:,1) = [W4r(1,1)+startW4t(1) W4r(1,2)+endW4r(1)+startW4t(1) ...
       W4r(1,3)+endW4r(1)+startW4t(1) W4r(1,4)+startW4t(1)];
wall4(:,2) = [W4r(2,1)+startW4t(2), W4r(2,2)+endW4r(2)+startW4t(2), ...
       W4r(2,3)+endW4r(2)+startW4t(2), W4r(2,4)+startW4t(2)];

% line_wall4 = [wall4(1,1) wall4(1,2); wall4(2,1) wall4(2,2)];

%% Data storage pre-allocation
Statistics = zeros(n,8);  %Matrix to store interference statics that
will be output at the end of the script
IntersectionPoints = NaN((PRF_1/f_scan_1_mu)/2,3,n);    % Matrix to
store intersection points (doesn't need to be more than half the number
of pulse per scan)
ReflectedInterferencePoints = NaN((PRF_1/f_scan_1_mu)/10,3,n);  %Matrix
to store of reflected interference (allocated 1/10 of all pulses)
DirectErroneousPoints = NaN((PRF_1/f_scan_1_mu)/2,3,n);   %Matrix to
store erroneous ranging points from direct interference
ReflectedErroneousPoints = NaN((PRF_1/f_scan_1_mu)/10,3,n); %Matrix to
store erroneous ranging points from direct interference less deadspace
ReflectedDeadspacePoints = NaN((PRF_1/f_scan_1_mu)/10,3,n); %Matrix to
store erroneous ranging points from direct interference that fall
within deadspace

%% Direct Interference Limits

% Angular Diameters of each Lidar
[azimuth_from_1to2, range_1to2] = cart2pol(x21, y21);  %Obtains the
azimuth from lidar 1 to lidar 2

angular_dia_2 = 2*atan(width_lidar_2/(2*range_1to2));  %Angular
diameter of lidar 2 from 1 (radians)
angular_dia_1 = 2*atan(width_lidar_1/(2*range_1to2));  %Angular
diameter of lidar 1 from 2 (radians)

% Direct Interference (DI) left and right limits (LL and RL) of scanner
1
% looking at scanner 2
```

```
DILL_1 = azimuth_from_1to2+angular_dia_2/2;       %Direct Interference
Left Limit for lidar 1
if DILL_1 >= 2*pi()
  DILL_1 = DILL_1-2*pi();
else
end

DIRL_1 = azimuth_from_1to2-angular_dia_2/2;       %Direct Interference
Rights Limit for lidar 1
if DIRL_1 < 0
  DIRL_1 = DIRL_1+2*pi();
else
end

% Direct Interference (DI) left and right limits (LL and RL) of scanner
2
% looking at scanner 1
if azimuth_from_1to2 >= pi()-angular_dia_1/2
  DILL_2 = azimuth_from_1to2-pi()+angular_dia_1/2;  %Direct
Interference Left Limit for lidar 2
else
  DILL_2 = azimuth_from_1to2+pi()+angular_dia_1/2;
end

if azimuth_from_1to2 >= pi()+angular_dia_1/2
  DIRL_2 = azimuth_from_1to2-pi()-angular_dia_1/2;  %Direct
Interference Right Limit for lidar 2
else
  DIRL_2 = azimuth_from_1to2+pi()-angular_dia_1/2;
end

%% Scanners' Scanning FOV Calculated
% Scanner 1 limits
left_limit_1 = azimuth_of_scan_1 + (scan_angle_1/2);    %Left limit of
scanning FOV relative to lidar orientation
if left_limit_1 >= 2*pi()
  left_limit_1 = left_limit_1-2*pi();
else
end

right_limit_1 = azimuth_of_scan_1 - (scan_angle_1/2);    %Right limit
of scanning FOV relative to lidar orientation
if right_limit_1 < 0
  right_limit_1 = right_limit_1+2*pi();
else
end

% Scanner 2 limits
left_limit_2 = azimuth_of_scan_2 + (scan_angle_2/2);    %Left limit of
scanning FOV relative to lidar orientation
if left_limit_2 >= 2*pi()
  left_limit_2 = left_limit_2-2*pi();
else
end

right_limit_2 = azimuth_of_scan_2 - (scan_angle_2/2);    %Right limit
of scanning FOV relative to lidar orientation
```

```
if right_limit_2 < 0
  right_limit_2 = right_limit_2+2*pi();
else
end


%% Interference Test

% Loop increments for each rotation of scanner 1
parfor i = 1:n   % i is the rotation number of scanner 1
  intersectionCounter = 0;
  directCounter = 0;
  nn = fix(number_of_scan_points_1(i)); %The number of scan angles
scanner 1 will complete for i^th rotation

  %Temporary memory allocation for inside parfor loop
  TempStatistics = zeros(1,8);  %Matrix to store interference statics
that will be output at the end of the script
  TempIntersectionPoints = NaN((PRF_1/f_scan_1_mu)/2,3);    % Matrix to
store intersection points (doesn't need to be more than half the number
of pulse per scan)
  TempReflectedInterferencePoints = NaN((PRF_1/f_scan_1_mu)/10,3);
%Matrix to store of reflected interference (allocated 1/10 of all
pulses)
  TempDirectErroneousPoints = NaN((PRF_1/f_scan_1_mu)/2,3);   %Matrix
to store erroneous ranging points from direct interference
  TempReflectedErroneousPoints = NaN((PRF_1/f_scan_1_mu)/10,3); %Matrix
to store erroneous ranging points from direct interference less
deadspace
  TempReflectedDeadspacePoints = NaN((PRF_1/f_scan_1_mu)/10,3); %Matrix
to store erroneous ranging points from direct interference that fall
within deadspace

  %% Loop increments for each ranging pulse of scanner 1
  for ii = 1:nn  %ii is the current pulse number scanner 1

    theta_1_prime = ((ii-1)*theta_inc1(i))-deg2rad(5);     %Scanner 1's
instantaneous angular orientation measured from unit circle 0degree
(LMS531 starts at -5 degrees)
    [x12,y12] = pol2cart(theta_1_prime,R_1max);  % Scanner 1's beam's
radiometric limit

    theta_2_prime = (theta_2_prime_0(i)+(ii-
1)*ratio_PRF2_1*theta_inc2(i))-deg2rad(5);  %Scanner 2's instantaneous
angle measured from unit circle 0degree

  %% Test Scan Limits
    %Tests whether theta_1_prime is within scanning FOV limits of
scanner 1
    theta_1_prime_within_left_limit = 0;    %Reset logic results from
previous iteration
    theta_1_prime_within_right_limit = 0;

    if right_limit_1 > left_limit_1   %The case when scanning FOV
contains 0degrees within its left and right limits
      if theta_1_prime >= right_limit_1
        theta_1_prime_within_right_limit = 1;
```

```
        theta_1_prime_within_left_limit = (theta_1_prime <
left_limit_1+2*pi());

      elseif theta_1_prime <= left_limit_1
        theta_1_prime_within_left_limit = 1;
        theta_1_prime_within_right_limit = (theta_1_prime >
right_limit_1-2*pi());
      end
    else
      theta_1_prime_within_right_limit = (theta_1_prime >
right_limit_1);
      theta_1_prime_within_left_limit = (theta_1_prime < left_limit_1);
    end


    theta_1_prime_in_limit = and(theta_1_prime_within_left_limit,
theta_1_prime_within_right_limit); % 1 when theta_1_prime is in limits,
0 else

    if theta_1_prime_in_limit == 1
      TempStatistics(1,1) = TempStatistics(1,1)+1;   %Increments 1 for
each ranging pulse transmitted by scanner 1
    else
    end

    %Test whether theta_2_prime is within scanning limits
    theta_2_prime_within_left_limit = 0;    %Reset logic results from
previous iteration
    theta_2_prime_within_right_limit = 0;

    if right_limit_2 > left_limit_2
      if theta_2_prime >= right_limit_2
        theta_2_prime_within_right_limit = 1;
        theta_2_prime_within_left_limit = (theta_2_prime <
left_limit_2+2*pi());

      elseif theta_2_prime <= left_limit_2
        theta_2_prime_within_left_limit = 1;
        theta_2_prime_within_right_limit = (theta_2_prime >
right_limit_2-2*pi());
      end
    else
      theta_2_prime_within_right_limit = (theta_2_prime >
right_limit_2);
      theta_2_prime_within_left_limit = (theta_2_prime < left_limit_2);
    end

    theta_2_prime_in_limit = and(theta_2_prime_within_left_limit,
theta_2_prime_within_right_limit);


    if theta_1_prime_in_limit == 1 && theta_2_prime_in_limit == 1
      % scanners are both within their search window, therefore, both
      % scanners are transmitting/receiving ranging pulses and
      % interference can occur so proceed with interference test
      %% Direct Interference Test
      % Check to see if there is direct interference
```

```
      theta_1_prime_within_DIRL = 0;     %Reset logic positions
      theta_1_prime_within_DILL = 0;
      theta_2_prime_within_DIRL = 0;
      theta_2_prime_within_DILL = 0;

      % Check to make sure Lidar 1 is oriented at lidar 2
      if DIRL_1 > DILL_1 % The case when scanner 2 is directly to the
right of scanner 1
        if theta_1_prime >= DIRL_1
          theta_1_prime_within_DIRL = 1;
          theta_1_prime_within_DILL = (theta_1_prime < DILL_1+2*pi());

        elseif theta_1_prime <= DILL_1
          theta_1_prime_within_DILL = 1;
          theta_1_prime_within_DIRL = (theta_1_prime > DIRL_1-2*pi());
        end
      else
        theta_1_prime_within_DIRL = (theta_1_prime > DIRL_1);
        theta_1_prime_within_DILL = (theta_1_prime < DILL_1);
      end

      theta_1_prime_within_DI = and(theta_1_prime_within_DIRL,
theta_1_prime_within_DILL); %Lidar 1 is looking at lidar 2

      % Check to make sure Lidar_2 is oriented at Lidar 1
      if DIRL_2 > DILL_2
        if theta_2_prime >= DIRL_2
          theta_2_prime_within_DIRL = 2;
          theta_2_prime_within_DILL = (theta_2_prime < DILL_2+2*pi());

        elseif theta_2_prime <= DILL_2
          theta_2_prime_within_DILL = 1;
          theta_2_prime_within_DIRL = (theta_2_prime > DIRL_2-2*pi());
        end
      else
        theta_2_prime_within_DIRL = (theta_2_prime > DIRL_2);
        theta_2_prime_within_DILL = (theta_2_prime < DILL_2);
      end

      theta_2_prime_within_DI = and(theta_2_prime_within_DIRL,
theta_2_prime_within_DILL); %Lidar 2 is looking at lidar 1

      if theta_1_prime_within_DI == 1 && ...
          theta_2_prime_within_DI == 1   % Direct interference has
occurred

        if TestNumber == 6
          ErroneousRange =
random('Lognormal',0.401090985039766,0.375838842535286);   %Generates
an erroneous ranging point from interference
          while ErroneousRange > R_1max
            ErroneousRange =
random('Lognormal',0.401090985039766,0.375838842535286);  %Ensures the
erroneous point is under max range of scanner 1
          end
        elseif TestNumber == 8
```

```
          ErroneousRange =
random('Lognormal',2.060438553980358,1.636550582178633);
          while ErroneousRange > R_1max
            ErroneousRange =
random('Lognormal',2.060438553980358,1.636550582178633);  %Ensures the
erroneous point is under max range of scanner 1
          end
        end

        directCounter = directCounter+1;
        TempStatistics(1,2) = TempStatistics(1,2)+1;   %Keeps count of
number of direct interferences points


[TempDirectErroneousPoints(directCounter,1),TempDirectErroneousPoints(d
irectCounter,2)] = pol2cart(theta_1_prime,ErroneousRange);
        TempDirectErroneousPoints(directCounter,3) = ii;
      %% Dissociated Interference
      elseif theta_1_prime_within_DI == 0 && ...
          theta_2_prime_within_DI == 1


      %% Reflected Interference
      elseif theta_1_prime_within_DI == 0 && ...
          theta_2_prime_within_DI == 0

      %If true, test for reflected interference; if not, exit loop

      [x22_relative,y22_relative] = pol2cart(theta_2_prime,R_2max);
      x22 = x22_relative+x21;     %Finds the absolute coordinate from
initial position of x21
      y22 = y22_relative+y21;     %Finds the absolute coordinate from
initial position of y21

      Beam1 = [x11 y11; x12 y12];   %Scanner 1's beam
      Beam2 = [x21 y21; x22 y22];   %Scanner 2's beam

%       Uncomment to troubleshoot where lidar 1 and 2 are looking
%           figure (1)
%           plot(Beam1(:,1),Beam1(:,2),'b',Beam2(:,1),Beam2(:,2),'r')
%
%       Ref for line intersection code:
https://blogs.mathworks.com/loren/2011/08/29/intersecting-
lines/?s_cid=fb_wall_10-21-11_loren_lines

      % Calculates slope and intercept of a line y=mx+b
      slope = @(line) (line(2,2) - line(1,2))/(line(2,1) - line(1,1));
      m1 = slope(Beam1);   %Slope of beam 1
      m2 = slope(Beam2);   %Slope of beam 2

      intercept = @(line,m) line(1,2) - m*line(1,1);
      b1 = intercept(Beam1,m1);  % y-intercept of beam 1
      b2 = intercept(Beam2,m2);  % y-intercept of beam 2

      if m1 == inf  %Occurs when the beam 1 is vertical
        xintersect = Beam1(1,1);  %x coordinate of beams' 1 and 2 (must
occur beam 1's origin if vertical)
```

```
      else
        xintersect = (b2-b1)/(m1-m2);  %x intersection beams 1
(calculated for lines not line segments)
      end

      yintersect = m1*xintersect + b1;  %y coordinate of intersection
between beams 1 and 2 (calculated for lines not line segments)

      isPointInside = @(xint,myline) ... % checks whether intersection
point lays within both beams (*does not fully account for radiometric
limits of both lidars)
        (xint >= myline(1,1) && xint <= myline(2,1)) || ...
        (xint >= myline(2,1) && xint <= myline(1,1));
      inside = isPointInside(xintersect,Beam1) && ...
           isPointInside(xintersect,Beam2);

         if inside == 1 %Record the point as an intersection point
           intersectionCounter = intersectionCounter+1
           TempStatistics(1,3) = TempStatistics(1,3)+1;  %Counts number
of intersection events have occurred
           TempIntersectionPoints(intersectionCounter,:) = [xintersect
yintersect ii];

         %% Interference Test
         %Checks to see if intersection point falls within target
         %geometry tolerance
         InterferenceTest =
inpolygon(xintersect,yintersect,wall1(:,1)',wall1(:,2)') || ...
              inpolygon(xintersect,yintersect,wall2(:,1)',wall2(:,2)')
|| ...
              inpolygon(xintersect,yintersect,wall3(:,1)',wall3(:,2)')
|| ...
              inpolygon(xintersect,yintersect,wall4(:,1)',wall4(:,2)');

          if InterferenceTest == 1

            TempStatistics(1,4) = TempStatistics(1,4)+1;   %Keeps count
of number of interferences points without accounting for deadspace from
receiver response
            TempReflectedInterferencePoints(TempStatistics(1,4),:) =
[xintersect yintersect ii];

        %% Receiver delay in detecting sequential events
          %Test to see if the false range falls inside of the
          % receiver delay time after the wall. Assumes that a
          % return will be detected at obstacle,
          % therefore, due to the response temporal resolution of
          % the detector, there will be deadspace of interference
          % points received during the temporal response time after
          % a target.

            ErroneousRange = 0+rand(1,1)*R_1max;   %Randomly generated
an erroneous range error at azimuth of interference event
            [Erroneous_x,Erroneous_y] =
pol2cart(theta_1_prime,ErroneousRange);
```

```
            if not(ErroneousRange > pdist([xintersect, yintersect; x11,
y11 ]) && ...
                  ErroneousRange - pdist([xintersect, yintersect; x11,
y11 ]) < reciever_delay_distance) %Erroneous point is outside of
deadspace


              TempStatistics(1,5) = TempStatistics(1,5)+1;   %Keeps
count of number of interferences points outside of the deadspace

              TempReflectedErroneousPoints(TempStatistics(1,5),:) =
[Erroneous_x Erroneous_y ii];

            else %Erroneous point is inside of deadspace

              TempReflectedDeadspacePoints(TempStatistics(1,4)-
TempStatistics(1,5),:) = [Erroneous_x Erroneous_y ii];

            end
          end
        end
      end
    end
  end
  TempStatistics(1,6) = TempStatistics(1,2)/TempStatistics(1,1);
%Calculates the fraction of direct intersection per rotation
  TempStatistics(1,7) = TempStatistics(1,5)/TempStatistics(1,1);
%Calculates the fraction of direct intersection per rotation
  TempStatistics(1,8) = TempStatistics(1,6) + TempStatistics(1,7);
%Calculate the total fraction of interfering per rotation


  % Transfer store the temp variables

  Statistics(i,:) = TempStatistics;
  IntersectionPoints(:,:,i) = TempIntersectionPoints;        % Matrix
to store intersection points (doesn't need to be more than half the
number of pulse per scan)
  ReflectedInterferencePoints(:,:,i) = TempReflectedInterferencePoints;
%Matrix to store of reflected interference
  DirectErroneousPoints(:,:,i) = TempDirectErroneousPoints;     %Matrix
to store erroneous ranging points from direct interference
  ReflectedErroneousPoints(:,:,i) = TempReflectedErroneousPoints;
%Matrix to store erroneous ranging points from direct interference less
deadspace
  ReflectedDeadspacePoints(:,:,i) = TempReflectedDeadspacePoints;
%Matrix to store erroneous ranging points from direct interference that
fall within deadspace

end

DirectErroneousPointsPlot = num2cell(DirectErroneousPoints,[1,2]);
DirectErroneousPointsPlot = vertcat(DirectErroneousPointsPlot{:});

ReflectedErroneousPointsPlot =
num2cell(ReflectedErroneousPoints,[1,2]);
```

```
ReflectedErroneousPointsPlot =
vertcat(ReflectedErroneousPointsPlot{:});


% Plot
figure(1)
p = plot(x11,y11,'ks',x21,y21,'kd',...
  wall1(:,1),wall1(:,2),'g',...

DirectErroneousPointsPlot(:,1),DirectErroneousPointsPlot(:,2),'r.',...

ReflectedErroneousPointsPlot(:,1),ReflectedErroneousPointsPlot(:,2),'r.
',...
  wall2(:,1),wall2(:,2),'g',wall3(:,1),wall3(:,2),'g',...
  x11,y11,'ks',x21,y21,'kd');
legend('Lidar 1','Lidar 2', 'In Tolerance Points', 'Out of Tolerance
Points','Location','northwest')
p(1).LineWidth = 2.1;
p(2).LineWidth = 2;
xlabel('Distance (m)')
ylabel('Distance (m)')
xlim([-90 90])
ylim([-10 90])
grid on
grid minor
box on
set(gcf,'position',[1 1 700 400]);

axes('Position',[.7 .7 .2 .2])
box on
s = plot(x11,y11,'ks',x21,y21,'kd',...
  wall1(:,1),wall1(:,2),'g',...

DirectErroneousPointsPlot(:,1),DirectErroneousPointsPlot(:,2),'r.',...

ReflectedErroneousPointsPlot(:,1),ReflectedErroneousPointsPlot(:,2),'r.
',...
   wall2(:,1),wall2(:,2),'g',wall3(:,1),wall3(:,2),'g',...
   x11,y11,'ks',x21,y21,'kd');
s(1).LineWidth = 2.1;
s(2).LineWidth = 2;
xlim([-6 6])
ylim([-1 6])
grid on
grid minor

%Statistics

AvgPulsePerRotation = mean(Statistics(:,1));     %Gives the average
number of pulses per rotation
AvgDirectInterference = mean(Statistics(:,2));  %Gives the average
direct interfering pulses
AvgIntersecting = mean(Statistics(:,2));     %Gives the average
intersecting pulses
AvgReflectInterferece = mean(Statistics(:,4));  %Gives the average
fraction of reflection interference pulse
```

```
AvgFractionInterference = mean(Statistics(:,5)); %Gives the average
fraction of all interference pulses
AvgF = AvgIntersecting/AvgPulsePerRotation;   %Average fraction of
intersection F

AverageStatistics = table(ExperimentName, AvgPulsePerRotation,
AvgDirectInterference,...
  AvgIntersecting, AvgReflectInterferece, AvgFractionInterference,
AvgF);

TotalPulses = sum(Statistics(:,1));     %Total Number of pulses
TotalDirect = sum(Statistics(:,2));     %Total Number of pulses
TotalIntersection = sum(Statistics(:,3));     %Total Number of pulses
TotalReflectionEvents = sum(Statistics(:,4));     %Total Number of
pulses
TotalReflectionEventsLessDeadspace = sum(Statistics(:,5));     %Total
Number of pulses
TotalInterferenceWithDS = TotalDirect+TotalReflectionEvents;
TotalInterferenceLessDS =
TotalDirect+TotalReflectionEventsLessDeadspace;
FactionDirect = TotalDirect/TotalPulses;
TotalF = TotalIntersection/TotalPulses;
FractionTotalReflected = TotalReflectionEvents/TotalPulses;
FractionReflectedLessDS =
TotalReflectionEventsLessDeadspace/TotalPulses;
FractionTotalInterference =
(TotalReflectionEventsLessDeadspace+TotalDirect)/TotalPulses;

TotalStatistics = table(ExperimentName, TotalPulses, TotalDirect,...
  TotalIntersection, TotalReflectionEvents,
TotalReflectionEventsLessDeadspace,...
  TotalInterferenceWithDS, TotalInterferenceLessDS, ...
  FactionDirect, TotalF, FractionTotalReflected,
FractionReflectedLessDS, FractionTotalInterference);

savefig(FigName)
saveas(figure(1),GraphicName)
%
save(VariablesName,'theta_2_prime_0','f_scan_1','f_scan_2','Statistics'
,...
%   'ReflectedInterferencePoints','DirectErroneousPoints',...
%   'ReflectedErroneousPoints','ReflectedDeadspacePoints',...
%   'IntersectionPoints')

save(VariablesName)


end
```

REFERENCES

[1] P. F. McManamon, G. Kamerman, and M. Huffaker, "A history of laser radar in the United States," in *SPIE Defense, Security, and Sensing*, Orlando, FL, USA, 2010, vol. 7684, p. 11: SPIE.

[2] L. D. Smullin and G. Fiocco, "Optical Echoes from the Moon," vol. 194, p. 1267, June 30, 1962.

[3] H. Jensen, "Performance Of An Airborne Laser Profiler," in *Airborne Photo-optical Instrumentation*, Cocoa Beach, FL, 1967, vol. 0008, p. 6: SPIE.

[4] R. C. Olsen, *Remote Sensing from Air and Space*, 2nd ed. Bellingham, WA, USA: SPIE Press, 2016.

[5] J. Rosette, J. Suárez, P. North, and S. Los, "Forestry Applications for Satellite Lidar Remote Sensing," vol. 77, no. 3, pp. 271-279, Mar. 2011.

[6] E. Widyaningrum and B. G. H. Gorte, "Challenges and opportunities: One stop processing of automatic large-scale base map production using airborne lidar data within gis environment case study: Makassar City, Indonesia," in *ISPRS Hannover Workshop: HRIGI 17 – CMRT 17 – ISA 17 – EuroCOW 17*, Hannover, Germany, 2017, vol. 42, pp. 365-369: Copernicus GmbH.

[7] J. Brady, "Army uses technology to increase aerial delivery accuracy," May 11, 2018. Accessed on: Mar. 22, 2018Available: https://www.army.mil/article/167678/army_uses_technology_to_increase_aerial_delivery_accuracy

[8] V. I. Feygels, J. Y. Park, J. Aitken, M. Kim, A. Payment, and V. Ramnath, "Coastal Zone Mapping and Imaging Lidar (CZMIL): first flights and system validation," in *SPIE Remote Sensing*, Edinburgh, United Kingdom, 2012, vol. 8532, p. 10: SPIE.

[9] J. T. Murray *et al.*, "Dust-Penetrating (DUSPEN) “see-through” lidar for helicopter situational awareness in DVE," in *SPIE Defense, Security, and Sensing*, Baltimore, MD, 2013, vol. 8737, p. 8: SPIE.

[10] J. H. Churnside and J. J. Wilson, "Airborne lidar imaging of salmon," *Appl. Opt.*, vol. 43, no. 6, pp. 1416-1424, Feb. 20, 2004.

[11] S. Turbide, L. Marchese, M. Terroux, and A. Bergeron, "Synthetic aperture ladar concept for infrastructure monitoring," in *SPIE Security + Defence*, Amsterdam, Netherlands, 2014, vol. 9250, p. 8: SPIE.

[12] J. A. Christian and S. P. Cryan, "A Survey of LIDAR Technology and Its Use in Spacecraft Relative Navigation," presented at the Navigation and Control Conf., Boston, MA, Aug. 19-22, 2013.

[13] J. Hecht, "Lidar for Self-Driving Cars," *Opt. Photon. News*, vol. 29, no. 1, pp. 26-33, Jan. 1, 2018.

[14] D. Watzenig and M. Horn, *Automated Driving Safer and More Efficient Future Driving*. Switzerland: Springer, Cham, 2017.

[15] V. Molebny, G. Kamerman, and O. Steinvall, "Laser radar: from early history to new trends," in *SPIE Security + Defence*, Toulouse, France, 2010, vol. 7835, p. 30: SPIE.

[16] T. B. Lee. (2018, Feb. 7,). *Why experts believe cheaper, better lidar is right around the corner*. Available: https://arstechnica.com/cars/2018/01/driving-around-without-a-driver-lidar-technology-explained/

[17] G. Kim, J. Eom, S. Park, and Y. Park, "Occurrence and characteristics of mutual interference between LIDAR scanners," in *SPIE Optics + Optoelectronics*, Prague, Czech Republic, 2015, vol. 9504, p. 9: SPIE.

[18] G. Kim, J. Eom, and Y. Park, "Investigation on the occurrence of mutual interference between pulsed terrestrial LIDAR scanners," in *2015 IEEE Intelligent Vehicles Symposium (IV)*, Soel, South Korea, 2015, pp. 437-442.

[19] A. L. Diehm, M. Hammer, M. Hebel, and M. Arens, "Mitigation of crosstalk effects in multi-LiDAR configurations," in *SPIE Security + Defence*, Berlin, Germany, 2018, vol. 10796, p. 12: SPIE.

[20] J. Petit, B. Stottelaar, M. Feiri, and F. Kargl, "Remote Attacks on Automated Vehicles Sensors: Experiments on Camera and LiDAR," presented at the Black Hat Europe, 2015. Available: https://pdfs.semanticscholar.org/e06f/ef73f5bad0489bb033f490d41a046f61878a.pdf

[21] H. Shin, D. Kim, Y. Kwon, and Y. Kim, "Illusion and Dazzle: Adversarial Optical Channel Exploits Against Lidars for Automotive Applications," in *Cryptographic Hardware and Embedded Systems – CHES 2017*, Taipei, Taiwan, 2017, pp. 445-467: Springer International Publishing.

[22] F. Zhang, P. Du, Q. Liu, M. Gong, and X. Fu, "Adaptive strategy for CPPM single-photon collision avoidance LIDAR against dynamic crosstalk," *Opt. Express*, vol. 25, no. 11, pp. 12237-12250, May 29, 2017.

[23] G. Kim, J. Eom, and Y. Park, "Design and implementation of 3D LIDAR based on pixel-by-pixel scanning and DS-OCDMA," in *SPIE OPTO*, San Francisco, CA, 2017, vol. 10107, p. 8: SPIE.

[24] G. Kim, J. Eom, and Y. Park, "Design of pulsed scanning lidar without mutual interferences," in *SPIE OPTO*, San Fransico, CA, 2018, vol. 10536, p. 6: SPIE.

[25] C.-H. Cheng, C.-Y. Chen, J.-D. Chen, D.-K. Pan, K.-T. Ting, and F.-Y. Lin, "3D pulsed chaos lidar system," *Opt. Express,* vol. 26, no. 9, pp. 12230-12241, April 30, 2018.

[26] T. Fersch, R. Weigel, and A. Koelpin, "A CDMA Modulation Technique for Automotive Time-of-Flight LiDAR Systems," vol. 17, no. 11, pp. 3507-3516, June 1, 2017.

[27] J. Hao *et al.*, "A novel CPPM anti-crosstalk collision avoidance lidar with ultra-low laser power," in *Eighth International Symposium on Advanced Optical Manufacturing and Testing Technology (AOMATT2016)*, Suzhou, China, 2016, vol. 9686, p. 9: SPIE.

[28] "Automotive LiDAR Market Report," Woodside Capital Partners; April, 2018, Available: https://www.osa.org/en-us/corporate_gateway/publication_report_library/automotive_lidar_market_report/.

[29] A. Al-Hourani, R. J. Evans, S. Kandeepan, B. Moran, and H. Eltom, "Stochastic Geometry Methods for Modeling Automotive Radar Interference," vol. 19, no. 2, pp. 333-344, Feb. 2018.

[30] T. S. Andreas John, "Conclusion and outlook how to solve still open challenges," in "MOre Safety for All by Radar Interference Mitigation," European CommisionDec. 21, 2012.

[31] M. Kunert and R. Bosch, "Project Final Report," in "MOre Safety for All by Radar Interference Mitigation," European Commision, Dec. 21, 2012.

[32] W. Weidmann and F. Torres, "Requirements and specification of a norm interferer," in "MOre Safety for All by Radar Interference Mitigation," European Commision, Aug. 31 2010.

[33] A. John, M. Kunert, and T. Schipper, "Estimation of interference risk from incumbent frequency users and services," in "MOre Safety for All by Radar Interference Mitigation," European Commision, Dec. 22, 2010.

[34] T. Schipper, "Multi-interference modeling and effects," in "MOre Safety for All by Radar Interference Mitigation," European Commision, Aug. 24 2012.

[35] G. M. Brooker, "Mutual Interference of Millimeter-Wave Radar Systems," vol. 49, no. 1, pp. 170-181, Feb. 1, 2007.

[36] R. L. S. Frank H. Sanders, Brent L. Bedford, David Franc, Timothy Pawlowitz, "Effects of RF Interference on Radar Receivers," in "Effects of Radio Frequency

Interference on Radar Receivers," US Department of Commerce, Washington, D.C.2006, Available: https://permanent.access.gpo.gov/gpo125/06-444.pdf.

[37] H. Tang, X. Wan, J. Yi, Y. Liu, and H. Ke, "Performance of the least squares filter for passive radar interference cancellation applications," vol. 11, no. 8, pp. 1208-1215, June 16, 2017.

[38] T. Schipper, "Simulation Setup Assessment: Interferer - Free Space Propagation - Victim Radar," in "MOre Safety for All by Radar Interference Mitigation," European Commision, Dec. 22 2011.

[39] T. Schipper, A. John, and M. Kunert, "Generation of an Interference Susceptibility Model for the Different Radar Principles," in "MOre Safety for All by Radar Interference Mitigation," European Commision, Feb. 28 2011.

[40] W. Wen-Qin and S. Huaizong, "Radar-to-Radar Interference Suppression for Distributed Radar Sensor Networks," vol. 6, no. 1, pp. 740-755, Jan. 9, 2014.

[41] M. Kunert, H. Meinel, C. Fischer, and M. Ahrholdt, "Report on interference density increase by market penetration forecast," in "MOre Safety for All by Radar Interference Mitigation," European Commision, Sep. 30, 2010.

[42] "Laser Radar: Progress and Opportunities in Active Electro-Optical Sensing," National Research Council, Washington, DC, USA, Book 2014.

[43] P. F. McManamon, *Field Guide to Lidar*. Bellingham, WA, USA: SPIE, 2015.

[44] P. P. Smith, "AMCW LIDAR Range Acquisition," in *Active Sensors for Local Planning in Mobile Robotics*, vol. 26, C. J. Harris, Ed. (World Scientific Series in Robotics and Intelligent Systems, Singapore: World Scientific Publishing Co Pte Ltd, 2014.

[45] R. Horaud, M. Hansard, G. Evangelidis, and C. Ménier, "An overview of depth cameras and range scanners based on time-of-flight technologies," *Mach. Vision and Appl.*, vol. 27, no. 7, pp. 1005-1020, 2016.

[46] V. Molebny, P. F. McManamon, O. Steinvall, T. Kobayashi, and W. Chen, "Laser radar: historical prospective—from the East to the West," *Opt. Eng.*, vol. 56, p. 24, 2016.

[47] S. Dimitrijev, "6.1.4 Breakdown Phenomena," in *Principles of Semiconductor Devices*2nd ed. New York, NY: Oxford University Press, p. 203.

[48] J. Shan, *Topographic Laser Ranging and Scanning Principles and Processing*. Boca Raton, FL, USA: CRC Press, 2009.

[49] P. Gatt, S. Johnson, and T. Nichols, "Geiger-mode avalanche photodiode ladar receiver performance characteristics and detection statistics," *Appl. Opt.*, vol. 48, no. 17, pp. 3261-3276, June 10, 2009.

[50] K. Seongjoon, L. Impyeong, and K. Yong Joon, "Simulation of a Geiger-Mode Imaging LADAR System for Performance Assessment," Article vol. 13, no. 7, pp. 8461-8489, July 3, 2013.

[51] G. Brooker, "Introduction to Sensors for Ranging and Imaging," ed. Raleigh, NC: SciTech Publishing, 2009.

[52] G. B. Popko, Y. Bao, T. K. Gaylord, and C. R. Valenta, "Beam Path Intersections between Two Coplanar Lidar Scanners," *Opt. Eng.*, vol. 58, no. 3, Mar. 2019.

[53] VLP-16 User Manual: Velodyne LiDAR, 2017. [Online]. Available: https://velodynelidar.com/vlp-16.html. Accessed on May. 25, 2018.

[54] LMS5xx Laser Measurement Sensors: Operating Instructions, Waldkirch, Germany: SICK AG, 2017. [Online]. Available: https://cdn.sick.com/media/docs/4/14/514/Operating_instructions_LMS5xx_LASER_MEASUREMENT_SENSORS_en_IM0037514.PDF. Accessed on Jan. 25, 2019.

[55] LMS5xx Laser Measurement Technology - Product Information, Waldkirch, Germany: SICK AG, 2012, p. 32. [Online]. Available: https://www.sick.com/us/en/detection-and-ranging-solutions/2d-lidar-sensors/lms5xx/lms531-11100/p/p275448. Accessed on Feb. 7, 2019.

[56] Velodyne LiDar Puck: Real-Time 3d LiDAR Sensor Datasheet, Morgan Hill, CA: Velodyne LiDAR, 2018. [Online]. Available: https://velodynelidar.com/vlp-16.html. Accessed on May. 25, 2018.

[57] LMS531 Security Outdoor Laser Measurement Sensors - Technical Information, Waldkirch, Germany: SICK AG, 2014, p. 32. [Online]. Available: https://www.sick.com/us/en/detection-and-ranging-solutions/2d-lidar-sensors/lms5xx/lms531-11100/p/p275448. Accessed on Feb. 7, 2019.